Photoinduced deformation in thin films containing azo-derivatives: reversible and directional matter transport controlled by light polarization and photomechanical surface effects

Fabbri Filippo

Thèse de doctorat de l'Ecole Polytechnique

Spécialité: Physique

présentée par

Filippo Fabbri

pour obtenir le titre de Docteur de l'Ecole Polytechnique

Sujet:

Déformation photoinduite dans les films minces contenant des dérivés de l'azobenzène: effets de polarisation, de proximité et de contact

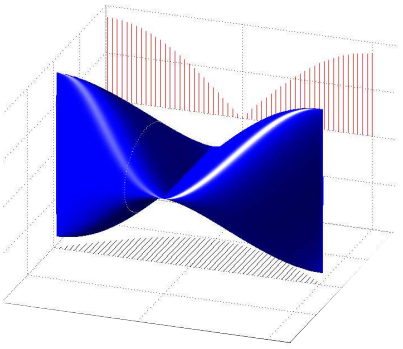

soutenue le 6 novembre 2009 devant le jury composé de:

M.	Renaud Bachelot	rapporteur
M.	Jean-Pierre Boilot	examinateur
M.	Daniel Courjon	président
Mme	Céline Fiorini	rapporteur
M.	Yves Lassailly	directeur de thèse
M.	Salvatore Monaco	co-directeur de thèse
M.	Jacques Peretti	examinateur

Abstract

In this work we use direct local-probe techniques to study the photomechanical phenomena induced at micro-nanoscale in photochromic thin films containing azobenzene molecules. We show the existence of different mechanisms at the origin of the photo-induced deformation and their crucial dependence on the spatial distribution of the light field polarization and intensity, which allows to coherently interpret far-field and near-field photodeformation phenomena so far observed. Moreover, we investigate the near-field deformation effects due to the interaction between the local probe and the sample surface. Finally, we present preliminary studies of the photomechanical effects in layered hybrid metal/azo-polymer structures which open perspectives in view of applications in the fields of nano-fabrication and nano-actuation of thin films and surfaces.

Acknowledgements

At the beginning it was like surgery by a mammoth. I had to spend these long days with all the circuitry wide open and the wrong voltages going up and down with no possible chance on earth of getting a reasonable signal. Every manipulation fixed one thing and ruined two, with unpredictable consequences... while that noise was killing me. It had been changing over and over, as the tiny little bug ran through the corridor or the sky switched from grey to dark-grey. Impossible to tell what exactly was going on, were we heading somewhere? If only the guy could read that oscilloscope more swiftly. Or just make a new tip for the microscope... Frankly, I had some kind of mistrust.

So far, everybody had been extremely professional with me. I had been kept fully functional by The Two Red-shifted Researchers, very fine people. I had even received a new brain by a funny, Questioning Man, who, by the way, has a deep baritone voice, I'd love to play music with him sometimes, but he is always too busy fixing stuff... Well, I felt so fit that I decided to reward them with some nice results on those tiny colored glasses of theirs...

But now, this new guy was really pushing my buttons ... and turning my knobs in every sense, trying to make me work with the wrong set-point and a broken tip! It was painful. I wonder how the Illustre Chief could do this to me, and accept this guy in the lab. I heard that he was sent by a Stylish Monk from Rome, who is very wise and knowledgeable. That was my only hope. But, I confess, I spent long nights praying that the young guy would rather remain at home with that Quebecoise Girl I met a few times (who really didn't like me) instead of coming to the lab.

To my great horror, he actually started coming more often. But something was changing. He was acting more and more carefully, similarly to The Two Red-shifted Researchers who had made me so happy before. I caught him listening to them while they were explaining him things and every time he was not blinding my photo-multiplicator, I watched him trying to calibrate me, with his notes, schemes and plots... uhm... Then the young guy started visiting me together with other people. At the beginning I recognized one of my parents, the Great Mechanic. He was asked to perform some surgery on me, in order to upgrade a couple of components. I trusted that experienced crafstman; I only hoped that the young guy had the scheme drawn right! Sometimes, there was also The Engineer Swat Team giving me some boost or buzz, extremely pleasant, or the Questioning Man wanting to fix some neurons of mine. Lately, I met the Great Mechanic II, who helped me with my last upgrades. A happy man, he doesn't know but I can hear him laughing from his office... Thanks also to those Exquisite Ladies, that helped so efficiently the guy to work out the papers and the orders I'm going to be a

full-option five-star microscope! And, I'll be not alone, since it seems that little brothers and sisters are on their way...

Well, actually things were going better. Now the guy could take the screwdriver and the wax-solder and calibrate me with no harm; he could even fabricate beautiful, sharp optical-fiber tips. I was feeling fully functional again and willing to play. So, it was a pleasure for me to fish out some nice results on the beloved colored glasses. I really wanted to give them more, but, I must admit, my fragile nature forces me to rest (ok, break down) more often than I would like to. The guy had it very hard to make those samples, even under the precious guide of The Eminent Chemists. But in the end it was a success and I was very pleased to see the young guy and The Two Red-shifted Researchers so excited, making models and calculations and writing pages and pages... If only the young guy had written those chapters and paragraphs in the right order in the first place, The Two Red-shifted Researchers could have slept more...

Well-well, now that days and weeks have passed I can tell, frankly, that we had a great time. Sometimes, students come to see me and I'm very proud hearing the guy and The Two Red-shifted Researchers telling about my grandiosity. Also, I have heard that my beauty has been praised in conferences all over the world and rumors report that they were really fun. Wow, I wish I weighted less, so I could have gone in person...

Recently, it was very exciting to officially celebrate and discuss the precious results of our work. The Illustre Jury was extremely kind and interested and I've never felt observed so much, so close, so in detail. I was almost turning red ... Moreover, it was extremely touching to see the whole Tribù coming over from so far away, to stay close to the guy and to organize the feast. It was amazing.

I'm only a little bit sad that the young guy is about to leave. I think I'm going to miss him. Well, well, maybe if there is time, I think I still have some nice results on those colored glasses, left up my sleeve...

With my greatest thanks to:

The Two Red-shifted Researchers:	Jacques Peretti and Yves Lassailly
The Stylish Monk:	Prof. Salvatore Monaco
The Illustre Jury:	Renaud Bachelot, Jean-Pierre Boilot, Daniel Courjon, Céline Fiorini
The Illustre Chief:	François Ozanam
The Questioning Man:	Fouad Maroun

The Eminent Chemists:	Khalid Lahlil, Anne Moraillon, Laetitia Vieille, Sandrine Perruchas, Thierry Gacoin, Jean-Pierre Boilot, Cédric Tard
The Great Mechanics:	André Wack, Dominique Clément, Bernard Mathon
The Engineer Swat Team:	Julien Monguillon, Didier Lenoir, Denis Coupvent-Desgraviers, Thomas Dachy, Patrice Delaroque
The Exquisite Ladies:	Anne-Marie Jonqueres, Eve Brunswic, Anne-Marie Herneq, Annie Stephan
The Tribù:	Mamma, Papo, Ludo, Benny, Nonni, Nina, Marco, Luigi, Genevieve, Mina, Nicole, Jacques, Claude-nuvola, Alain,...
My Quebecoise girl:	Eugénie

A special thank to:

Jean-Noël Chazalviel, Catherine Henry de Villeneuve and Ubirajara Pereira Rodrigues Filho for the fascinating and intense introduction to the mysteries of the IR-ATR.

Robert Cortès for the interesting conversations and also for all the explanations on the X-ray that he gave to Hugo and to the other students, that I over-heard.

Alistair Rowe, Daniel Paget, Hervé Henry, Mathis Plapp and François Devreux for the fruitful discussions.

Georges Lampel and Lionel Solomon for their pearls of wisdom.

Mme Dorothée Normand-Cyrot for her support and her kindness.

François Plais for the wonderful collaboration with the CAPS.

And also many many thanks to all the other people with which I worked, talked, played, danced, ate, chatted, brought tables, cooked, cleaned, brought tables back, laughed, spoken Chinese, Brazilian and Vietnamese. I had really a fantastic time.

Filippo Fabbri

Contents

List of Figures

List of Tables

L'opera che comunica ha una complessità pari a quella di colui che osserva.
La visione dell'opera nasce dal loro incontro.

Giancarlo Moscara

La verità del gigante è nel nano.

Pinuccio Saponaro

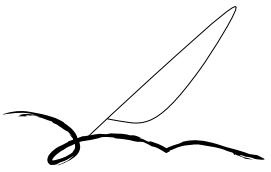

Introduction

The present work is dedicated to the study of the photodeformation effects induced at micro-nanoscale in photoactivable systems. In particular, we investigate the photomechanical response of photochromic thin films containing an azobenzene derivate, the Disperse Red 1 (DR1) grafted to a mineral sol-gel matrix or to an organic polymer (PMMA) backbone. Since their first discovery in 1995 [1, 2], these phenomena have been widely investigated under various illumination configurations [3–9]. Experiments performed with far field photo-excitation by focused gaussian beams [10, 11], Bessel beams [12] and interfering beams [1, 2, 8, 13, 14] have demonstrated that the efficiency of the deformation process and the shape of the photoinduced pattern are very much dependent on the light polarization distribution. Experiments performed with near-field excitation by a local light source [6, 15] have shown a specific photomechanical response which exhibits apparent contradictory behaviors when compared to far field configurations, but which confirms the important role of the polarization.

The understanding of the mechanisms at the origin of the photodeformation phenomena is still debated [16–18]. First, it requires to establish the relationship between the photodeformation and the properties of the light excitation, namely power density, dose, polarization and spatial distribution. Several studies have shown the influence of these parameters on the deformation efficiency [3], but direct measurements of the correlation between the local light field structure and the photoinduced deformation are lacking. Second, the characterization of the reversibility and the repeatability of the photodeformation is still an open question. It has been demonstrated that under particular polarization configurations it is possible to optically erase the photoinscribed structures [19, 20], but very little is known on the possibility to obtain successive reversible deformation cycles. Finally, the directionality of the deformation phenomena has not been clearly addressed. Several observations demonstrate the fundamental role of the polarization on the orientation of the photoinduced relief pattern [3], but very little information is available on the direction of the matter migration.

In this work, we study in detail the formation of surface relief gratings (SRG) induced by projecting an interference pattern. The aim of this work is to bring new direct experimental data on the photodeformation processes in order to identify and characterize the underlying mechanisms. Our approach is based on near-field techniques, which allow to measure in-situ and in real-time the information on the local spatial distribution of the light field and the corresponding photoinduced relief pattern.

In **Chapter 1**, we introduce the photochromic properties of the azobenzene molecule and we present the most relevant and spectacular photodeformation phenomena that have been observed so far, which are admitted to be directly related to the photoisomerization transition of the azobenzene units. We briefly discuss some interpretations that have been proposed as well as the most debated and open questions.

In **Chapter 2**, we detail the experimental apparatus and methods used in this work. We describe our measurement system constituted of a shear-force topography detection coupled to a SNOM microscope, and we characterize its performances. We also introduce the photochromic materials that we have studied and the experimental procedures that we have developed for their synthesis.

In **Chapter 3**, we investigate the microscopic mechanisms at the origin of the photoinduced deformation in photochromic thin films containing azobenzene derivatives. On this purpose, we study the formation of SRG under excitation with an interference pattern. We distinguish two kinds of photodeformation phenomena.
First, we study the deformation corresponding to the matrix photoexpansion, produced by the free volume increase necessary for the azobenzene isomerization. By using a single uniform beam to pre-irradiate the sample before the projection of the interference pattern, we manage to single out a plastic and an elastic contributions to the photoexpansion and we propose a fist-order model that describes the dependence between the light dose and the photoinduced deformation.
Second, we study the photo-induced matter migration phenomena. We use a configuration where the optical pattern is the superimposition of an intensity and a polarization interference patterns and we vary the relative amplitude of each contribution. In sol-gel Si-DR1 films we observe that the material deformation is fully governed by the polarization pattern, while in PMMA-DR1 films it depends on both the intensity and polarization patterns. These results demonstrate that two distinct microscopical mechanisms are at the origin of the mass transport and their relative efficiencies depend on the nature of the matrix. The matter migration mechanisms governed by the polarization are compatible with models based on the electromagnetic interactions [16]. The transport mechanisms which depend on the intensity pattern are coherent with a description based on the statistical motion of molecular entities [21].

Subsequently, we use a configuration where the interference pattern is assisted by a third incoherent beam. In this configuration, previous studies have shown that the efficiency of the photodeformation process is strongly increased [5]. In our experiment, since we measure in real-time both the intensity pattern and the topography, we have access to the direction of the mass transport with respect to the optical pattern. We demonstrate that in sol-gel Si-DR1 films the direction of the mass transport depends on the light polarization distribution. Thus, for a given intensity pattern, switching in real-time the light polarization produces an alternating photoinduced mass transport. This clearly demonstrates both the directionality and the reversibility of the matter migration. In a PMMA-DR1 film, the assisting-beam experiment exhibits two subsequent matter transport regimes, which result from the competition of the intensity and polarization driven processes. At a short time scale the intensity dependent mechanism is dominant, whereas at longer time scale, the polarization dependent mechanism prevails.

In **Chapter 4**, we demonstrate the possibility to use the photodeformation properties of azobenzene containing materials for the patterning of hybrid metal/azo-polymer structures. We show that the photodeformation induced in the underlying photochromic thin film is mechanically transferred on the overlying metallic layer. This sets the basis for a new nanofabrication technique.
Moreover, we present near-field photodeformation effects observed in the vicinity of the near-field probe. We show that the photomechanical response is related to both the "mechanical" interaction between the tip and the metal surface, and the photoactivity of the underlying photochromic film.

In **Chapter 5**, we present some preliminary results on nanostructured hybrid metal/azo-polymer systems and we discuss potential applications in the fields of nanofabrication in thin films and surfaces.

Bibliography

[1] A. Natansohn, P. Rochon, M. S. Ho, and C. Barret. Azo polymers for reversible optical storage .6. poly[4-[2-(methacryloyloxy)ethyl]azobenzene]. *Macromolecules*, 28(12):4179–4183, June 1995.

[2] D. Y. Kim, S. K. Tripathy, Lian Li, and J. Kumar. Laser-induced holographic surface relief gratings on nonlinear optical polymer films. *Applied Physics Letters*, 66 (10):1166–1168, 1995. doi: 10.1063/1.113845. URL http://link.aip.org/link/?APL/66/1166/1.

[3] Almeria Natansohn and Paul Rochon. Photoinduced motions in azo-containing polymers. *Chemical Reviews*, 102(11):4139–4176, 10 2002. URL http://dx.doi.org/10.1021/cr970155y.

[4] Kevin G. Yager and Christopher J. Barrett. Novel photo-switching using azobenzene functional materials. *Journal of Photochemistry and Photobiology A: Chemistry*, 182(3):250 – 261, 2006. ISSN 1010-6030. doi: DOI:10.1016/j.jphotochem.2006.04.021. URL http://www.sciencedirect.com/science/article/B6TGY-4K18VSP-1/2/c00807901259cd303aba19c5442fe822. Proceedings of 7th AIST International Symposium on Photoreaction Control and Photofunctional Materials, 7th AIST International Symposium on Photoreaction Control and Photofunctional Materials.

[5] Ke Yang, Suizhou Yang, Xiaogong Wang, and Jayant Kumar. Enhancing the inscription rate of surface relief gratings with an incoherent assisting light beam. *Applied Physics Letters*, 84(22):4517–4519, 2004. doi: 10.1063/1.1757643. URL http://link.aip.org/link/?APL/84/4517/1.

[6] N. Landraud, J. Peretti, F. Chaput, G. Lampel, J. P. Boilot, K. Lahlil, and V. I. Safarov. Near-field optical patterning on azo-hybrid sol-gel films. *Applied Physics Letters*, 79(27):4562–4564, December 2001.

[7] S. P. Bian, J. M. Williams, D. Y. Kim, L. A. Li, S. Balasubramanian, J. Kumar, and S. Tripathy. Photoinduced surface deformations on azobenzene polymer films. *Journal Of Applied Physics*, 86(8):4498–4508, October 1999.

[8] Nirmal K. Viswanathan, Srinivasan Balasubramanian, Lian Li, Sukant K. Tripathy, and Jayant Kumar. A detailed investigation of the polarization-dependent surface-relief-grating formation process on azo polymer films. *Japanese Journal of Applied Physics*, 38(Part 1, No. 10):5928–5937, 1999. doi: 10.1143/JJAP.38.5928. URL http://jjap.ipap.jp/link?JJAP/38/5928/.

[9] N. K. Viswanathan, D. Y. Kim, S. P. Bian, J. Williams, W. Liu, L. Li, L. Samuelson, J. Kumar, and S. K. Tripathy. Surface relief structures on azo polymer films. *Journal Of Materials Chemistry*, 9(9):1941–1955, September 1999.

[10] S. Bian, L. Li, J. Kumar, D. Y. Kim, J. Williams, and S. K. Tripathy. Single laser beam-induced surface deformation on azobenzene polymer films. *Applied Physics Letters*, 73(13):1817–1819, 1998. doi: 10.1063/1.122292. URL http://link.aip.org/link/?APL/73/1817/1.

[11] T. Fukuda and D. Barada. Photoinduced mass transport by one-dimensional gaussian beam irradiation: Width and polarization dependence. *Japanese Journal of Applied Physics*, 45(1B):470–474, JAN 2006. ISSN 0021-4922. doi: 10.1143/JJAP.45.470. 3rd International Conference on Molecular Electronics and Bioelectronics, Tokyo, JAPAN, MAR 03-04, 2005.

[12] T. Grosjean and D. Courjon. Photopolymers as vectorial sensors of the electric field. *Optics Express*, 14(6):2203–2210, 2006.

[13] Masahide Itoh, Kenji Harada, Shun ichi Kamemaru, and Toyohiko Yatagai. Holographic recording on azo-benzene functionalized polymer film. *Japanese Journal of Applied Physics*, 43(7B):4968–4971, 2004. doi: 10.1143/JJAP.43.4968. URL http://jjap.ipap.jp/link?JJAP/43/4968/.

[14] D. Garrot, Y. Lassailly, K. Lahlil, J. P. Boilot, and J. Peretti. Real-time near-field imaging of photoinduced matter motion in thin solid films containing azobenzene derivatives. *Applied Physics Letters*, 94(3):033303, 2009. doi: 10.1063/1.3073742. URL http://link.aip.org/link/?APL/94/033303/1.

[15] Renaud Bachelot, Fekhra H'Dhili, Dominique Barchiesi, Gilles Lerondel, Radouane Fikri, Pascal Royer, Nathalie Landraud, Jacques Peretti, Frederic Chaput, Georges Lampel, Jean-Pierre Boilot, and Khalid Lahlil. Apertureless near-field optical microscopy: A study of the local tip field enhancement using photosensitive

azobenzene-containing films. *Journal of Applied Physics*, 94(3):2060–2072, 2003. doi: 10.1063/1.1585117. URL http://link.aip.org/link/?JAP/94/2060/1.

[16] K. Yang, S. Z. Yang, and J. Kumar. Formation mechanism of surface relief structures on amorphous azopolymer films. *Physical Review B*, 73(16):165204, April 2006.

[17] B. Bellini, J. Ackermann, H. Klein, Ch Grave, Ph Dumas, and V. Safarov. Light-induced molecular motion of azobenzene-containing molecules: a random-walk model. *Journal of Physics-Condensed Matter*, 18(33, Sp. Iss. SI):S1817–S1835, AUG 23 2006. ISSN 0953-8984. doi: {10.1088/0953-8984/18/33/S04}. Meeting on Molecular Nanomachines, Les Houches, FRANCE, JAN 17-21, 2005.

[18] M. L. Juan, J. Plain, R. Bachelot, P. Royer, S. K. Gray, and G. P. Wiederrecht. Stochastic model for photoinduced surface relief grating formation through molecular transport in polymer films. *Applied Physics Letters*, 93(15):153304, 2008. doi: 10.1063/1.2999625. URL http://link.aip.org/link/?APL/93/153304/1.

[19] X. L. Jiang, L. Li, J. Kumar, D. Y. Kim, and S. K. Tripathy. Unusual polarization dependent optical erasure of surface relief gratings on azobenzene polymer films. *Applied Physics Letters*, 72(20):2502–2504, May 1998.

[20] CR Mendonca, A Dhanabalan, DT Balogh, L Misoguti, DS dos Santos, MA Pereira-da Silva, JA Giacometti, SC Zilio, and ON Oliveira. Optically induced birefringence and surface relief gratings in composite langmuir-blodgett (lb) films of poly[4 '-[[2-(methacryloyloxy)ethyl]ethylamino]-2-chloro-4-nitroazobenzene] (hpdr13) and cadmium stearate. *Macromolecules*, 32(5):1493–1499, 1999. ISSN 0024-9297.

[21] P. Lefin, Fiorini C., and Nunzi J-M. Anisotropy of the photo-induced translation diffusion of azobenzene dyes in polymer matrices. *Pure and Applied Optics: Journal of the European Optical Society Part A*, 7:71–82(12), 1998. URL http://www.ingentaconnect.com/content/iop/pao/1998/00000007/00000001/art00011.

Chapter 1

The azobenzene molecules: photochromic materials and photodeformation effects

1.1 Introduction

Although the photochromic properties of the azobenzene molecules have been known for almost a century [1] nowadays the spectacular effects induced by their isomerization still draw great attention [2–16]. In particular, the photomechanical effects obtained under polarized light are among the most studied and widely debated, since the first observation of matter transport phenomena over a long range (hundreds of nm), in 1995 [17, 18].

In this chapter, after a brief description of the azobenzene molecules, we present some of the most remarkable results reported in the literature concerning the photoinduced deformation phenomena observed in the far and in the near field. In particular, we focus on the open problems and the most debated interpretations.

1.2 The azobenzene molecules

1.2.1 The isomerization

The structure of the azobenzene molecule consists in two phenyl rings connected by an azo group -N=N-, as is depicted in **Figure 1.1**. The molecule exists in two isomeric configurations, the more stable trans (E) isomer and the metastable cis (Z) isomer, the

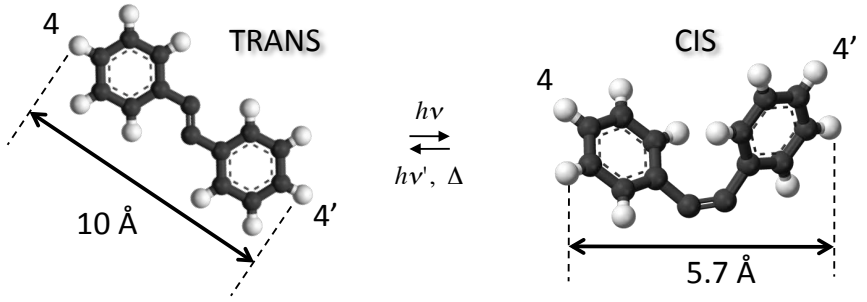

FIGURE 1.1: The trans/cis photoisomerization of the azobenzene molecule.

two forms being separated by an energetic barrier of typically 50 kJ/mol at room temperature [19]. The trans/cis isomerization can be induced by the absorption of a photon, in the UV-visible absorption band, while the reverse transition can be produced either optically or by thermal activation. The thermal activation time depends on several factors (environment, type of molecule, functional groups, etc.) and can range from ms up to hours [20].

For the trans form, the absorption probability is strongly anisotropic and depends on the angle ϕ between the orientation of the molecule dipole and the polarization of the incident light, like $cos^2\phi$, while for the cis isomer the absorption probability is almost isotropic [21]. The quantum yields for the trans-to-cis and cis-to-trans transitions have been measured both in solution and in a polymeric matrix and the obtained respective values are: $\eta_{T\to C} \simeq 0.1$, $\eta_{C\to T} \simeq 0.5$ [21, 22]. The interconversion between the two isomers produces an evident re-organization of the molecular geometry. Passing from the trans to the cis form, the distance between the 4 and 4' C atoms changes from 10 to 5.6 $\mathring{A}$ [23] and the isomerization of the molecule requires a free volume increase of 0.2 nm^3 [24]. A variation of the dipolar momentum has also been measured in various azobenzene derivatives [6, 25, 26].

1.2.2 The photoisomerization mechanism

The isomerization is induced by the excitation of an electron belonging to a nonbonding (n) or a bonding (π) orbital towards the lowest non occupied π orbital, denoted π^*. A description of the energy levels involved is shown in **Figure 1.2** [27], where[1]:

- $n \to \pi^*$ indicates: ground state $\to$ S1 (first molecular singlet state);
- $\pi \to \pi^*$ indicates: ground state $\to$ S2 (second molecular singlet state).

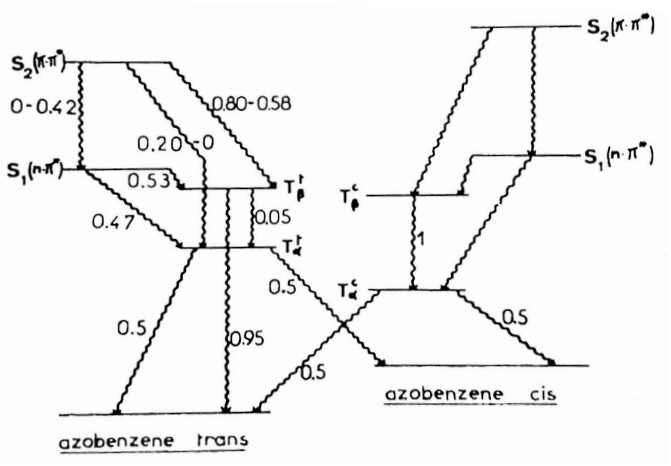

FIGURE 1.2: Azobenzene molecule: energy levels Jablonski diagram, supposing triplet states. The de-excitation probabilities reported have been proposed by Lemarie et al. [27].

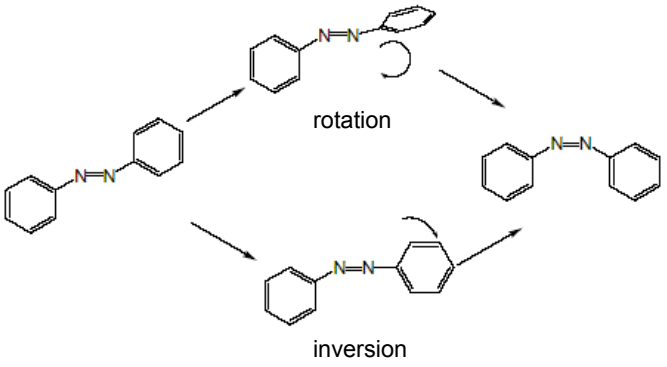

FIGURE 1.3: Azobenzene photoisomerization: rotation and inversion mechanisms.

The relaxation (de-excitation) may occur through different pathways involving several intermediate states and corresponding transition probabilities and leads either to the relaxation towards the initial state or to the transition in to the isomer state. The mechanism governing the interconversion between the two forms has long been studied during the second half of the last century, and is still matter of debate. The two most accredited hypothesis are depicted in **Figure 1.3**. In one case (top), the isomerization is accomplished through the ROTATION of a phenyl ring around the -N=N- group, while in the other case it is obtained via an INVERSION of a phenyl ring in the plane of the molecule [28].

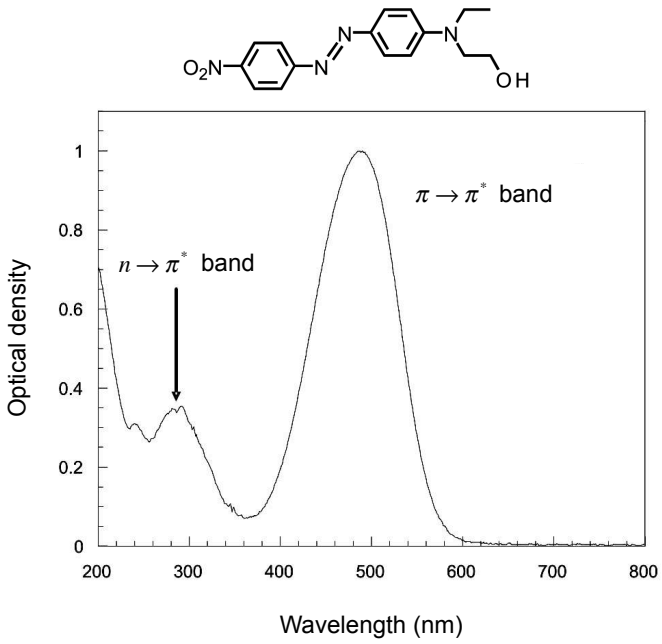

FIGURE 1.4: Disperse-Red 1 (DR1) molecule and its absorption spectrum in THF [29]: the order of the $\pi \rightarrow \pi^*$ and $n \rightarrow \pi^*$ is inverted.

1.2.3 The azobenzene families: classification

The azobenzene molecule has a great variety of derivatives, depending on the functionalization of the 4 and/or the 4' C terminal atoms. It is possible to obtain their classification in three categories, in relation to the order of the transition energies involved in the photo-excitation [19].

- The molecules of the azobenzene family, which are characterized by a $n - \pi^*$ transition of low intensity in the visible range and by a $\pi - \pi^*$ band of strong intensity in the UV, which are well separated. In this case, it is possible to isolate the cis form since the cis $\rightarrow$ trans thermal relaxation is relatively slow [20].

- The molecules belonging to the aminoazobenzene family, which present a superposition of the $n - \pi^*$ and $\pi - \pi^*$ bands and a more rapid cis $\rightarrow$ trans thermal relaxation.

- The molecules of the type pseudo-stilbene, which have a $\pi - \pi^*$ band situated at high wavelengths, while the $n - \pi^*$ and $\pi - \pi^*$ bands energy order is inverted (S2 < S1), generally because of an electro-donnor and electro-actractor functional groups present on the phenyl rings (see **Figure 1.4**). For these molecules the cis $\rightarrow$ trans thermal relaxation is relatively fast.

[1] We note that generally the $n \rightarrow \pi^*$ transition happens at lower energies than the $\pi \rightarrow \pi^*$.

In general, the absorption bands of the trans isomer are located at higher wavelengths with respect to the cis form. In the case of the pseudo-stilbene, the absorption peaks of the trans and the cis forms are very close, so the photoisomerization of the two species can be excited by the same wavelength, generally in the blue-green range. In condition of constant temperature and illumination, it is possible to generate continuous trans → cis → trans photoisomerization cycling, leading to a photostationary equilibrium between the trans and the cis populations. Turning the light off, the cis isomers undergo thermal relaxation towards the trans state, with a characteristic time of a few seconds or even shorter.

1.2.4 Molecular reorientation

The strong anisotropy of the absorption probability characterizing the trans isomer contributes, together with the statistical reorientation of the molecules, to the depletion of the molecule orientational distribution along the light electric field direction. After a trans-cis isomerization cycle, each molecule can return to the trans state with an orientation slightly different from the initial one. Assuming that the initial orientation was along the polarization axis, the probability of absorption and further isomerization is reduced. This leads to a statistical re-orientation of the molecules away from the direction parallel to the light polarization, a phenomenon known as *angular hole-burning*, which, under linearly polarized light, causes birefringence and linear dichroism [30], that can be observed in viscous liquids and polymers. The photoinduced optical anisotropy can relax, in the absence of irradiation, due to Brownian motion. It can also be partially erased by irradiation using circularly polarized light, which favors a more isotropic orientational distribution of the molecules [31].

1.3 Photoinduced deformation in azo-containing materials

1.3.1 Photodeformation phenomena in polymeric matrices containing azo-derivatives

The incorporation of azobenzene derivative molecules into a polymeric matrix leads to peculiar photodeformation phenomena, which have drawn great attention in the past 15 years. As it was discovered in 1995 by two research teams simultaneously [17, 18], the projection of an interference pattern on an azo-containing thin film induces the formation of Surface Relief Gratings (SRG) having the same spatial period of the optical interference grating and an amplitude up to hundreds of nm. An example of SRG formed using this method on a sol-gel film containing DR1 molecules is shown in **Figure 1.5**.

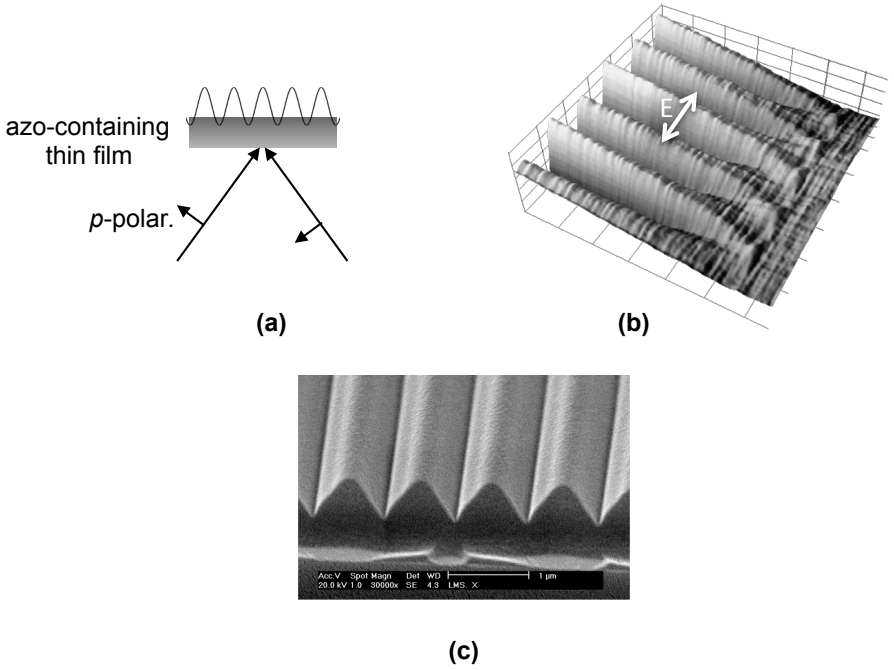

FIGURE 1.5: Photoinduced SRG on an azo-containing thin film under p-polarized light. (a) Scheme of the inscription experiment by projection of an interference pattern; (b) shear-force image of the SRG growth (3D representation); (c) SEM image of the SRG.

The study of the SRG formation has been performed using indirect methods such as diffraction efficiency measurements, and the actual surface relief pattern was measured only by ex-situ topography imaging such as AFM. Various parameters have been found to contribute to the photoresponse of the material, some can be related to properties of the material, others are characteristic of the illumination.

Material The presence of the azobenzene group seems to be a necessary condition for the SRG formation. Several studies [18, 32] have shown that the substitution with other chromophores inhibits any photodeformation. Indeed, the concentration and the type of incorporation (host/guest, grafting, etc.) of the dye in the material affects the deformation efficiency [2]. Also the matrix structure seems to have an important role. It has been demonstrated [33] that in polymeric matrices, the increase of the polymer chain molecular weight slows down the deformation dynamics. Finally, it has been observed [34] that the presence of a thin polymeric layer ($\simeq 1\ nm$) on the sample surface diminishes the photodeformation amplitude, which is completely inhibited for a layer thickness of 20 nm. This seems to indicate that a free surface is a necessary condition.

Illumination The photodeformation can be induced using rather low field power densities, of the order of the mW/mm^2. It has been observed that the deformation grows

with the exposure light dose, either under illumination with interfering beams [10, 16–18] and single focused beams [35, 36]. On the other hand, in relation to the light field polarization configuration various different deformation mechanisms seem to be activated, which result in different SRG growth amplitudes, speed and spatial distribution with respect to the optical intensity.

Since the light field polarization has been observed to be a critical parameter influencing the photodeformation phenomena, we will briefly resume the principal observations so far reported under various polarization configurations.

1.3.1.1 The dependence on the polarization

Several studies have shown that the SRG formation is very weak under *s*-polarized light, while a higher efficiency is observed using *p*-polarized light [5, 10, 16, 37, 38]. In particular, under projection of an intensity gradient, by illumination either with a focused gaussian beam or with an interference pattern, the resulting deformation is in $\pi - phase$ with the illumination: reliefs are formed in the dark areas, while grooves are induced in the bright zones. Under illumination with a polarization interference pattern ($\pm 45°$ or orthogonally circularly polarized interfering beams) the highest deformation efficiency is observed [37–39]. This indicates that an intensity gradient is not a necessary condition, while the effect of the polarization seems preponderant. On the other hand, a quite weak deformation is observed under an *s*- and a *p*-polarized interfering beams with the formation of a double period SRG. Very recently, it has been demonstrated, using the superimposition of an interference pattern to an homogeneous, incoherent *p*-polarized assisting beam, that the deformation efficiency obtained under *s*-polarized interference is increased [10], with a relief growth *in phase* with the light field [40]. This supports the critical influence of the light field polarization on the photodeformation phenomena.

1.3.1.2 Photodeformation mechanisms: interpretations

The understanding of the mechanisms at the origin of these phenomena is still debated. The observation of a deformation in $\pi - phase$ with the illumination has suggested the existence of a mechanism of *matter migration*, due to the photoisomerization of the azobenzene molecules induced in the enlightened zones [2]. The mechanical work done during each interconversion would produce an overall transport of matter, which is accumulated in the darker zones, where the molecules are not photoactivated. This interpretation is the most shared, even if hardly compatible with the high efficiency observed under irradiation with a polarization interference pattern, and several modeling

approaches have been proposed. A class of models considers the statistical redistribution of the molecules due to the elementary displacement of each azobenzene, following an isomerization cycle [25, 41]. In this sense, the mass migration is related to the distribution of the absorption probability of each photoactive unit, hence to the spatial distribution of the light intensity and to the light polarization. Another class of models considers the photochromic material as a viscoelastic system whose photofluidification depends on the photoisomerization of the azobenzene molecules [10, 11, 42]. The Navier-Stokes formalism is used to describe the matter transport phenomena, which are supposed to be produced by the electromagnetic forces due to the interactions between the light field and the material. In the case of the statistical models, the matter transport is mainly related to the anisotropic photoresponse of the molecules, while in the other type of models the movement is mainly due to the interaction between the electromagnetic field and the material, while the azobenzene photoisomerization has a 'softening' effect.
Another photodeformation mechanism has been recently identified, the *matrix photoexpansion*, which has been observed, by different techniques [16, 43], in the illuminated zones, independently from the polarization. It has been attributed to the augmentation of the matrix volume in the enlightened zones, as a consequence of the molecular steric re-arrangement in order to gain the free volume necessary to accomodate molecules after the photoisomerization. Although the obtained deformation has been observed to be permanent in several experiments, the existence of an elastic regime has been reported [43, 44].

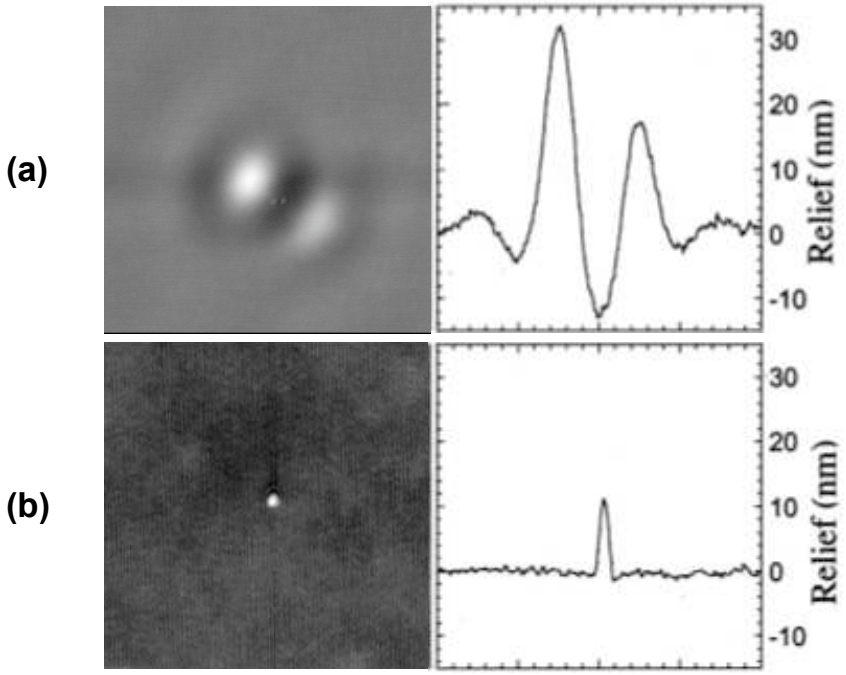

FIGURE 1.6: Far-field (a) and near-field (b) photoinduced deformation on a sol-gel DR1 film [7].

1.3.1.3 Far-field and near-field experiments

The observation of the photoinduced deformation obtained by illumination in the far and in the near field reveals a contradictory behavior (**Figure 1.6**). Irradiating the sample using a metal-coated tip in the far field (tip-to-sample distance $> \lambda/2\pi$) a groove is observed in correspondence of the enlightened zone, while two lobes appear on the sides, whose orientation is parallel to the light field polarization (a). On the other hand, when the experiment is performed illuminating in the near field, a relief is observed in the illuminated zone, underneath the tip (b), with a diameter corresponding to the tip aperture.

The behavior observed in the far-field experiment has the same characteristic as the matter transport observed under *p*-polarized interference, where matter migrates from the bright fringes towards the dark fringes along the light electric field direction. On the other hand, the phenomenon observed in the near-field experiments [7, 29, 45, 46] is similar to the results obtained using the superposition of an *s*-polarized intensity gradient and a *p*-polarized assisting beam [40], where matter migration towards the irradiated zones is obtained.

1.4 Conclusions

The photomechanical response in azo-containing thin films depends on the characteristics of the material and of the illumination. In particular, an important influence of the light polarization on the amplitude, the dynamics and the orientation of the photoinduced deformation has been observed. Two mechanisms seem to be at the origin of the deformation. On one hand, the matrix photoexpansion, which produces small reliefs in the enlightened zones and is related to the matrix re-organization subsequent to the photoisomerization cycles of the azobenzene molecules. On the other hand, the matter migration, a more complex mechanism, whose interpretation is still debated. It has generally been observed a matter motion from the enlightened zones towards the darker areas, its efficiency being strongly dependent on the light polarization. However, under combined exposure to an incoherent homogenous assisting beam and to a perpendicularly polarized interference pattern, a relief growth in correspondence to the illuminated zones is observed. A similar discrepancy is observed between the far-field and the near-field experiments, where, in the first case, matter migrates away from the illuminated zones, while in the second case it is accumulated in the vicinity of the illuminating tip. Several different approaches have been proposed to model these phenomena, however the lack of direct correlated data on the light field spatial distribution and the photoinduced deformation makes it very arduous to obtain a complete description.

Bibliography

[1] G. S. Hartley. The cis-form of azobenzene. *Nature*, 140:281, 1937.

[2] Almeria Natansohn and Paul Rochon. Photoinduced motions in azo-containing polymers. *Chemical Reviews*, 102(11):4139–4176, 10 2002. URL http://dx.doi.org/10.1021/cr970155y.

[3] Kevin G. Yager and Christopher J. Barrett. Novel photo-switching using azobenzene functional materials. *Journal of Photochemistry and Photobiology A: Chemistry*, 182(3):250 – 261, 2006. ISSN 1010-6030. doi: DOI:10.1016/j.jphotochem.2006.04.021. URL http://www.sciencedirect.com/science/article/B6TGY-4K18VSP-1/2/c00807901259cd303aba19c5442fe822. Proceedings of 7th AIST International Symposium on Photoreaction Control and Photofunctional Materials, 7th AIST International Symposium on Photoreaction Control and Photofunctional Materials.

[4] S. P. Bian, J. M. Williams, D. Y. Kim, L. A. Li, S. Balasubramanian, J. Kumar, and S. Tripathy. Photoinduced surface deformations on azobenzene polymer films. *Journal Of Applied Physics*, 86(8):4498–4508, October 1999.

[5] Nirmal K. Viswanathan, Srinivasan Balasubramanian, Lian Li, Sukant K. Tripathy, and Jayant Kumar. A detailed investigation of the polarization-dependent surface-relief-grating formation process on azo polymer films. *Japanese Journal of Applied Physics*, 38(Part 1, No. 10):5928–5937, 1999. doi: 10.1143/JJAP.38.5928. URL http://jjap.ipap.jp/link?JJAP/38/5928/.

[6] K. Ichimura, S. K. Oh, and M. Nakagawa. Light-driven motion of liquids on a photoresponsive surface. *Science*, 288(5471):1624–1626, June 2000.

[7] N. Landraud, J. Peretti, F. Chaput, G. Lampel, J. P. Boilot, K. Lahlil, and V. I. Safarov. Near-field optical patterning on azo-hybrid sol-gel films. *Applied Physics Letters*, 79(27):4562–4564, December 2001.

[8] C Hubert, C Fiorini-Debuisschert, I Maurin, JM Nunzi, and P Raimond. Spontaneous patterning of hexagonal structures in an azo-polymer using light-controlled mass transport. *Advanced Materials*, 14(10):729, 2002. ISSN 0935-9648.

[9] T. Ikeda, M. Nakano, Y. L. Yu, O. Tsutsumi, and A. Kanazawa. Anisotropic bending and unbending behavior of azobenzene liquid-crystalline gels by light exposure. *Advanced Materials*, 15(3):201, February 2003.

[10] Ke Yang, Suizhou Yang, Xiaogong Wang, and Jayant Kumar. Enhancing the inscription rate of surface relief gratings with an incoherent assisting light beam. *Applied Physics Letters*, 84(22):4517–4519, 2004. doi: 10.1063/1.1757643. URL http://link.aip.org/link/?APL/84/4517/1.

[11] P. Karageorgiev, D. Neher, B. Schulz, B. Stiller, U. Pietsch, M. Giersig, and L. Brehmer. From anisotropic photo-fluidity towards nanomanipulation in the optical near-field. *Nature Materials*, 4(9):699–703, 2005.

[12] Yann Gilbert, Renaud Bachelot, Alexandre Vial, Gilles Lerondel, Pascal Royer, Alexandre Bouhelier, and Gary Wiederrecht. Photoresponsive polymers for topographic simulation of the optical near-field of a nanometer sized gold tip in a highly focused laser beam. *Opt. Express*, 13(10):3619–3624, 2005. URL http://www.opticsexpress.org/abstract.cfm?URI=oe-13-10-3619.

[13] T Muraoka, K Kinbara, and T Aida. Mechanical twisting of a guest by a photoresponsive host. *Nature*, 440(7083):512–515, 2006. ISSN 0028-0836. doi: 10.1038/nature04635.

[14] Sarah Angelos, Eunshil Choi, Fritz Vogtle, Luisa De Cola, and Jeffrey I. Zink. Photo-driven expulsion of molecules from mesostructured silica nanoparticles. *The Journal of Physical Chemistry C*, 111(18):6589–6592, May 2007. ISSN 1932-7447. URL http://dx.doi.org/10.1021/jp070721l.

[15] Leonid M. Goldenberg, Yuri Gritsai, Olga Kulikovska, and Joachim Stumpe. Three-dimensional planarized diffraction structures based on surface relief gratings in azobenzene materials. *Opt. Lett.*, 33(12):1309–1311, 2008. URL http://ol.osa.org/abstract.cfm?URI=ol-33-12-1309.

[16] D. Garrot, Y. Lassailly, K. Lahlil, J. P. Boilot, and J. Peretti. Real-time near-field imaging of photoinduced matter motion in thin solid films containing azobenzene derivatives. *Applied Physics Letters*, 94(3):033303, 2009. doi: 10.1063/1.3073742. URL http://link.aip.org/link/?APL/94/033303/1.

[17] A. Natansohn, P. Rochon, M. S. Ho, and C. Barret. Azo polymers for reversible optical storage .6. poly[4-[2-(methacryloyloxy)ethyl]azobenzene]. *Macromolecules*, 28(12):4179–4183, June 1995.

[18] D. Y. Kim, S. K. Tripathy, Lian Li, and J. Kumar. Laser-induced holographic surface relief gratings on nonlinear optical polymer films. *Applied Physics Letters*, 66 (10):1166–1168, 1995. doi: 10.1063/1.113845. URL http://link.aip.org/link/?APL/66/1166/1.

[19] H. Rau. *Photochemistry and Photophysics, Volume II*. CRC - Boca Raton, FL, 1989.

[20] T. Buffeteau, F. Lagugne Labarthet, M. Pezolet, and C. Sourisseau. Dynamics of photoinduced orientation of nonpolar azobenzene groups in polymer films. characterization of the cis isomers by visible and ftir spectroscopies. *Macromolecules*, 34 (21):7514–7521, 09 2001. URL http://dx.doi.org/10.1021/ma010279j.

[21] Thomas Garm Pedersen, P. S. Ramanujam, Per Michael Johansen, and Søren Hvilsted. Quantum theory and experimental studies of absorption spectra and photoisomerization of azobenzene polymers. *J. Opt. Soc. Am. B*, 15(11):2721–2730, 1998. URL http://josab.osa.org/abstract.cfm?URI=josab-15-11-2721.

[22] R. Loucif-Saibi, K. Nakatani, J. A. Delaire, M. Dumont, and Z. Sekkat. Photoisomerization and second harmonic generation in disperse red one-doped and -functionalized poly(methyl methacrylate) films. *Chemistry of Materials*, 5(2):229–236, 05 1993. URL http://dx.doi.org/10.1021/cm00026a014.

[23] Akihiro Abe, Hideyuki Kobayashi, Tokiji Kawamura, Masazumi Date, Toshiyuki Uryu, and Kei Matsuzaki. Statistical properties of the poly(n-vinylcabazole) chain as estimated from an nmr analysis of 2,4-bis-n-cabazolylpentane. *Macromolecules*, 21(12):3414–3419, 05 2002. URL http://dx.doi.org/10.1021/ma00190a011.

[24] Takuya Naito, Kazuyuki Horie, and Itaru Mita. Photochemistry in polymer solids: 12. effects of main-chain structures and formation of hydrogen bonds on photoisomerization of azobenzene in various polymer films. *Polymer*, 34(19): 4140 – 4145, 1993. ISSN 0032-3861. doi: DOI:10.1016/0032-3861(93)90680-9. URL http://www.sciencedirect.com/science/article/B6TXW-48DYJYS-JP/2/37738f5b094ac9744a1da7051ed1b5c5.

[25] P. Lefin, Fiorini C., and Nunzi J-M. Anisotropy of the photo-induced translation diffusion of azobenzene dyes in polymer matrices. *Pure and Applied Optics: Journal of the European Optical Society Part A*, 7:71–82(12), 1998. URL http://www.ingentaconnect.com/content/iop/pao/1998/00000007/00000001/art00011.

[26] Bharat Kumar and K. A. Suresh. Kinetics of trans-cis isomerization in azobenzene dimers at an air-water interface. *Physical Review E (Statistical, Nonlinear, and Soft Matter Physics)*, 80(2):021601, 2009. doi: 10.1103/PhysRevE.80.021601. URL http://link.aps.org/abstract/PRE/v80/e021601.

[27] J. Lemarie J. Royanette, R. Arnaud. *Can. J. Chem.*, 52:1858, 1974.

[28] Hermann Rau and Erik Lueddecke. On the rotation-inversion controversy on photoisomerization of azobenzenes. experimental proof of inversion. *Journal of the American Chemical Society*, 104(6):1616–1620, 05 2002. URL http://dx.doi.org/10.1021/ja00370a028.

[29] Nathalie Landraud. *Ph.D. Thesis: Nanostructuration optique de films sol-gel photochromiques par microscopie en champ proche*. Ecole Polytechnique, 2002.

[30] T. Todorov, L. Nikolova, and N. Tomova. Polarization holography. 1: A new high-efficiency organic material with reversible photoinduced birefringence. *Appl. Opt.*, 23(23):4309–4312, 12 1984. URL http://ao.osa.org/abstract.cfm?URI=ao-23-23-4309.

[31] CR Mendonca, A Dhanabalan, DT Balogh, L Misoguti, DS dos Santos, MA Pereira-da Silva, JA Giacometti, SC Zilio, and ON Oliveira. Optically induced birefringence and surface relief gratings in composite langmuir-blodgett (lb) films of poly[4 '-[[2-(methacryloyloxy)ethyl]ethylamino]-2-chloro-4-nitroazobenzene] (hpdr13) and cadmium stearate. *Macromolecules*, 32(5):1493–1499, 1999. ISSN 0024-9297.

[32] Bruno Darracq, Frédéric Chaput, Khalid Lahlil, Jean-Pierre Boilot, Yves Levy, Valerie Alain, Lionel Ventelon, and Mireille Blanchard-Desce. Novel photorefractive sol-gel materials. *Optical Materials*, 9(1-4):265 – 270, 1998. ISSN 0925-3467. doi: DOI:10.1016/S0925-3467(97)00151-1. URL http://www.sciencedirect.com/science/article/B6TXP-3VN034S-1R/2/d8ca3a3d5859c851560f624c5988f362. Materials, Physics and Devices For Molecular Electronics and Photonics.

[33] Christopher J. Barrett, Almeria L. Natansohn, and Paul L. Rochon. Mechanism of optically inscribed high-efficiency diffraction gratings in azo polymer films. *The Journal of Physical Chemistry*, 100(21):8836–8842, 05 1996. URL http://dx.doi.org/10.1021/jp953300p.

[34] Nirmal K. Viswanathan, Srinivasan Balasubramanian, Lian Li, Jayant Kumar, and Sukant K. Tripathy. Surface-initiated mechanism for the formation of relief gratings on azo-polymer films. *The Journal of Physical Chemistry B*, 102(31):6064–6070, 07 1998. URL http://dx.doi.org/10.1021/jp981425z.

[35] S. Bian, L. Li, J. Kumar, D. Y. Kim, J. Williams, and S. K. Tripathy. Single laser beam-induced surface deformation on azobenzene polymer films. *Applied Physics Letters*, 73(13):1817–1819, 1998. doi: 10.1063/1.122292. URL http://link.aip.org/link/?APL/73/1817/1.

[36] T. Grosjean and D. Courjon. Photopolymers as vectorial sensors of the electric field. *Optics Express*, 14(6):2203–2210, 2006.

[37] Masahide Itoh, Kenji Harada, Shun ichi Kamemaru, and Toyohiko Yatagai. Holographic recording on azo-benzene functionalized polymer film. *Japanese Journal of Applied Physics*, 43(7B):4968–4971, 2004. doi: 10.1143/JJAP.43.4968. URL http://jjap.ipap.jp/link?JJAP/43/4968/.

[38] Daisuke Barada, Takashi Fukuda, Masahide Itoh, and Toyohiko Yatagai. Numerical analysis of photoinduced surface relief grating formation by particle method. *Optical Review*, 12(4):271–273, 07 2005. URL http://dx.doi.org/10.1007/s10043-005-0271-z.

[39] Md. Zahangir Alam, Tomoko Ohmachi, Tomonari Ogata, Takamasa Nonaka, and Seiji Kurihara. Photoisomerization behavior and photoinduced surface relief gratings on azopolymer film by a monochromatic light irradiation. *Optical Materials*, 29(4):365 – 370, 2006. ISSN 0925-3467. doi: DOI:10.1016/j.optmat.2005.10.005. URL http://www.sciencedirect.com/science/article/B6TXP-4HWXP03-1/2/a147cc79fda983a71b38c57eca1896f8.

[40] K. Yang, S. Z. Yang, and J. Kumar. Formation mechanism of surface relief structures on amorphous azopolymer films. *Physical Review B*, 73(16):165204, April 2006.

[41] M. L. Juan, J. Plain, R. Bachelot, P. Royer, S. K. Gray, and G. P. Wiederrecht. Stochastic model for photoinduced surface relief grating formation through molecular transport in polymer films. *Applied Physics Letters*, 93(15):153304, 2008. doi: 10.1063/1.2999625. URL http://link.aip.org/link/?APL/93/153304/1.

[42] Jayant Kumar, Lian Li, Xin Li Jiang, Dong-Yu Kim, Taek Seung Lee, and Sukant Tripathy. Gradient force: The mechanism for surface relief grating formation in azobenzene functionalized polymers. *Applied Physics Letters*, 72(17):2096–2098, 1998. doi: 10.1063/1.121287. URL http://link.aip.org/link/?APL/72/2096/1.

[43] Oleh M. Tanchak and Christopher J. Barrett. Light-induced reversible volume changes in thin films of azo polymers: The photomechanical effect. *Macromolecules*, 38(25):10566–10570, 11 2005. URL http://dx.doi.org/10.1021/ma051564w.

[44] O. Henneberg, Th. Geue, M. Saphiannikova, U. Pietsch, A. Natansohn, P. Rochon, and K. Finkelstein. Investigation of material flow on inscribing a polymer surface grating probing x-ray and vis light scattering. *Colloids and Surfaces A: Physicochemical and Engineering Aspects*, 198-200:107–111, 2 2002. URL http://www.sciencedirect.com/science/article/B6TFR-454JBTJ-H/2/38ea38366b3f32725df1c36aec2d7c14.

[45] Renaud Bachelot, Fekhra H'Dhili, Dominique Barchiesi, Gilles Lerondel, Radouane Fikri, Pascal Royer, Nathalie Landraud, Jacques Peretti, Frederic Chaput, Georges Lampel, Jean-Pierre Boilot, and Khalid Lahlil. Apertureless near-field optical microscopy: A study of the local tip field enhancement using photosensitive azobenzene-containing films. *Journal of Applied Physics*, 94(3):2060–2072, 2003. doi: 10.1063/1.1585117. URL http://link.aip.org/link/?JAP/94/2060/1.

[46] R. Bachelot, A. Bouhelier, G. Wiederrecht, Y. Gilbert, L. Novotny, and P. Royer. Longitudinal sensitivity of the photoinduced molecular migration in azobenzene-containing films. *Proceedings of the SPIE - The International Society for Optical Engineering*, 6335:63350E–1–9, 2006.

Chapter 2

Experimental setup and sample preparation

2.1 Experimental setup

This work aims to study the photomechanical processes induced at nanoscale in thin films containing azo-polymers. In particular, we want to establish a correlation between the light pattern and the resulting deformation. For this purpose we have developed a combined shear-force/SNOM microscope which allows to detect simultaneously, in

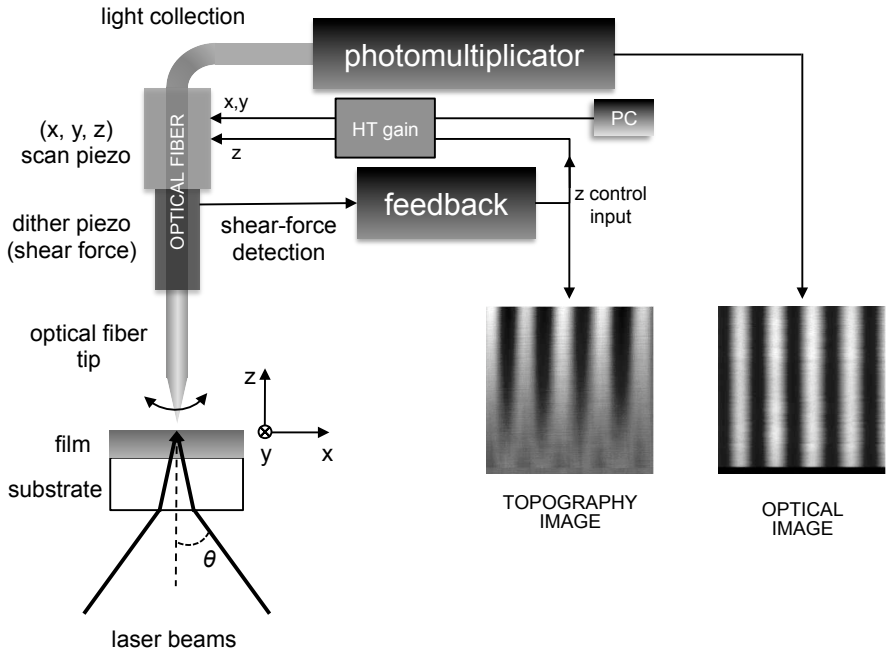

FIGURE 2.1: Principle of the coupled measurement system.

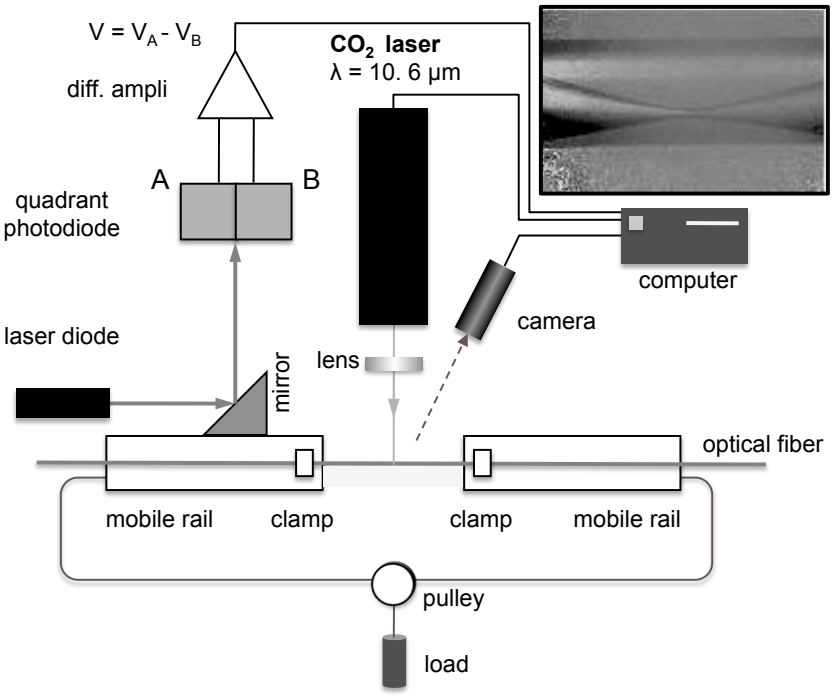

FIGURE 2.2: Probe fabrication: heat-pulling.

real-time, in-situ and at nanoscale, both the optical image and the surface topography (**Figure 2.1**). In this experiment, the sample is a thin photochromic film deposited on a glass substrate. During illumination, a tapered optical fiber tip provides simultaneous detection of the transmitted light intensity and of the shear-force topography.

2.1.1 Probe fabrication

The nano-probe is obtained by heat-pulling of an optical fiber[1]. The principle of the process is depicted in **Figure 2.2**. The optical fiber is clamped on two rails and put in tension by a constant load. Fiber heating is provided by a CO_2 laser. A computer controls a series of CO_2 laser pulses (ms) in order to produce a step-by-step pulling of the fiber. Each pulling step is detected on a quadrant photodiode, by the reflection of a laser beam on a mirror soldered on one rail. A microscope equipped with a video camera allows to observe the process and to measure the fiber diameter. When a critical diameter has been reached (15 μm in our experimental conditions), a last laser pulse is applied to obtain the rupture, producing two symmetrical tips.

[1]Multimode, 125 μm core

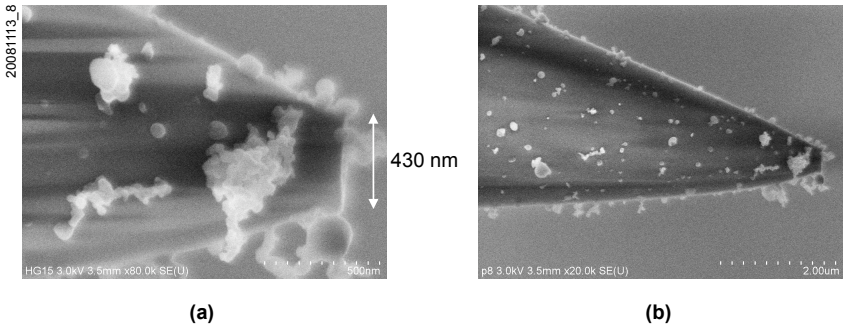

FIGURE 2.3: Tip apex diameter. (a-b) Higher and lower magnified SEM images of the apex of an optical fiber tip fabricated by heat-pulling.

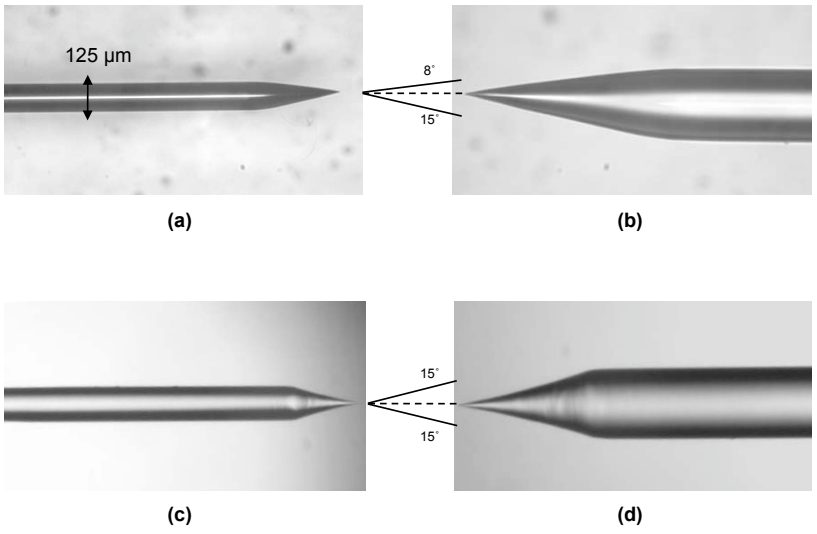

FIGURE 2.4: Tip anistropy. Optical microscope 5x (left) and 10x (right) images of an optical fiber tip fabricated by heat-pulling: (a-b) side view; (c-d) top view.

The apex geometry is approximately that of a truncated cone. We can obtain an apex diameter of typically 400 *nm* (**Figure 2.3**), with a repeatability that mainly depends on the detection of the critical diameter. As we can see in **Figure 2.2** and **Figure 2.4**(a-b), due to the laser assisted fabrication process, the tip has an asymmetric shape, which can lead to several problems (poor intensity contrast, polarization anisotropy, etc.) in the imaging of the light field spatial distribution. This is taken into account in a calibration procedure that we employ systematically (see 2.1.4.2), in order to maximize the homogeneous collection of the light field.

We further decrease the tip apex diameter by chemical etching in HF. The concentration of the HF solution, the temperature and the etching time allow to control the final

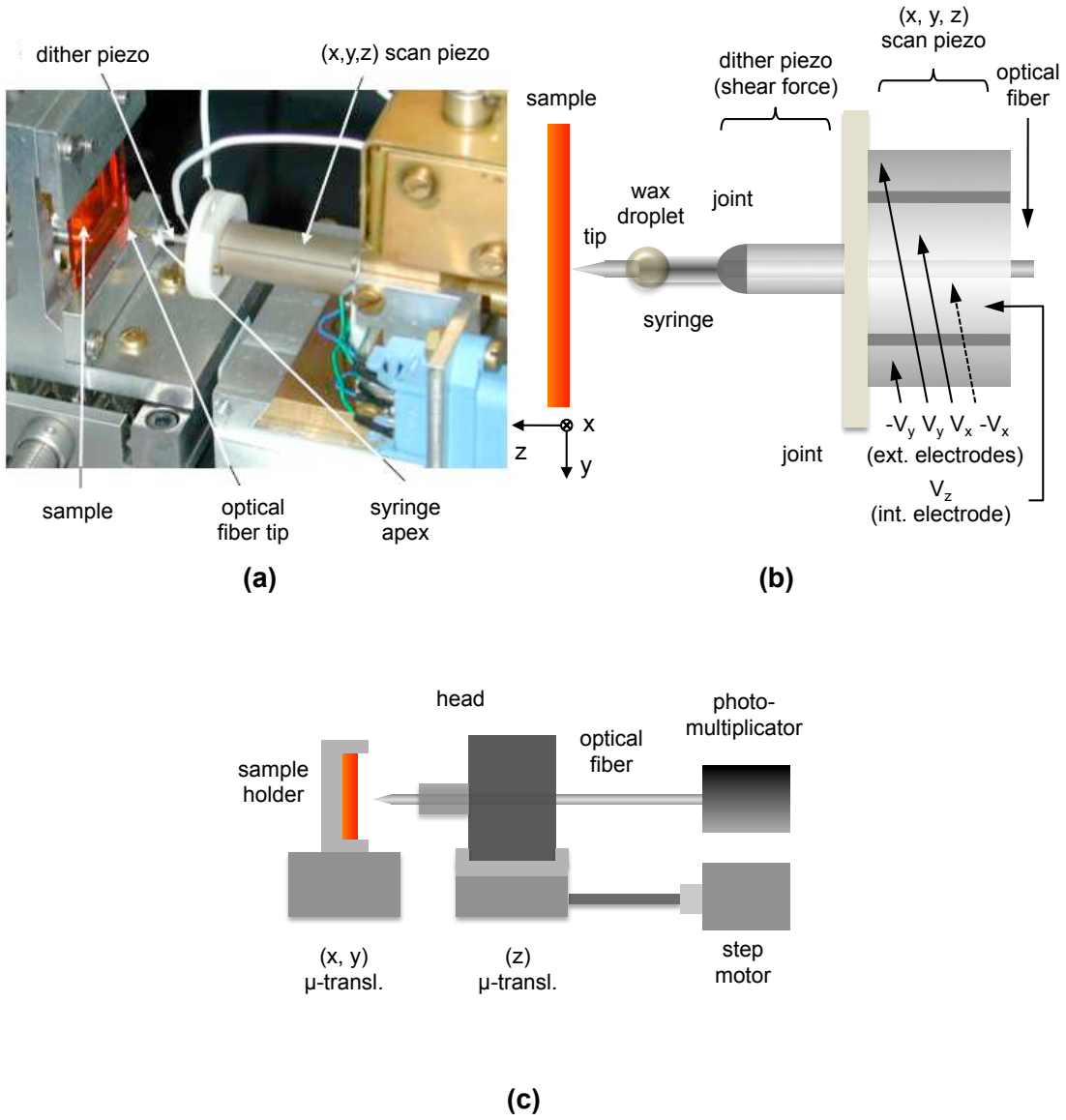

FIGURE 2.5: The microscope: head

diameter with a sufficient precision of a few tens of nm [1].

2.1.2 The microscope

The core of the coupled measurement system is the microscope head, which is depicted in **Figure 2.5**(a-b). A syringe apex is fixed by means of araldite glue on the small dither piezo tube (8 x 1.3 mm). This one is joined to the (x, y, z) scan piezo tube (30 x 10 mm), which is fixed on the head body. The optical fiber slides inside the syringe apex and the two piezo tubes, and comes out on the back of the head. The tapered extremity is fixed on the syringe apex by means of a wax droplet, while on the other

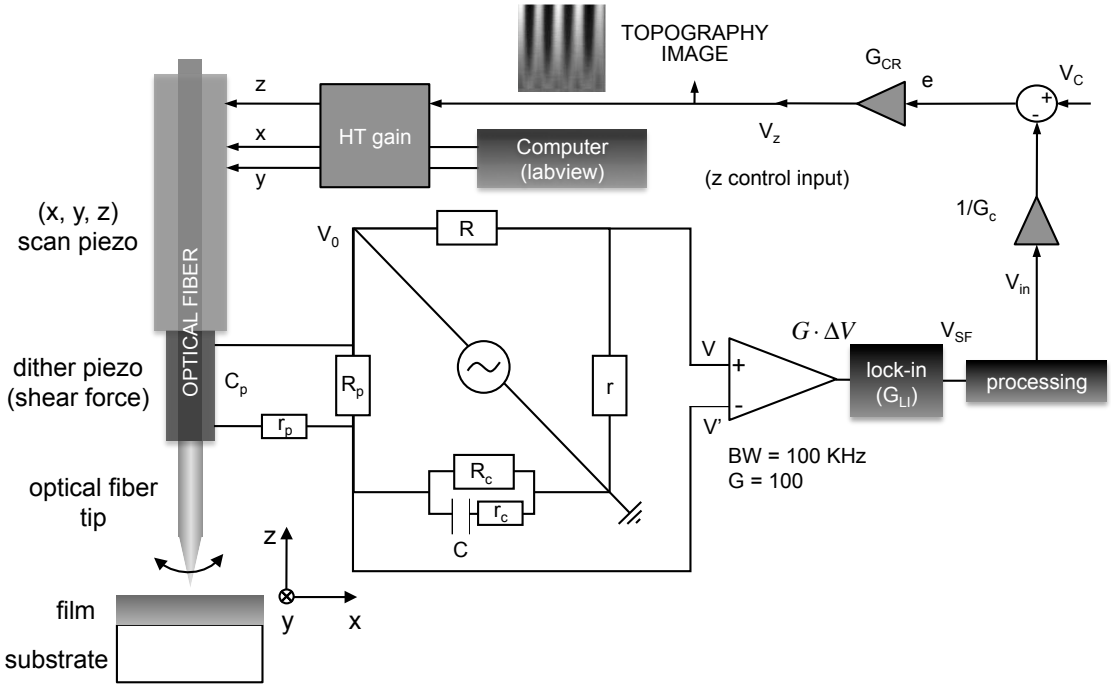

FIGURE 2.6: Shear-force microscopy: detection electronics and feedback.

end, the optical fiber is connected to a photomultiplier.

The (x, y, z) scan piezo tube has four external electrodes and one internal electrode, driven by a voltage between 0 and 400 V, which allow a maximum excursion of 30 μm along the x, y axis and 2 μm along the z-axis. The head is mounted on a translation stage driven by a step motor, every step corresponding to a 200 nm displacement along the z-axis, which allows a precise setting of the tip-to-sample distance within the range of the (x, y, z) piezotube extension. This is achieved first, by a visually controlled coarse approach and, subsequently, by an automatic approach based on the shear-force feedback, that we will detail later.

The sample is mounted in front of the head, on a sample holder equipped with manual translational stages along the x and z directions of the sample surface plane, having a precision of 10 μm.

2.1.3 Shear-force microscopy

The shear-force topography measurement is based on the detection of the vibration amplitude of a tip oscillating along the x-axis. In our system (**Figure 2.6**), this oscillation is obtained by means of an alternating voltage V_0 applied to the dither piezo tube. The electrical behavior of the dither piezo tube is essentially capacitive. Using a Wheatstone bridge we detect the variation of this capacitance due to the mechanical constraints imposed on the dither piezo tube by the tip. Driving the tip at a resonant

frequency causes a significant capacitance variation. This gives a high sensitivity to further variations of the tip vibration amplitude. In particular, when the tip interacts with the sample surface, the consequent vibration amplitude variations reflect to a variation of the piezo capacitance, which constitute the shear-force signal proportional to the tip-surface interaction shear-forces.

In order to accurately place the vibration resonance frequency, we use a tip-ending length of a few mm. This allows to precisely set the resonance. We drive the tip-ending free length of the optical fiber at its second harmonic, since the fundamental vibration mode gives a very strong mechanical constraint and a large vibration amplitude. The choice of the drive frequency is a compromise between the low s/n ratio obtained with low frequencies (low time constant) and the limitation due to the standard electronics. The frequency is adjusted by choosing the tip-ending free length L with respect to the syringe apex. The $i-th$ harmonic frequency f_i varies as[2]:

$$f_i = \frac{k_i^2}{2\pi}\sqrt{\frac{EI}{\rho S}}\frac{1}{L^2} \tag{2.1}$$

where $k_i = \alpha_i L$ and α_i is solution of:

$$cosh(\alpha_i L)\cdot cos(\alpha_i L) + 1 = 0 \tag{2.2}$$

E is the Young modulus of the fiber, I is its inertia moment, ρ is the material density, S is the fiber section and L is the tip-ending free length (neglecting the tip shape, whose contribution is not significant). We usually work at the second harmonic frequency f_2, with typical values[3] of about $50 \div 60\ kHz$ for $L = 3.5 \div 3\ mm$.

2.1.3.1 Dimensioning

The impedance of the dither piezo tube is essentially capacitive[4], far from the tube resonance. To avoid thermal effects a fixed resistor R_p is put in parallel with C_p and shortcuts the resistive part of the piezotube impedance. The total impedance of this part is Z_p. On the detection branch the R_c and r_c tunable resistors allow to balance the resistive parts (R_p and r_p) of the piezo branch. Together with the C capacitor, they form the detection impedance Z. The opposite branches (R and r) of the bridge are purely resistive. The tunable resistors R and r are set to balance the C_p/C_r ratio at high frequency.

[2] See for example [2].
[3] See also **Figure 2.8**
[4] A very small resistance r_p models the dissipations

R_p is chosen to short-cut C_p at low frequencies. In fact, the piezotube's equivalent impedance includes also a parallel resistance, but it is very large and suffers thermal drifts. So R_p has a value low enough to shortcut that resistance; moreover, the condition $R_p > 1/C_p\omega$ must be respected in the frequency range of interest (typically above 10 kHz), to have the system be sensitive to the variations of C_p. This implies also that R_c, which is used to compensate R_p, must fulfill the same condition. Hence R_p has been fixed at 332 $k\Omega$ and R_c is a potentiometer of 500 $k\Omega$, while C is a 220 pF capacitor whose value is of the order of C_p, in order to optimize the $\Delta V/V_0$ ratio, as will be shown later. The r_c resistor is a potentiometer of 5 $k\Omega$ and it helps in the tuning of the bridge, compensating the weak serial resistance of the piezo branch.

Finally, R and r are the complementary branches of a 1 $k\Omega$ potentiometer. The total value of the resistance branch $R + r$ is chosen large enough to limit the current flowing in that branch. On the other hand, the resistance value should be low enough to keep its noise much smaller than the full scale resonance signal.

The excitation voltage V_0 is chosen to obtain a tip vibration amplitude of typically 10 nm. This is achieved for a value of the voltage V_{exc} exciting the piezotube of typically 10 mV. The corresponding shear-force signal at resonance $\Delta V \simeq 100\mu V$. Thus, the value of the resistive branch $R + r$ is chosen equal to $1k\Omega$. Indeed, at T = $300°K$ a resistance of $\simeq$ 1 $k\Omega$, within a band Δf = 100 KHz induces a voltage fluctuation $\delta V = [4kT(R + r)\Delta f]^{1/2}$ that is $\delta V \simeq 1\mu V$, much smaller than the $100\mu V$ shear-force signal. As already mentioned, typical driving frequencies are between 25 and 60 KHz (avoiding frequencies close to other parasitic mechanical resonances).

We will now show that this configuration allows to measure a shear-force signal ΔV proportional to the piezoelectric capacitance variation δC_p.

2.1.3.2 Shear-force detection

Far from the resonance the tip and the dither piezotube vibrate almost as a unique body and the bridge is balanced:

$$R/r = Z_p^0/Z = Y/Y_p^0 \tag{2.3}$$

where $Y_p = 1/Z_p$ is the admittance of the branch containing the piezotube, while $Y = 1/Z$ is the admittance of the detection branch.

At the input of the differential amplifier the signals are:

$$V = \frac{r}{r+R}V_0 = \frac{Y_p^0}{Y+Y_p^0}V_0 \tag{2.4}$$

$$V' = \frac{Z}{Z+Z_p}V_0 = \frac{Y_p}{Y+Y_p}V_0 \tag{2.5}$$

and the differential output signal $\Delta V = V - V'$ is zero.

When the system is excited at a resonance frequency the piezotube branch's admittance Y_p^0 changes:

$$Y_p = Y_p^0 + \delta Y_p \tag{2.6}$$

and the bridge is unbalanced:

$$\Delta V = -\delta V' \tag{2.7}$$

$$\frac{dV'}{dY_p} = \frac{(Y+Y_p)-Y_p}{(Y+Y_p)}V_0 = \frac{Y}{(Y+Y_p)}V_0 \tag{2.8}$$

it results that the signal varies like $-\delta V'$:

$$\Delta V = -\delta V' = \frac{YY_p}{(Y+Y_p)^2} \cdot \frac{\delta Y_p}{Y_p} \cdot V_0 \tag{2.9}$$

From this equation it easily seen that he quantity $\Delta V/V_0$ is maximum for $Y = Y_p$. Thus we choose $C \simeq C_p$ and in the frequency range of interest we have:

$$\Delta V \simeq -\frac{\delta C_p}{C_p} \cdot V_{exc} \simeq \frac{1}{2}\frac{\delta C_p}{C_p}V_0 \tag{2.10}$$

The signal ΔV depends on the tip-to-surface separation. At the resonance, if the tip is far from the surface, its vibration amplitude is maximum, since no damping forces from the surface are present. We define ΔV_R the voltage corresponding to this situation. On the other hand, if the tip is close to the surface the vibration amplitude is damped by

the tip-surface interaction forces. So, the ΔV signal decreases. It has been measured [3] that this phenomenon can be described by:

$$\Delta V = \Delta V_R \left[1 - exp\left(-\frac{d}{d_0}\right)\right] \tag{2.11}$$

where $d = z_{surf} - z$ is the tip-to-surface distance (z_{surf} and z being the coordinates of the tip and of the surface, respectively), d_0 is the characteristic distance ($\simeq 1\ nm$), ΔV_R is the maximum amplitude of ΔV at the resonance frequency.

Considering the linear relationship between the V_z applied on the scan piezo and its z displacement (which determines the tip-to-sample separation):

$$z = \gamma |V_z| \tag{2.12}$$

we obtain:

$$\Delta V = \Delta V_R \left[1 - exp\left(-\frac{V_z - V_{surf}}{v_0}\right)\right] \tag{2.13}$$

where V_z, V_{surf}, v_0 are the voltages corresponding to the respective z positions.

ΔV is amplified through a gain $G = 100$ and is filtered via a lock-in amplifier (gain G_{LI}) locked on the tip excitation frequency. This constitutes the shear-force signal:

$$V_{SF} = G \cdot G_{LI} \cdot \Delta V_{RMS} \tag{2.14}$$

When the tip is far from the sample surface, V_{SF} takes the value V_{SF}^{∞} corresponding to the free vibration amplitude of the tip. When the tip approaches the surface, the shear-force interaction induces a decrease of the tip vibration and V_{SF} decreases. Thus, we process the signal by adding a constant voltage ΔV_{∞} to $-V_{SF}$ and we obtain the signal $V_{in} = V_{SF}^{\infty} - V_{SF}$ (**Figure 2.7**(a)). This signal is used in the feedback loop.

2.1.3.3 Feedback

The processed DC voltage V_{in} is used to define the process set-point (**Figure 2.7**). An adjustable attenuator G_C varies the amplitude of V_{in}. This voltage is compared to a

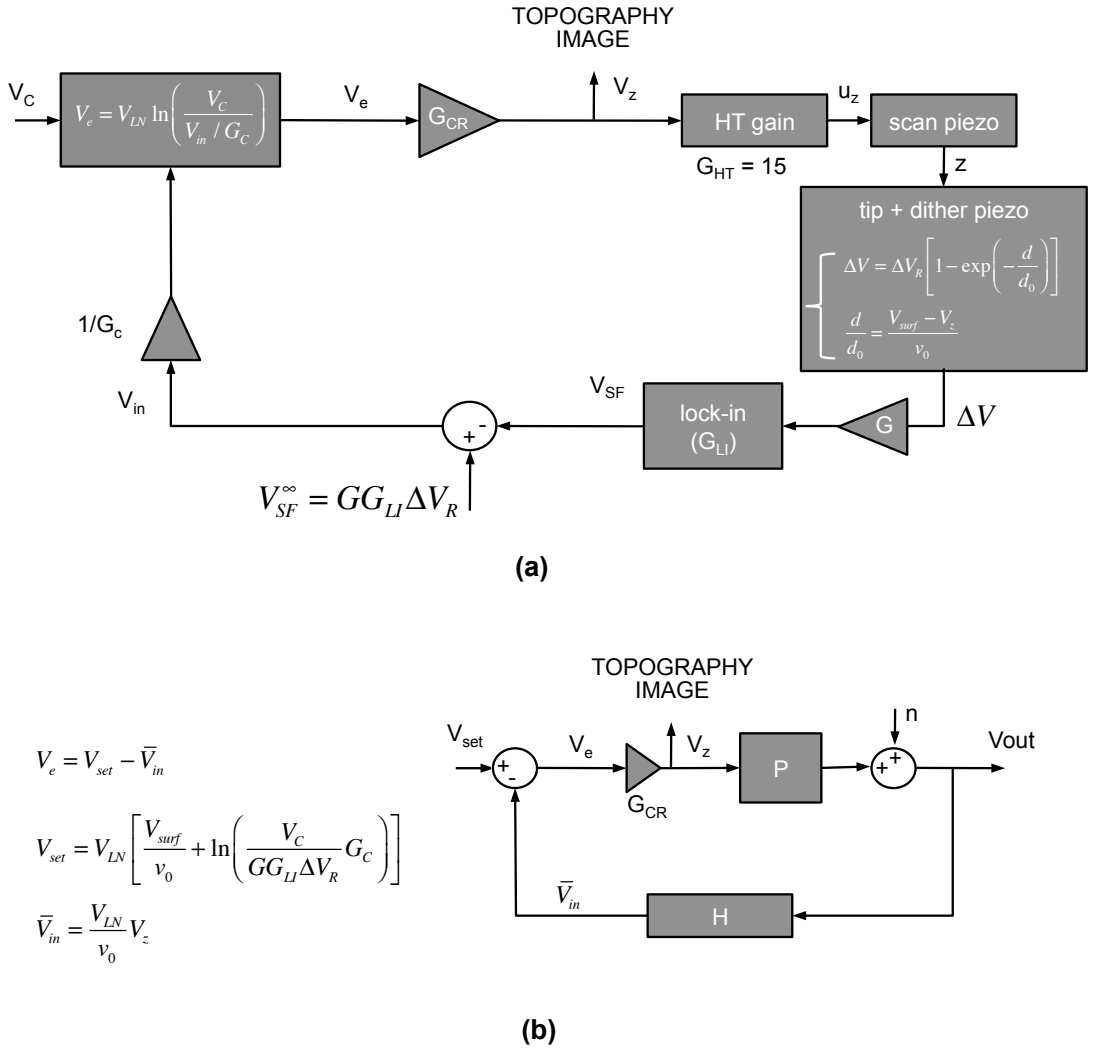

FIGURE 2.7: Shear-force microscopy: feedback loop.

fixed voltage V_C, generating the error signal V_e which is used for the control action. The comparison is operated by a logarithmic amplifier, which allows to extract V_z from V_{in} and so to generate a proportional feedback control action on the current V_z voltage via the gain G_{CR}:

$$\begin{aligned} V_z &= G_{CR}\left\{V_{LN}\ln\left(\frac{V_C}{V_{in}/G_C}\right)\right\} \\ &= G_{CR}\left\{V_{LN}\ln\left(\frac{V_C G_C}{GG_{LI}\Delta V_R}\left[exp\left(-\frac{V_z - V_{surf}}{v_0}\right)\right]\right)\right\} \\ &= G_{CR}\left\{V_{LN}\ln\left(\frac{V_C G_C}{GG_{LI}\Delta V_R}\right) + \frac{V_{LN}V_{surf}}{v_0} - \frac{V_{LN}}{v_0}V_z\right\} \\ &= G_{CR}\cdot V_e \end{aligned} \tag{2.15}$$

The feedback gain G_{CR} is obtained through the combination of two low-pass filters having different cut-off frequencies:

$$G_{CR} = \left[\frac{G_{fast}}{1+i\omega\tau_{LI}}\right]_{\omega\ll\frac{1}{\tau_{LI}}} + \left[\frac{G_{slow}}{1+i\omega\tau_{slow}}\right]_{\omega\ll\frac{1}{\tau_{slow}}} \tag{2.16}$$

The G_{slow} gain acts at lower frequencies ($\tau_{slow} \simeq s$), while the G_{fast} gain acts also at higher frequencies ($\tau_{LI} \simeq \mu s$). The slow filter gain is fixed at $G_{slow} = 10$, while G_{fast} is manually adjustable by the user, in order to optimize imaging.

The effect of the feedback control is put in evidence in **Figure 2.7**(b), where the feedback loop is re-drawn taking into account only the three main functional blocks, namely: the process **P** (which includes the HT gain, the scan piezo, the dither piezo and the tip), the measurement system **H** (signal gain G, lock-in, compensation) and the control action $\mathbf{G_{CR}}$. The equivalent set-point $\mathbf{V_{set}}$ is fixed through the adjustable attenuator G_C:

$$V_{set} = V_{LN}\left[\frac{V_{surf}}{v_0} + \ln\left(\frac{V_C}{GG_{LI}\Delta V_R}G_C\right)\right] \tag{2.17}$$

The disturbing actions are modeled with the noise n that affects the output voltage of the process V_{out}. We can write the expression of V_{out}:

$$V_{out} = \frac{HPG_{CR}}{1+HPG_{CR}}V_{set} + \frac{1}{1+HPG_{CR}}n \tag{2.18}$$

Hence, for $HPG_{CR} \gg 1 \Rightarrow V_{out} \to V_{set}$, which means that the feedback gain G_{CR} drives V_{in} towards the set-point fixed through G_C.

The physical role of the feedback is to avoid the collision of the tip on the sample's surface. The piezotube elongates for higher V_z values and retracts for lower values. Since:

$$V_z = G_{CR}\cdot\left(V_{set} - \bar{V}_{in}\right) \tag{2.19}$$

and

$$V_{set} = V_{LN}\left[\frac{V_{surf}}{v_0} + \ln\left(\frac{V_C}{GG_{LI}\Delta V_R}G_C\right)\right] \tag{2.20}$$

a decrease of G_C produces the piezotube stretch and the retraction of the tip away from the surface, while increasing G_C the tip is approached to the surface. Also, an increase of the shear-force signal $\bar{V}_{in}$ produces the tip retraction, which avoids the tip collision on the surface, while a decrease of $\bar{V}_{in}$ induces an elongation of the piezotube, so the

tip approaches the surface. For this reason, we record the V_z signal as the image of the surface topography.

The overall feedback loop is implemented via a modified commercial STM electronic fabricated by Park Scientific Instruments (STM-SU2-210 et SPC-400, 1992).

Data are recorded using a Labview 6.1^{TM} routine, which is used also to generate the (x,y) control voltages. Topography images are stored into a 256 $\times$ 256 matrix, in a binary file.

2.1.3.4 Performances and calibration

Typically, we place the tip second harmonic (tip f2) in the region between 48 and 61 KHz. The resonance frequency of the tip can be tuned by varying its length L, as the frequency varies like $\frac{1}{L^2}$ (eq. 2.2). For our microscope, the fit with the experimental data gives a value of $\alpha \simeq 610$, as shown in **Figure 2.8**(f). The tip resonance frequency is chosen far enough from the (x, y, z) piezo resonances situated at $\simeq 7\ KHz$ and $\simeq 45\ Khz$, and also from the resonances due to other mechanical couplings (like the tip-syringe coupling at 11 KHz). This is shown in a typical excitation spectrum in **Figure 2.8**(a)), where the measured voltages (at the lock-in output) are normalized with respect to the differential amplifier gain $G = 100$ (**Figure 2.6**). In (b) we report the detail of the tip second harmonic, analog to a damped resonator having a quality factor $Q \simeq 160$, which, at a working frequency of $56kHz$, gives a response time of the order of the ms. We must point out that the characteristics of the response depend much on the wax droplet that fixes the tip to the dither piezo tube. When its form is particularly inhomogeneous and the fixation not uniform it can cause the excitation of other vibration modes of the tip, which lead to the apparition of multiple resonance peaks.
The working frequency is chosen also in relation to the noise spectra characterizing the microscope head. In **Figure 2.8**(c-e) we show the spectra measured unplugging the excitation signal and recording the output lock-in signal, scanning its reference frequency. We perform the measurement in three configurations:

(c) Feedback electronics off The voltage that powers the (x, y, x) piezo tube is turned off. In this case we notice the $1/f$ noise decrease, with a peak to peak noise amplitude of 10 μV around our working frequency (56 kHz).

(d) Feedback electronics on - open loop The (x, y, x) piezo tube is powered, but is all retracted. The excitation signal is unplugged, then the shear-force signal is zero and the system is operated in open loop. Also in this configuration the noise decreases with increasing frequency, with a peak to peak noise at the working

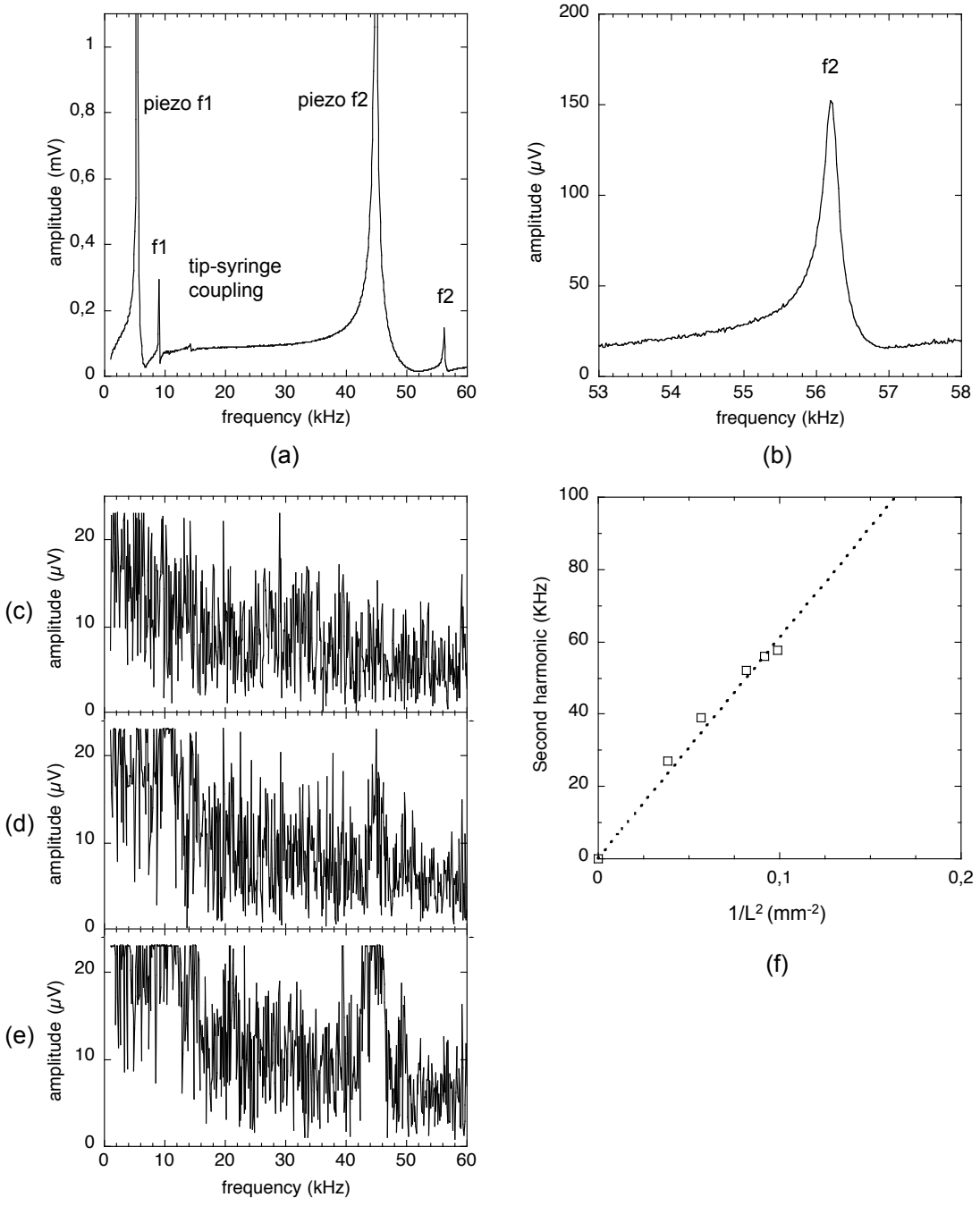

FIGURE 2.8: Tip excitation and noise spectra. (a-b) Excitation spectrum and zoom around the tip second harmonic. Noise spectra: (c) feedback electronic off; (d) feedback electronic on, but open loop; (e) feedback electronic on with closed loop simulation. (f) Calibration of the second harmonic.

frequency of 10 μV. The two structures at the resonant frequencies of the piezo tube and of the fiber tip are present, with a wider amplitude for the first structure.

(e) Feedback electronics on - closed loop The (x, y, x) piezo tube is powered and the feedback electronics is input a DC signal that simulates the shear-force signal. In this condition the average noise amplitude is moderately wider, the peak corresponding to the piezo tube second harmonic is more evident. However, the noise amplitude remains approximately of 10 μV at the working frequency.

2.1.4 Scanning Near-field Optical Microscope (SNOM)

The photo-activation of our samples is achieved by means of two coherent blue[5] laser beams, that we will call the interfering beams, whose wavelength is close to the sample absorption peak[6], and of a third incoherent homogeneous green[7] laser beam, that we will call the assisting beam, whose wavelength corresponds to an absorption 30% weaker. These are combined in several different ways, obtaining a variety of local intensity and polarization geometries and dynamics.

At the sample surface, we measure the transmitted optical field by a scanning near-field optical microscope. We use a tapered optical fiber tip that has the double function of diffracting the local electromagnetic field (aperture-less SNOM) and also of collecting the light through its small aperture of $\simeq 50\ nm$ (aperture SNOM). The near-field image is measured by means of a photomultiplier and recorded using a Labview^{TM} routine, then stored into a 256×256 matrix in a binary file, as previously described for the shear-force microscopy.

2.1.4.1 Optical setup

The optical experimental setup is depicted in **Figure 2.9**(a). It is constituted by two optical paths. The first one leads the green assisting laser beam, through a linear polarizer, in normal incidence on the surface, by means of two mirrors. The laser output polarization is $\simeq 40°$ with respect to the y-axis, so a linear polarizer is sufficient to obtain s or p linear polarizations. The second path leads the blue laser out-front beam through a half-wave plate and a beam-splitter, which separates the beam into two beams, of same intensity. These two beams recombine on the sample surface, with an incidence angle $\theta = 16.5°$. A polarizer on each of these beam paths define the orientation of the light polarization. The blue laser out-front beam is initially linearly polarized along the

[5] $\lambda = 473\ nm$.
[6] See **Figure 2.18**.
[7] $\lambda_a = 532\ nm$.

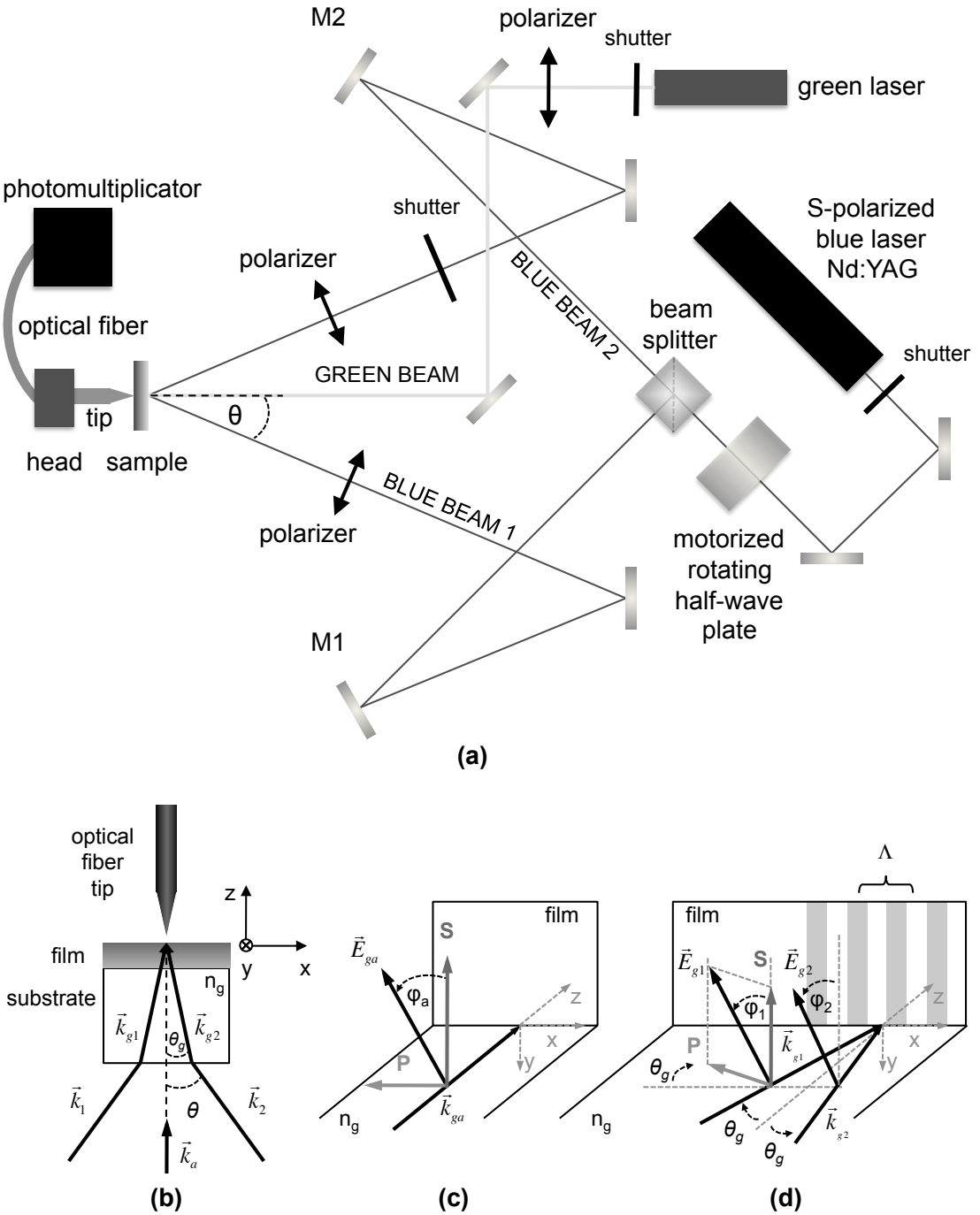

FIGURE 2.9: Optical setup. (a) optical path; (b) geometry at the sample surface; (c) green assisting beam: geometry within the substrate; (d) blue interfering beams: geometry within the substrate.

y-axis (s). Rotating the half-wave plate by an angle α rotates the polarization of the two split beams by the angles $\varphi_1 = \varphi_2 = 2\alpha$ with respect to the y-axis. The spot size of the three beams is typically 1 mm^2. The maximum output light power is 15 mW for the blue laser and is 20 mW for the green laser. This corresponds to a maximum intensity of 2.5 mW per blue beam et 2.1 mW for the green assisting beam at the sample surface. Three shutters allow to temporally control the activation of the different beams, enabling a great variety of different combinations. In particular it is possible to superimpose a uniform illumination at 532 nm to an optical interference pattern at 473 nm.

In (b-d) we see the detail of the geometry at the substrate/film interface. The assisting beam and interfering beam wavevectors inside the glass substrate are indicated respectively with k_{ga}, k_{g1}, k_{g2}, the refractive index inside the substrate $n_g \simeq 1.51$. The green assisting beam **Figure 2.9**(c) illuminate the sample at normal incidence, that is:

$$\vec{k}_{ga} = k_a \begin{pmatrix} 0 \\ 0 \\ n_g \end{pmatrix} \tag{2.21}$$

where $k_a = 2\pi/\lambda_a$ ($\lambda_a = 532\ nm$). On the other hand, the left (1) and right (2) blue beams form each one an angle θ_g with the z-axis **Figure 2.9**(b and d) so that:

$$\vec{k}_{g1} = k \begin{pmatrix} n_g sin\theta_g \\ 0 \\ n_g cos\theta_g \end{pmatrix} = \begin{pmatrix} k_x \\ 0 \\ k_z \end{pmatrix} \tag{2.22}$$

$$\vec{k}_{g2} = k \begin{pmatrix} -n_g sin\theta_g \\ 0 \\ n_g cos\theta_g \end{pmatrix} = \begin{pmatrix} -k_x \\ 0 \\ k_z \end{pmatrix} \tag{2.23}$$

where $k = 2\pi/\lambda$ ($\lambda = 473\ nm$).

Changing the polarization axis φ_a, φ_1, φ_2 for the various beams leads to vary the respective components' amplitude along the different axis[8]. For the green assisting beam, in normal incidence, the field can be only along the x and the y-axis. As an example, for the field represented in (b) we have:

[8] In the case of s- and p- interference pattern we have respectively $\varphi_1 = \varphi_2 = 0°$ and $\varphi_1 = \varphi_2 = 90°$

$$\vec{E}_{ga} = E^0_{ga} \begin{pmatrix} -sin\varphi_a \\ -cos\varphi_a \\ 0 \end{pmatrix} cos\left(\omega t + \vec{k}_{ga} \cdot \vec{r}\right) \tag{2.24}$$

where $E^{s,0}_a$ is the field amplitude inside the substrate.

On the other hand, for the blue beams, a component along the z-axis can be present, for $\varphi_1, \varphi_2 \neq 0$:

$$\vec{E}_{g1}(t,\vec{r}) = \vec{E}^0_{g1} cos\left(\omega t + \vec{k}_{g1} \cdot \vec{r}\right) = E^0_{g1} \begin{pmatrix} -sin\varphi_1\ cos\theta_g \\ -cos\varphi_1 \\ sin\varphi_1 sin\theta_g \end{pmatrix} cos\left(\omega t + \vec{k}_{g1} \cdot \vec{r}\right) \tag{2.25}$$

$$\vec{E}_{g2}(t,\vec{r}) = \vec{E}^0_{g2} cos\left(\omega t + \vec{k}_{2} \cdot \vec{r}\right) = E^0_{g2} \begin{pmatrix} -sin\varphi_2\ cos\theta_g \\ -cos\varphi_2 \\ -sin\varphi_2\ sin\theta_g \end{pmatrix} cos\left(\omega t + \vec{k}_{g2} \cdot \vec{r}\right) \tag{2.26}$$

where E^0_{g1}, E^0_{g2} are the respective field amplitudes inside the substrate. So, for two beams of equal amplitude $E^0_{g1} = E^0_{g2} = E^0_g$ the expression for the total interfering light field is obtained by superimposing the two fields $\vec{E}_{g1}(t,\vec{r})$ and $\vec{E}_{g2}(t,\vec{r})$:

$$\vec{E}_{g,tot}(t,\vec{r}) = \vec{E}_{g1}(t,\vec{r}) + \vec{E}_{g2}(t,\vec{r}) \tag{2.27}$$

whose x-, y- and z- components are:

$$\begin{aligned} \vec{E}^x_{g,tot} \;=\; & -\left(sin\varphi_1 + sin\varphi_2\right)\left[E^0_g cos\left(\omega t + k_z z\right) cos\theta_g\right] cos(k_x x)\hat{x} \\ & +\left(sin\varphi_1 - sin\varphi_2\right)\left[E^0_g sin\left(\omega t + k_z z\right) cos\theta_g\right] sin(k_x x)\hat{x} \end{aligned} \tag{2.28}$$

$$\begin{aligned} \vec{E}^y_{g,tot} \;=\; & -\left(cos\varphi_1 + cos\varphi_2\right)\left[E^0_g cos\left(\omega t + k_z z\right)\right] cos(k_x x)\hat{y} \\ & +\left(cos\varphi_1 - cos\varphi_2\right)\left[E^0_g sin\left(\omega t + k_z z\right)\right] sin(k_x x)\hat{y} \end{aligned} \tag{2.29}$$

$$\begin{aligned} \vec{E}^z_{g,tot} \;=\; & \left(sin\varphi_1 - sin\varphi_2\right)\left[E^0_g cos\left(\omega t + k_z z\right) sin\theta_g\right] cos(k_x x)\hat{z} \\ & -\left(sin\varphi_1 + sin\varphi_2\right)\left[E^0_g sin\left(\omega t + k_z z\right) sin\theta_g\right] sin(k_x x)\hat{z} \end{aligned} \tag{2.30}$$

We note that for $\varphi_1 = -\varphi_2 = \varphi$ and for every fixed z, the x-component is proportional to $sin(k_x x)$ while the y- and the z- components are proportional to $cos(k_x x)$, where $k_x = 2\pi n_s sin\theta_g/\lambda$. This means that the x-component intensity is $\Lambda/2$ spatially shifted with respect to the other two components[9], where the spatial period Λ is determined by:

$$\Lambda = \frac{\lambda}{2sin\theta} \simeq 830\ nm \tag{2.31}$$

Moreover, changing the value of φ allows to shift from a configuration of complete amplitude spatial modulation ($\varphi = 0°$) to a configuration of complete polarization spatial modulation ($\varphi = 45°$), which allows to distinguish the effects due to the intensity from the effects caused by the polarization. These important characteristics will be used extensively in **Chapter 3**.

The local light field is collected by means of the optical fiber nano-tip, which performs a scan on the (x, y) plane driven by the (x, y, z) piezo tube (see 2.1), and is measured by a photomultiplier.

2.1.4.2 SNOM calibration

As we have seen in 2.1.1 the tip fabrication process leads systematically to an asymmetry of the tip geometry, which can produce an unbalanced collection of the light field incident from the various beams and also a dependence on the polarization of the measured intensity. In particular, when creating an interference pattern, this can result in a very poor intensity contrast.
In order to minimize the effects of the asymmetry, we have developed the following procedure, in which we measure how the field collection in the tip depends on its orientation, with respect to the two blue beams.

1. We check the coincidence of the two spots at the surface of a clean glass plate and on the two mirrors M1 and M2 (**Figure 2.9**) in order to be sure that the beams are symmetrically incident.

2. We approach the tip at a few μm from the surface of the glass plate. During this procedure the tip is not fixed by the wax droplet, it is clamped by a latch chuck on the back of the head which can be rotated around the tip axis.

[9] For the details of the calculation see **Appendix A**

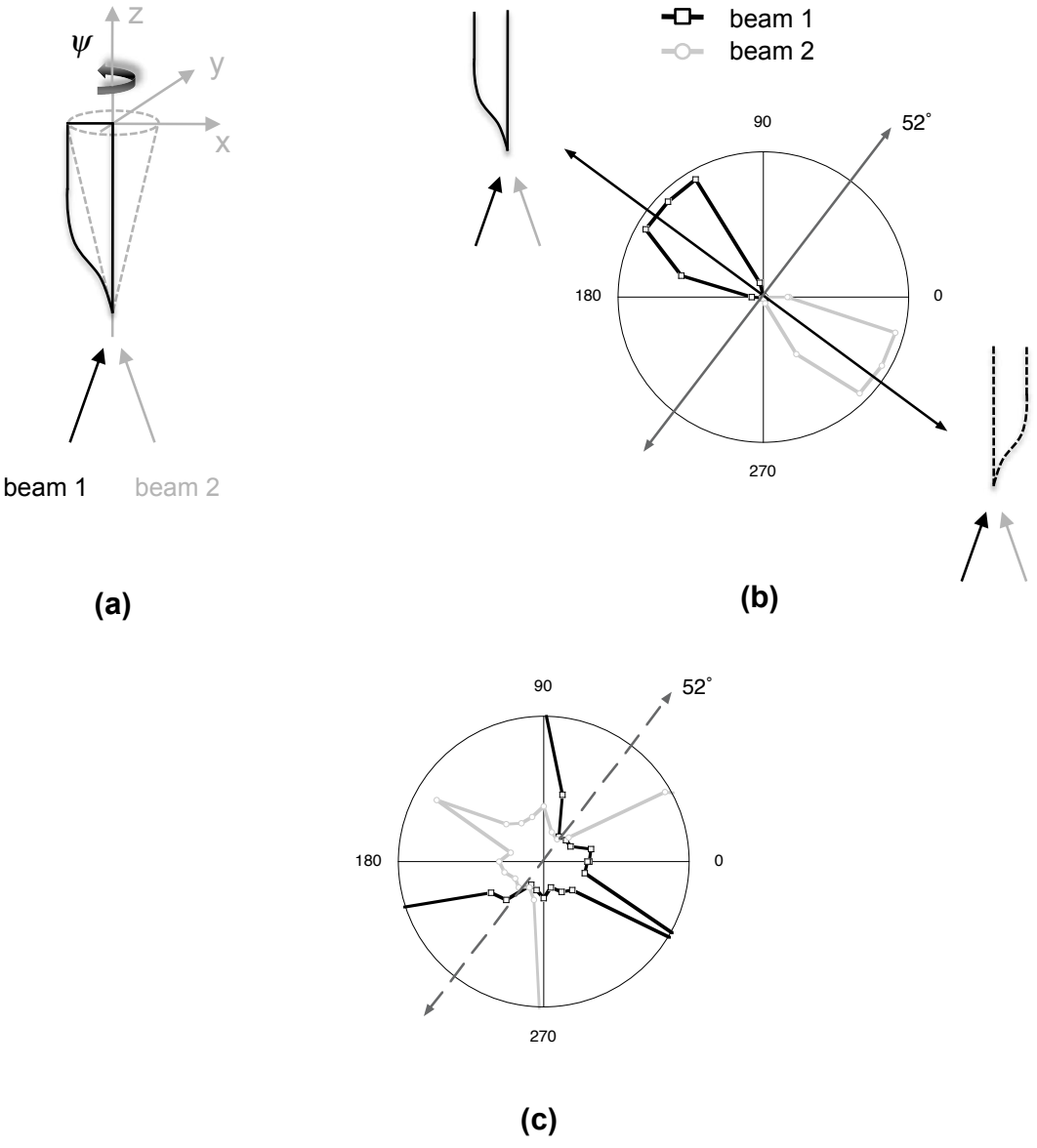

FIGURE 2.10: Polar diagram: (a) measurement principle; (b) efficiency angular distribution: the two lobes maxima correspond to the tip asymmetry maximally exposed to the beam 1 or to the beam 2, respectively; (c) zoom showing the tip orientation corresponding to symmetric light collection.

3. We measure the light collected for various orientation of the tip around the z-axis, varying the angle ψ under irradiation with each beam separately (see **Figure 2.10**(a)) .

In **Figure 2.10**(a-c) we show the principle of this procedure and a typical efficiency polar diagram. For the beam 1 (black) and the beam 2 (grey) the collection efficiency is asymmetrically distributed, producing two lobes which characterize the magnitude of the tip asymmetry. Each lobe shows the maximum collection efficiency corresponding to the tip oriented so that the asymmetry is maximally exposed to the beam 1 or to the beam 2, respectively, as depicted in **Figure 2.10**(b).
Once identified the angle of maximum asymmetry, we orient the tip at 90° with respect to that value, in order to obtain the most balanced light collection efficiency. In **Figure 2.10**(c) the zoom on the centre of the efficiency polar diagram shows that for this angle the collection efficiency is the same for the two beams.

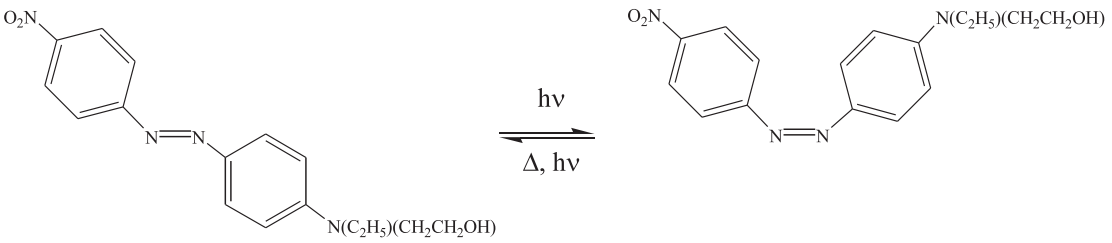

FIGURE 2.11: Disperse Red 1 molecule.

2.2 Sample preparation

2.2.1 The photochrome and the matrices

The photodeformation effects studied in this work are based on the photochromic properties of a derivative of the azobenzene molecule, the Disperse Red 1 (DR1), which is represented in **Figure 2.11**. As we have mentioned in **Chapter 1**, this molecule belongs to the pseudo-stilbene family. The presence of the electro-donor ($N(C_2H_5)(C_2H_4OH)$) and electro-acceptor (NO_2) groups para-substituted in the phenyl rings causes the partial superposition of the trans and cis isomers absorption spectra [4], which allows to excite both the trans $\rightarrow$ cis and cis $\rightarrow$ trans transitions employing a single wavelength, where the wavelength corresponding to the trans isomer absorption peak is[10] $\simeq 480\ nm$. Moreover, the cis $\rightarrow$ trans isomerization can be thermally activated and the average lifetime of the cis isomer is rather short [5], which contributes to the trans $\rightarrow$ cis $\rightarrow$ trans cycling of the molecules.

We have chosen to study the photodeformation effects produced by the DR1 photoisomerization in a mineral and in an organic matrices. The mineral matrix is a silica backbone obtained using a sol-gel proceeding that allows to preserve a certain degree of mobility of the molecules and can be performed at low temperature, which allows to incorporate organic molecules without thermal degradation. Moreover, this technique allows a great variety of deposition methods and is particularly suitable for the deposition of thin films via spin-coating, giving a good control of the film thickness and of the surface quality.
The organic matrix we have selected is the Poly[(methyl methacrylate)-co-(Disperse Red 1 methacrylate)] (PMMA-DR1), which is a polymer grafted with the DR1 units, commercially available[11]. The PMMA-DR1 is the mostly used azo-polymer for the study of photo-induced deformation phenomena.

[10] See **Figure 2.18** and **Figure 2.19**.
[11] Sigma-Aldrich® reference: 570435. Price: 1000 €/g.

2.2.2 Synthesis of the sol-gel Si-DR1 samples

2.2.2.1 The sol-gel process

The sol-gel process is based on two simple chemical reactions, which are initiated in presence of water and of a polymerizing agent, in our case the tetraethoxysilane (TEOS) $Si(OC_2H_5)_4$.

- **Hydrolysis**. The *ethoxy* groups on the TEOS molecules are hydrolyzed by water, producing ethanol. This reaction is catalyzed in both acid and basic environments, its minimum speed is at pH 7.

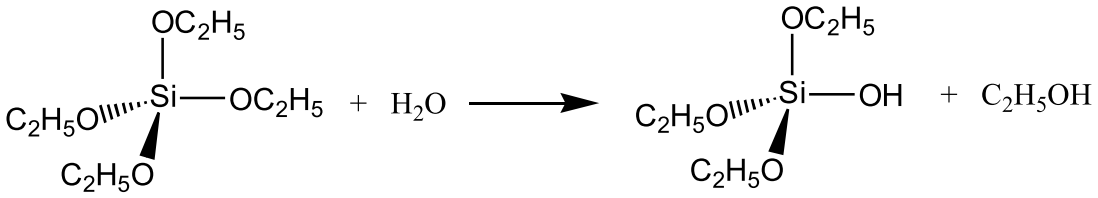

FIGURE 2.12: hydrolysis.

- **Condensation**. In this step either an ethanol molecule is expelled due to an alcoxolation reaction between an *ethoxy* group and a *silanol* group (**Figure 2.13**), or a water molecule is expelled due to an oxolation reaction between two *silanol* groups (**Figure 2.14**).

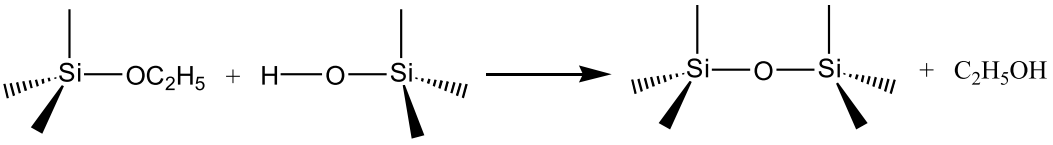

FIGURE 2.13: alcoxolation.

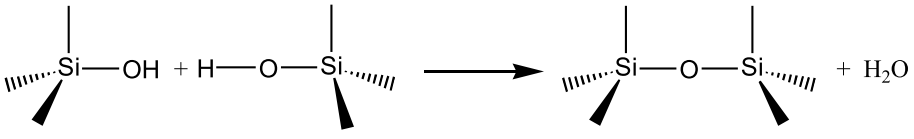

FIGURE 2.14: oxolation.

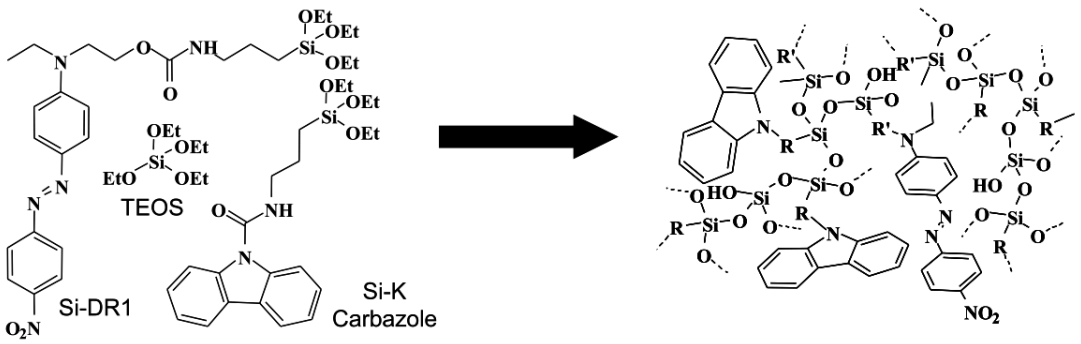

FIGURE 2.15: Sol-gel Si-DR1 matrix formation.

In both cases, the consequence is the formation of a **Si-O-Si** bridge, which is the building block of the inorganic backbone. For the TEOS, the condensation speed is minimum at pH 2-3 and maximum at pH 7. Instead, for higher pH the reversibility of the reaction may be non negligible.

The condensation reaction is faster than the hydrolisis at pH ≥ 7, while the hydrolysis dominates in acid environments. Hence, to avoid the formation of particles due to the preponderant formation of monomeres it is important to work at low pH (2-3). In this condition most of the monomers having a sylanol group are free to form the tridimensional matrix. First, very small particles are formed ($0.5 \div 2\ nm$) because of chain cyclization. Then, these particles starts aggregating, forming a polymeric network that doesn't precipitate and extends slowly occupying a growing volume fraction, which will constitute the sol. As the viscosity grows and the liquid is trapped into the sol, the sol-gel transition is reached. The material obtained is solid and transparent in most of the cases.

2.2.2.2 DR1 grafting into the sol-gel matrix

The incorporation of organic molecules into a mineral matrix can be done either by direct inclusion into the matrix (host/guest, doping) or by chemical grafting on the matrix backbone. The second method has been preferred, since it allows a higher concentration of the chromophore.
The principle is shown in **Figure 2.15**. The DR1 molecule is functionalized with an alkoxysilane group, which participates to the formation of the mineral matrix during the sol-gel process. A carbazole spacer is used to avoid the aggregation of the organic molecules.

The DR1 functionalization is achieved via a nucleophile addiction reaction of the DR1 molecule on a (3-isocyanatopropyl)triethoxysilane (ICPTEOS) which leads to the formation of the molecule shown in **Figure 2.16** that we will name Si-DR1.

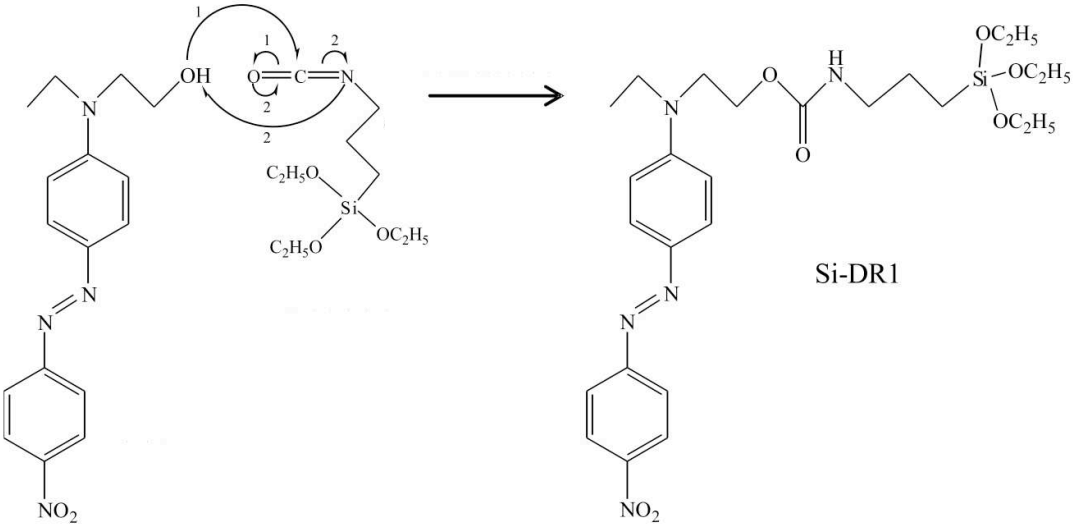

FIGURE 2.16: Si-DR1 preparation.

The spacer has been chosen following the results reported in [6], where the role of a carbazole molecule bearing an alkoxysilane group, that we will call Si-K, has been studied in the synthesis of photoactive materials constituted by linear and non linear molecules. In this case, the absence of Si-K lead to the aggregation of DR1 molecules. The Si-K molecule is obtained with the reaction shown in **Figure 2.17**.

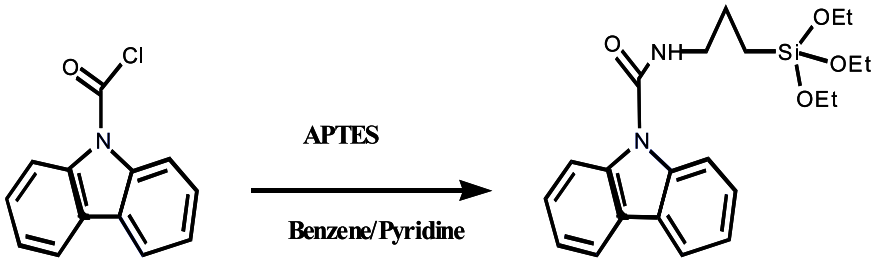

FIGURE 2.17: Si-K preparation.

The synthesis of the sol-gel matrix bearing the DR1 molecules proceeds as explained above, starting from the three precursors: TEOS, Si-DR1 and Si-K. These are mixed in the following molar ratio: Si-K/Si-DR1/TEOS = 4/2/1 in THF. This solvent has been chosen for its miscibility with water and for its good solvent power towards the three precursors.

A pH = 1 HCl solution is used to favor hydrolysis, with a ratio of 4 $H2O$ molecules for every Si, in order to convert the most of the ethoxy groups in sylanol groups.

		Si-DR1	Si-K		
1	g	0,207	0,307	+ 1,2 cm^3 THF	hydrolysis (2 hours)
	mol	$3,68 \cdot 10^{-4}$	$7,37 \cdot 10^{-4}$		
		TEOS	H_2O (pH = 1)		
2	cm^3	0,041	0,093		
	mol	$1,84 \cdot 10^{-4}$	$5,15 \cdot 10^{-3}$		
		Pyridine			
3	cm^3	0,099		+ 0,5 cm^3 THF	condensation
	mol	$1,22 \cdot 10^{-3}$			
4	filter 0,2 µm				

TABLE 2.1: Sol-gel Si-DR1 preparation: experimental procedure.

The solution is left 2 hours with a beater, at room temperature and in the darkness, in order to protect the DR1 dyes [7]. Once the hydrolysis completed a small quantity of THF is added to adjust the viscosity of the sol. Then, the compound is filtered ($0.2\mu m$). The whole experimental procedure is reported in **Table 2.1**.

#	Composition	Concentration	Thickness
A	Filtered solution	C_0	1500 nm
B	0.3 cm^3 A 0.3 cm^3 THF	$C_0/2$	450 nm
C	0.3 cm^3 B 0.3 cm^3 THF	$C_0/4$	230 nm
D	0.3 cm^3 C 0.3 cm^3 THF	$C_0/8$	130 nm
E	0.3 cm^3 D 0.3 cm^3 THF	$C_0/16$	75 nm

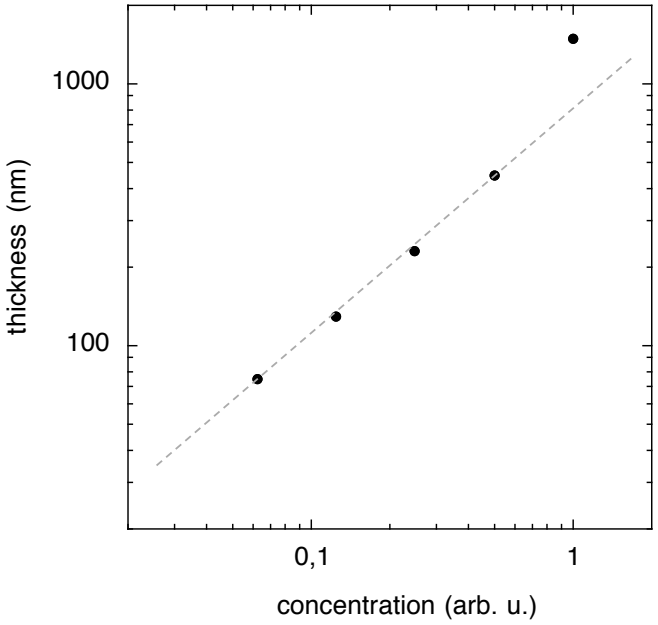

TABLE 2.2: Sol-gel Si-DR1 preparation: film thickness versus solution concentration [3]. Data are plotted in logarithmic scales.

2.2.2.3 Film deposition

In order to obtain the photochromic thin films we spin-coat the filtered compound on a glass plate previously cleaned to eliminate any organic residuals[12]. We use a micro-pipe to deposit 300 μL of the solution on the glasse plate and we evaporate the solvent for 40 s spinning at 6000 rpm, under a laminar flow hood. Using different concentration of the initial solution we can obtain a film thickness ranging between 75 nm and 1 μm. The film thickness is measured by SEM. A correlation has been established between the solution concentration and the film thickness, which is reported in **Table 2.2** [3]. The corresponding absorption spectra are reported in **Figure 2.18**.

[12] HF, H_2SO_4 and ultra-sonic cleaning.

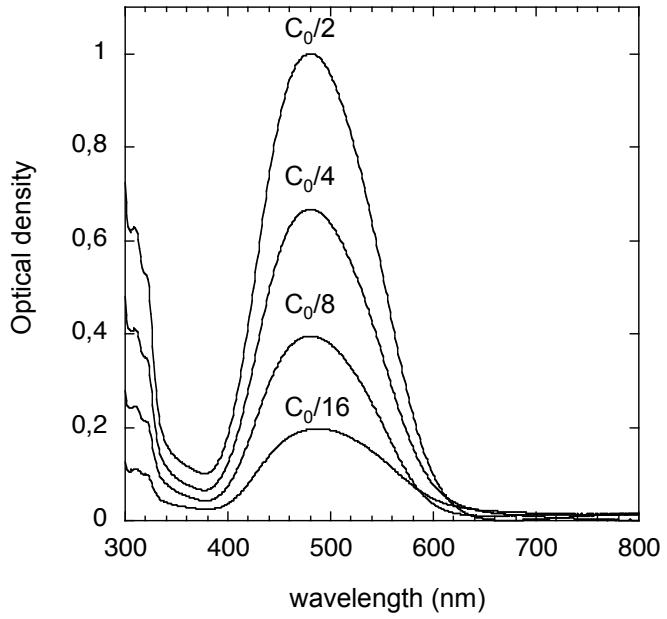

FIGURE 2.18: Sol-gel Si-DR1: absorption spectra.

The average DR1 density in the film can be estimated considering that $3.68 \times 10^{-4} mol$ of the azo-dye, which correspond to $2,2 \times 10^{20}$ DR1 molecules, are added to a volume of approximately 1.4 $mm^3 = 1.4 \times 10^{20} nm^3$. So, we obtain an average density of 1 DR1 molcule per nm^3.

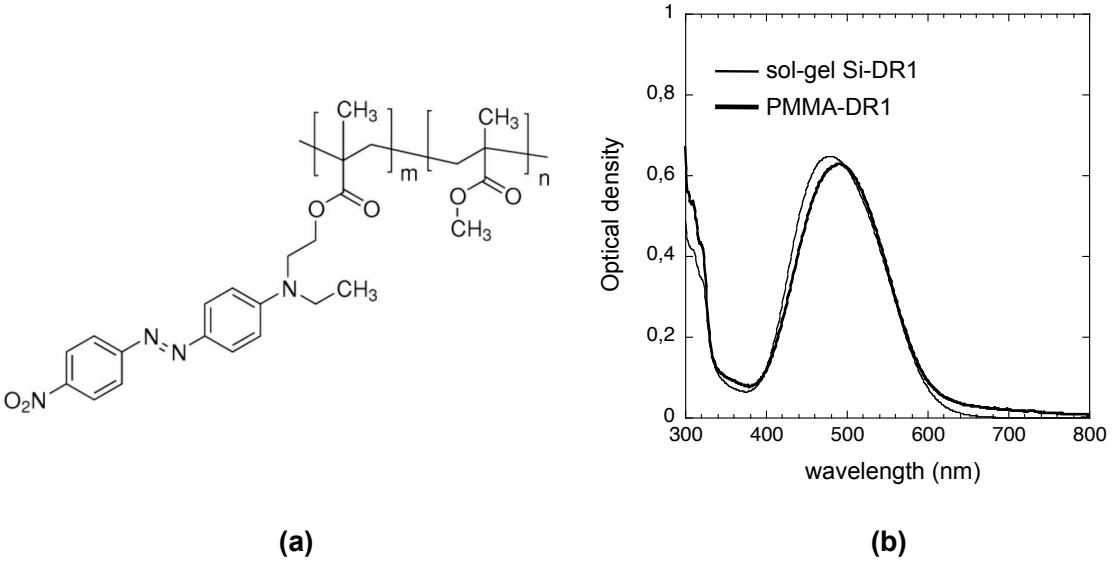

FIGURE 2.19: PMMA-DR1.

2.2.3 PMMA-DR1 film preparation

As for the organic matrix, the procedure is easier, since the compound is available commercially. The co-polymer is represented in **Figure 2.19**(a) where we see the DR1 unit bonded to the polymer backbone, in a molar concentration of 15 %. In order to have the same density of 1 chromophore per nm^3 that we have in a sol-gel Si-DR1 film, we dissolve 25 mg of PMMA-DR1 in 1 mL of dichloromethane. Referring to **Table 2.2** we use a $C_0/4$ concentration and after spin-coating we obtain a sample thickness of typically $180 \div 200$ nm. As we can see in **Figure 2.19**(b), the absorption of a 180 nm thick PMMA-DR1 sample is comparable to the absorption obtained on a sol-gel Si-DR1 sample of similar thickness.

2.2.4 Sample caracterization

We characterize the morphology of the films by shear-force microscopy. In **Figure 2.20** we show the topography measured for a sol-gel Si-DR1 (a) and a PMMA-DR1 (b) $C_0/4$ samples (thickness $\simeq$ 200 nm). They present a similar surface roughness of approximately 0.5 nm and similar sparsely distributed small defects (4 nm deep and 100 nm wide holes), probably due to the deposition proceeding. In some cases we have obtained a higher density of deeper defects, as shown in (c) in the case of a $C_0/4$ sol-gel sample (12 nm deep and 300 nm wide holes).

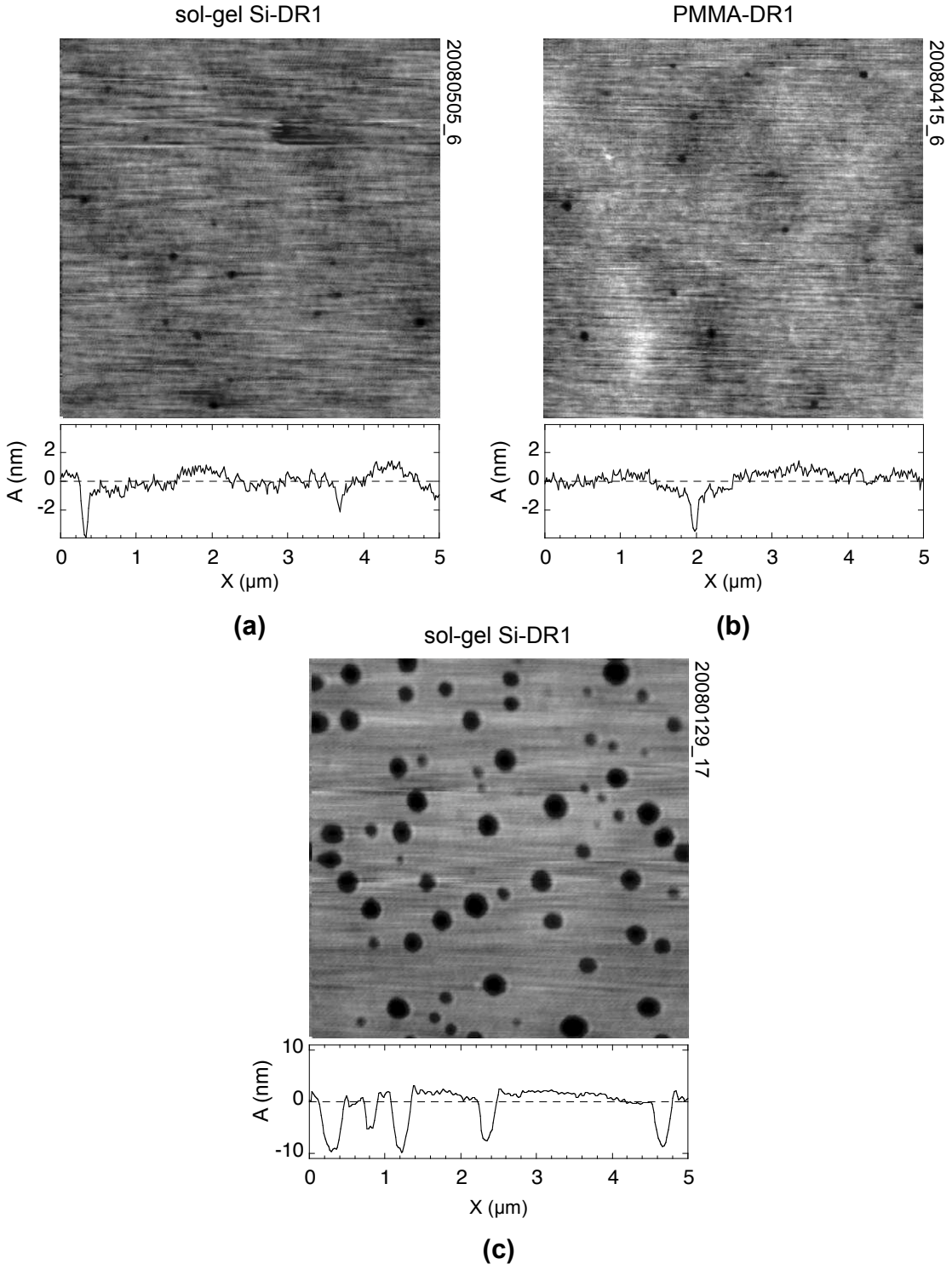

FIGURE 2.20: Sample characterization: (a) and (c) sol-gel Si-DR1 samples, concentration = $C_0/4$, thickness $\simeq 200\ nm$; (b) PMMA-DR1 sample, same thickness. Shear-force images, 256×256 pixel, $5 \times 5\ \mu m$.

2.3 Conclusions

We have described our coupled shear-force/SNOM measurement system, detailing the principles of each microscopy technique and their implementation in our experimental setup. We have shown the steps of fabrication of the nano-probe and its calibration for both the shear-force and the SNOM measurements. Also, we have described the types of samples studied in this work, the experimental procedure for their synthesis and deposition as well as for their characterization.

Bibliography

[1] Nathalie Landraud. *Ph.D. Thesis: Nanostructuration optique de films sol-gel photochromiques par microscopie en champ proche.* Ecole Polytechnique, 2002.

[2] Singiresu S. Rao. *Mechanical Vibrations (4th Edition).* Prentice Hall, 2003.

[3] Damien Garrot. *PhD Thesis: Etude par microscopie en champ proche des phénomènes de migration de matière photo-induite dans les matériaux photochromiques.* Ecole Polytechnique, 2006.

[4] H. Rau. *Photochemistry and Photophysics, Volume II.* CRC - Boca Raton, FL, 1989.

[5] C. Barrett, A. Natansohn, and P. Rochon. Cis-trans thermal isomerization rates of bound and doped azobenzenes in a series of polymers. *Chemistry of Materials*, 7(5): 899–903, 05 2002. URL http://dx.doi.org/10.1021/cm00053a014.

[6] B. Darracq. *PhD thesis: Etude de mecanisme de migration et d'orientation moleculaire dans des films minces sol-gel : deformation de surface et proprietes optiques non-lineaires quadratiques.* Université Paris-Sud, 1999.

[7] J. Biteau, F. Chaput, K. Lahlil, J. P. Boilot, G. M. Tsivgoulis, J. M. Lehn, B. Darracq, C. Marois, and Y. Levy. Large and stable refractive index change in photochromic hybrid materials. *Chemistry Of Materials*, 10(7):1945–1950, July 1998.

Chapter 3

Microscopic mechanisms at the origin of the photo-induced deformation in azobenzene-containing thin films

3.1 Introduction

It is widely established [1–7] that the surface relief grating (SRG) growth efficiency induced under polarized interference in azo-containing thin films strongly depends on the light polarization. In particular, higher efficiencies have been observed in presence of a polarization grating. Also, as recently shown, the SRG growth efficiency can be enhanced by combining an assisting beam with the interfering beams [3, 8]. The influence of the polarization configuration on the SRG growth efficiency has been deduced by indirect techniques, such as diffraction efficiency measurements. However, the nature of the deformation and its dependence on the spatial distribution of the light field has not been completely established.

In this chapter, we will study the SRG inscription in thin films containing azobenzene derivatives. We use the direct techniques described in **Chapter 2**, which allow us to correlate the topography and the optical measurements in situ, in real-time and at nanoscale. These techniques have already allowed to identify two types of photodeformation processes: a local matrix photoexpansion due to the free volume increase necessary for the azobenzene photoisomerization, and a photo-induced mass transport whose relation to the azobenzene photoisomerization is still debated.

Our aim is the comprehension of the mechanisms at the origin of these photodeformation

phenomena. First, we study the photodeformation produced by matrix photoexpansion and we evidence a plastic and an elastic contributions. Second, we study the polarization and intensity effects on the matter migration phenomena, in both sol-gel Si-DR1 and PMMA-DR1 samples. We identify the coexistence of two distinct microscopic mechanisms, one driven by the light polarization distribution and the other one by the light intensity pattern. We then demonstrate that the relative efficiency of these mechanisms depends on the nature of the matrix bearing the chromophore. This leads to coherently explain several observations in the far and in the near field, not completely understood up to now.

3.2 Elastic and plastic matrix deformation induced by the azobenzene photoisomerization

It has been shown in a previous work [9] that the first stages of the SRG formation under illumination are characterized by a very fast deformation of moderate amplitude. This deformation process is attributed to a matrix photoexpansion, resulting from the increase of the molecular free volume due to the photoinduced interconversion between the trans and the cis isomers. Photoexpansion has been found to depend on the light intensity and to arise for any polarization state of the exciting light.

Figure 3.1 shows the first stages of the SRG formation kinetics measured with near-field techniques upon illumination with an s- and a p-polarized interference patterns. The sample is a sol-gel Si-DR1 film having a thickness of 200 nm. It is illuminated through the substrate by two interfering beams (**Figure 3.1**(a,e)) having a 1 mW/mm^2 power density and a wavelength $\lambda = 473$ nm, with an angle of incidence at the sample surface $\theta = 16.5°$, in air. The interference pattern obtained in this configuration has a spatial period of 830 nm. It is described in detail in **Appendix A** for the different configurations of the light polarization, in particular, for the s-polarization, which corresponds to the electric field along the y-axis, and for the p-polarization, which corresponds to the electric field parallel to the incident plane. In (b-c) we show the optical and topographical images simultaneously obtained by Scanning Near-field Optical Microscopy and Shear-force microscopy, respectively, under illumination with an s-polarized interference pattern. The horizontal axis corresponds to the x-axis, while on the vertical axis we represent the time t. The corresponding time-evolution of the SRG amplitude is reported in (d). The same is shown in (f-h) for the experiment performed under p-polarized light. The time-evolution of the SRG amplitude is directly measured by the topography profile along a scanning line across the interference pattern. Over the scanning width, N interference periods are measured, each one producing a dark and

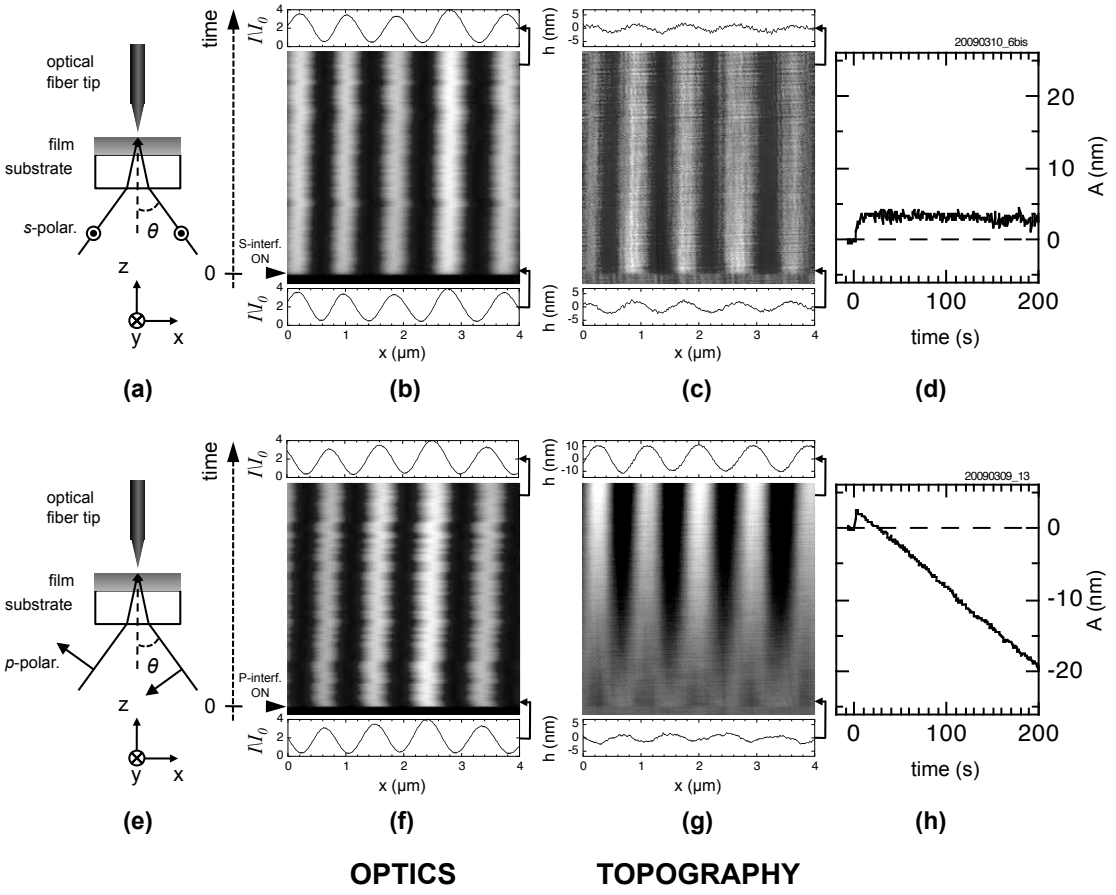

FIGURE 3.1: SRG inscription in a sol-gel Si-DR1 film under an s- and a p-polarized interference patterns. (a) Experimental setup scheme of the projection of an s-polarized interference pattern; (b-c) optical and topographical images, scanning over the same line, simultaneously obtained by Scanning Near-field Optical Microscopy and Shear-force microscopy, respectively, during the first 200 s of illumination. The scan-range is 4 μm. (d) Time-evolution of the SRG amplitude $A(t)$, expressed in nm. Note that the sign of the SRG growth amplitude and slope is positive when the SRG are spatially *in phase* with the interference pattern while it is negative when the SRG are half-a-period ($\Lambda/2$) spatially shifted (so-called π-*phase*) with respect to the interference pattern. (e-h) The same is shown for p-polarized light.

a bright fringes. The deformation amplitude is defined as the difference between the surface height of two adjacent dark and bright fringes h^{bright}, h^{dark}. Then, at each time t, we calculate the average deformation amplitude $A(t)$ over the N interference periods within the scanning line.

$$A(t) = \frac{1}{N} \sum_{i}^{N} \left(h_i^{bright}(t) - h_i^{dark}(t) \right) \tag{3.1}$$

Note that according to this procedure the SRG growing spatially *in phase* with the light intensity profile I corresponds to a positive sign of the deformation amplitude A and of its slope, while the SRG half-a-period ($\Lambda/2$) spatially shifted with respect to the light

intensity distribution is represented[1] with a negative sign.
Matrix photoexpansion is observed under both s-polarized (**Figure 3.1**(a-d)) and p-polarized (e-h) interference patterns. As the illumination is turned on (at $t = 0$), it produces the rapid growth of a SRG of weak amplitude, spatially *in-phase* with the illumination. This SRG growth kinetics corresponds to the initial positive rise of the deformation amplitude $A(t)$. In the case of p-polarized light, subsequently to the photoexpansion, we observe the rapid decrease of $A(t)$ which becomes negative and reaches large absolute values. This corresponds to the growth of a new SRG half-a-period spatially shifted with respect to the interference pattern. This phenomenon corresponds to a photo-induced lateral matter motion which takes place between the bright and dark fringes. Note that, instead, matter migration is not observed under s-polarized light, in a sol-gel Si-DR1 sample.

Shutting down the illumination, the deformation induced by the matrix photoexpansion has been observed to be irreversible while a part relaxes [10, 11]. In order to discriminate between the plastic and the elastic contributions of the photodeformation we have measured the amplitude of the SRG that forms subsequently to a pre-irradiation of the material with a uniform laser beam. In this way, the matrix photoexpansion is first generated over the whole enlightened area. Then, while projecting an interference pattern having the same polarization, the photoexpansion is further induced only in the bright fringes, giving rise to the formation of a SRG. For different pre-irradiation doses, the amplitude of the reliefs should vary as a function of the residual deformability of the material. In this sense, the projection of an interference pattern is used to quantify the contribution of the plastic deformation to the SRG formation.

So, we have performed the same experiment as presented in **Figure 3.1** but for different pre-irradiation doses. In **Figure 3.2** we show the photodeformation results obtained on the same sol-gel Si-DR1 sample for different uniform pre-irradiation doses using a single beam. The experience is performed in two steps, as schematized in **Figure 3.2**(a-b). First, we pre-irradiate the sample, during a time t, using only the right beam. This induces a uniform matrix photoexpansion. Then, we wait 20 s, allowing eventually a relaxation of the deformation. Subsequently, we turn on both beams to project the interference pattern. The amplitude of the SRG obtained during the interference pattern projection is shown in **Figure 3.2**(c) for both s (top graph) and p (bottom graph) polarizations. For different pre-irradiation doses, the subsequent projection of an interference pattern always induces matrix photoexpansion in the bright fringes. However, the amplitude of this deformation decreases for increasing values of the pre-irradiation dose. The same behavior is observed for both polarizations.
Note that, with p-polarized light, subsequently to the photoexpansion, matter migration

[1] We consider only these two cases as we do not need to describe other spatial relationships.

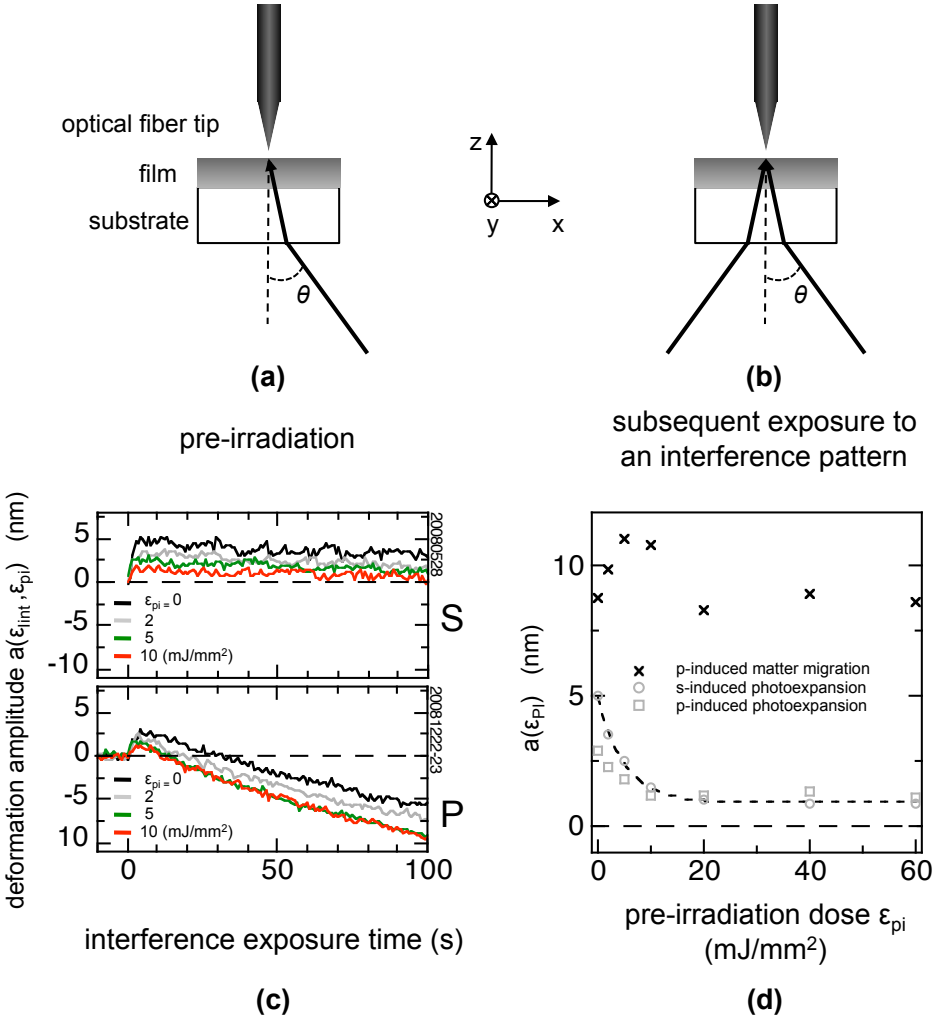

FIGURE 3.2: Photoexpansion and matter migration deformation amplitudes under successive irradiations. (a-b) Experimental setup for the pre-irradiation and the interference pattern projection, $\theta = 16.5°$. (c) Photoinduced deformation under s-polarized (top) and p-polarized (bottom) interfering beams; (d) photoexpansion dependence on the pre-exposure dose, for the s (❍) and the p (❑) polarizations; the dotted curve indicates the interpolating curve; (✕) indicates mass migration induced under p-polarized light. Laser power density: 1 mW/mm^2 per beam; sample = sol-gel Si-DR1, $\simeq$ 200 nm thick.

arises which is not significantly affected by the pre-irradiation.

In **Figure 3.2**(d) we plot the saturation amplitude of the photoexpansion observed for both polarizations. We also plot on the same figure the deformation amplitude due to mass transport in the p-polarized configuration. While the matter migration (✕) is essentially not affected by the pre-irradiation, we see that the amplitudes of the SRG induced by the matrix photoexpansion (s ❍ and p ❑) start to decrease for a dose of 10 mJ/mm^2, from a maximum of 5 nm, obtained without pre-irradiation, to a minimum of 1 nm. This accounts for the plastic deformation induced by the matrix photoexpansion. The more free space is acquired by each molecule during pre-irradiation, the smaller

further matrix photoexpansion is needed during the following irradiation in the bright areas of the interference pattern. The plastic deformation due to the the photoexpansion mechanism is almost completed after a rather small light dose. We observe that this behavior is approximately the same under s- and p-polarized light.
We used higher pre-exposure doses up to 2000 mJ/mm^2 (data up to 60 mJ/mm^2 are shown in **Figure 3.2**(d)) but the deformation subsequently produced by the interference pattern is the same as for 10 mJ/mm^2 (1 nm). The remaining deformation of 1 nm amplitude corresponds to the elastic deformation associated to the photoexpansion. Part of the photoexpansion is elastic and is relaxed after the pre-irradiation. The elastic photodeformation represents about 20 % (1 nm over 5 nm) of total photoexpansion, which is in agreement with what has been observed so far [10, 11].

3.2.1 Discussion

The matrix photoexpansion exists for both p and s polarizations. An s-polarized interference pattern produces a maximum deformation amplitude of $\simeq 5$ nm, which is about $\simeq 2\%$ of the film thickness. We observe a decrease in the photoexpansion SRG amplitude when the sample is uniformly irradiated prior to the projection of the interference pattern. This suggests that raising the probability of the photo-isomerization events during the pre-exposure allows to gain more free molecular volume needed by the molecule photoisomerization cycles. However, a residual deformability of $\simeq 1$ nm is observed, even for extremely long pre-irradiation time (i.e. 2000 s). Thus, a weak mechanical relaxation takes place after the steric re-arrangement subsequent to the pre-irradiation, which corresponds to the elastic part of the deformation. Any further illumination produces an extra matrix photoexpansion to recover the molecular free volume lost during the relaxation. This extra-expansion of the matrix is observed as a surface deformation under projection of an interference patter subsequent to the pre-irradiation.

The decrease in the SRG amplitude due to the pre-irradiation accounts for the plastic behavior of the photoresponse, while the residual photodeformation is related to its elastic behavior. Here we will analyze only the case of s-polarized light, which allows to single out the photoexpansion from the photoinduced matter migration in sol-gel Si-DR1 thin films.

The total photodeformation $a(\epsilon)$ can be expressed by:

$$a(\epsilon) = a_{el}(\epsilon) + a_{pl}(\epsilon) \tag{3.2}$$

where ϵ is the dose and $a_{el}(\epsilon), a_{pl}(\epsilon)$ are the amplitudes of the elastic and the plastic parts, respectively.

Defining ϵ_{pi} the pre-irradiation light dose and ϵ_{int} the interfering beam light dose we can describe the photodeformation obtained in the pre-irradiation experiments of **Figure 3.2**(c) as:

$$a(\epsilon_{int}, \epsilon_{pi}) = a(\epsilon_{int}, 0) - a_{pl}(\epsilon_{pi}) \tag{3.3}$$

where $a_{pl}(\epsilon_{pi})$ is the plastic deformation induced by the pre-irradiation. The deformation amplitude $a(\epsilon_{int}, \epsilon_{pi})$ obtained under exposure to the interfering beam dose ϵ_{int} after a pre-irradiation dose ϵ_{pi} is equal to the photodeformation amplitude $a(\epsilon_{int}, \epsilon_{pi} = 0)$ obtained under exposure to the interference pattern without pre-irradiation diminished of the plastic photoexpansion $a_{pl}(\epsilon_{pi})$ due to the pre-irradiation dose ϵ_{pi}. By taking into account only the *saturation* deformation amplitudes observed in **Figure 3.2**(c) we obtain the curve in **Figure 3.2**(d) relative to the matrix photoexpansion, which represents:

$$a(\epsilon_{int} = \infty, \epsilon_{pi}) = a(\infty, 0) - a_{pl}(\epsilon_{pi}) \tag{3.4}$$

This allows to deduce the *saturation* plastic deformation amplitude:

$$a_{pl}(\epsilon_{pi}) = a(\infty, 0) - a(\infty, \epsilon_{pi}) \tag{3.5}$$

which can be simply rewritten:

$$a_{pl}(\epsilon) = a(\infty, 0) - a(\epsilon) \tag{3.6}$$

The experimental variation of $a_{pl}(\epsilon)$ is plotted in **Figure 3.3**(a). By using eq. 3.2, we can easily obtain the amplitude of the elastic part of the photodeformation:

$$a_{el}(\epsilon) = a(\epsilon) - a_{pl}(\epsilon) \tag{3.7}$$

In **Figure 3.3**(b-c) we show the variation of $a_{el}(\epsilon)$ deduced from the experimental data obtained with two different interference power densities, 4 mW/mm^2 and 1.5 mW/mm^2 respectively.

The behavior of $a_{pl}(\epsilon)$ and $a_{el}(\epsilon)$ indicates that the plasticity of the photodeformation grows with the irradiation dose, reaching a maximum amplitude of about 4 nm at $\epsilon_{pi} \simeq 10\ mJ$. On the other hand, the elastic deformation amplitude exhibits a transient feature for low doses and beyond reaches a plateau.
We note that the amplitude of $a_{el}(\epsilon)$ at saturation is slightly larger for 4 mW/mm^2 irradiation power density (b) than for 1.5 mW/mm^2 irradiation power density (c). This is coherent with the stress-strain model for an elastic deformation. However, we are

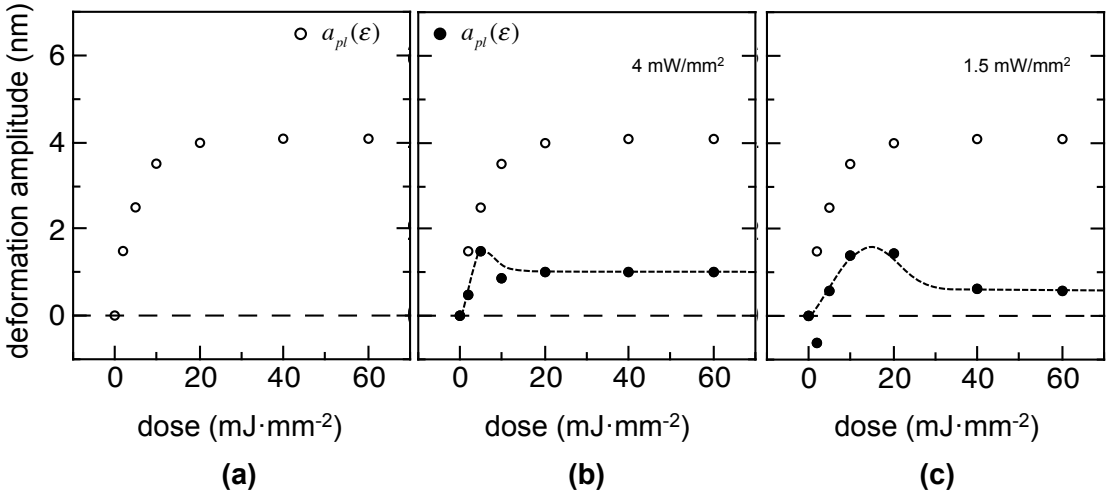

FIGURE 3.3: Photoexpansion: plastic and elastic deformation. (a) Plastic deformation amplitude $a_{pl}(\epsilon)$ (b) Elastic deformation $a_{el}(\epsilon)$amplitude at 4 mW/mm^2; c) Elastic deformation $a_{el}(\epsilon)$ amplitude at 1.5 mW/mm^2.

not able to perform a detailed analysis of $a_{el}(\epsilon)$ at small doses and further investigations would be needed to fully determine the variation of a_{el} as a function of the power density.

Concerning the plastic deformation, **Figure 3.3**(a) clearly shows that a_{pl} builds up with an increasing dose and reaches a maximum a_{pl}^{max} when the free volume required for the free isomerization of the molecule is reached. We can perform a phenomenological analysis relative to the dependence of the plastic part $a_{pl}(\epsilon)$ on the dose ϵ. We may assume that the more $a_{pl}(\epsilon)$ is close to the maximum deformation a_{pl}^{max} needed to accommodate the constraint produced in the matrix by the molecular photoisomerization, the smaller will be the further deformation required in order to relax this constraint. The plastic deformation dynamics takes place within the characteristic dose η and we can write the evolution of $a_{pl}(\epsilon)$ as:

$$\frac{d}{d\epsilon}\left(a_{pl}(\epsilon)\right) = -\frac{a_{pl}^{max} - a_{pl}(\epsilon)}{\eta} \tag{3.8}$$

which leads to:

$$a_{pl}(\epsilon) = a_{pl}^{max}\left(1 - e^{-\epsilon/\eta}\right) \tag{3.9}$$

In **Figure 3.4**(a) we show the fitting of the experimental variation of $a_{pl}(\epsilon)$ obtained with $a_{pl}^{max} = 4\ nm$ and $\eta \simeq 5\ mm^2/mJ$. Then, from eq. 3.2, considering that $a_{el}(\epsilon)$ is constant (neglecting the transient feature of $a_{el}(\epsilon)$ at low ϵ), we obtain for the total photoexpansion amplitude $a(\epsilon)$ the variation plotted in **Figure 3.4**(b), which fits

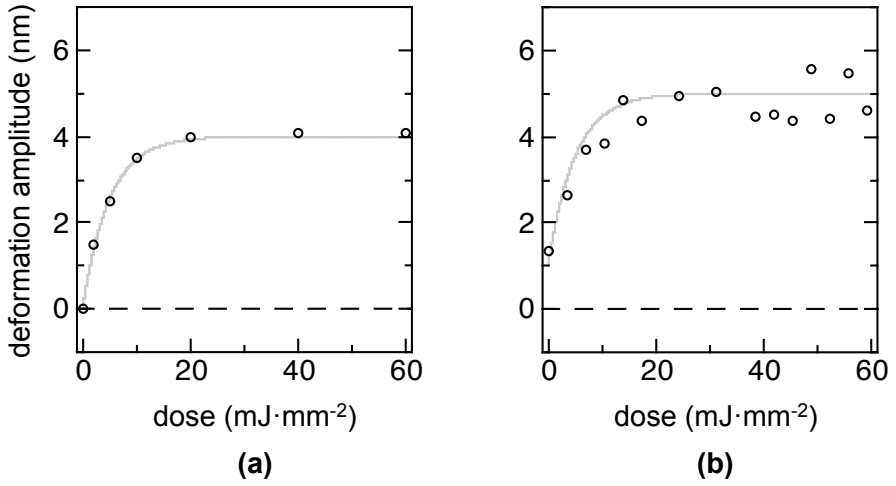

FIGURE 3.4: Photoexpansion as a function of the light dose. (a) $a_p l(\epsilon)$. (b) $a(\epsilon)$, for $\epsilon_{pi} = 0$. Experimental data (◯) and exponential fit (grey curve).

remarkably well the experimental data. Note that taking $a_{el}(\epsilon)$ as constant is fully justified, if the characteristic time of the elastic deformation is shorter than the one of the plastic deformation, which is a very reasonable assumption.

In this simple description all the microscopic aspects of the observed phenomena hide behind the characteristic quantity η which depends on the experimental conditions, on the mechanical properties of the material, on the film thickness, etc. Moreover, the interplay between the elastic and the plastic deformation mechanisms is not taken into account while these mechanisms are obviously coupled at the microscopic level. However, the above phenomenological model allows to suitably describe the observed growth of the plastic photodeformation amplitude due to the matrix photoexpansion and its saturation at high doses.

In conclusion, this study confirms that the photoexpansion is dependent mainly on the distribution of the light intensity and not on the distribution of the light polarization. The resulting deformation shows a combination of an elastic and a plastic contributions, which depend on the irradiation dose. We have been able to single out the dynamics of both contributions.

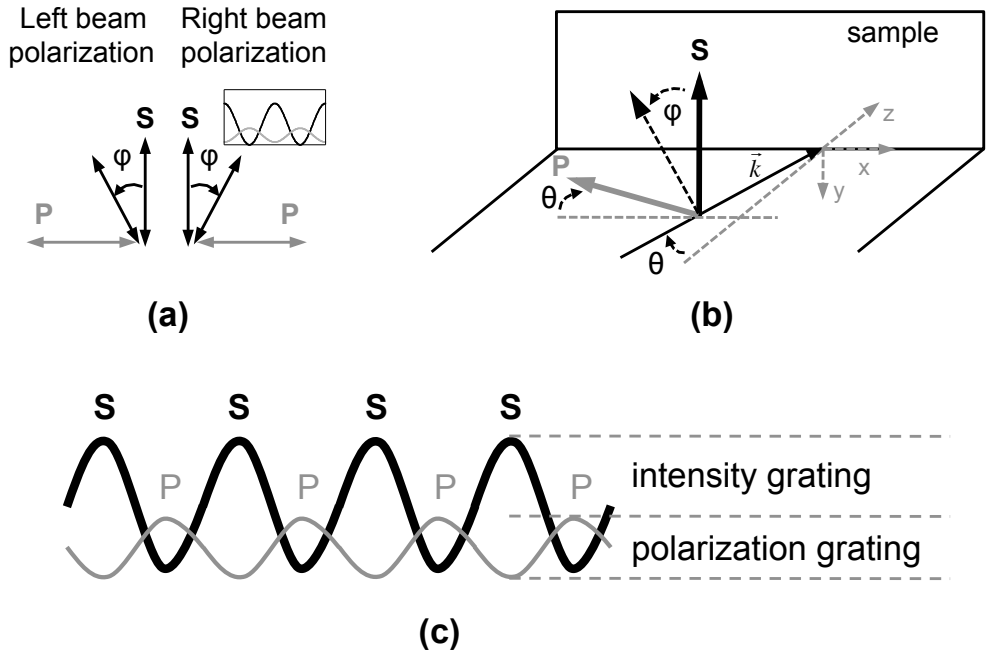

FIGURE 3.5: a) Spatially shifted interference patterns using two linearly polarized beams with opposite polarization axis angles φ, with respect to the s-polarization axis (y-axis). $\varphi = 0°$ corresponds to both beams s-polarized; $\varphi = 90°$ corresponds to both beams p-polarized; any value of φ in-between corresponds to different ratios of the s and p interference pattern intensities; at $\varphi = 45°$ the s and the p interference patterns have the same amplitude; b) s and p axis definition with respect to the xyz frame; (c) intensity and polarization gratings.

3.3 Influence of the spatial distribution of the light intensity and polarization on the mass migration

As shown in **Figure 3.1**, subsequently to the photoexpansion, the projection of an interference pattern produces the growth of a SRG of large amplitude which results from a photo-induced lateral mass transport. This process is found to strongly depend on the light polarization. However, the respective role of the light polarization and light intensity patterns are not well understood. Our objective is, thus, to establish the relation between the optical pattern and the photo-induced mass transport process. For this purpose, we adopt the configuration depicted in **Figure 3.5**(a) where the polarization axes of both interfering beams form symmetric angles φ with respect to the y-axis[2]. This creates the superimposition of an s- and a p-polarized interference patterns spatially shifted of half a period[3] ($\Lambda/2$) along the x-axis. The s and the p polarizations are defined in **Figure 3.5**(b). As shown in (c), this configuration generates a light background having a spatially modulated polarization and giving rise to the polarization grating.

[2] In the formalism reported in **Chapter 2** this means $\varphi_1 = -\varphi_2 = \varphi$.
[3] $\Lambda \simeq 830\ nm$.

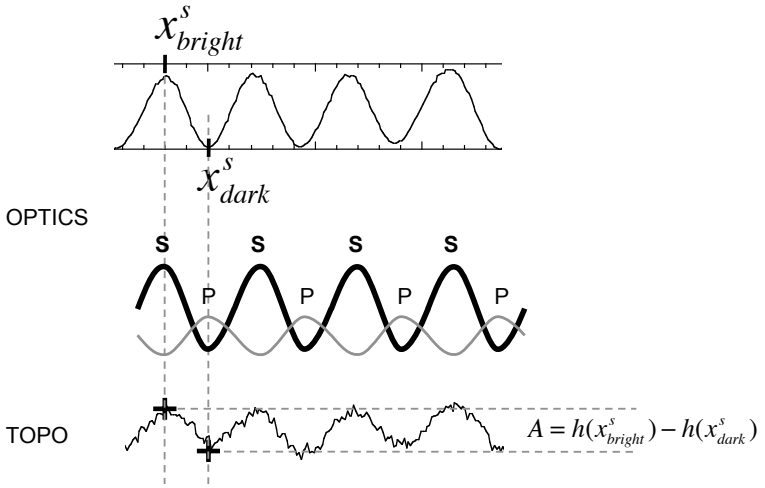

FIGURE 3.6: Deformation amplitude measurement convention.

It is superimposed to a spatially modulated intensity pattern of constant polarization, which constitutes an intensity grating. Changing the value of the polarization angle φ allows to tune the amplitude of the polarization versus the intensity gratings. $\varphi = 0°$ corresponds to a pure intensity grating while $\varphi \simeq 45°$ corresponds to a pure polarization grating[4].

3.3.1 Experimental results

In order to define an absolute spatial reference, we compute the deformation amplitude A as:

$$A = h(x^s_{bright}) - h(x^s_{dark}) \tag{3.10}$$

where x^s_{bright} and x^s_{dark} are defined in **Figure 3.6**. So, we choose the s-polarized interference pattern as the spatial reference. We consider an average value of A, obtained by performing the measure over several periods of the SRG (typically 5 periods).
In **Figure 3.7** we report the deformation amplitude kinetics for different values of φ. As expected, s-polarized interfering beams ($\varphi = 0°$) do not induce matter migration (**Figure 3.7**(a)): we observe only the weak deformation caused by the matrix photoexpansion in the bright fringes. What is extremely remarkable is that at $\varphi = 5°$ we observe matter migration which produces a deformation of $\simeq$ 20 nm in 400 s (**Figure 3.7**(b)). The positive sign of the profile indicates an *in phase* growth of the relief with respect to the light field interference pattern, which denotes matter accumulation in the enlightened zones. We remark that in this configuration a small amount of p-polarized intensity ($0.019\ mW/mm^2$) is half-a-period spatially shifted with respect to the more intense (2.5

[4]In our experimental conditions the exact value would be $\varphi = 47.5°$, as explained in **Appendix A**.

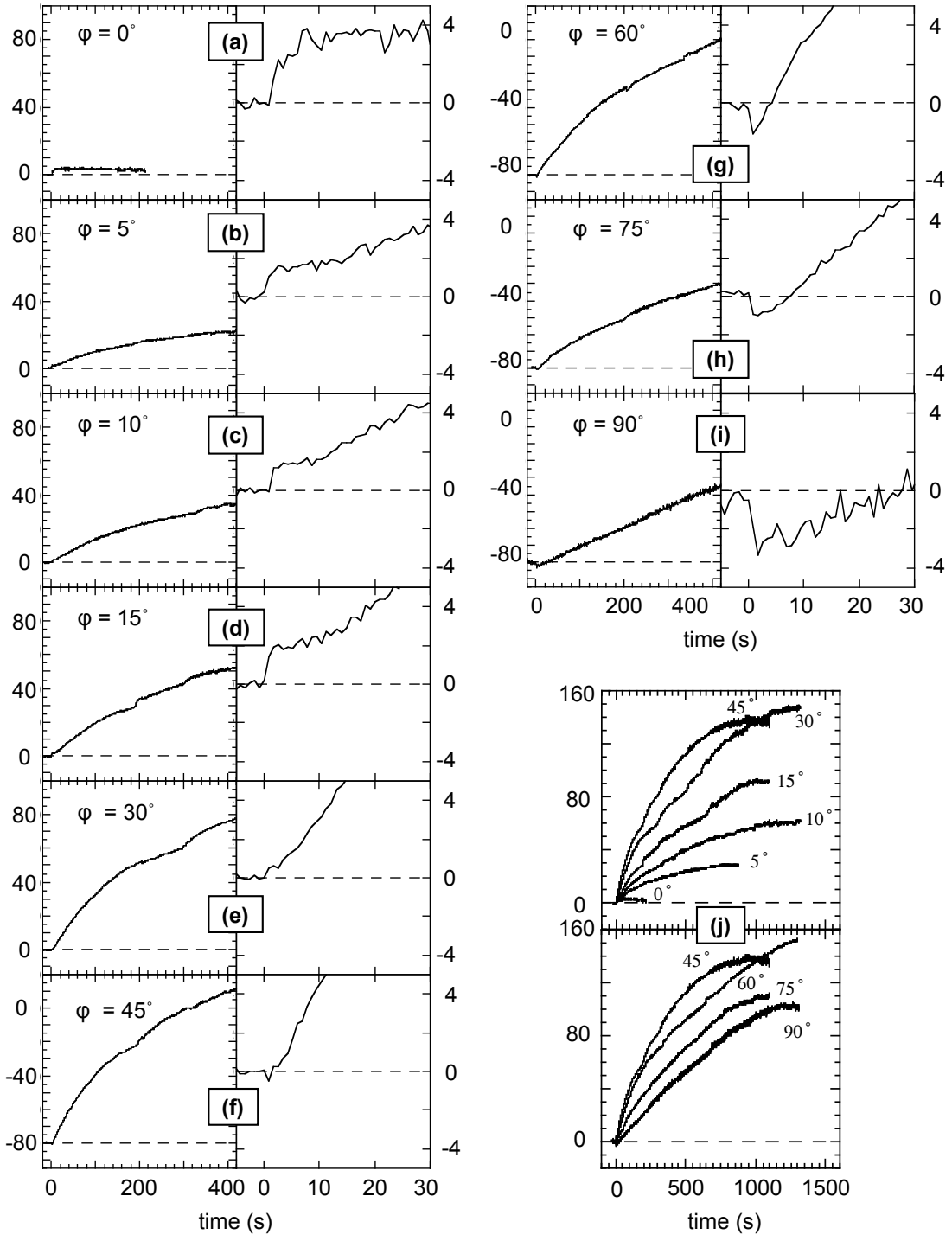

FIGURE 3.7: Dependence on the polarization axis angle φ. (a-i): for every φ we report the full deformation kinetics over 400 s, (left) and the detail of the first 30 s (right); (j): full kinetics comparison for $\varphi < 45°$ (top) and for $\varphi \geqslant 45°$ (bottom). The sign of the SRG amplitude indicates the SRG phase with respect to the s interference pattern: $> 0 \Rightarrow$ *in-phase*, $< 0 \Rightarrow \pi$*-phase*. Laser power density: 1 mW/mm^2 per beam (blue); sample = sol-gel Si-DR1 $\simeq$ 200 nm thick.

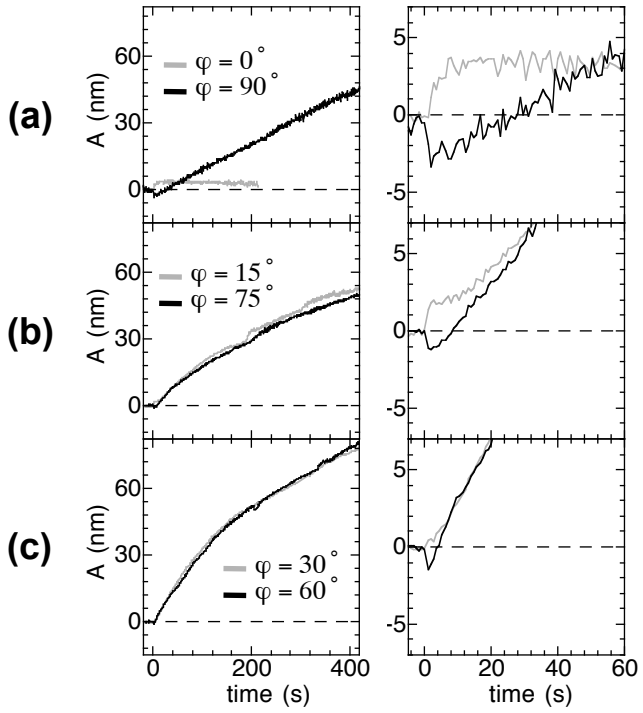

FIGURE 3.8: Mass-migration-induced SRG growth efficiency: symmetries and asymmetries. (a-c) For various values of φ we report the full deformation kinetics over 400 s, (left) and the detail of the first 60 s (right).

mW/mm^2) s-polarized interference pattern.

Raising the value of φ increases the p-polarized component and diminishes the s-polarized component. We observe an *in-phase* matter migration more and more efficient, as the two polarization components tend to have the same intensity (**Figure 3.7**(b-e)).

On the other hand, starting from the p-polarized interfering beams configuration ($\varphi = 90°$) and diminishing the polarization angle φ we also observe a growth of matter migration efficiency. In these configurations a low amplitude s-polarized intensity pattern is half-a-period spatially shifted with respect to the more intense p-polarized interference pattern. As the polarization angle φ decreases, the s-component increases while the p-component diminishes. We observe a more and more efficient matter migration, as the contribution of each intensity component reaches similar values (**Figure 3.7(i)-(g)**). In agreement with this trend, we measure a maximum for the matter migration efficiency in for $\varphi = 45°$ (**Figure 3.7(f)**), where the s and p components have the same amplitude. Plotting the deformation kinetics obtained for complementary values of the polarization angle φ reveals a remarkable symmetry (**Figure 3.8**(b-c)), as the curves of the time evolution deformation amplitude are completely superposed.

We can evaluate the matter migration efficiency by normalizing the time evolution of the SRG amplitude with respect to the kinetics observed at $\varphi = 45°$, since it is the most

φ	I_P	I_S	I_x	I_y	I_z	photoexp. *(nm)*	matter migr. rate *(nm/s)*
0	0.0	2.5	0.0	2.5	0.0	3.0	not observed
5	0.019	2.5	0.018	2.5	0.0007	1.7	0.080
10	0.076	2.4	0.073	2.4	0.0027	1.3	0.13
15	0.17	2.3	0.16	2.3	0.0060	1.7	0.18
20	0.29	2.2	0.28	2.2	0.010		
25	0.45	2.0	0.43	2.0	0.016		
30	0.63	1.9	0.61	1.9	0.023	0.50	0.39
35	0.83	1.7	0.80	1.7	0.030		
40	1.0	1.5	1.0	1.5	0.037		
45	1.3	1.2	1.2	1.2	0.045	not observed	0.50
50	1.5	1.0	1.4	1.0	0.053		
55	1.7	0.82	1.6	0.82	0.060		
60	1.9	0.62	1.8	0.62	0.068	1.5	0.35
65	2.1	0.44	2.0	0.44	0.074		
70	2.2	0.29	2.1	0.29	0.079		
75	2.3	0.17	2.3	0.17	0.084	1.0	0.19
80	2.4	0.075	2.3	0.075	0.087		
85	2.5	0.019	2.4	0.019	0.089		
90	2.5	0.0	2.4	0.0	0.090	2.0	0.12

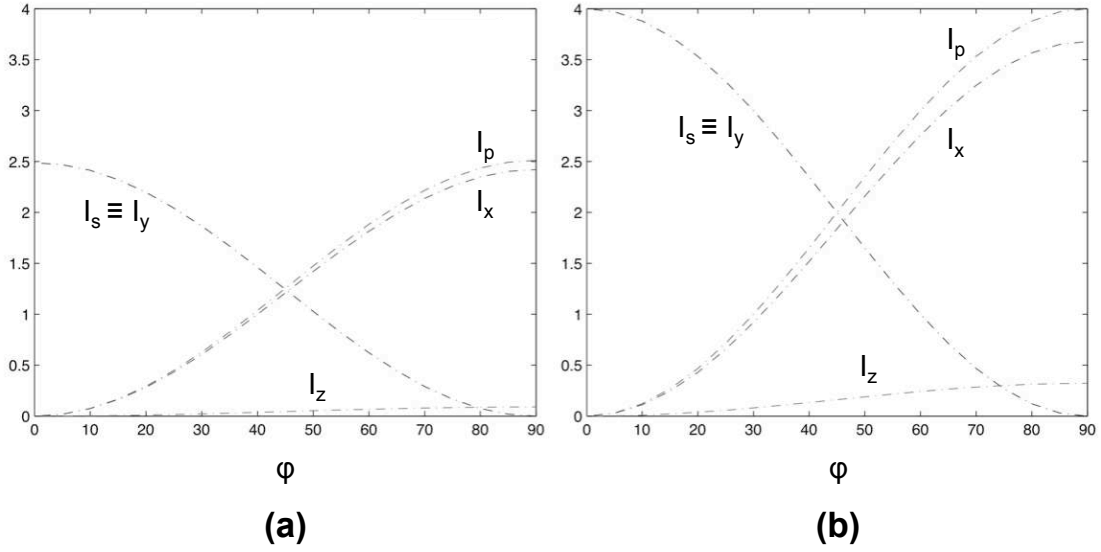

TABLE 3.1: Variation of the photodeformation versus the polarization angle φ and the field components' intensities. Matter migration rate is evaluated over the first 100 s of irradiation, since in this range the evolution is quasi-linear. The SRG growth rate induced by the photoexpansion is always $\simeq$ 1 nm/s, when it is present. The field intensities are calculated for two incident beams having an intensity of 1 mW each and considering the losses due to the substrate-air interface (relative refractive index = 1.5). We supposed a similar index for the substrate and the sol-gel film. NB. values are truncated to 2 significant digits. (a) Transmitted field component intensities in glass (n = 1.5); (b) Field component intensities in air. $I_p = I_x + I_z$, $I_s = I_y$.

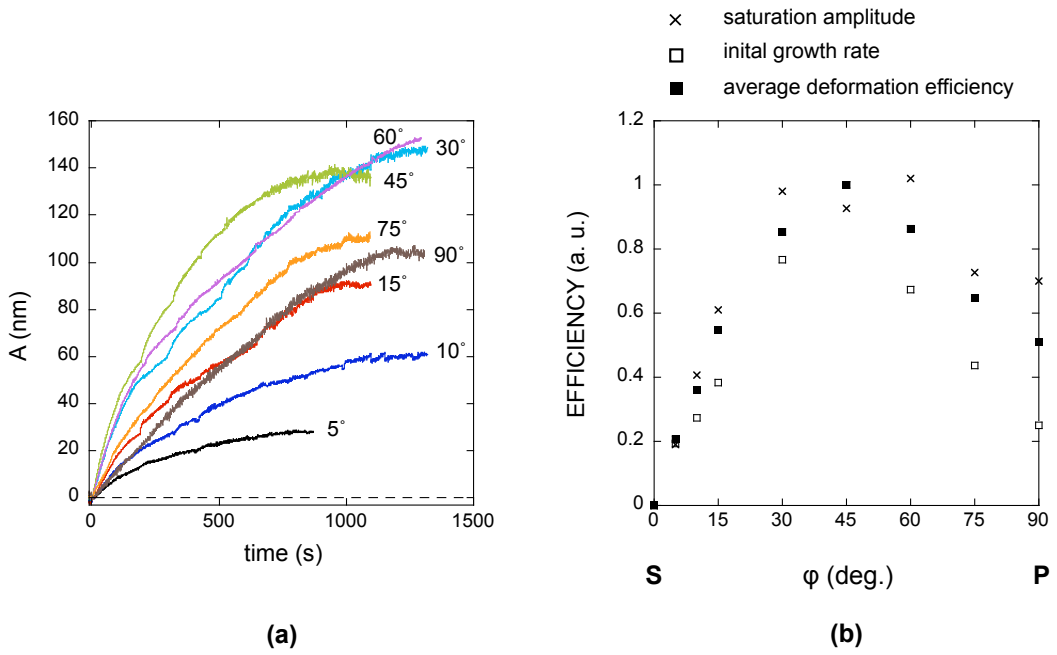

FIGURE 3.9: Mass migration SRG growth efficiency: (a) mass migration SRG growth kinetics for various polarization axis angles φ; (b) kinetic curves in (a) normalized with respect to the curve obtained at $\varphi = 45°$; (c) SRG growth: saturation amplitude (✕), computed as the maximum SRG amplitude normalized with respect to a fixed arbitrary value (150 *nm*); SRG growth rate (□) measured as the slope of the SRG growth over the first 100 *s* and normalized with respect to the growth rate observed at $\varphi = 45°$; deformation efficiency (■) computed as the time averaged values of the curves in (b) over their respective overall growth time.

efficient case, and by averaging over their respective overall growth time, in order to take into full account the growth rate and the saturation amplitude of the deformation kinetics. This is represented in **Figure 3.9** where we show (a) the kinetics (absolute value) of the SRG formation associated with matter migration for the various angles, (b) the mass migration efficiency (■) compared to the maximum deformation values (✕) normalized with respect to an arbitrary value of 150 *nm* and the SRG growth rate (□) averaged on the first 100 *s* (since in this range the evolution is quasi-linear) and normalized with respect to the growth rate at $\varphi = 45°$, for the different polarization axis angles.

We observe that the parameters describing the SRG growth are distributed quite symmetrically around the configuration at 45°, except for the case of the *s* and *p* polarizations. A more detailed analysis of the electromagnetic field distribution will show that the two polarization configurations are indeed not symmetric.

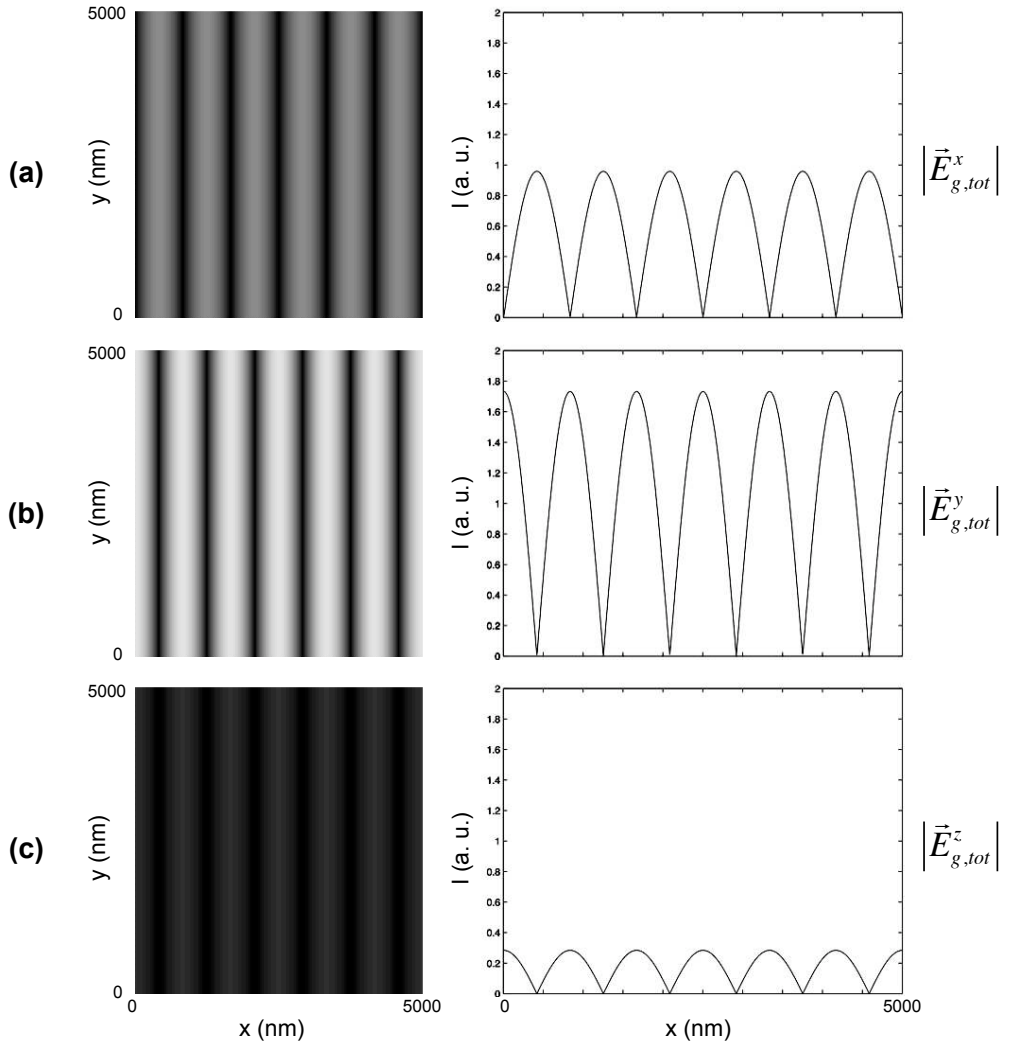

FIGURE 3.10: (a-c) left: calculated field amplitude spatial distribution (absolute values) of (a) $\vec{E}^x_{g,tot}$, (b) $\vec{E}^y_{g,tot}$, (c) $\vec{E}^z_{g,tot}$ on the xy-plane, for a polarization angle of $\varphi = 30°$; right: amplitude profile (absolute value) along the x-axis, corresponding to each field component; incidence angle = 16.5°, $\lambda = 473\ nm$, period $\simeq 830\ nm$, 1 mW/mm^2 per beam.

3.3.2 Interpretation

We consider the time averaged[5] spatial distribution of the electric field amplitudes $|\vec{E}^x_{g,tot}|, |\vec{E}^y_{g,tot}|, |\vec{E}^z_{g,tot}|$ in the xy plane ($z = 0$). In **Figure 3.10**(left) we show the calculation performed in the case of $\varphi = 30°$ from top to bottom (x-, y-, z- components of the light field, respectively), while on the right we report the corresponding amplitude profiles along the x-axis. The relative spatial shift of the x-, y- and z- component projections on the x-axis is the same for every xy-plane[6], if we neglect the contribution of the absorption in the film along the z-axis. In this sense, we remark that the light

[5] Over a period $T \simeq 10^{-15}\ s$.
[6] See **Appendix A**.

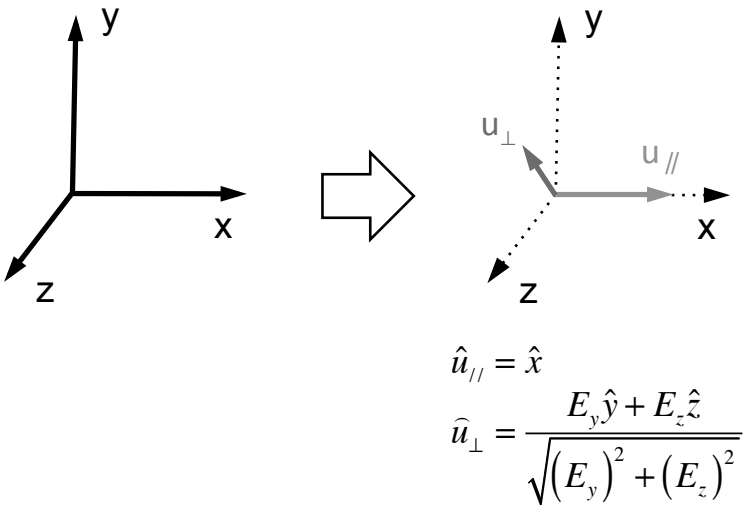

FIGURE 3.11: New coordinates.

field projection on the x-axis $\vec{E}^x_{g,tot}$ is always $\Lambda/2$ spatially shifted[7] with respect to both the y- and z- components $\vec{E}^y_{g,tot}, \vec{E}^z_{g,tot}$, which instead have the same spatial phase[8].

The spatial distribution of the polarization leads us to choose a suitable description for the interference light field. Considering the polarization angles $\varphi_1 = -\varphi_2 = \varphi$ and equal interfering beam amplitudes $E^0_{g1} = E^0_{g2} = E^0_g$ the total light field is[9]:

$$\begin{aligned}
\vec{E}_{g,tot}(\vec{r},t) &= \vec{E}^0_{g1} cos(\omega t + k n_g (x sin\theta_g + z cos\theta_g)) \\
&+ \vec{E}^0_{g2} cos(\omega t + k n_g (-x sin\theta_g + z cos\theta_g)) \\
&= E^0_g \begin{pmatrix} -sin\varphi\ cos\theta_g \\ -cos\varphi \\ sin\varphi sin\theta_g \end{pmatrix} cos(\omega t') \\
&+ E^0_g \begin{pmatrix} sin\varphi\ cos\theta_g \\ -cos\varphi \\ sin\varphi\ sin\theta_g \end{pmatrix} cos(\omega t' - 2\phi_x)
\end{aligned} \tag{3.11}$$

where we have used:

$$\omega t + n_g k z cos\theta_g = \omega t' \tag{3.12}$$

$$\phi_x = n_g k x sin\theta_g = \frac{\pi x}{\Lambda} \tag{3.13}$$

[7] Where $\Lambda \simeq 830\ nm$ is the interference pattern spatial period.
[8] As shown in eq. 2.28-2.30, see also **Appendix A**.
[9] See **Appendix A**.

As shown in **Figure 3.11**, we define a new coordinate frame: the axis along the x direction, represented by the versor $\hat{u}_{\parallel} = \hat{x}$ and the orthogonal axis $\hat{u}_{\perp} = \frac{E_y\hat{y} + E_z\hat{z}}{\sqrt{(E_y)^2 + (E_z)^2}}$ where E_y, E_z are the amplitude of the respective field projections on the y- and z-axis at an arbitrary point (x, y, z).

In this sense, for each z, we decompose the total field in two components along the new $\hat{u}_{\parallel}$ and $\hat{u}_{\perp}$ axes, respectively, and as a function of x and t only:

$$\vec{E}_{g,tot}(x,t) = \vec{E}_{\parallel}(x,t) + \vec{E}_{\perp}(x,t) \tag{3.14}$$

$$\begin{aligned} \vec{E}_{\parallel}(x,t) &= -E_g^0 sin\varphi cos\theta_g \left[cos\omega t' - cos(\omega t' - 2\phi_x)\right] \hat{u}_{\parallel} \\ &= 2E_g^0 sin\varphi cos\theta_g sin(\omega t' - \phi_x) sin(\phi_x)\hat{u}_{\parallel} \end{aligned} \tag{3.15}$$

$$\boxed{\vec{E}_{\parallel}(x,t) = E_{\parallel}^0(\varphi) sin(\omega t' - \phi_x) sin(\phi_x)\hat{u}_{\parallel}} \tag{3.16}$$

$$\begin{aligned} \vec{E}_{\perp}(x,t) &= E_g^0\sqrt{cos^2(\varphi) + sin^2(\varphi)sin^2(\theta_g)}\left[cos\omega t' + cos(\omega t' - 2\phi_x)\right] \hat{u}_{\perp} \\ &= 2E_g^0\sqrt{cos^2(\varphi) + sin^2(\varphi)sin^2(\theta_g)} cos(\omega t' - \phi_x) cos(\phi_x)\hat{u}_{\perp} \end{aligned} \tag{3.17}$$

$$\boxed{\vec{E}_{\perp}(x,t) = E_{\perp}^0(\varphi) cos(\omega t' - \phi_x) cos(\phi_x)\hat{u}_{\perp}} \tag{3.18}$$

where:

$$E_{\parallel}^0(\varphi) = 2E_g^0 sin\varphi cos\theta_g \tag{3.19}$$

$$E_{\perp}^0(\varphi) = 2E_g^0\sqrt{cos^2(\varphi) + sin^2(\varphi)sin^2(\theta_g)} \tag{3.20}$$

Equations 3.16 and 3.18 describe the temporal evolution and the spatial distribution (along the x-axis) of the $\vec{E}_{\parallel}(x,t)$ and $\vec{E}_{\perp}(x,t)$ field components. Since the two components are temporally in quadrature, for each x they give rise to an elliptical polarization described by:

$$\boxed{\left(\frac{E_{\parallel}}{E_{\parallel}^0(\varphi)sin(\phi_x)}\right)^2 + \left(\frac{E_{\perp}}{E_{\perp}^0(\varphi)cos(\phi_x)}\right)^2 = 1} \tag{3.21}$$

where the two semi-axes of the ellipse $E_{\parallel}^{0}(\varphi)sin(\phi_x)$ and $E_{\perp}^{0}(\varphi)cos(\phi_x)$ depend on the x coordinate, on the polarization angle φ and on the incidence angle θ_g (see eq. 3.19 and 3.20). Along the x-axis the elliptic polarization can degenerate to linear polarization along the $u_{\parallel}$ direction when $\phi_x = \pi/2$ (i.e. $x = \Lambda/2, (3/2)\Lambda, ...$) or the $u_{\perp}$ direction when $\phi_x = 0$ (i.e. $x = 0, 2\Lambda, ...$). Also, it gives rise to circular polarization when $|E_{\parallel}^{0}sin(\phi_x)| = |E_{\perp}^{0}cos(\phi_x)|$ (i.e. $x = \frac{\Lambda}{\pi}artg\left(\pm\frac{E_{\perp}^{0}(\varphi)}{E_{\parallel}^{0}(\varphi)} + 2n\pi\right), n = 0, 1, 2...$). This is represented in **Figure 3.12**(a), for a single spatial period $\Lambda \simeq 830\ nm$ and for a polarization angle $\varphi = 30°$. The x-coordinate corresponding to the circular polarization is indicated by white arrows (only in the first half-period, at $x = 0.35\Lambda$).
Note that the values $E_{\parallel}^{0}(\varphi)$ and $E_{\perp}^{0}(\varphi)$ are generally different, except when $tg\varphi = 1/\sqrt{cos2\theta_g}$, where their values are equal. In this particular case, writing the field intensity, for $E_{\parallel}^{0}(\varphi) = E_{\perp}^{0}(\varphi) = E^{0}(\varphi)$:

$$\begin{aligned} I_{tot}(x) = 2 < E_{tot}^{*}E_{tot} > &= \frac{2}{T}\int_{t_0}^{t_0+T}\left[E_{\parallel}^{0}(\varphi)sin(\omega t' - \phi_x)sin(\phi_x)\right]^2 dt \\ &+ \frac{2}{T}\int_{t_0}^{t_0+T}\left[E_{\perp}^{0}(\varphi)cos(\omega t' - \phi_x)cos(\phi_x)\right]^2 dt \\ &= (E_{\parallel}^{0}(\varphi))^2 sin^2(\phi_x) + (E_{\perp}^{0}(\varphi))^2 cos^2(\phi_x) \\ &= (E^{0}(\varphi))^2 \end{aligned} \tag{3.22}$$

we obtain that the field intensity is constant along the x-axis, but the polarization remains spatially modulated (eq. 3.21). In the general case, the difference between $E_{\parallel}^{0}$ and $E_{\perp}^{0}$ leads to the spatial modulation of the intensity ($I_{tot}(x) = (E_{\parallel}^{0}(\varphi))^2 sin^2(\phi_x) + (E_{\perp}^{0}(\varphi))^2 cos^2(\phi_x)$).

This suggests to decompose the total light field in a component having a constant polarization and a spatially modulated intensity ($\vec{E}_{int}$) and a component having a constant intensity and a spatially modulated polarization ($\vec{E}_{pol}$):

$$\vec{E}_{tot}(x,t) = \vec{E}_{int}(x,t) + \vec{E}_{pol}(x,t) \tag{3.23}$$

$$\vec{E}_{int}(x,t) = E_{int}sin(\omega t' - \phi_x + \psi)sin(\phi_x + \psi)\hat{v} \tag{3.24}$$

$$\begin{aligned} \vec{E}_{pol}(x,t) &= E_{pol}\left[sin(\omega t' - \phi_x)sin(\phi_x)\hat{u}_{\parallel} + cos(\omega t' - \phi_x)cos(\phi_x)\hat{u}_{\perp}\right] \\ &= E_{pol}^{\parallel}(t,x)\hat{u}_{\parallel} + E_{pol}^{\perp}(t,x)\hat{u}_{\perp} \end{aligned} \tag{3.25}$$

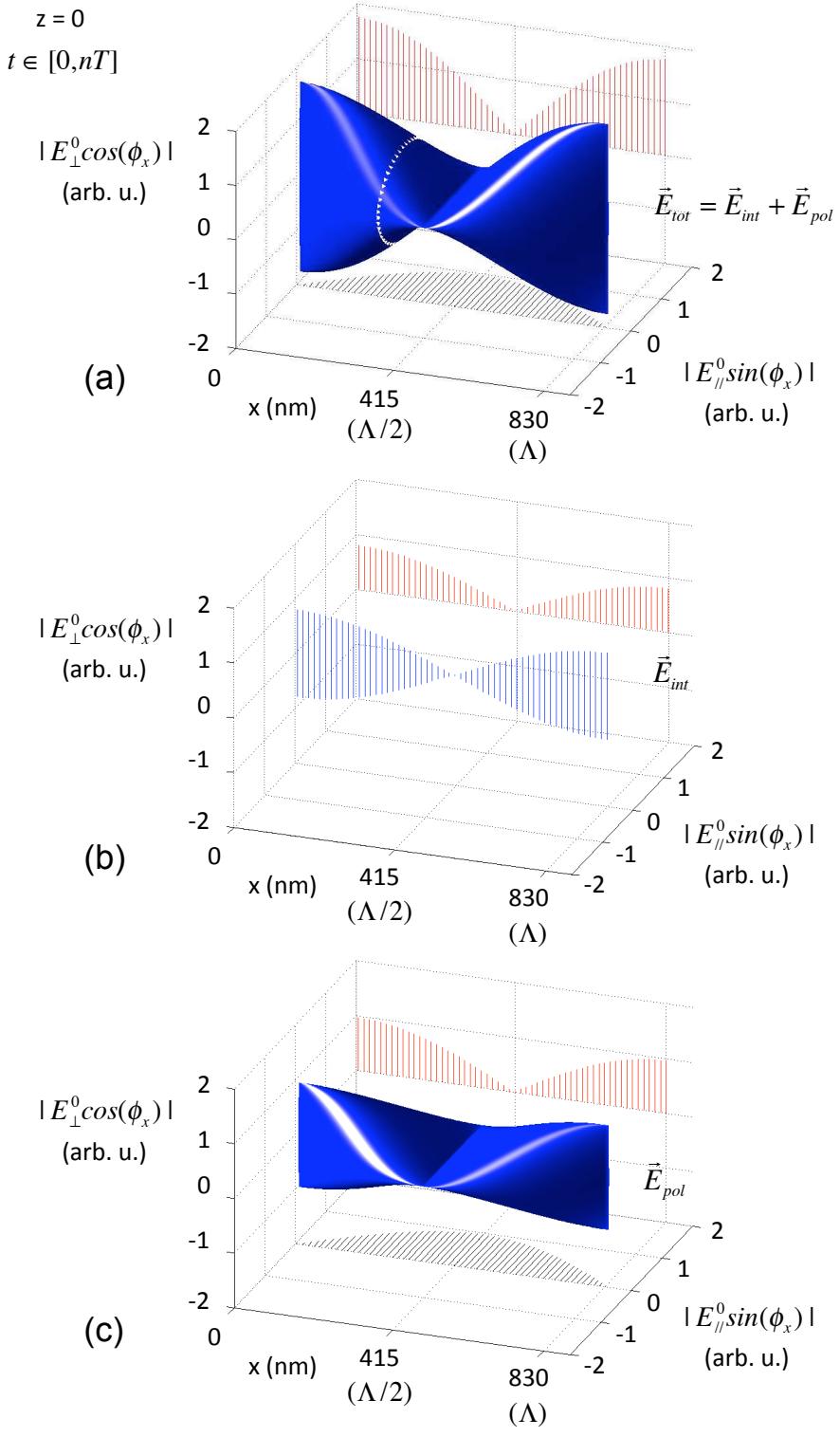

FIGURE 3.12: Decomposition of the interference field spatial distribution: calculation of the polarization and intensity spatial modulations along the x-axis performed for a polarization axis angle $\varphi = 30°$; incidence angle $\theta = 16.5°$, $\lambda = 473\ nm$, spatial period: $\Lambda \simeq 830\ nm$, $1\ mW/mm^2$ per beam, $T = 10^{-15}\ s$. (a-c): $E_{||}^{0}|sin(\phi_x)|$ (black), $E_{\perp}^{0}|cos(\phi_x)|$ (red) and resultant field (blue) during a temporal interaval multiple of T. (a) Total field, the white triangles indicate the state of circular polarization (shown only in the first spatial half-period $\Lambda/2$); (b) amplitude modulated component $\vec{E}_{int}$; (c) polarization modulated component $\vec{E}_{pol}$.

where:

$$\begin{cases} \text{if} \quad E_{\parallel}^{0} \leq E_{\perp}^{0}(\varphi) \Longleftrightarrow tg\varphi \leq 1/\sqrt{cos2\theta_g} & \text{then} \quad \psi = \pi/2,\ \hat{v} = \hat{u}_{\perp} \\ \text{if} \quad E_{\parallel}^{0} > E_{\perp}^{0}(\varphi) \Longleftrightarrow tg\varphi > 1/\sqrt{cos2\theta_g} & \text{then} \quad \psi = 0,\ \hat{v} = \hat{u}_{\parallel} \end{cases} \tag{3.26}$$

and the field amplitudes are:

$$E_{int} = |E_{\parallel}^{0}(\varphi) - E_{\perp}^{0}(\varphi)| \tag{3.27}$$

$$\begin{aligned} E_{pol} &= \min\{E_{\parallel}^{0}(\varphi), E_{\perp}^{0}(\varphi)\} \\ &= \frac{E_{\parallel}^{0}(\varphi) + E_{\perp}^{0}(\varphi) - |E_{\parallel}^{0}(\varphi) - E_{\perp}^{0}(\varphi)|}{2} \\ &= \frac{1}{2}\left(E_{\parallel}^{0}(\varphi) + E_{\perp}^{0}(\varphi)\right)\left[1 - \frac{|E_{\parallel}^{0}(\varphi) - E_{\perp}^{0}(\varphi)|}{\left(E_{\parallel}^{0}(\varphi) + E_{\perp}^{0}(\varphi)\right)}\right] \end{aligned} \tag{3.28}$$

We note that in our geometry the condition stated in 3.26 reads: $0° \leq \varphi \leq 47.5°$ and $47.5 < \varphi \leq 90°$ respectively.

This decomposition is shown in **Figure 3.12**(b-c) where, respectively, $\vec{E}_{int}$ and $\vec{E}_{pol}$ are depicted. The first component is linearly polarized along the $\hat{v}$ direction and its intensity is spatially modulated. The second component has a spatially modulated polarization, while its intensity is constant. In this case, the polarization ellipse is:

$$\boxed{\left(\frac{E_{pol}^{\parallel}}{E_{pol} sin(\phi_x)}\right)^2 + \left(\frac{E_{pol}^{\perp}}{E_{pol} cos(\phi_x)}\right)^2 = 1} \tag{3.29}$$

where $E_{pol}^{\parallel}$ and $E_{pol}^{\perp}$ are defined in eq. 3.25.

In **Figure 3.13** we report the calculated[10] values of E_{int} and E_{pol} (eq. 3.27, 3.28) as a function of φ, together with the normalized saturation amplitude (✕), the normalized growth rate (□) and the average normalized efficiency (■), previously estimated (see **Figure 3.9**). The good agreement between experimental values and E_{pol} shows a direct correlation between the polarization spatial modulation and the matter migration processes. When the light field is *s*-polarized, $E_{pol} = 0$ and the interference field is a pure intensity grating, which does not give rise to matter migration. Increasing the spatial modulation of the polarization leads to a more efficient matter migration, which reaches

[10] Unitary interfering beams: $E^0 = 1$.

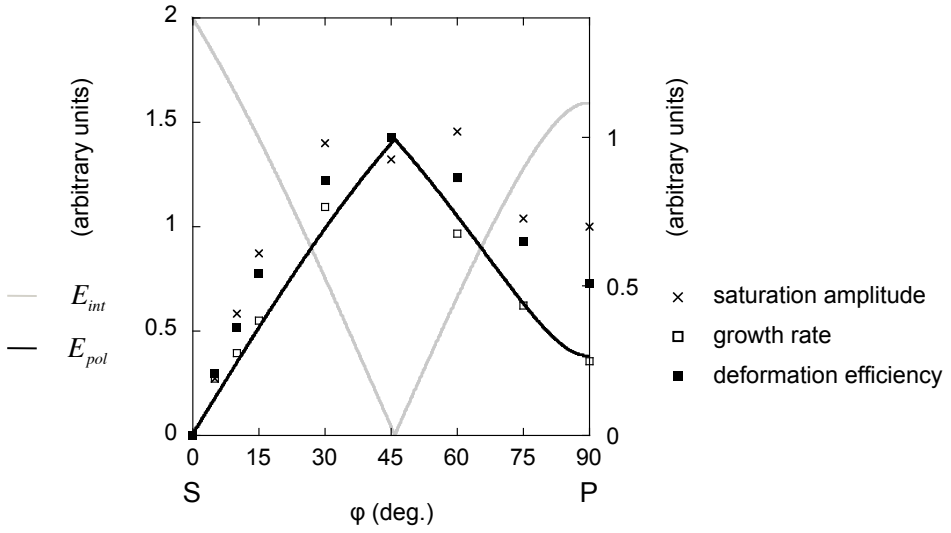

FIGURE 3.13: Correlation between matter migration SRG growth and the calculated intensity and polarization spatial modulations E_{int} and E_{pol} (eq. 3.27, 3.28), as a function of the polarization axis φ. Calculated values are not scaled and expressed in arbitrary units. SRG growth is described by several parameters calculated in **Figure 3.9**: saturation amplitude (×), computed as the maximum SRG amplitude normalized with respect to a fixed arbitrary value (150 nm); SRG growth rate (□) measured as the slope of the SRG growth over the first 100 s and normalized with respect to the growth rate observed at $\varphi = 45°$; average normalized deformation efficiency (■).

its maximum at $\varphi = 45°$, extremely close to the maximum of E_{pol} at $\varphi = 47.5°$, where the interference field is a pure polarization grating.

This observation explains the asymmetry between the matter migration observed under s-polarized and p-polarized interference patterns, with respect to the symmetric behavior observed for 30°-60°and 15°-75°configurations. Even if complementary, s and p are not symmetric from the point of view of E_{pol}, since $E_{pol} = 0$ in the first case while $E_{pol} = 0.37$ in the second one. In this sense, a polarization configuration symmetric to s should have a $E_{pol} = 0$ as well. This could be obtained, for example, with a light field having only an $\vec{E}_{\parallel}$ component and no $\vec{E}_{\perp}$ component. Unfortunately this configuration would require p-polarized interfering beams in normal incidence ($\theta = 0°$), hence inducing an infinite spatial period interference pattern.

3.3.3 Discussion

The experiments performed with the superimposition of a polarization and an intensity gratings of variable amplitude show that the SRG formation is mainly governed by the spatial modulation of the polarization. This is clearly seen when comparing the variation of the polarization spatial modulation with the SRG formation efficiency as a function of φ (**Figure 3.13**).

Our results address a fundamental problem in the comprehension of the mechanism at the origin of the photodeformation phenomena observed in azo-containing materials. It is well established [1] that these phenomena depend on the photoisomerization of the azobenzene units. The rate of the isomerization events is dependent on the intensity of the light field, which has been so far considered as prevalently governing the photodeformation. Indeed, we observe the maximum of the SRG growth efficiency when the light field intensity is constant and the spatial modulation of the polarization is maximum. On the other hand, when the light polarization is not spatially modulated the SRG growth efficiency drops to its minimum, even if the light intensity is spatially modulated. This indicates a preponderant effect of the light field rather than of the light intensity. Our findings explain the highest SRG inscription efficiency observed so far in the experiments performed using a polarization interference pattern ($\pm 45°$ or circularly left and right) [3, 12–14]. Note that a polarization interference pattern is obtained by orthogonally polarized interfering beams. When using s- and a p-polarized interfering beams, a polarization pattern of constant intensity is also obtained, but the deformation efficiency vanishes [15]. This is due to the fact combining s- and a p-polarized beams leads to a spatial modulation of the polarization between $\vec{E}_{\perp}$ and the $\vec{E}_{\parallel}$ components equal to zero: $E_{pol} = 0$, according to eq. 3.28.

Let us remark that, since mass transport is governed by the polarization spatial distribution, it is not straightforward to relate the rate of photoisomerization events with the matter migration efficiency. Another interesting remark is that the deformation amplitude sign is always positive (see **Figure 3.7**). By definition (see **Figure 3.6**) this means that the SRG growth is always in phase with the s-polarized interference pattern. In our experiments the light field is constituted by the superposition of an s-polarized and a p-polarized interference patterns. In particular, as shown in **Figure 3.10**, the s-polarized field component (i.e. polarized along the y-axis) is superimposed to the z-polarized field component, while the x-polarized field component is $\Lambda/2$ spatially shifted[11]. So, matter is driven towards the superimposed y and z components (the $E_{\perp}$ field component), while it is driven away from the x-polarized component (the $E_{\parallel}$ field component).
In order to verify the influence of the light polarization on the directionality of the matter migration we should project a fixed intensity profile and change the polarization of the light. This can be obtained by supporting to the two interfering beams with an *assisting beam*, which is the object of the next section.

[11] Where $\Lambda \simeq 830\ nm$ is the interference pattern spatial period.

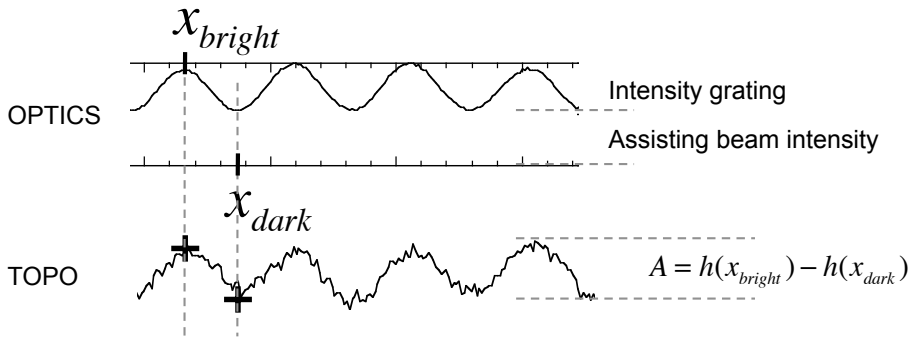

FIGURE 3.14: Deformation amplitude convention.

3.4 Photoinduced SRG formation with an assisting beam

We investigate different polarization configurations, where an incoherent beam is superimposed to two interfering beams. In this way, we keep fixed the light intensity pattern and we vary only the spatial distribution of the light polarization. In order to study the directionality of the matter transport we use the intensity pattern spatial distribution as absolute spatial reference, by using the following convention for the deformation amplitude A:

$$A = h(x_{bright}) - h(x_{dark}) \tag{3.30}$$

where x_{bright} and x_{dark} are defined in **Figure 3.14**. So, $A > 0$ indicates matter migration towards the brighter fringes, while $A < 0$ indicates matter transport towards the darker fringes.

3.4.1 *p*-assisted *s*-interfering beams

SS+P

We use a green[12] ($\lambda = 532\ nm$) laser beam in normal incidence on the sample to assist two blue ($\lambda = 473\ nm$) interfering beams. **Figure 3.15**(a) shows the setup in the case of a p-assisted s-polarized interfering beams. In (b) are reported the time evolution of the optical input transmitted intensity I (top) and the corresponding grating formation dynamics (bottom - solid curve); the dotted curve indicates the deformation obtained without the assisting beam, on the same sample in the same conditions. The complete optical and the topography images are shown in (c) and (d).

At $t = 0$ the s-interfering beams are turned on, keeping the assisting beam off. This produces the rapid ($0.4\ nm/s$), modest deformation amplitude ($\simeq 3\ nm$) characteristic of the matrix photoexpansion in the zones corresponding to the bright fringes, i. e. the deformation is *in phase* with the interference pattern. Turning on the single green beam

[12] Laser 2000 ™, maximum nominal power density = 21 mW/mm^2

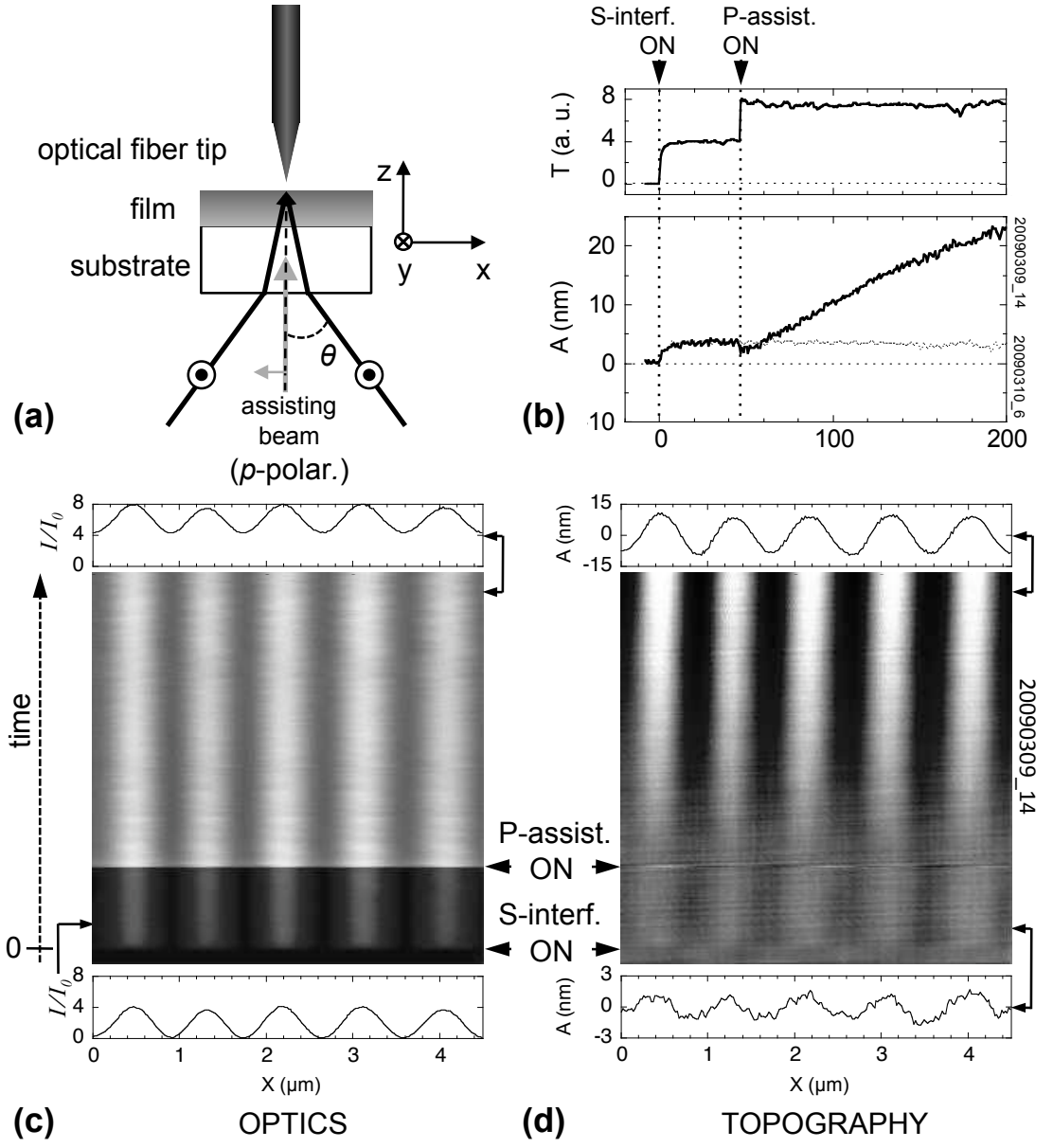

FIGURE 3.15: Photoinduced matter migration using p-assisted s-polarized interfering beams. (a) Experimental setup; (b) transmitted light intensity T in arbitrary units (top) and the corresponding photoinduced deformation amplitude A expressed in nm (solid curve), the dotted curve indicates the deformation obtained in the same conditions without the assisting beam; (c-d) optical and topography images, scanning over the same line, scan-range = 5 μm (we show only 4.5 μm). Laser power density: 1 mW/mm^2 per beam (blue), 2.1 mW/mm^2 per beam (green); sample = sol-gel Si-DR1, $\simeq$ 200 nm thick.

leads to a rapid small decrease in the grating amplitude. As exemplified in **Figure 3.16**, this is probably due to the matrix photoexpansion in the zones that were not previously irradiated (i.e. the zones corresponding to the dark fringes) which now are exposed to the assisting beam. Instead, the zones exposed to the bright fringes experiment a weaker photoexpansion, as they have already been exposed to light and, for what we have shown in the previous section, the pre-irradiation dose is sufficient to considerably reduce the photoresponse. Then, the net gratings amplitude due to the photoexpansion is smaller, as experimentally observed.

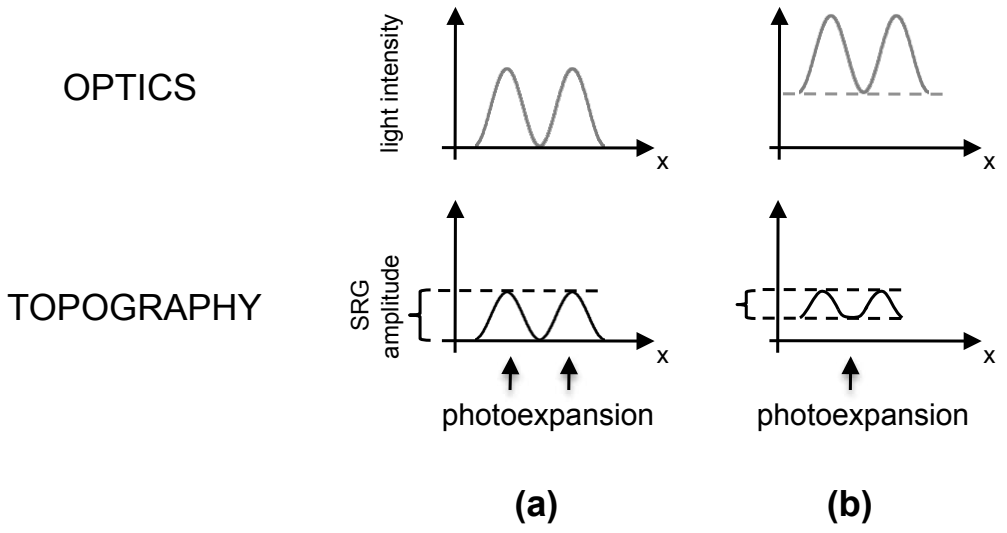

FIGURE 3.16: Photoexpansion using an assisting beam.(a) Light present in the bright fringes of the interference pattern induces the photoexpansion of the matrix, hence the formation of the gratings. (b) When an assisting beam is superposed the previously non irradiated zones undergo photexpansion as well, leading to a diminution in the grating amplitude.

Subsequently to the grating amplitude decrease, a relief growth is observed *in phase* with the grating pattern previously induced by the photoexpansion, which means that the growth is also *in phase* with the bright fringes of the interference pattern. The large amplitude and slow rate (0.2 nm/s) of this deformation process with respect to photoexpansion are characteristic of the matter migration phenomena [9]. It is extremely remarkable that in this case matter migrates towards the enlightened zones. A similar effect has been reported, to our knowledge, only once [8], but with no direct correlated measurements of the optical pattern and of the surface relief.

This photo-induced mass transport regime arises in the opposite direction with respect to the matter migration commonly observed using p-polarized light, where matter is transported away from the brightest areas towards the dark ones. It indicates that the difference between the molecular activity (i. e. photoisomerzation) induced in the brighter and the darker zones cannot be the only one cause at the origin of the matter

migration processes. However, it is fully compatible with our previous observations described in Section 3.3 and indicates that photo-induced mass transport arises from the areas which coincide with $\vec{E}_{\parallel}$ components of the electric field towards the areas which coincide to the $\vec{E}_{\perp}$ components of the light electric field. We will discuss this point in more detail in 3.4.5.

3.4.2 *s*-assisted *p*-interfering beams

PP+S

In **Figure 3.17** we report the photodeformation results obtained with the same setup presented in the previous section, but using an *s*-polarized beam to assist *p*-polarized interfering beams. At $t = 0$ we expose the sample to *p*-polarized interfering beams, keeping the *s*-polarized assisting beam off. We first observe the rapid matrix photoexpansion *in phase* with the interference pattern, producing a deformation of approximately 4 nm. This is followed by the rapid depletion of the enlightened areas caused by the matter migration towards the darker fringes. We represent this $\pi - phase$ change in the topography by a negative growth of the deformation amplitude time evolution, **Figure 3.17**(b) (bottom).

After $\simeq 80\,s$, when the SRG profile is clearly in $\pi - phase$ with respect to the light intensity profile, we turn on the *s*-polarized assisting beam: almost instantly, a deformation enhancement is observed in phase with the previous deformation. So, matter continues to migrate in the same direction, but more efficiently, the growth rate varying from 0.13 nm/s to 0.15 nm/s. It must be noted that a certain contribution to the deformation enhancement observed as the assisting beam is switched on has to be imputed to matrix photoexpansion (**Figure 3.18**). Indeed, the matrix photoexpansion takes place only in the enlightened zones, prior to matter migration towards the darker zones. When the assisting beam is on, the photoexpansion mechanism is activated predominantly in the darker zones where matter accumulates, contributing to the grating amplitude enhancement. This is the inverse phenomenon with respect to the one described in 3.4.1 where the SRG amplitude decreases subsequently to the assisting beam activation.

Qualitatively, it seems that in the case of *s*-assisted *p*-polarized interference, a weaker deformation enhancement is obtained with respect to the case of *p*-assisted *s*-polarized interference (**Figure 3.27**). We must point out however, that the latter experiments have been performed turning on the three beams simultaneously, while in the former the assisting beam has been turned on after $\simeq 80\,s$.

Delaying the assisting beam with respect to the interfering beams could have an effect on the deformation enhancement. So we have repeated both experiments turning on the assisting and the interfering beams simultaneously. It would provide us, also, a full

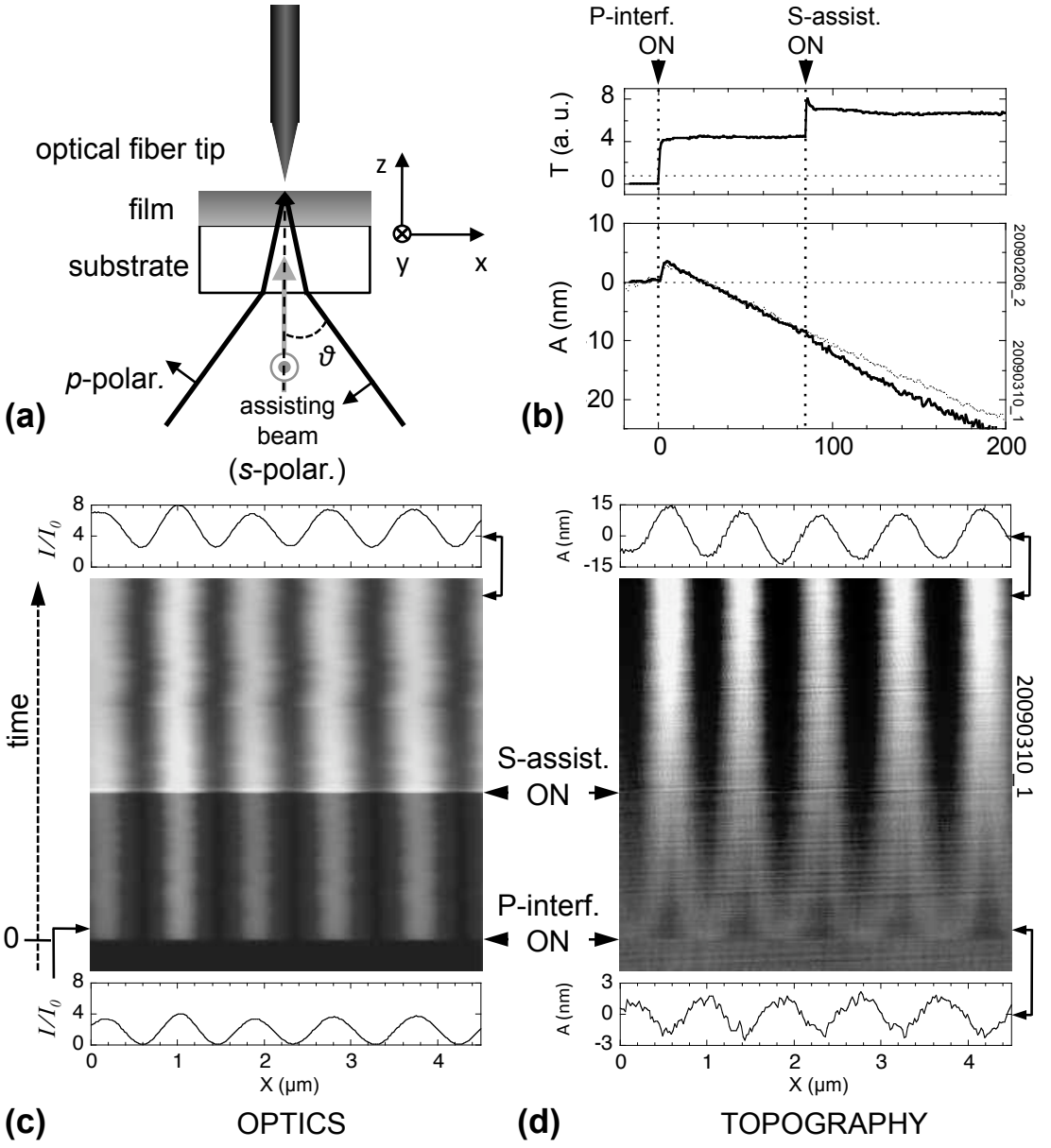

FIGURE 3.17: Photoinduced matter migration using *s*-assisted *p*-polarized interfering beams. (a) Experimental setup; (b) transmitted light intensity T in arbitrary units (top) and the corresponding photoinduced deformation amplitude A expressed in nm (solid curve), the dotted curve indicates the deformation obtained in the same conditions without the assisting beam; (c-d) optical and topography images, scanning over the same line, scan-range = 5 μm (we show only 4.5 μm). Laser power density: 1 mW/mm^2 per beam (blue), 2.1 mW/mm^2 per beam (green); sample = sol-gel Si-DR1, $\simeq$ 200 nm thick.

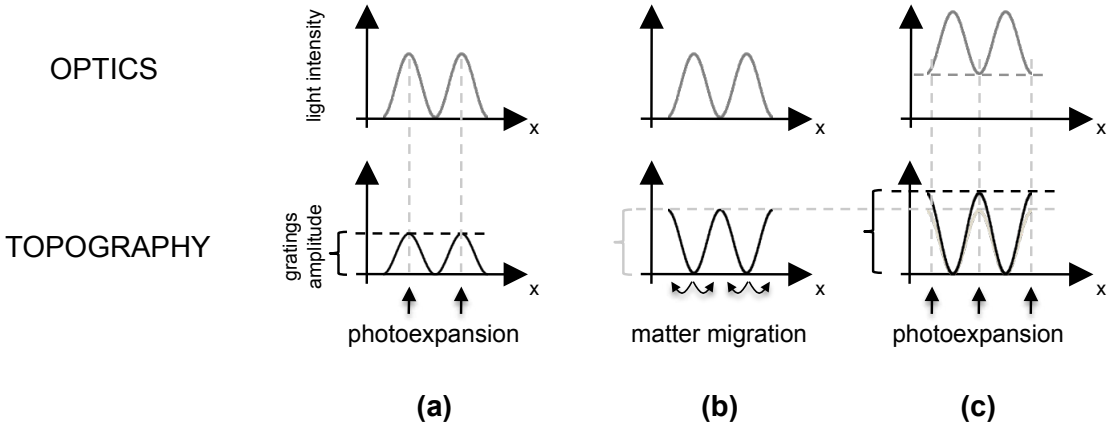

FIGURE 3.18: Photoexpansion using an assisting beam: *s*-assisted *p* interference. (a) Light located in the bright fringes of the interference pattern induces the photoexpansion of the matrix, hence the formation of SRG. (b) Matter migrates towards the dark zones. (c) When an assisting beam is superimposed to the interfering beams the previously non irradiated zones undergo photexpansion as well, leading to an increase in the SRG amplitude.

comparison of the two polarization configurations in the same conditions. We report the deformation kinetics in **Figure 3.19**[13].

PP+S, SS+P no delay

In the case of *p*-assisted *s*-polarized interference (**Figure 3.19**(a-c)), at $t = 0$ when the 3 beams are turned on we observe a weak matrix photoexpansion ($\simeq 1\,nm$), due to the weak light intensity contrast, followed by the same matter migration behavior as previously described: an efficient relief growth , with a SRG growth rate of $\simeq 0.2\,nm/s$. For the *s*-assisted *p* interference configuration (**Figure 3.19**(d-f)), once the light excitation on, a similar weak matrix photoexpansion ($\simeq 1\ nm$) is observed in the enlightened zones. Then, matter starts migrating away from the bright areas, towards the dark zones. In this case, the migration rate is $\simeq 0.23\,nm/s$ which is almost the double with respect to the non assisted case (dotted curve).

Figure 3.20 compares the growth kinetics obtained over a long exposure time for both polarization configurations. It is remarkable that, in the case of *s*-assisted *p*-interfering beams, the acceleration of the grating formation observed is effective mainly in the first 300 *s*. At long time, the growth reaches approximately the same efficiency as in the non assisted case.

[13]The contrast of the optical image for the *p*-assisted *s*-polarized interference configuration is rather poor, which is probably due to an anisotropy of the tip.

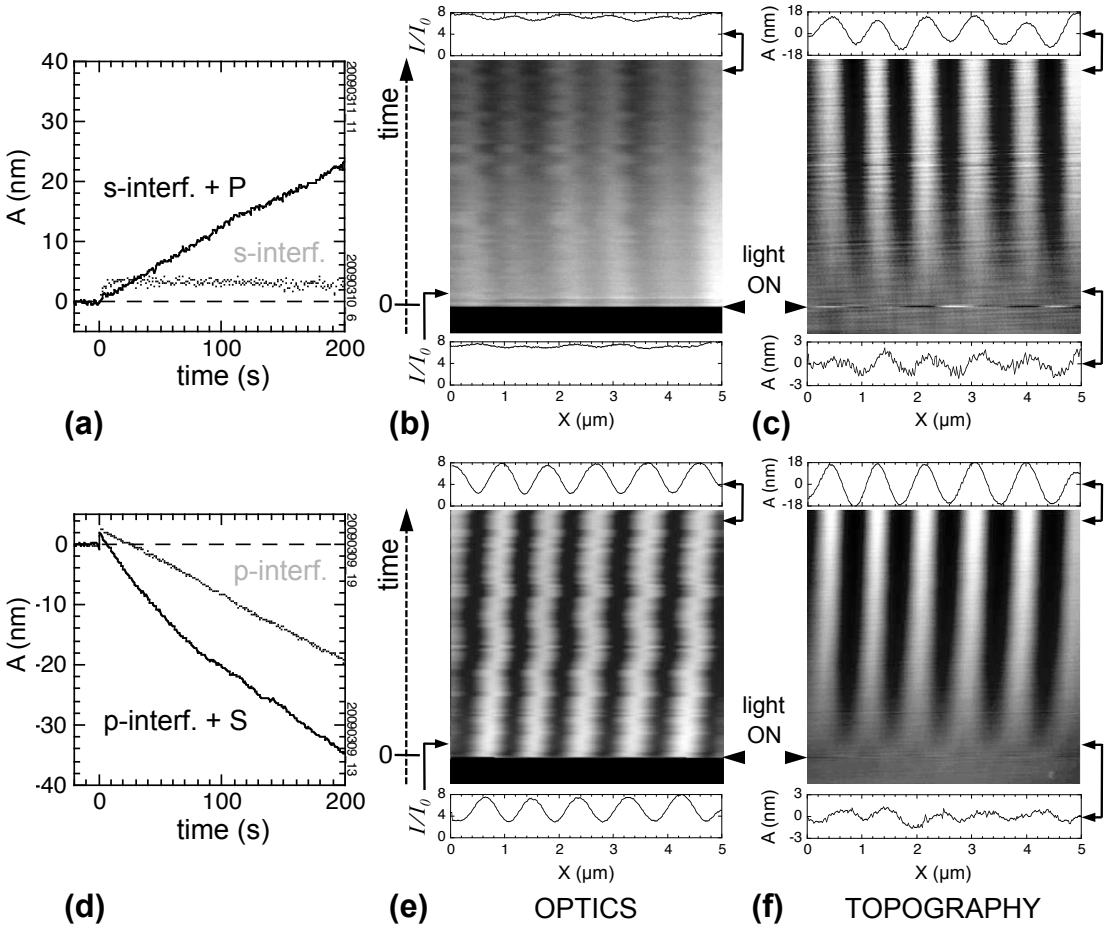

FIGURE 3.19: Enhanced matter migration using simultaneous orthogonally polarized assisted and interfering beams. (a-c) *s*-assisted *p*-interfering beams. (a) solid curve: time evolution of the deformation amplitude, dotted curve: deformation amplitude without the assisting beam; (b-c) optical and topography images, scanning over the same line, scan-range = 5 μm; (d-f) *p*-assisted *s*-interfering beams. (d) solid curve: time evolution of the deformation amplitude, dotted curve: deformation amplitude without the assisting beam; (e-f) optical and topography images, scanning over the same line, scan-range = 5 μm; Laser power density: 1 mW/mm^2 per beam (blue), 2.1 mW/mm^2 per beam (green); sample = sol-gel Si-DR1, $\simeq$ 200 nm thick.

In conclusion, the association of an assisting beam with two interfering beams of orthogonal polarization bolsters up the SRG formation. It evidences two matter migration directions, which are governed by the polarization configuration. Delaying the assisting beam with respect to the interfering beams reduces the bolster effect in the case of *s*-assisted *p* interference, while it has no influence in the case of *p*-assisted *s* interference.

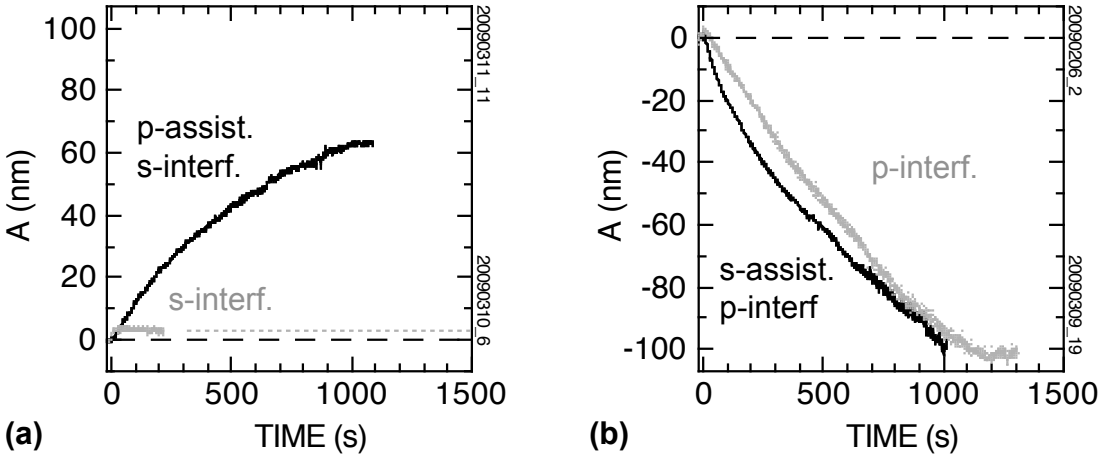

FIGURE 3.20: Enhanced matter migration using simultaneous orthogonally polarized assisted and interfering beams. (a) *s*-assisted *p*-interfering beams; b) *p*-assisted *s*-interfering beams: time evolution of the deformation amplitude (solid curve), the dotted curve represents the deformation amplitude without the assisting beam. Laser power density: 1 mW/mm^2 per beam (blue), 2.1 mW/mm^2 per beam (green); sample = sol-gel Si-DR1 $\simeq$ 200 nm thick.

3.4.3 Identically polarized beams

The increased efficiency of the SRG formation process is obtained when the assisting beam polarization is perpendicular to the interference pattern polarization. This is a necessary condition, since using the same polarization for the assisting beam and the interference pattern has a detrimental effect. In **Figure 3.21** we report the case of *PP+P* *p*-assisted *p*-polarized interference. In (a-c) we activate the interfering beams at $t = 0$ keeping the assiting beam off. As expected, we observe the matrix photoexpansion in the bright fringes. Then matter begins to migrate towards the darker zones. As matter migration starts, the assisting beam is switched on (t = 20 s)[14]. We observe a sudden jump in the deformation amplitude produced by the photoexpansion in the dark fringes of the interference pattern, as we did in the case of *s*-assisted *p*-polarized interference (**Figure 3.18**). Subsequently to the effect of the photoexpansion, the deformation kinetics retrieves a rate characteristic of the photoinduced matter migration. But it is slightly lower than the non assisted case, since the contrast between the dark and the bright fringes is lowered by the assisting beam.

We repeat this experiment by activating the assisting and the interfering beams simultaneously (d-f). As the beams are turned on we observe a weaker matrix photoexpansion, which is expected since the contrast is weaker when the assisting beam is kept off at

[14]In this case we decided to turn the assisting beam on earlier with respect to the previos experiments, since we have seen that the greatest effects of the assisting beam are measured during the first 300 s of matter migration.

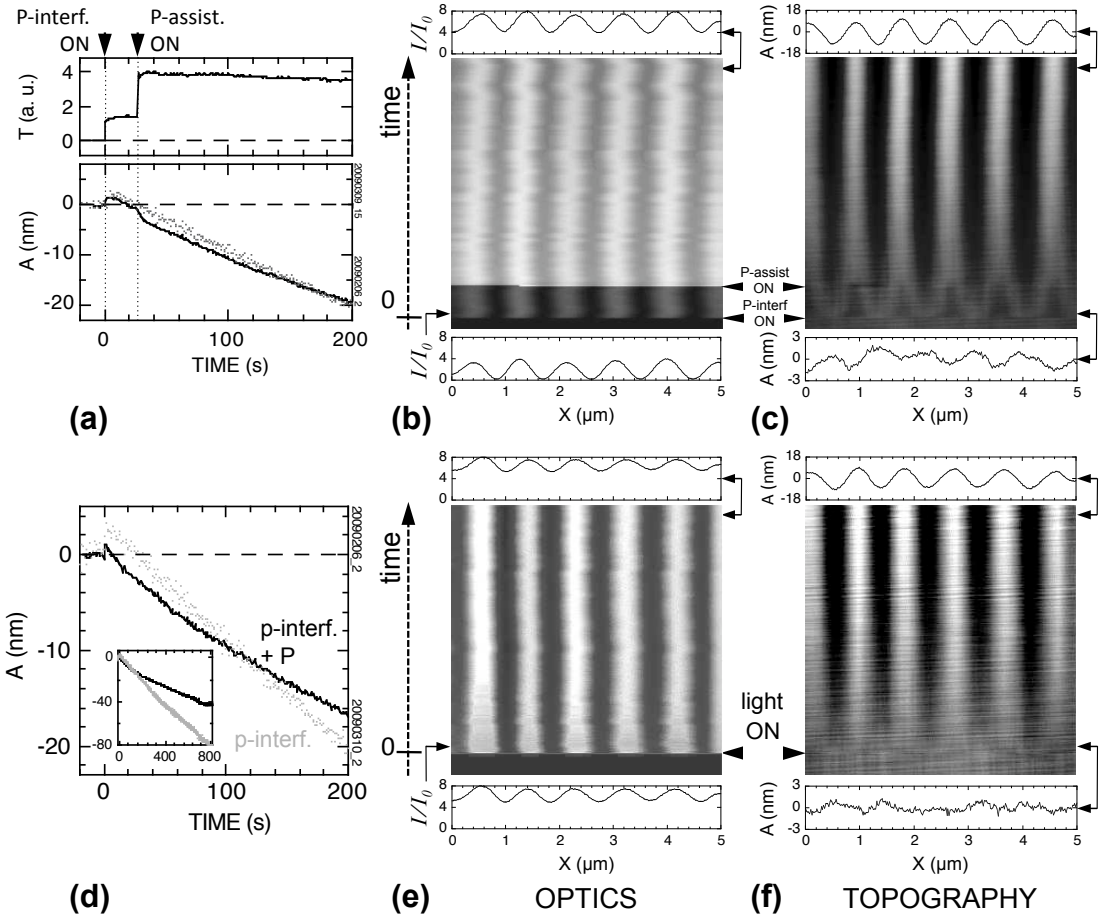

FIGURE 3.21: Photoinduced SRG formation with a p interference pattern assisted with a p-polarized incoherent beam. Laser power density = 1 mW/mm^2 per beam (blue), 2.1 mW/mm^2 per beam (green); sample = sol-gel Si-DR1 $\simeq$ 200 nm thick. (a-c) delayed assisting beam: (a) light profile (top) and the corresponding deformation amplitude (bottom, solid curve), the dotted curve indicates the deformation without the assisting beam; (b) and (c) optical and topographical images recorded in the time range of curve (a), scanning over one line, scan range = 5 μm; (d-f) same as (a-c) but with simultaneous interfering and assisting beams: the inset in (d) represents the time evolution over 800 s.

$t = 0$. Subsequently, we clearly see that matter migration is less efficient then in the non assisted case.

Finally, in **Figure 3.22** we report the photodeformation effects obtained under s-polarized assisting and interfering beams, which are simultaneously activated at $t = 0$. *SS+S* As in the other cases, matrix photoexpansion is measured right after the exposure, with the formation of weak amplitude gratings. Then the deformation amplitude drops to zero, producing almost a surface flattening after about 30 s, in agreement with previous results [16]. Therefore, no matter migration is observed.

The results so far obtained are summarized in **Table 3.2**. In particular, we notice that

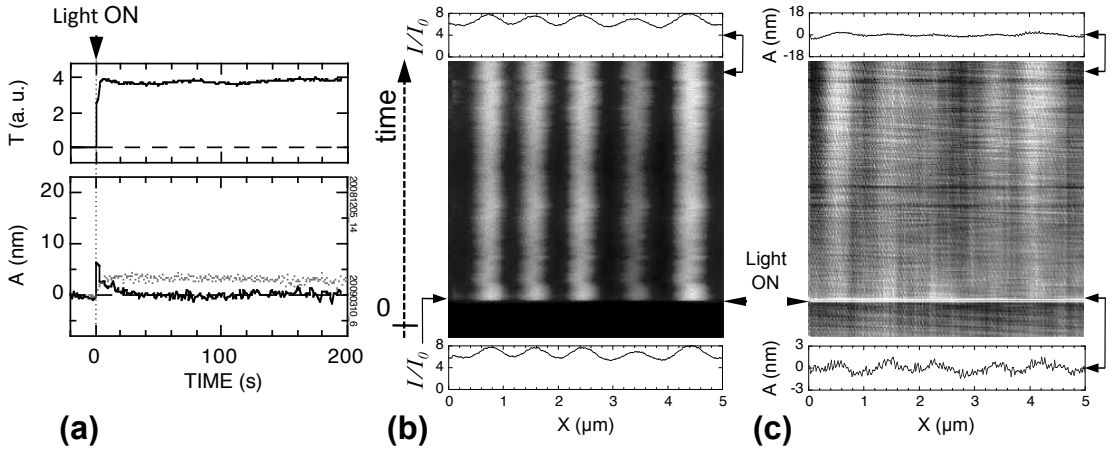

FIGURE 3.22: *s*-assisted *s* interference. (a-c) simultaneous interfering and assisting beams: (a) light profile (top) and the correspondent deformation amplitude (bottom, solid curve), dotted curve indicates the deformation without the assisting beam; (b) and (c) optical abnd topography images relative to (a) scanning over one line, scan range = 5 μm; laser = 1 mW/mm^2 per beam (blue), 2.1 mW/mm^2 per beam (green); sample = sol-gel Si-DR1 $\simeq$ 200 nm thick.

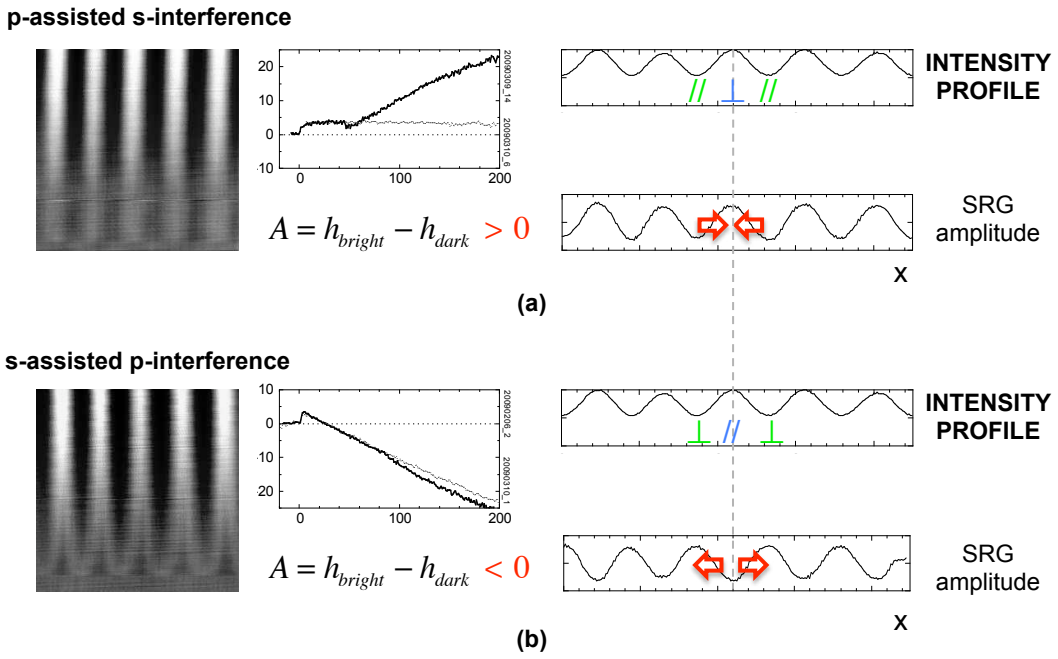

FIGURE 3.23: Directional matter migration: (a) *p*-assisted *s* interference; (b) *s*-assisted *p* interference.

Assist. pol.	Interf. pol.	Photoexpansion		Matter migration		Matter migr. enhancement
		in phase	$\pi - phase$	*in phase*	$\pi - phase$	
S	S	✔	×	×	×	×
P	**P**	✔	×	×	✔	×
P	**S**	✔	×	✔	×	✔
S	P	✔	×	×	✔	✔

TABLE 3.2: Polarization dependence of the assisted photoinduced deformation phenomena.

the photoresponses for the two orthogonal configurations p-assisted s interference and s-assisted p interference have opposite spatial phases. This can be clearly seen in **Figure 3.23** where we show that, for an identical intensity profile, matter is driven (a) towards or (b) away from the bright fringes. It is remarkable that in both cases matter accumulates in the zones illuminated with a $E_\perp$ field component, while it is driven away from the zones illuminated with a $E_\parallel$ field component[15].

By spatially modulating in real-time the interference pattern polarization and keeping constant its intensity profile, we expect to obtain an oscillating surface deformation, that is, a reversible, alternating, directional mass migration.

3.4.4 Directional reversible matter transport driven by the polarization of the light

We use the experimental setup described in **Figure 3.24**. A half-wave plate calibrated at our working wavelength (blue, $\lambda = 473\ nm$) is mounted on a motorized rotation, which is used to switch the polarization of the interfering beams between the s and the p states. Another halfwave plate is used to correct the phase, after the beam-splitter, of the reflected beam with respect to the transmitted beam. In fact, we measure an optical phase shift switching from p- to s-polarized interfering beams, which is probably due to a different path length of the reflected and the transmitted beams at the interface of the beam-splitter. In this way, when changing the polarization, the spatial distribution of the dark and bright zones will remain constant, for s and p polarization configurations. A p-polarized beam in normal incidence is used to assist the interfering beams[16].

In **Figure 3.25** we report the photodeformation obtained on a sol-gel sample, 200 nm thick. At $t = 0$ the exposure to s-polarized interfering beams induces the photoexpansion

[15] For the definition of $E_\perp$ and $E_\parallel$ see section 3.3.2.

[16] The most efficient configuration for this experiment would be to switch between p-assisted s interference and s-assisted p interference. Due to the lack of a second motorized rotation to change the polarization of the assisting beam, we used a fixed p-polarized assisting beam, which only slightly reduces the matter migration efficiency in the short time range (see **Figure 3.21**).

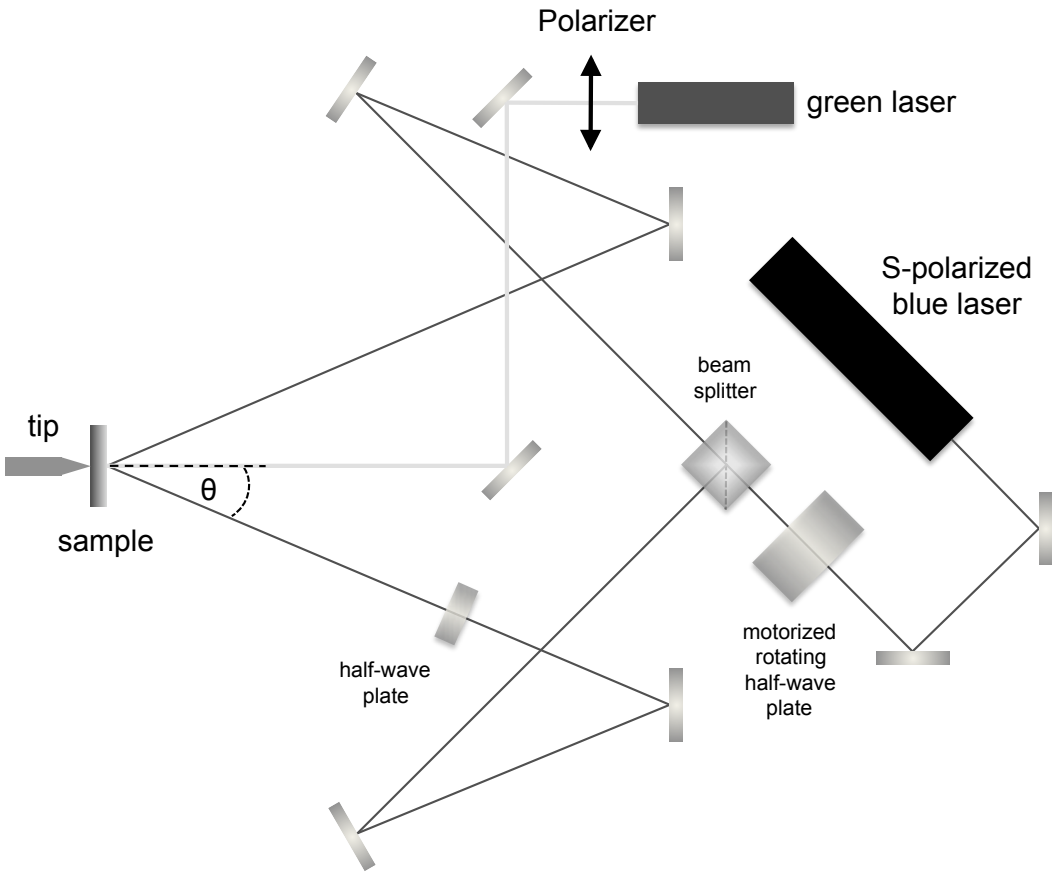

FIGURE 3.24: Reversible directional matter transport: *ss-p* and *pp-p* configurations. In order to switch the interfering beams' polarization between the s and the p states, a rotation of 90°is imposed to the motorized rotating halfwave plate, which has the two axis oriented long the s and the p directions. Another halfwave plate is used to compensate the phase of the reflected beam from the beam splitter. Blue laser: $(\lambda = 473\,nm)$. Green laser: $(\lambda = 532\,nm)$.

of the matrix in the bright fringes (deformation amplitude $\simeq 4\ nm$), followed by a slight elastic relaxation. As we turn on the p-polarized assisting beam ($t = 40\ s$), we observe a quick increase of the deformation *in phase* with the bright fringes. By changing the interfering beam polarization to p ($t = 100\ s$), the brighter zones are quickly depleted, as matter migrates in the opposite direction, i. e. towards the darker zones. Switching back to s reverses the matter migration orientation, which again conveys matter towards the bright areas. It is important to underline that no spatial shift of the intensity profile along the x-axis appears during all the experiment[17], so we observe a true effect of the light polarization. Switching back and forth between both polarizations allows to obtain six oscillations in $\simeq 10\ min$, before the sample photoresponse starts weakening (probably because of a photo-bleaching effect). In figure **Figure 3.26**(a) we show a 3D plot relative to the first 400 s of **Figure 3.25**. In (b), for the same time range, we plot

[17]In **Figure 3.25** we see a little drift towards the right, due to small piezoelectric non-linearities.

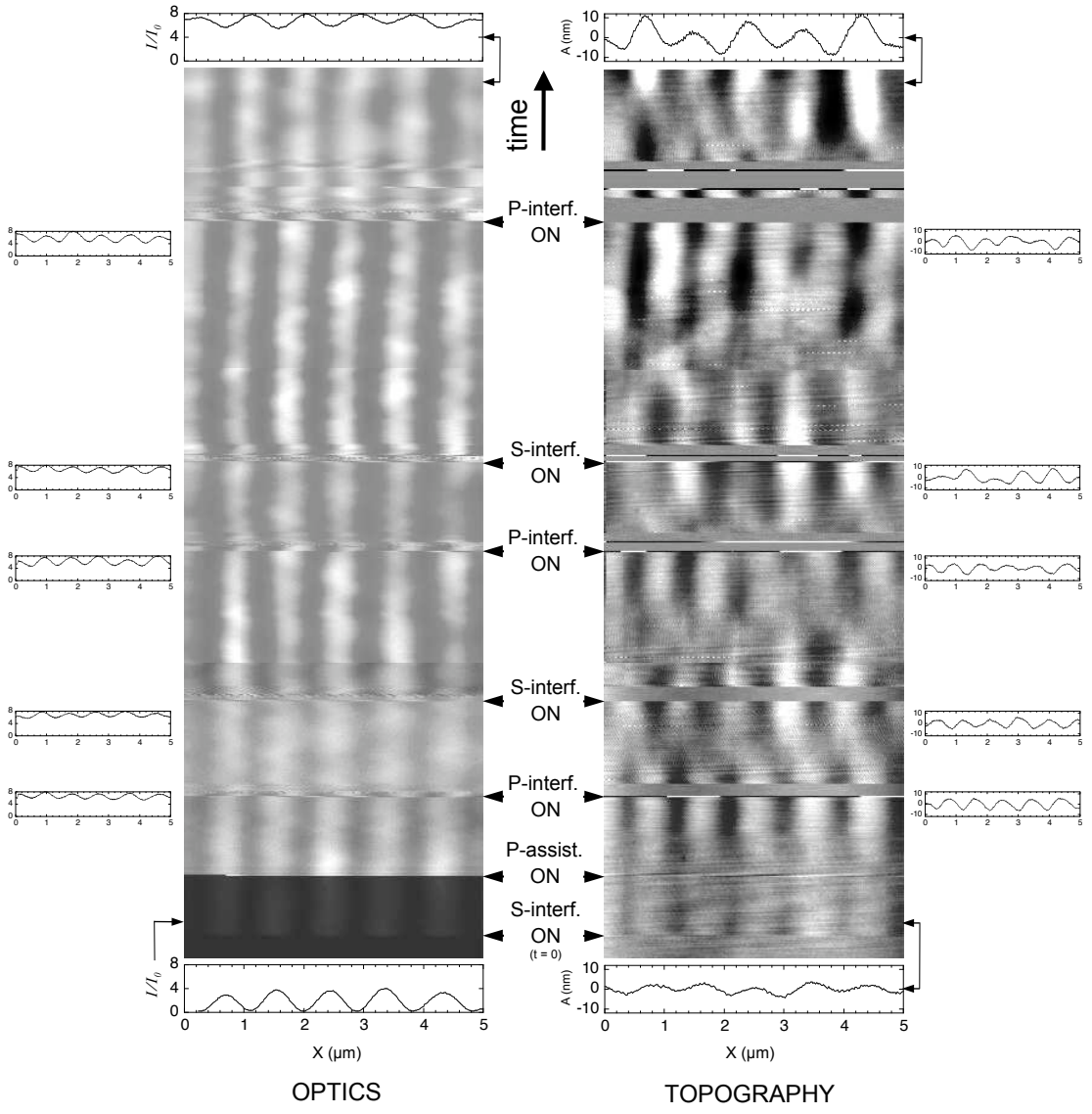

FIGURE 3.25: Reversible directional matter transport driven by polarization switching alternatively between *ss-p* and *pp-p* polarization configurations. Optical and topography images over a period of $\simeq$ 10 min. Scan is performed on the same line over a range of 5 μm. Assisting beam power density: 2.1 mW/mm^2; interfering beam power densities: 1 mW per beam. Sample = sol-gel DR1 200 nm thick.

the deformation amplitude, which is estimated, for every scan line, as the average height difference between the peaks and the grooves.

It must be pointed out that we did not perform any optimization of the oscillation rate in terms of amplitude and light intensity used, which could allow a greater number of surface oscillations before that photobleaching occurs.

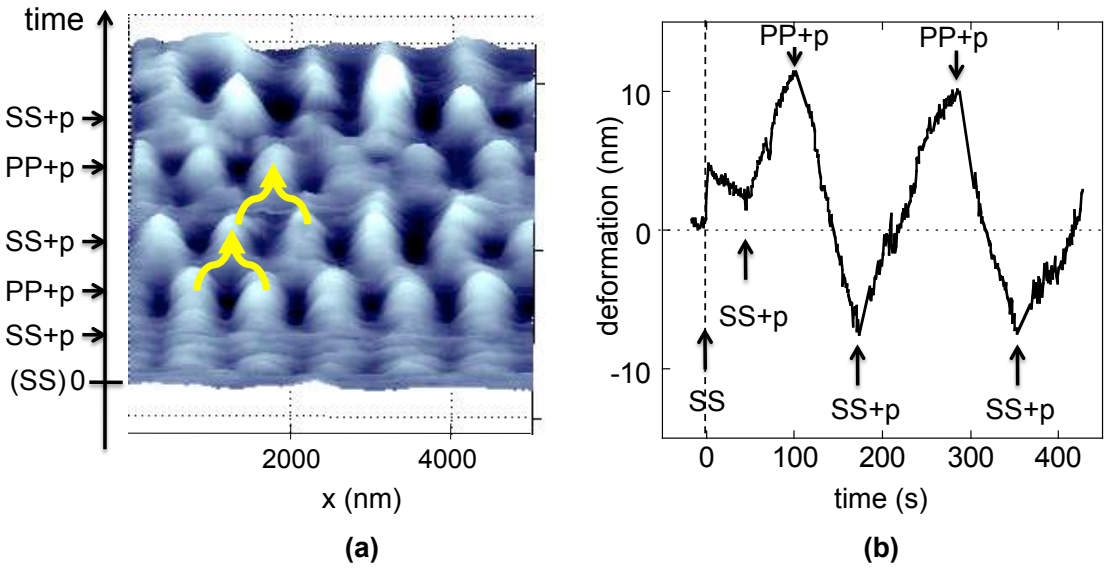

FIGURE 3.26: Reversible directional matter transport driven by polarization. (a) 3D plot of topography data recorded scanning on the same line over a range of 5 μm; (b) deformation amplitude calculated, for each scan line, as the average height difference between the peaks and the grooves.

In conclusion, these results clearly show the directionality of the mass migration phenomena. We demonstrate that the matter transport direction, orientation and efficiency are governed by the polarization spatial distribution. Matter can be alternatively driven towards the zones characterized by a prevalent $E_{\perp}$ field component, and pushed away from zones of prevalent $E_{\parallel}$ field component.

3.4.5 Discussion

The use of an assisting beam superimposed to an interference pattern is known to rise up the efficiency of the SRG formation in azobenzene containing thin films. This arises when using assisting beams incoherent and perpendicularly polarized with respect to the interfering beams.

However, we must distinguish between the SRGs resulting from the matrix photoexpansion and those produced by matter migration. The effect of an assisting beam on the first phenomenon leads to the erasure of any deformation. In fact, the uniform illumination with an assisting beam induces a uniform photoexpansion of the film. Thus, photoexpansion-induced SRGs form only in a transitory regime at the beginning of the simultaneous exposure of the film to both the interference pattern and the assisting beam. Subsequently, photoexpansion reaches the saturation all over the film and the SRGs vanish (**Figure 3.22**). This supports the interpretation of the photoexpansion as

resulting from a matrix reorganization to allow the increase in the volume necessary for the free isomerization of the azobenzene units. This phenomenon is essentially dependent on the light intensity and is independent of the assisting beam polarization with respect to the polarization of the interference pattern. Indeed, it is almost equivalent to the effect of a pre-irradiation (see section 3.2).
The effect of an assisting beam on the SRG formation resulting from matter migration is completely different. When the assisting beam and the interference pattern have the same polarization, the formation of SRG by matter migration is slowed down, while when they have a perpendicular polarization it is accelerated. Thus, the use of an assisting beam shows an effect of the polarization modulation on the matter migration phenomena.

Its most spectacular aspect occurs when a p-polarized beam assists an s-polarized interference pattern. Indeed, with no assisting beam, an s-polarized interference pattern does not induce the formation of matter migration SRG[18]. But, in presence of a p-polarized assisting beam an efficient mass transport is induced, which leads to the formation of large amplitude SRG. Similarly, we observe the acceleration of the matter migration SRG formation under s-assisted p-interference.
Moreover, the interplay between polarization spatial modulation and intensity spatial modulation is critical. This is demonstrated by the reversible, directional mass migration obtained by changing the interference pattern polarization while not spatially shifting the intensity profile. This configuration allows to invert the polarization spatial distribution with respect to the intensity spatial distribution. The directionality of the mass migration is determined by the intensity/polarization configuration. In particular, matter transport is always observed towards the zones illuminated by a field component having a polarization perpendicular to the intensity gradient ($\vec{E}_{\perp}$) and away from zones illuminated by a field component having a polarization parallel to the intensity gradient ($\vec{E}_{\parallel}$). Thus, depending on the spatial distribution of the light polarization with respect to the intensity distribution, the matter migration may take place either towards the brighter zones or towards the darker zones. In particular, as we have seen in 3.4.4 inverting in real-time the polarization spatial distribution and maintaining the same intensity spatial distribution leads to a reversible directional mass migration. This is coherent with our previous findings (see section 3.3) that the matter migration efficiency is driven by the polarization spatial distribution rather than by the light intensity.

In the assisting beam experiment, the polarization modulation is introduced by the assisting beam. Thus, varying the assisting beam amplitude allows to vary the polarization modulation. In order to quantitatively analyze the correlation between the spatial modulation of the polarization and the mass migration efficiency, we have performed

[18] At least in sol-gel DR1 samples.

experiments with different assisting beam intensities. In order to vary the polarization modulation from zero we consider the case of p-assisted s-polarized interference for which there is no modulation of the polarization when the assisting beam is off (see 3.4.1).

In **Figure 3.27** we show the deformation kinetics obtained on a sol-gel sample[19] (quantitative data are reported in **Table 3.3**) for different power densities of the p-polarized assisting beam, while the s-polarized interfering beams have always the same power density of 1 mW/mm^2 per beam. In this experiment, the interfering and the assisting beams are switched on simultaneously at $t = 0$, in order to measure the full evolution of the assisted photoinduced deformation. The growth rate is the slope of the deformation kinetics: for the matrix photoexpansion mechanism it is measured at $t = 0$, while for the mass migration mechanism it is measured over the first 100 s of irradiation, during which the deformation amplitude is quasi-linear.

With no assisting beam (**Figure 3.27**(a)), the photoinduced deformation is only due to photoexpansion, which is characterized by a high rate and a low efficiency with a maximum deformation of $\simeq 7\ nm$. Using 0.4 mW p-polarized assisting beam (**Figure 3.27**(b)) is sufficient to activate the matter migration with a low SRG growth rate of 0.04 nm/s. In this case, as the light intensity contrast[20] is $\simeq 90\%$, we measure a smaller deformation due to the photoexpansion ($\simeq 4\ nm$). When increasing the intensity of the assisting beam (hence reducing the contrast), the photoexpansion contribution to the deformation vanishes (it almost disappears in (d) where the optical contrast is $\simeq 78\%$), while matter migration is more and more efficient (d-f). At the maximum power density available for the assisting beam, 2.1 mW/mm^2, where the ratio between the assisting and the incident beams power densities is $\simeq 1$, we obtain a higher SRG growth rate of 2.1 nm/s.

Let us define the spatial modulation of the polarization as $E_{pol} = \min\{E^0_{\parallel}, E^0_{\perp}\}$ (by analogy with section 3.3.2). The parallel component is provided only by the assisting beam[21] ($E^0_{\parallel} = \sqrt{I_{\text{assist}}}$) while the perpendicular component is given by the interfering beams ($E^0_{\perp} = \sqrt{I_{\text{interf}}}$). For assisting beam intensities smaller than the intensity interference pattern amplitude, we have: $E_{pol} = E^0_{\parallel} = \sqrt{I_{\text{assist}}}$. So, we expect that the efficiency of the SRG formation increases as $\sqrt{I_{\text{assist}}}$.

In **Figure 3.28** we compare the SRG growth rate experimentally observed (□) and the corresponding values of $\sqrt{I_{\text{assist}}}$. The close correlation between the experimental

[19] In this experiment we used a 450 nm thick sol-gel sample, as we wanted to better discriminate between the photoexpansion and the matter migration mechanisms. As shown in [9], the photoexpansion mechanism is dependent on the thickness, while [15] matter migration efficiency doesn't significantly change using a 200 nm or a 450 nm thick sample.

[20] Defined as $\frac{I_{max} - I_{min}}{I_{max}}$, where I_{max} and I_{min} are the maximum and the minimum intensity values of the total light field.

[21] We recall that the p-polarized assisting beam is in normal incidence on the sample.

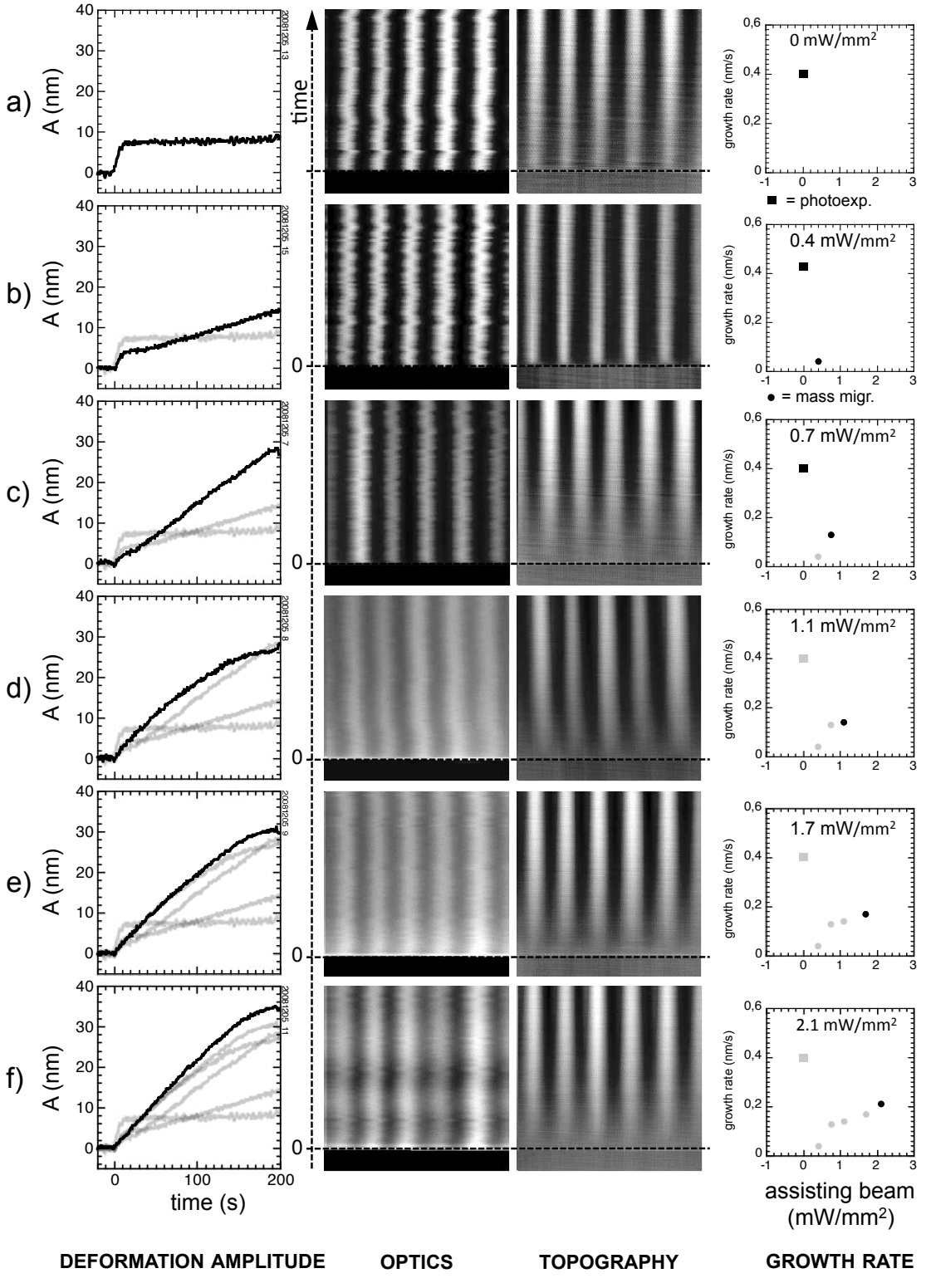

FIGURE 3.27: p-assisted s-polarized interfering beams: dependence of the photodeformation mechanisms on the assisting beam power density. Interfering beams' power density: 1 mW/mm^2 per beam ($\lambda = 473\ nm$; assisting beam ($\lambda = 532\ nm$): (a) 0, (b) 0.4, (c) 0.7, (d) 1.1, (e) 1.7, (f) 2.1 mW/mm^2. From the top to the bottom: the photoinduced deformation corresponding to various p-polarized beam power densities (mW/mm^2). From left to right : the kynetics of the grating formation, the optical near-field image and the corresponding shear-force topography image (x-range = 5 μm). The SRG growth rate is reported in the last column on the right: squares indicate the SRG growth rate due to photoexpansion, while circles indicate the SRG growth rate due to matter migration (in each plot are reported in grey the values of the previous cases, for comparison).

S+S (mW/mm^2)	**P** (mW/mm^2)	**photoexp (nm/s)**	**matter migr. (nm/s)**
2	0	0.4	0
2	0.4	0.4	0.04
2	0.75	0.4	0.13
2	1.1	0	0.14
2	1.7	0	0.17
2	2.1	0	0.21

TABLE 3.3: Dependence of the matter-migration-induced SRG growth rate on the irradiation power density under *s*-polarized interfering blue beams assisted by a *p*-polarized green beam. The incident power density of the interfering (S+S) and the assisting (P) beams are given in mW/mm^2; the SRG growth rate is given in nm/s. Sample: sol-gel Si-DR1, 450 nm thick.

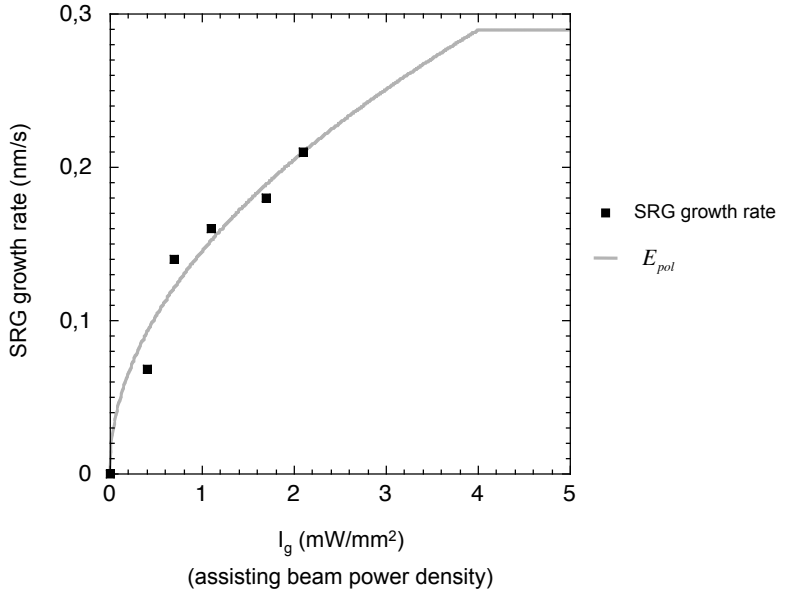

FIGURE 3.28: Correlation between the SRG growth rate and the spatial modulation of the polarization under *p*-assisted *s*-polarized interference. Data relative to the experiments reported in **Figure 3.27**. Best fit of E_{pol} (in arbitrary units) for a scaling factor of 0.1445. Assisted beam power density = 2.1 mW/mm^2, interfering beams' power density = 1 mW/mm^2, sample: sol-gel-DR1, thickness $\simeq$ 200 nm.

data and the calculated values of the spatial modulation of the polarization indicates that also in the experiments with an assisting beam this parameter governs the mass migration efficiency. Moreover, it suggests that the deformation efficiency is dependent mainly on the less intense field. This seems to be in agreement also with the saturating behavior of the growth rate when the assisting field intensity I_{assist} increases. Therefore, the maximum growth rate would be obtained for $I_{\text{assist}} = I_{\text{interf}}$ and further raising of the assisting beam intensity ($I_{\text{assist}} > I_{\text{interf}}$) should not lead to a growth rate increase. Experiments in these two cases may confirm our hypothesis.

From a quantitative point of view, the matter migration rate observed in the assisted

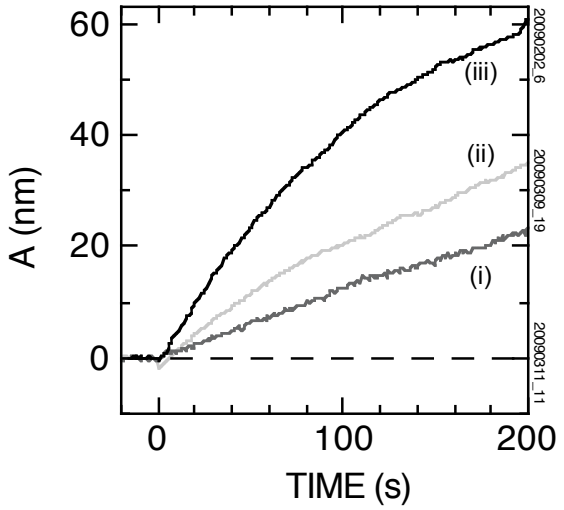

FIGURE 3.29: Assisted beam mass migration efficiency. (i) p-assisted s interference (ii) s-assisted p interference (iii) $\varphi = 45°$. Assisted beam power density $= 2.1\ mW/mm^2$, interfering beam power density $= 1\ mW/mm^2$, sample: sol-gel-DR1, thickness $\simeq 200\,nm$.

configurations is of the same order of magnitude of the transport rates observed with the superposition of two spatially shifted s and p interference patterns (see 3.3). This is shown in **Figure 3.29**, where we report the comparison between the deformation kinetics obtained by matter migration using the assisted configurations (i-ii) and the superposition of two s and p interference patterns having the same intensity (at $\varphi = 45°$) (iii). Under p-assisted s interference the matter migration rate[22] is 0.1 nm/s (i), under p-assisted s interference it is 0.2 nm/s (ii) while in the case of the superposed interference patterns it is 0.4 nm/s. The less efficient matter migration observed in the assisted cases can be due to several reasons. In the assisted configurations is present a superposition of the $\vec{E}_{\parallel}$ and $\vec{E}_{\perp}$ components in the brighter fringes, which may activate matter migration processes in opposite directions. Moreover, the sample absorption at the assisting beam wavelength[23] is smaller than the absorption at the interfering beam wavelength[24]. Finally, the incoherence of the assisting beam with the interfering beams may reduce the effects of the spatial modulation of the polarization. In order to verify these points and to study more completely the assisted configuration we should perform experiments with assisting and interfering beams of the same wavelength.

The dependence of the matter migration efficiency and directionality on the spatial distribution of the light polarization and intensity is also in agreement with several observations so far reported in the far and in the near field. Difficulties in the interpretation

[22] Evaluated over the first 100 s of SRG growth.
[23] $\lambda_g = 532\ nm$
[24] See 2.2

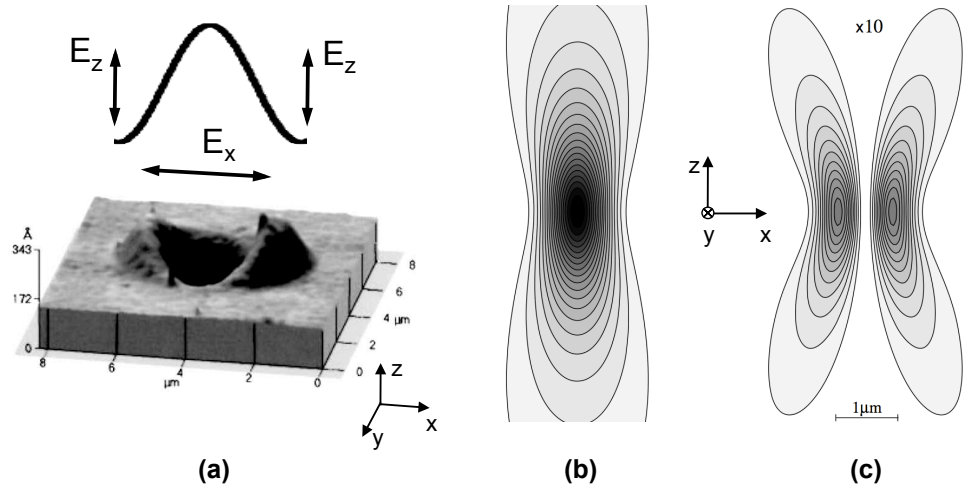

FIGURE 3.30: Far-field photodeformation under a p-polarized gaussian beam (a) we report the experiment performed in [17] and a scheme of the intensity profile relative to the E_x and E_z field components; (b-c) theoretical field distribution ([18], pag. 52) for a gaussian beam (in the calculation $\lambda = 800nm$) (b): total field distribution; (c) E_z field distribution.

of these experiments have been raised, since in the far field matter was observed to migrate away from the enlightened zones, while in the near-field matter migrated towards the bright areas. By considering the dependence of the matter migration efficiency, direction and orientation on the spatial distribution of the polarization, we obtain a coherent interpretation of these phenomena. As an example, we will report experiments performed in the far field using a single focused gaussian beam or a Bessel beam, as well as in the near field, such as local probe illumination and apertureless SNOM.

Gaussian beam

In the experiments reported in ref. [17], a gaussian laser beam is focused on the sample using spherical and cylindrical lenses and a 10 × microscope objective. Photoinduced matter migration has been observed using p-polarized light, while approximately no mass transport has been reported for the s polarization. Matter migrates along the $\vec{E}_{\parallel}$ polarization direction, from the centre towards the periphery. In this configuration, the amplitude of the $\vec{E}_{\perp}$ component decreases going from the periphery towards the centre of the spot, where its amplitude is zero and, instead, the amplitude of the $\vec{E}_{\parallel}$ is maximum [18] as depicted in **Figure 3.30**. So, matter accumulates in the zones where the intensity of the $\vec{E}_{\perp}$ component is maximum, while the zones corresponding to the maximum intensity of the $\vec{E}_{\parallel}$ component are depleted, which is in line with our results. Similar observations have also been reported in [19], using highly focused HG_{00} and HG_{10} beams.

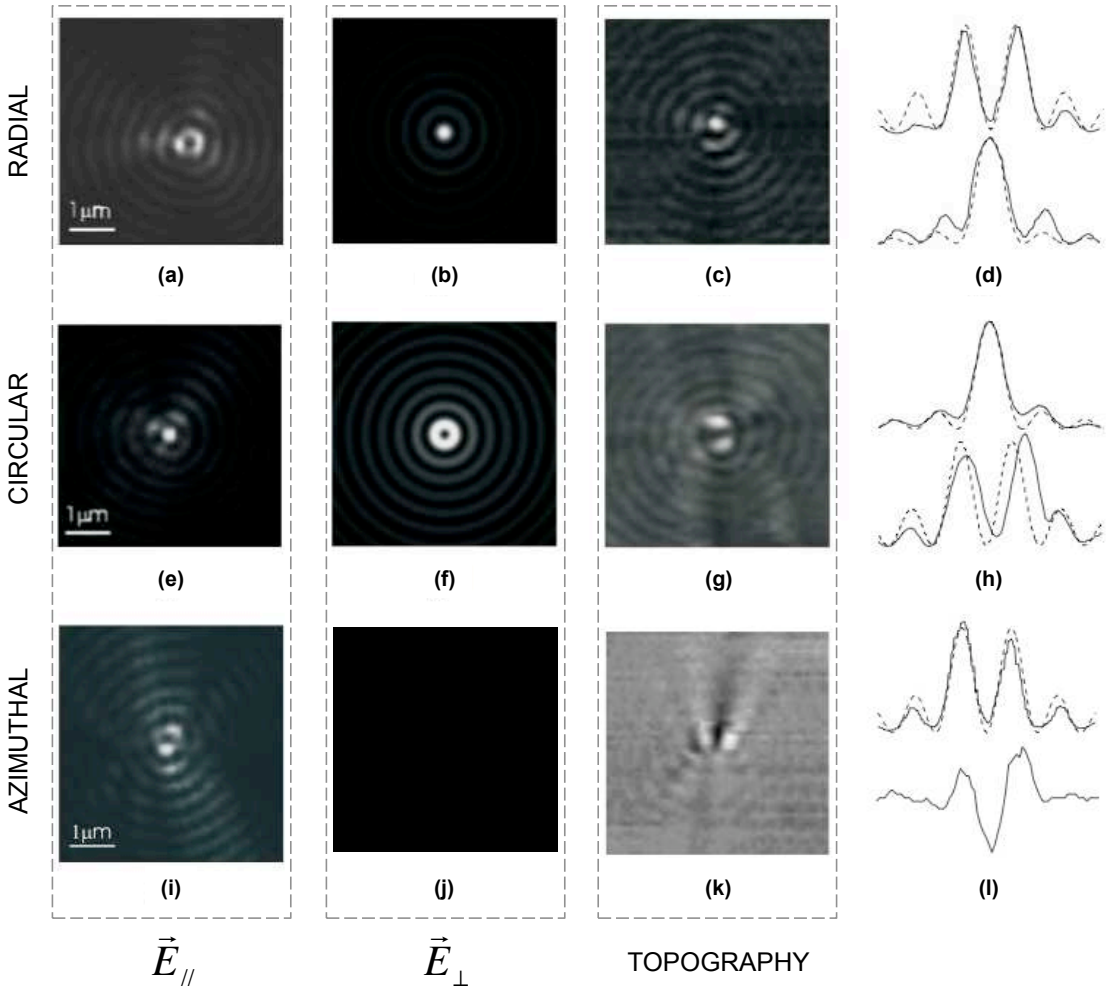

FIGURE 3.31: Matter migration under a Bessel beam. We report the experimental results obtained in ref. [20] in the case of radially (a-d), circularly (e-h) and azimuthally (i-l) polarized light. (a), (e), (i): measured $\vec{E}_{\parallel}$ field intensity spatial distribution on the xy plane; (b), (f), (j): calculated $\vec{E}_{\perp}$ field intensity spatial distribution on the xy plane; (c),(g),(k): shear-force topography measurements photoinduced by the corresponding light field; (d),(h),(l): (top) $\vec{E}_{\parallel}$ calculated (dashed) and measured (solid) intensity profiles, (bottom) $\vec{E}_{\perp}$ calculated (dashed) intensity profile and measured (solid) topography profile. Sample = PMMA-DR1, 100 nm thick, light dose = 20 J/cm^2 (0.5 s exposure at a 40 W/cm^2 laser beam, $\lambda = 514\,nm$).

Bessel beam

A Bessel beam is characterized by the superposition of two orthogonally polarized periodic field components, one polarized in the x, y plane ($\vec{E}_{\parallel}$) and the other one polarized along the z-axis ($\vec{E}_{\perp}$). According to the polarization (radial, circular or azimuthal) their intensities are described by J_0^2 and J_1^2 square Bessel functions, which are half a period spatially shifted. For example, a radially polarized Bessel beam **Figure 3.31**(a-b)[25] has a maximum $\vec{E}_{\perp}$ and a zero $\vec{E}_{\parallel}$ intensities in the origin, while for a circularly polarized

[25] **Figure 3.31** has been reproduced from [20].

Bessel beam (e-f) the distribution is inverted. In the particular case of an azimuthally polarized Bessel beam (i-j), the $\vec{E}_{\perp}$ component is zero.

In **Figure 3.31**(c,g,k) we report the results that have been obtained on a PMMA-DR1 thin film having a thickness of 100 nm, using a 200 mJ/mm^2 light dose, in the three polarization configurations, respectively. Under radial and circular polarizations, a relief growth is observed always in correspondence of the $\vec{E}_{\perp}$ component, while matter is driven away from the $\vec{E}_{\parallel}$ component. This is the same behavior that we have observed in our experiments, confirming that the orientation of the matter migration is strictly dependent on the spatial distribution of the field polarization.

Only in the case of an azimuthally polarized Bessel beam (i-l), the observed matter accumulation is associated to the $\vec{E}_{\parallel}$ component. In this case an extremely weak deformation is produced ($\simeq 2$ nm). We note that in this polarization configuration only the $\vec{E}_{\parallel}$ component is present, since the $\vec{E}_{\perp} = 0$, so the amplitude of the spatial modulation of the polarization $E_{pol} = 0$. This is the symmetric configuration with respect to the s-polarized interference that we have used in our experiments, where $\vec{E}_{\parallel} = 0$ and $E_{pol} = 0$. In this case, we observe also a weak relief growth in phase with the light intensity, which is due to the matrix photoexpansion. This suggests that the matter accumulation observed in the bright zones using an azimuthally polarized Bessel beam could be due to the matrix photoexpansion as well.

Local probe illumination and apertureless SNOM

In the experiments involving near-field illumination through the aperture of a metallized optical fiber ($\simeq 40$ nm aperture [21]), matter accumulation is observed in the enlightened zones ([4, 22]). The irradiating light field is transversally polarized ($\vec{E}_{\parallel}$) and far from the tip apex (in the bulk and in the periphery) the light polarization is essentially transversal. However, a longitudinal component along the z axis ($\vec{E}_{\perp}$) is present in the vicinity of the tip apex [18]. So, matter accumulates towards the area where the $\vec{E}_{\perp}$ is maximum and away from the transversally polarized light, which is the same behavior that we observe in our experiments.
Similar results have been obtained in the experiments using irradiation by apertureless SNOM [23, 24]. When p-polarized light is concentrated, in near field, using a laser beam incident on a metal coated tip brought close to the sample's surface, the growth of a relief is observed in the vicinity of the tip. When s-polarized light illuminates the tip, the effect is qualitatively similar, but much weaker then using p-polarized light. This is also coherent with our observations, since in this case the light field has almost only one

component, along the s direction.

We conclude that the photodeformation phenomena in sol-gel Si-DR1 thin films are dependent not only on the spatial distribution of the light intensity but also on the distribution of the field polarization. In particular, the latter governs the efficiency and the orientation of a directional reversible matter migration process. According to the field spatial distribution, this can induce matter accumulation towards the zones where the field polarization is perpendicular to the intensity gradient, or can drive matter away from the field components parallel to the intensity gradient. These results are in agreement with several observations reported in the far and in the near field and allow to coherently interpret a certain number of unexplained phenomena.

3.5 Matter migration phenomena in PMMA-DR1

3.5.1 Matter migration under *s*- and *p*-polarized light

Generally, photoinduced deformation in azo-containing materials are performed in polymer matrices like PMMA. The results reported so far show that under s-polarized interference very weak photoinduced deformations occur. This is consistent with our observations in sol-gel Si-DR1 thin films and we may interpret the weak photoinduced deformation has being due to matrix photoexpansion. However, in a previous study [15] photoinduced matter migration has been observed under the exposure to s-polarized interference.

We have used the techniques presented in the previous sections to study the photomechanical phenomena in the PMMA-DR1 material described in section 2.2.3. In **Figure 3.32** we show the photoinduced deformation obtained on a PMMA-DR1 sample 180 nm thick under irradiation with an interference pattern using a very weak power density, 70 $\mu W/mm^2$ per beam (blue laser, $\lambda = 473\ nm$), for both s and p polarizations[26]. In (a-b) we show the optical and topography images, obtained scanning over the same line with a range of 5 μm, of the first $\simeq 200\ s$ of irradiation using s-polarized light. In (e-top) is plotted the average transmitted light intensity corresponding to (a) while in (e-bottom) is reported the average profile evolution corresponding to (b). The same is shown for p-polarized light (c-d) and (f).

At $t = 0$, turning the laser on, we observe in both cases the growth of a weak relief ($\simeq 1\ nm$) *in phase* with the bright fringes of the interference pattern, which can be

[26]The SNOM signal of the optical image for the p polarization is very weak, which might be due to the anistropic sensibility of the tip for s and p polarizaitions, which is exalted at low light intensitites.

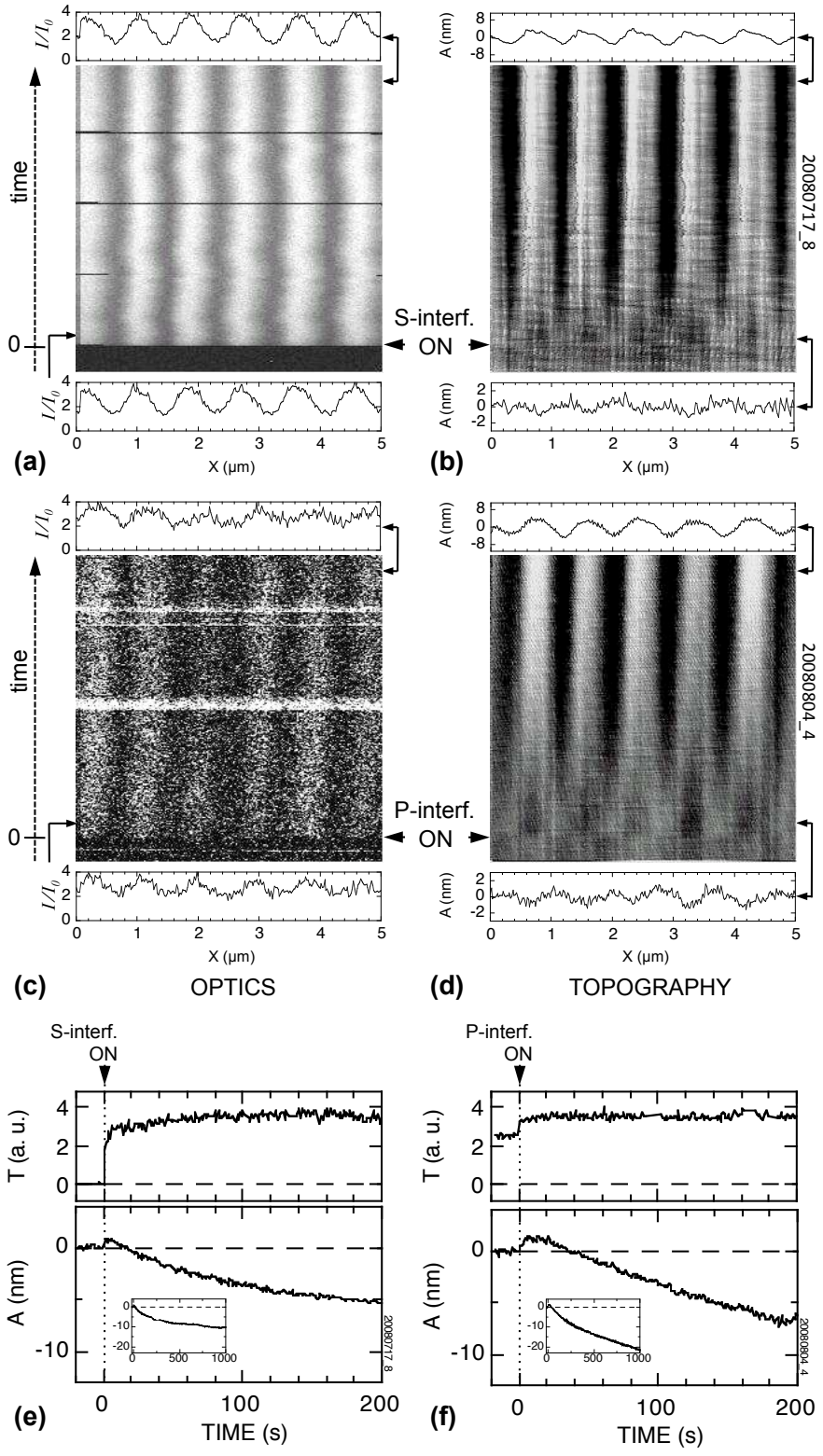

FIGURE 3.32: PMMA-DR1: polarization effects on the photoinduced deformation. (a-b) *s*-polarized light: optical and topography images obtained scanning over the same line with a range of 5 μm. The first $\simeq 200$ s of irradiation are shown. (e-top) average transmitted light intensity corresponding to (a), (e-bottom) average profile evolution corresponding to (b). The same is shown for *p*-polarized light in (c-d) and (f). Laser power density = 70 $\mu W/mm^2$ per beam (blue laser, $\lambda = 473$ nm).

attributed to the matrix photoexpansion in the brighter areas.
Subsequently, we observe, for both polarizations, a $\pi - phase$ topography shift with respect to the interference pattern. This is represented in (e-f) by the negative sign of the deformation amplitude. Comparing the photodeformation effects over time ((e-f) insets) in the two polarization configurations, we note that the deformation amplitude is higher under p-polarized light ($\simeq$ 20 nm in 1000 s) than under s-polarized light ($\simeq$ 10 nm in 750 s), while the growth rates (measured during the first 10 s, where the growth is quasi-linear) are almost similar ($\simeq 0.05\ nm/s$).

The π-phase deformation obtained under s and p-polarized light demonstrates that in PMMA-DR1 matter migration occurs in both configurations. This is very different from the results that we have obtained previously in sol-gel Si-DR1. We indeed observed matter migration only in the presence of a modulation of the spatial distribution of the polarization, the matter motion taking place from the field components $\vec{E}_{\parallel}$ parallel to the intensity gradient and towards the field components $\vec{E}_{\perp}$ perpendicular to the intensity gradient. In the presence of a pure intensity modulation, corresponding to the s-polarized interference configuration, no mass transport arises in sol-gel Si-DR1 films. In PMMA-DR1, we instead observe matter migration under an s-polarized interference pattern. This mass transport corresponds to a matter motion away from the $\vec{E}_{\perp}$ field component, which is the opposite direction with respect to the polarization-driven matter migration phenomenon. This suggests the existence of a second microscopic migration mechanism, which depends on the light intensity pattern. Note that the polarization-driven mechanism is however also active in PMMA-DR1 since the efficiency of the overall photodeformation process is larger under p-polarized interference than under s-polarized interference.

In order to evaluate the respective efficiency of the intensity-dependent and polarization-dependent mechanisms we will perform the same experiments and analyses as those presented in sections 3.3 and 3.4.1. First we study the effect of a p-polarized assisting beam on the matter migration induced under an s-polarized interference pattern. Second, we measure the efficiency as a function of the angle between the polarization of the interfering beams.

3.5.2 Photoinduced matter migration in PMMA-DR1 under *p*-assisted *s*-polarized interference

In **Figure 3.33** we show the photodeformation obtained under p-assisted s-polarized interfering beams on a PMMA-DR1 film 180 nm thick. The experimental setup (a) is the same as in section 3.4.1. The blue interfering beams ($\lambda = 473\ nm$) have each one a

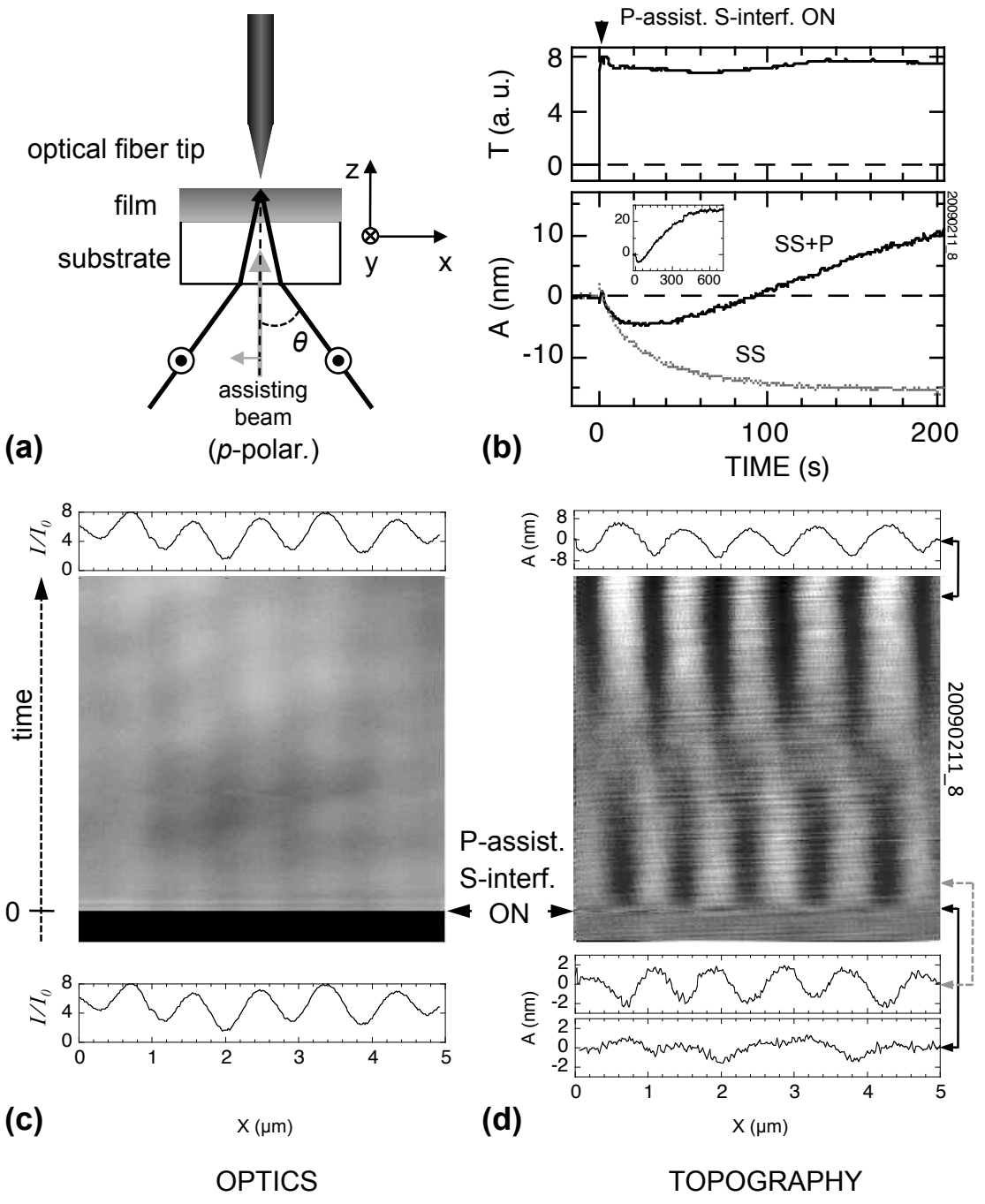

FIGURE 3.33: PMMA-DR1 photodeformation under simultaneous p-assisted s-interfering beams. (a) Experimental setup; (b) transmitted light intensity T in arbitrary units (top) and the corresponding photoinduced deformation amplitude A expressed in nm (solid curve), the dotted curve indicates the deformation obtained in the same conditions without the assisting beam; (c)-(d) optical and topography images, scanning over the same line, scan-range = 4.5 μm. Laser power density: 2 mW/mm^2 per beam (blue - non assisted experiment), 1 mW/mm^2 per beam (blue), 2.1 mW/mm^2 per beam (green); sample = PMMA-DR1, $\simeq$ 180 nm thick.

power density of 1 mW/mm^2 while the green ($\lambda = 523\ nm$) assisting beam, in normal incidence, has a power density of 2.1 mW/mm^2. In (b) we report the first 200 s of the average transmitted light profile T (top) in arbitrary units, and (bottom) the deformation amplitude A of the assisted (solid curve) and non-assisted (dotted curve) photodeformations. In (c) and (d) we show the optical and topography images relative to (a), with the detail of the profiles at some instants of interest[27]. Turning on simultaneously the three beams at $t = 0$, we observe instantly a very weak deformation (0.8 nm), in phase with the s interference pattern, which can be attributed to the matrix photoexpansion, which here yields a low magnitude photodeformation, since the intensity contrast across the interference pattern is reduced by the uniform assisting beam (see 3.4.1).
The photoexpansion is followed by a *π-phase* deformation which reaches a maximum amplitude of 5 nm after 25 s of exposure time. Subsequently, we observe an inversion of the photodeformation process, which leads to the growth of a SRG *in phase* with the s interference pattern, i. e. shifted by half an interference period with respect to the preceding deformation. This SRG amplitude finally saturates at a value of 26 nm after about 500 s.
The first stage of the mass transport, which gives a *π-phase* deformation, clearly corresponds to the intensity-dependent mechanism, which is observed also under non-assisted s-polarized light (dotted curve). On the other hand, the subsequent *in-phase* deformation is consistent with the polarization-dependent mass migration. These observations show that the two deformation processes produce matter transport in opposite directions, with different kinetics. In the conditions of the current experiment, the intensity-dependent matter transport appears to dominate at low time scales, while it is fully overcome by the polarization-driven process at longer time.

3.5.3 Intensity versus polarization matter migration mechanisms in PMMA-DR1

In order to fully describe the relative weight of the intensity-dependent mechanism versus the polarization-dependent mechanism, we perform an analysis of the photoinduced matter migration obtained by varying the polarization angle φ of the interfering beams. This allows to control the relative amplitude of the intensity and polarization patterns.

Figure 3.34(a) shows the matter migration deformation amplitude for φ values of $0°, 45°, 90°$. Since these configurations present different mass migration directions, we choose the same convention adopted in 3.3.1 (see **Figure 3.6**). So, the sign of the deformation amplitude A and of its growth rate is given by the direction of the mass transport:

[27] On the optical image, we plot the transmitted light profile averaged over 200 s, since the measured contrast is very weak.

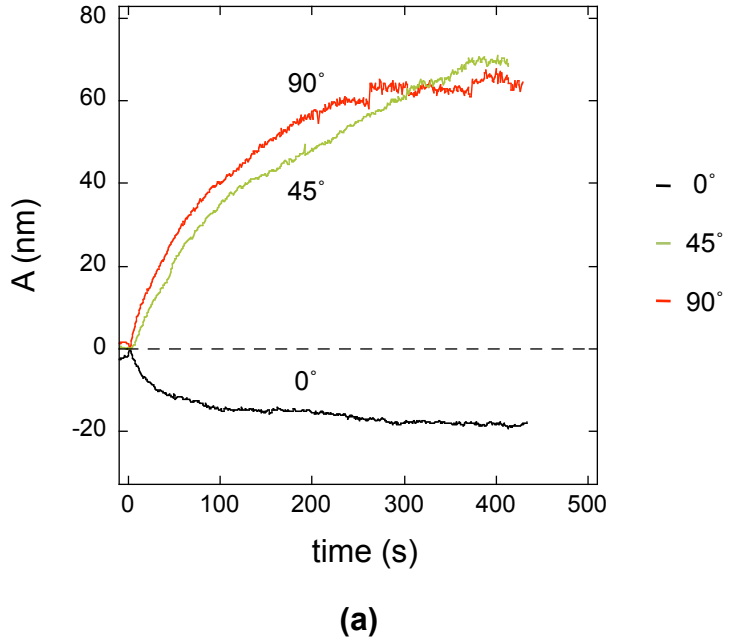

(a)

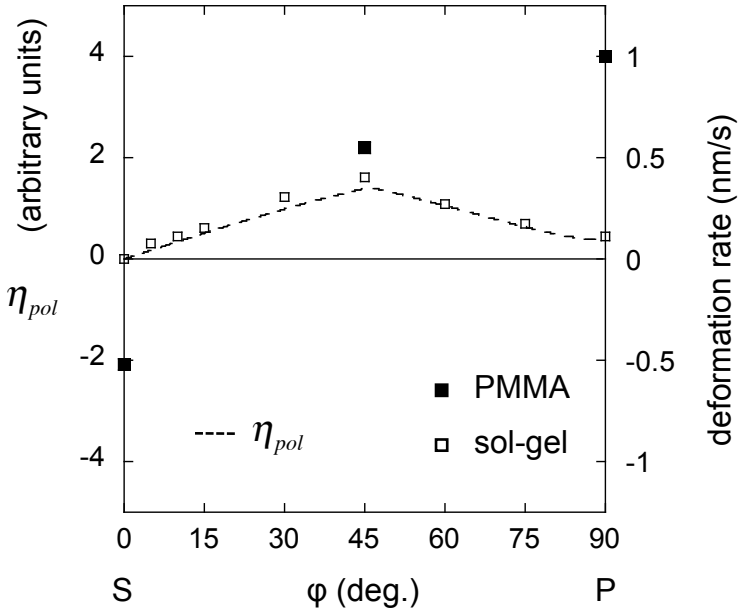

(b)

FIGURE 3.34: PMMA-DR1: deformation efficiency vs amplitude and polarization spatial modulation. (a) Mass migration kinetics for SS, PP and ±45 polarizations; (b) SRG growth rate estimated on the first 100 *s* in PMMA-DR1 (■) and in sol-gel Si-DR1 (□). The variation of η_{pol} is plotted on the same graph (dashed curve).

a positive sign stands for matter transport towards the zones illuminated with the $\vec{E}_\perp$ field components while a negative sign indicates matter migration away from these zones. According to this sign convention, in PMMA-DR1 *s*-polarized interference ($\varphi = 0°$) produces negative deformations, while *p*-polarized interference ($\varphi = 90°$) and polarization interference ($\varphi = 45°$) produce positive deformations.

We consider the SRG growth rate during the first 100 *s* of illumination[28] as the relevant experimental quantity that characterizes the matter migration efficiency. In **Figure 3.34**(b) we plot this average growth rate, for both PMMA-DR1 (■) and sol-gel Si-DR1 (□). Clearly, the variation of the SRG growth rate is very different in the two matrices. As reported in section 3.3.2 for a sol-gel matrix[29], the matter migration efficiency is very well described by the spatial modulation of the light field polarization E_{pol} (dashed curve). The mass migration efficiency in PMMA-DR1 results quite uncorrelated with the spatial modulation of the polarization, which suggests that in the PMMA matrix E_{pol} is not the appropriate quantity to describe the two mechanisms at the origin of the photodeformation. Thus, we define two quantities η_{pol} and η_{int} that characterize the respective efficiencies of the polarization-driven mechanism and the intensity-driven mechanism. In order to keep coherence with what we have done for sol-gel samples, we take $\eta_{pol} = E_{pol}$.

In order to describe the intensity-driven matter transport mechanism we use a statistical directional displacement model, so-called 'inch-worm' like motion, similar to the one proposed in ref. [25]. Under illumination, each molecule has a certain probability of undergoing isomerization, according to its orientation with respect to the electric field. For each isomerization event, a displacement happens along the molecular axis. Its contribution to the matter migration across the intensity modulation pattern (i.e. *x*-axis) depends on the orientation of the molecular axis. For example, molecules excited along the *x*-axis will fully contribute to the displacement, while molecules excited orthogonally to the *x*-axis will not contribute. Considering an isotropic angular distribution of the molecules, we can calculate $< p_\parallel >_\Omega, < p_\perp >_\Omega$, the displacement probabilities averaged on $\Omega = 4\pi$ str, corresponding respectively to the illumination with the $E_\parallel$ and the $E_\perp$ components:

$$< p_\parallel >_\Omega \;=\; 4\left(\frac{1}{4\pi}\int_0^{\frac{\pi}{2}} cos^2(\theta) cos\theta sin\theta \, d\theta \int_0^{\pi} d\phi\right) = \frac{1}{4} \tag{3.31}$$

$$< p_\perp >_\Omega \;=\; 4\left(\frac{1}{4\pi}\int_0^{\frac{\pi}{2}} cos^2(\theta) sin^2(\theta) \, d\theta \int_0^{\pi} sin\phi d\phi\right) = \frac{1}{8} \tag{3.32}$$

[28] Where the growth is quasi-linear.
[29] See **Figure 3.13**.

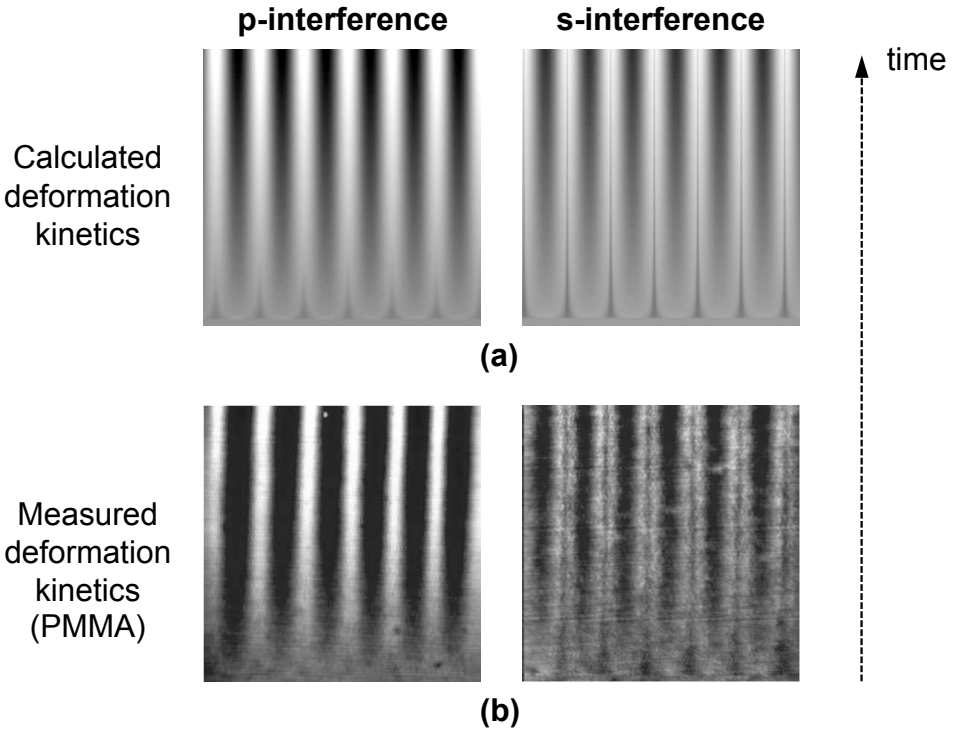

FIGURE 3.35: PMMA-DR1: statistical model. (a) Simulations; (b) Experimental results (shear-force images of the photodeformation obtained on a 135 nm thick PMMA-DR1 sample, reproduced from ref. [15]). Sample thickness = 100 nm, laser wavelength $\lambda = 473$ nm, laser power = 1 mW per beam.

where θ and ϕ describe the molecule orientation in the space.
So we obtain that:

$$< p_{\parallel} >_{\Omega} = 2 < p_{\perp} >_{\Omega} \tag{3.33}$$

We recall that our experimental illumination configuration is characterized by the superimposition of a $E_{\parallel}$ and $E_{\perp}$ interference patterns, spatially shifted one from the other along the x-axis by half an interference period (see section 3.3.2). The relative intensity of both the interference pattern depends on the value of φ. Since the statistical displacement relies strictly on the spatial distribution of the light field intensity, we can define a displacement efficiency η_I as:

$$\eta_I = < p_{\parallel} >_{\Omega} \left(E^0_{\parallel}(\varphi)\right)^2 - < p_{\perp} >_{\Omega} \left(E^0_{\perp}(\varphi)\right)^2 \tag{3.34}$$

where the first term describes matter migration away from the $\parallel$ field component and the second one matter migration away from the $\perp$ field component. Therefore a positive efficiency indicates matter migration towards the $\perp$ field component.

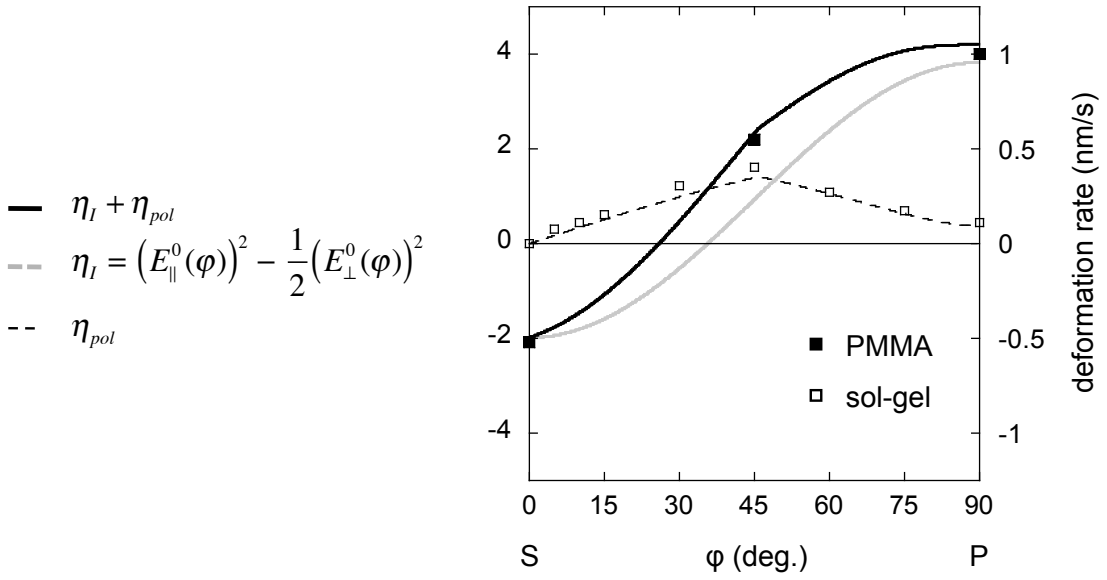

FIGURE 3.36: PMMA-DR1: deformation efficiency vs amplitude and polarization spatial modulation. SRG growth rate: PMMA (■ - estimated on the first 100 s), sol-gel (□); η_{pol} (black dashed curve); η_I (grey curve); $\eta_I + \eta_{pol}$ (black solid curve).

Figure 3.35 shows the calculated images of the deformation kinetics for a PMMA-DR1 thin film having a thickness of $\simeq 100\ nm$. Simulations are performed for both s and p polarizations and are compared with the experimental results obtained on samples of the same thickness. The model seems to describe very well the matter migration phenomena observed with both polarizations. In particular, it describes the main features of the deformation kinetics: matter transport away from the illuminated areas (for both polarizations) and p-induced transport more efficient than s-induced transport. Moreover, in the case of s-polarized light the simulation reproduces the central groove within the reliefs, experimentally observed, which supports the less efficient matter transport produced by the $E_\perp$ field component.

In **Figure 3.36** we report the matter migration efficiency together with the variation of η_I (grey curve) as a function of the polarization angle φ. We note a rather good agreement between the variation of this parameter and the matter migration rate (■) in PMMA. Very surprisingly, the sum $\eta_I + \eta_{pol}$ (black solid curve) shows a remarkable agreement with the measured SRG growth rate.
This indicates that in PMMA-DR1 the mass migration efficiency is governed by the superimposition of two mechanisms: one which is well described by a statistical directional matter migration model, depending mainly on the photoisomerization rate, i. e. on the intensity pattern, and the other which depends on the spatial distribution of the light polarization and is compatible with models based on microscopic transport mechanisms originating from the electromagnetic forces [8].

Note that the two mechanisms can be singled out by setting the polarization angle φ. At $\varphi = 0°$ the polarization mechanism is inhibited, since $\eta_{pol} = 0$; at $\varphi = 35°$ the statistical mechanism should vanish, since $\eta_I = 0$. These two angles provide SRG formation of opposite spatial phase. At $\varphi = 26°$, the two mechanisms are expected to compensate each other, since $\eta_I = \eta_{pol}$. No SRG growth should be observed in this condition. Further experiments in these polarization configurations might confirm our interpretation.

The weighted contribution of the polarization-dependent and the intensity-dependent mechanisms in sol-gel Si-DR1 and PMMA-DR1 stresses out the fundamental role of the matrix in matter migration processes. Both materials allow the polarization-driven mechanism with almost the same efficiency. However, the statistical mechanism is inhibited in the tridimensional mineral matrix of sol-gel thin films, while it is very efficient in the linear polymer matrix of PMMA. It is most likely that the relative influence of both mechanisms on the migration efficiency is also influenced by the polymer chain length. First indications in this sense have already been reported in ref. [26].

The photomechanical response of a PMMA-DR1 thin film is found to be very different from the one of the sol-gel Si-DR1 thin films. Indeed, the results that we have obtained in PMMA-DR1 demonstrate the existence of two distinct mechanisms at the origin of matter migration phenomena. One is the mechanism observed in sol-gel Si-DR1 thin films, which is governed by the light polarization pattern. The other one does not exist in sol-gel Si-DR1 but prevails in our PMMA-DR1 material. Our results show that it is related to the light intensity pattern and it is well described by a statistical migration process, along the molecule dipole axis. Although it is governed by the intensity pattern, the efficiency of this mechanism depends also on the polarization through the absorption anisotropy of the molecules.

3.6 Conclusions

In this chapter we have studied in detail the relationship between the spatial distribution of the light field and the photodeformation in azo-containing sol-gel and PMMA matrices.

The early stage of the deformation corresponds to matrix photoexpansion which is known to be related to the increase in the free volume necessary for the free isomerization of the azobenzene molecules. We have studied independently the plastic and the elastic contributions of the deformation due to photoexpansion and we have determined their characteristic time constants and relative amplitudes.

The subsequent photomechanical response of the material corresponds to lateral matter migration. The microscopic origin of the mass transport is still debated. Several models have been proposed to describe the experimental observations. Some are based on the statistical direction displacement of molecular entities which is proportional to the photoisomerization rates, others consider the response of the material to the electromagnetic force which depends on the light polarization pattern. Our experiments demonstrate that both kinds of mechanisms coexist with relative efficiencies that depend on the host matrix and on the illumination conditions.

In sol-gel Si-DR1 thin films the matter migration efficiency is fully governed by the polarization pattern. The deformation efficiency is maximum for a pure polarization pattern while no mass transport arises in a pure intensity pattern. The matter transport always points from a field component parallel to the intensity gradient, towards a field component perpendicular to the intensity gradient. It can be reversed by switching the spatial polarization distribution.

In PMMA-DR1 thin films we have evidenced two mechanisms: the one that depends on the polarization pattern as observed in sol-gel Si-DR1 films and another one which is driven by the intensity pattern and is not present in silica matrix.

The study of the mass transport efficiency as a function of the relative weight of the intensity and polarization patterns allows us to determine the contribution of both mechanisms to the photomechanical response of the materials. Our results demonstrate the origins of the mass transport directionality. They provide a coherent explanation for photoindued deformation phenomena previously reported in the far and in the near field, which were often considered as contradictory.

Note that in all the analysis of our results we have only considered the initial deformation rate as the relevant experimental characteristic of the mass transport process. A complete analysis would require to take into account also the whole kinetics including the maximum deformation value that can be reached. However, the interpretation of the mass transport saturation is a very complex problem. Indeed, several factors

contribute to limit the SRG growth. First, the sample thickness determines the available matter that can be transported. Moreover, after each photoisomerization cycle the molecular re-orientation away from the electric field reduces the absorption probability (phenomenon known as *angular hole burning*[30]). The exposure time is also an important factor, since the probability of molecular photobleaching increases with the doses. Finally, the interplay between the statistical and the polarization mechanisms may give an important contribution to the deformation saturation. Further investigations are required to address this issue, which remains an open question.

[30] See 1.2.4.

Bibliography

[1] Almeria Natansohn and Paul Rochon. Photoinduced motions in azo-containing polymers. *Chemical Reviews*, 102(11):4139–4176, 10 2002. URL http://dx.doi.org/10.1021/cr970155y.

[2] Kevin G. Yager and Christopher J. Barrett. Novel photo-switching using azobenzene functional materials. *Journal of Photochemistry and Photobiology A: Chemistry*, 182(3):250 – 261, 2006. ISSN 1010-6030. doi: DOI:10.1016/j.jphotochem.2006.04.021. URL http://www.sciencedirect.com/science/article/B6TGY-4K18VSP-1/2/c00807901259cd303aba19c5442fe822. Proceedings of 7th AIST International Symposium on Photoreaction Control and Photofunctional Materials, 7th AIST International Symposium on Photoreaction Control and Photofunctional Materials.

[3] Ke Yang, Suizhou Yang, Xiaogong Wang, and Jayant Kumar. Enhancing the inscription rate of surface relief gratings with an incoherent assisting light beam. *Applied Physics Letters*, 84(22):4517–4519, 2004. doi: 10.1063/1.1757643. URL http://link.aip.org/link/?APL/84/4517/1.

[4] N. Landraud, J. Peretti, F. Chaput, G. Lampel, J. P. Boilot, K. Lahlil, and V. I. Safarov. Near-field optical patterning on azo-hybrid sol-gel films. *Applied Physics Letters*, 79(27):4562–4564, December 2001.

[5] S. P. Bian, J. M. Williams, D. Y. Kim, L. A. Li, S. Balasubramanian, J. Kumar, and S. Tripathy. Photoinduced surface deformations on azobenzene polymer films. *Journal Of Applied Physics*, 86(8):4498–4508, October 1999.

[6] Nirmal K. Viswanathan, Srinivasan Balasubramanian, Lian Li, Sukant K. Tripathy, and Jayant Kumar. A detailed investigation of the polarization-dependent surface-relief-grating formation process on azo polymer films. *Japanese Journal of Applied Physics*, 38(Part 1, No. 10):5928–5937, 1999. doi: 10.1143/JJAP.38.5928. URL http://jjap.ipap.jp/link?JJAP/38/5928/.

[7] N. K. Viswanathan, D. Y. Kim, S. P. Bian, J. Williams, W. Liu, L. Li, L. Samuelson, J. Kumar, and S. K. Tripathy. Surface relief structures on azo polymer films. *Journal Of Materials Chemistry*, 9(9):1941–1955, September 1999.

[8] K. Yang, S. Z. Yang, and J. Kumar. Formation mechanism of surface relief structures on amorphous azopolymer films. *Physical Review B*, 73(16):165204, April 2006.

[9] D. Garrot, Y. Lassailly, K. Lahlil, J. P. Boilot, and J. Peretti. Real-time near-field imaging of photoinduced matter motion in thin solid films containing azobenzene derivatives. *Applied Physics Letters*, 94(3):033303, 2009. doi: 10.1063/1.3073742. URL http://link.aip.org/link/?APL/94/033303/1.

[10] O. Henneberg, Th. Geue, M. Saphiannikova, U. Pietsch, A. Natansohn, P. Rochon, and K. Finkelstein. Investigation of material flow on inscribing a polymer surface grating probing x-ray and vis light scattering. *Colloids and Surfaces A: Physicochemical and Engineering Aspects*, 198-200:107–111, 2 2002. URL http://www.sciencedirect.com/science/article/B6TFR-454JBTJ-H/2/38ea38366b3f32725df1c36aec2d7c14.

[11] Oleh M. Tanchak and Christopher J. Barrett. Light-induced reversible volume changes in thin films of azo polymers: The photomechanical effect. *Macromolecules*, 38(25):10566–10570, 11 2005. URL http://dx.doi.org/10.1021/ma051564w.

[12] Daisuke Barada, Takashi Fukuda, Masahide Itoh, and Toyohiko Yatagai. Numerical analysis of photoinduced surface relief grating formation by particle method. *Optical Review*, 12(4):271–273, 07 2005. URL http://dx.doi.org/10.1007/s10043-005-0271-z.

[13] Md. Zahangir Alam, Tomoko Ohmachi, Tomonari Ogata, Takamasa Nonaka, and Seiji Kurihara. Photoisomerization behavior and photoinduced surface relief gratings on azopolymer film by a monochromatic light irradiation. *Optical Materials*, 29(4):365 – 370, 2006. ISSN 0925-3467. doi: DOI:10.1016/j.optmat.2005.10.005. URL http://www.sciencedirect.com/science/article/B6TXP-4HWXP03-1/2/a147cc79fda983a71b38c57eca1896f8.

[14] Masahide Itoh, Kenji Harada, Shun ichi Kamemaru, and Toyohiko Yatagai. Holographic recording on azo-benzene functionalized polymer film. *Japanese Journal of Applied Physics*, 43(7B):4968–4971, 2004. doi: 10.1143/JJAP.43.4968. URL http://jjap.ipap.jp/link?JJAP/43/4968/.

[15] Damien Garrot. *PhD Thesis: Etude par microscopie en champ proche des phénomènes de migration de matière photo-induite dans les matériaux photochromiques*. Ecole Polytechnique, 2006.

[16] Ke Yang, Suizhou Yang, Xiaogong Wang, and Jayant Kumar. Response to "comment on 'enhancing the inscription rate of surface relief gratings with an incoherent assisting light beam' " [appl. phys. lett. [bold 86], 146101 (2005)]. *Applied Physics Letters*, 86(14):146102, 2005. doi: 10.1063/1.1899756. URL http://link.aip.org/link/?APL/86/146102/1.

[17] S. Bian, L. Li, J. Kumar, D. Y. Kim, J. Williams, and S. K. Tripathy. Single laser beam-induced surface deformation on azobenzene polymer films. *Applied Physics Letters*, 73(13):1817–1819, 1998. doi: 10.1063/1.122292. URL http://link.aip.org/link/?APL/73/1817/1.

[18] Bert Hecht and Lukas Novotny. *Principles of Nano-Optics*. Cambridge University Press, NY, 2006.

[19] Yann Gilbert, Renaud Bachelot, Pascal Royer, Alexandre Bouhelier, Gary P. Wiederrecht, and Lukas Novotny. Longitudinal anisotropy of the photoinduced molecular migration in azobenzene polymer films. *Opt. Lett.*, 31(5):613–615, 2006. URL http://ol.osa.org/abstract.cfm?URI=ol-31-5-613.

[20] T. Grosjean and D. Courjon. Photopolymers as vectorial sensors of the electric field. *Optics Express*, 14(6):2203–2210, 2006.

[21] Nathalie Landraud. *Ph.D. Thesis: Nanostructuration optique de films sol-gel photochromiques par microscopie en champ proche*. Ecole Polytechnique, 2002.

[22] S. Patane, A. Arena, M. Allegrini, L. Andreozzi, M. Faetti, and M. Giordano. Near-field optical writing on azo-polymethacrylate spin-coated films. *Optics Communications*, 210(1-2):37 – 41, 2002. ISSN 0030-4018. doi: DOI:10.1016/S0030-4018(02)01764-9. URL http://www.sciencedirect.com/science/article/B6TVF-46DM01B-1/2/8b0232f74db3ef8025b362e10902392d.

[23] Renaud Bachelot, Fekhra H'Dhili, Dominique Barchiesi, Gilles Lerondel, Radouane Fikri, Pascal Royer, Nathalie Landraud, Jacques Peretti, Frederic Chaput, Georges Lampel, Jean-Pierre Boilot, and Khalid Lahlil. Apertureless near-field optical microscopy: A study of the local tip field enhancement using photosensitive azobenzene-containing films. *Journal of Applied Physics*, 94(3):2060–2072, 2003. doi: 10.1063/1.1585117. URL http://link.aip.org/link/?JAP/94/2060/1.

[24] R. Bachelot, A. Bouhelier, G. Wiederrecht, Y. Gilbert, L. Novotny, and P. Royer. Longitudinal sensitivity of the photoinduced molecular migration in azobenzene-containing films. *Proceedings of the SPIE - The International Society for Optical Engineering*, 6335:63350E–1–9, 2006.

[25] P. Lefin, Fiorini C., and Nunzi J-M. Anisotropy of the photo-induced translation diffusion of azobenzene dyes in polymer matrices. *Pure and Applied Optics: Journal of the European Optical Society Part A*, 7:71–82(12), 1998. URL http://www.ingentaconnect.com/content/iop/pao/1998/00000007/00000001/art00011.

[26] Christopher J. Barrett, Almeria L. Natansohn, and Paul L. Rochon. Mechanism of optically inscribed high-efficiency diffraction gratings in azo polymer films. *The Journal of Physical Chemistry*, 100(21):8836–8842, 05 1996. URL http://dx.doi.org/10.1021/jp953300p.

Chapter 4

Photomechanical response of hybrid metal/azo-polymer layered structures

Viswanathan and co-workers have shown that the photoinduced deformation in azo-containing thin films can be inhibited if a non-optically-active thin polymeric layer having a thickness of only 20 nm is deposited on the photochromic film surface [1]. In this chapter, we study the photomechanical response of layered structures where the photochromic thin film is covered by a metallic thin layer. We will explore both far-field and near-field effects and we will show that a photodeformation process occurs through the whole hybrid structures, which exhibits specific characteristics when compared to the uncoated photochromic material.

4.1 Far field photomechanical response of hybrid metal/azo-polymer layered structures

In this section, we study the formation of SRG under excitation with an interference pattern in two types of systems: a sol-gel Si-DR1 film having a thickness of 200 nm coated with a 20 nm-thick gold layer and a PMMA film having a thickness of 180 nm coated with a 20 nm-thick gold layer. The photochromic thin films have been prepared as described in **Chapter 2**. The gold thin layers have been evaporated on top of the photochromic films under vacuum at room temperature.

In **Figure 4.1** we show the topography and optical characterization of the two hybrid systems. We report for each system a 5×5 μm topography image (top) obtained by

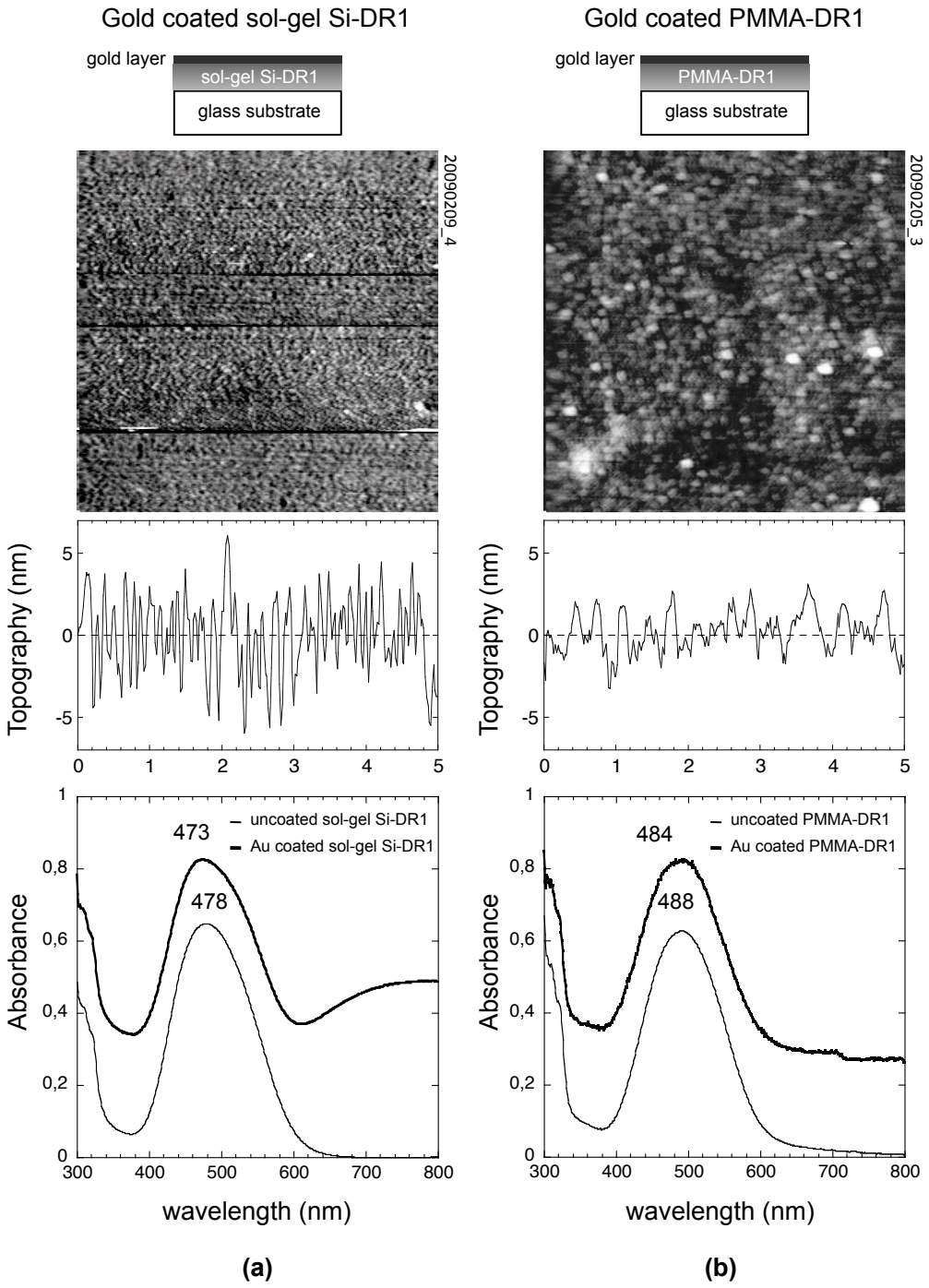

FIGURE 4.1: Hybrid systems: (a) sol-gel Si-DR1 ($\simeq 200\ nm$ thick), coated with a 20 nm layer of gold; (b) PMMA-DR1 ($\simeq 180\ nm$ thick), coated with a 20 nm layer of gold: shear-force topography image $5 \times 5\ \mu m$ (top) and the corresponding profile (middle); bottom: absorbance of the uncoated (hair curve) and coated (bold curve) materials.

shear-force microscopy, the characteristic surface roughness (middle) and the absorption spectra before (hair curve) and after (bold curve) the gold coating.
The metal layer deposited on the sol-gel sample has a roughness of about 2 nm RMS, and a grain lateral size of about 20 nm. The metal layer deposited on the PMMA film has a roughness slightly smaller of about 1 nm RMS, and a grain lateral size of about 80 nm. The absorption spectra of the coated samples exhibit the contribution of both the photochromic film and the gold layer.

4.1.1 Gold coated sol-gel Si-DR1

In **Figure 4.2** we show the photodeformation obtained under s- and p-polarized interfering beams ($\lambda = 473$ nm, beam power density: 1 mW/mm^2) on a sol-gel Si-DR1 sample coated with gold. In (a-b) we show the optical and topography images (256 $\times$ 256 pixel) recorded over an area of 5 $\times$ 5 μm under s-polarized light, while in (c) we plot the average transmitted light T (top) and the observed deformation amplitude A (bottom, solid curve) corresponding to (a-b), where the dotted curve indicates the photodeformation obtained on an uncoated sol-gel Si-DR1 of similar thickness as the sol-gel Si-DR1 film constituting the hybrid system. The same is shown in (d-f) in the case of p-polarized light.

For the s-polarization (a-c), as shown in **Chapter 3**, we expect a weak deformation *in phase* with the bright fringes consequent to the matrix photoexpansion in the enlightened zones. Instead, we observe no surface deformation. Under p-polarized light (d-f) we do not observe the usual short-time deformation regime *in phase* with the illumination. This indicates that the gold coating inhibits the matrix photoexpansion.
However, under p-polarized light (d-f), we still observe a deformation in $\pi - phase$ with the interference pattern, which we identify with the mass migration from the $\vec{E}_{\parallel}$ field component towards the $\vec{E}_{\perp}$ field component. In **Figure 4.2**(f) the deformation amplitude induced by mass migration for the gold coated film (solid curve) is compared to the deformation observed on the uncoated film (dotted curve). We note that for the first 400 s both samples have the same deformation kinetics, with an initial deformation rate of 0.13 nm/s. Then, we observe a smaller saturation value (54 nm) at 800 s in the case of the coated system, while the uncoated system has grown up to 80 nm in the same time, reaching a saturation value of 105 nm in about 1200 s.

These observations indicate that the gold coating reduces by about a factor of two the photodeformation but does not inhibit the mass transport.

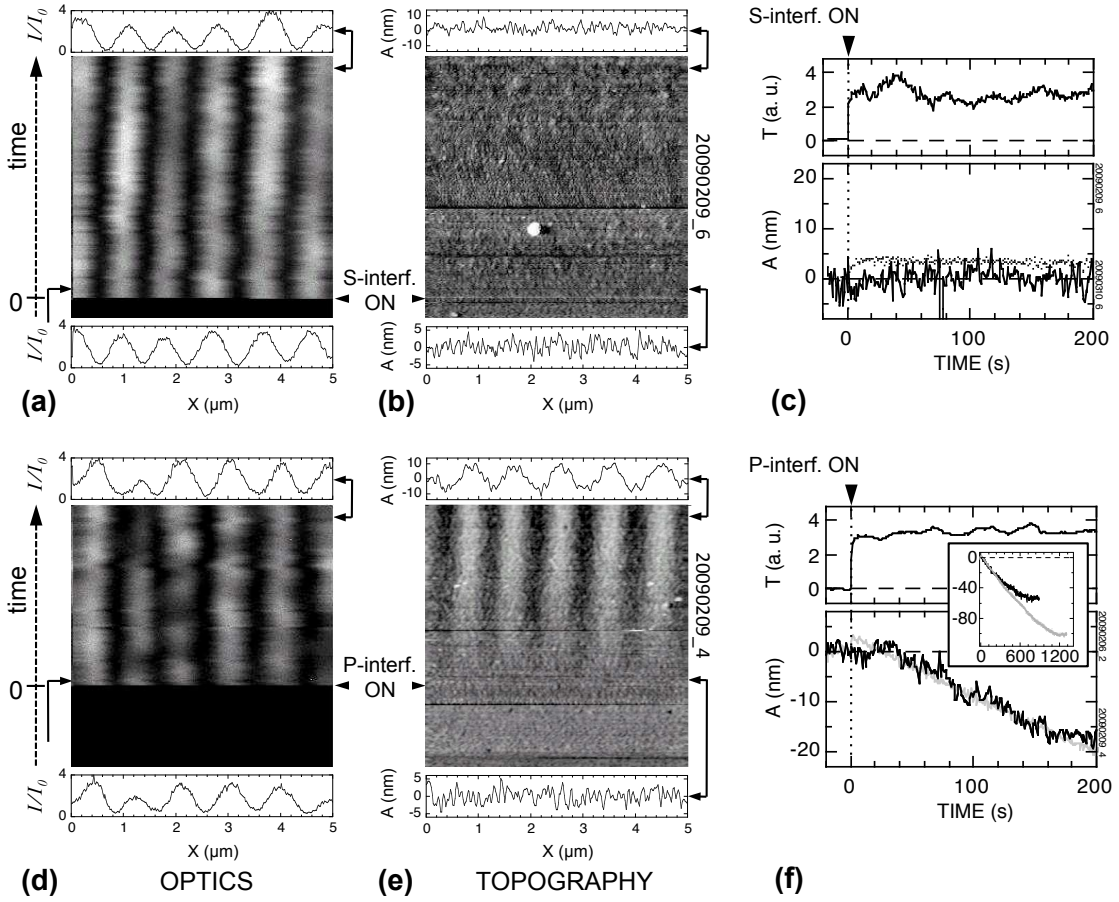

FIGURE 4.2: Photodeformation under interfering beams of a gold coated sol-gel Si-DR1. (a-c): *s*-polarized light, (a-b) optical and topography images (256 × 256 pixel) recorded over a 5×5 μm area, (c) plot of the average transmitted light T in arbitrary units (top) and of the deformation amplitude (bottom, solid curve) as a function of time. The dotted curve indicates the deformation obtained without the gold coating. (d-f): same, for *p*-polarized light. The laser wavelength is $\lambda = 473$ nm and each beam has a power density of 1 mW/mm^2. The sample is a sol-gel Si-DR1 film ($\simeq 200$ nm thick), coated with a 20 nm layer of gold.

4.1.2 Gold coated PMMA-DR1

In **Figure 4.3** we show the photodeformation obtained in the case of a PMMA-DR1 sample coated with gold, in the same working conditions as in 4.1.1. Under *s*-polarized light (a-c) and *p*-polarized light (d-f) we cannot measure any *in-phase* deformation when the light is turned on[1]. Instead, we clearly observe a $\pi-phase$ deformation corresponding to matter migration which, under both polarizations, is very similar to the deformation obtained in an uncoated sample (dotted curves in (c) and (f)). Similarly to what we have observed with uncoated samples, matter migration is governed by the intensity pattern for both polarizations.

[1]Perhaps a very weak deformation is observed at $t = 0$ under *p*-polarized light.

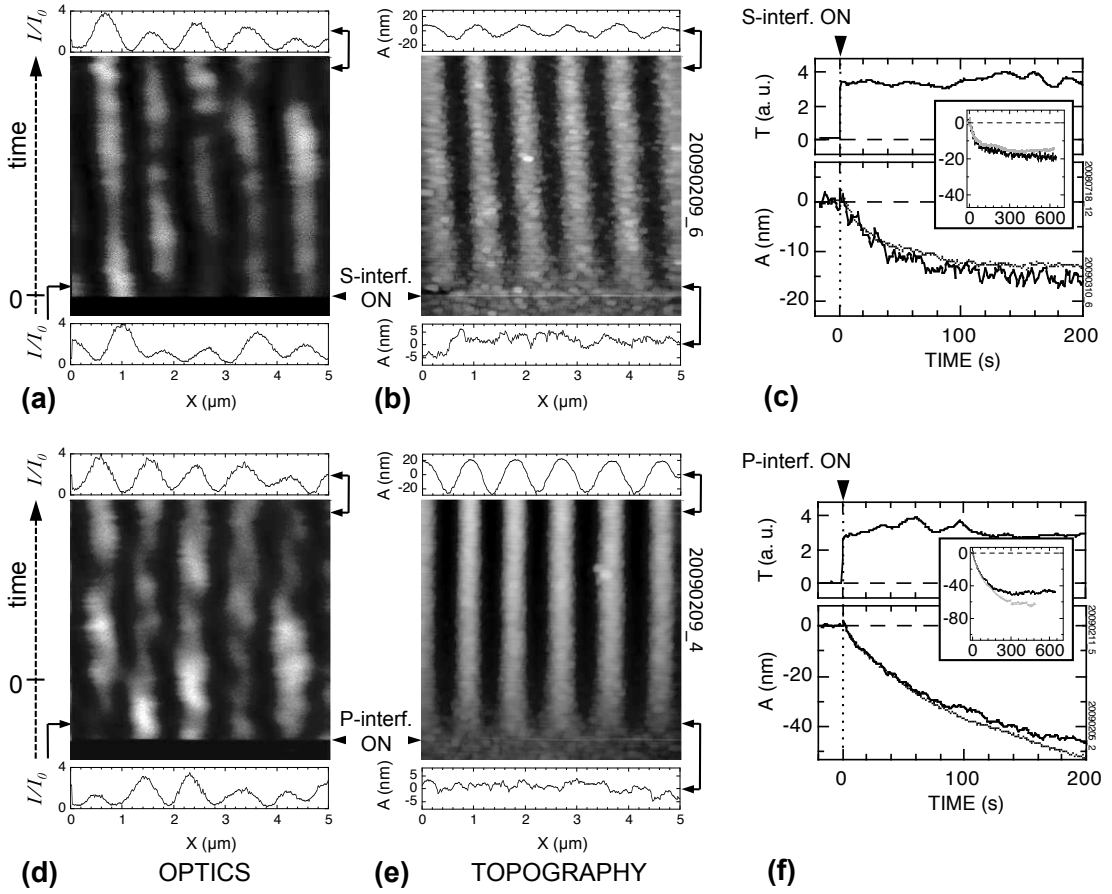

FIGURE 4.3: Photodeformation under interfering beams of gold coated PMMA-DR1. (a-c): *s*-polarized light, (a-b) optical and topography images (256 × 256 pixel) recorded over a $5 \times 5\ \mu m$ area, (c) plot of the average transmitted light T in arbitrary units (top) and of the deformation amplitude (bottom, solid curve) as a function of time. The dotted curve indicates the deformation obtained without the gold coating. (d-f): same, for *p*-polarized light. The laser wavelength is $\lambda = 473\ nm$ and each beam has a power density of 1 mW/mm^2. The sample is a PMMA-DR1 film ($\simeq 180\ nm$ thick), coated with a 20 nm layer of gold.

As obtained for the sol-gel Si-DR1 coated system, we find that under *p*-polarized light, the maximum deformation amplitudes are less than in the uncoated system. We measure a maximum value of 50 nm after about 300 s of exposure, while in the uncoated case we have 60 nm after the same irradiation time. Instead, under *s*-polarized light the curves almost coincide and reach a saturation amplitude of 16 (uncoated) and 18 (coated) nm in 400 s.

In **Figure 4.4** we show the comparison, in the same irradiation conditions, between the coated and uncoated systems, for both photochromic films, exposed to *s*-, *p*- and orthogonally 45°polarized light. As seen above, we note that the matter migration rate in the coated systems are similar for short time scales, while the deformation in the uncoated system tends to reach larger amplitudes for long exposure time. We also

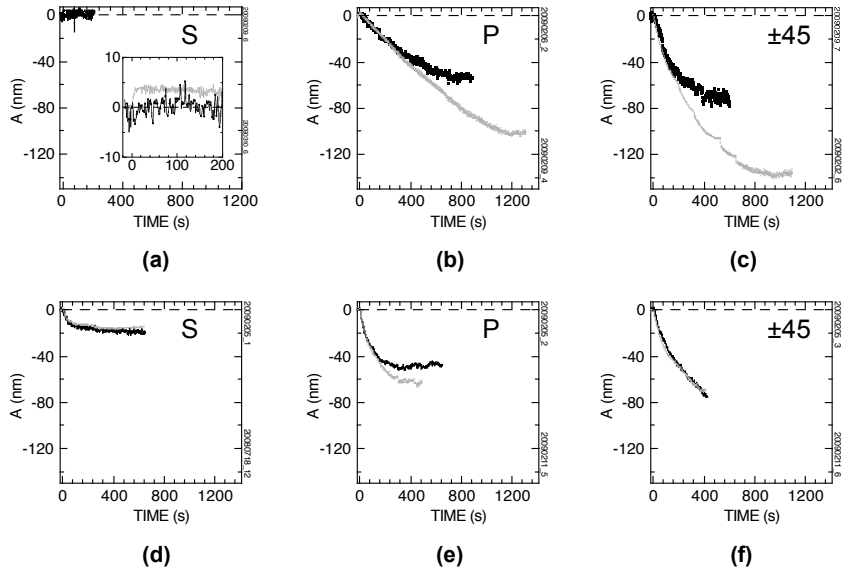

FIGURE 4.4: Polarization effect on the photodeformation of hybrid systems: gold coated sol-gel Si-DR1 and PMMA-DR1. Dark curves = coated systems; grey curves = uncoated systems. (a-c) Photochromic film = sol-gel Si-DR1 ($\simeq$ 200 nm thick): (a) s-polarized intererence (b) p-polarized intererence, (c) orthogonally 45°polarized interference; (d-f) Photochromic film = PMMA DR1 ($\simeq$ 180 nm thick): (d) s- polarized interference, (e) p-polarized interference, (f) orthogonally 45°polarized interference. Laser (blue, $\lambda = 473$ nm) power density: 1 mW/mm^2 per beam.

note that in the case of a PMMA-DR1 film the discrepancy between the deformation amplitude for the coated and uncoated systems is less than in the case of the sol-gel Si-DR1 film, which could indicate a higher deformability of the organic matrix.
It is interesting that the deformation amplitude induced in the sol-gel coated system under orthogonally 45°-polarized light is considerably less efficient than in the uncoated case (70 nm versus 120 nm in 600 s), while instead in the PMMA system no difference is observed (70 nm in 400 s).

4.1.3 Discussion

In hybrid metal/azo-polymer layered structures we first observe that photoexpansion is inhibited in the sense that it does not give rise to the formation of a SRG, when projecting an intensity interference pattern. This is an important difference with respect to the behavior observed in uncoated photochromic thin films.
In contrast, although slightly attenuated, the SRG formation due to photoinduced matter migration is not inhibited by the surface coating, with both sol-gel and PMMA

underlying photoactive layers. This is in contradiction with the mass migration inhibition previously reported in layered structures using a polymer coating.

In conclusion, these results suggest that the photoexpansion may be a free-surface initiated process, while the mass transport could be mainly a bulk phenomenon. It seems, thus, that the inhibition of the photoinduced deformation by a coating layer is specific of all-polymer structures. Therefore, the photomechanical patterning of azobenzene-containing materials can be extended to more complex hybrid structures and open new perspectives in the field of nanofabrication.

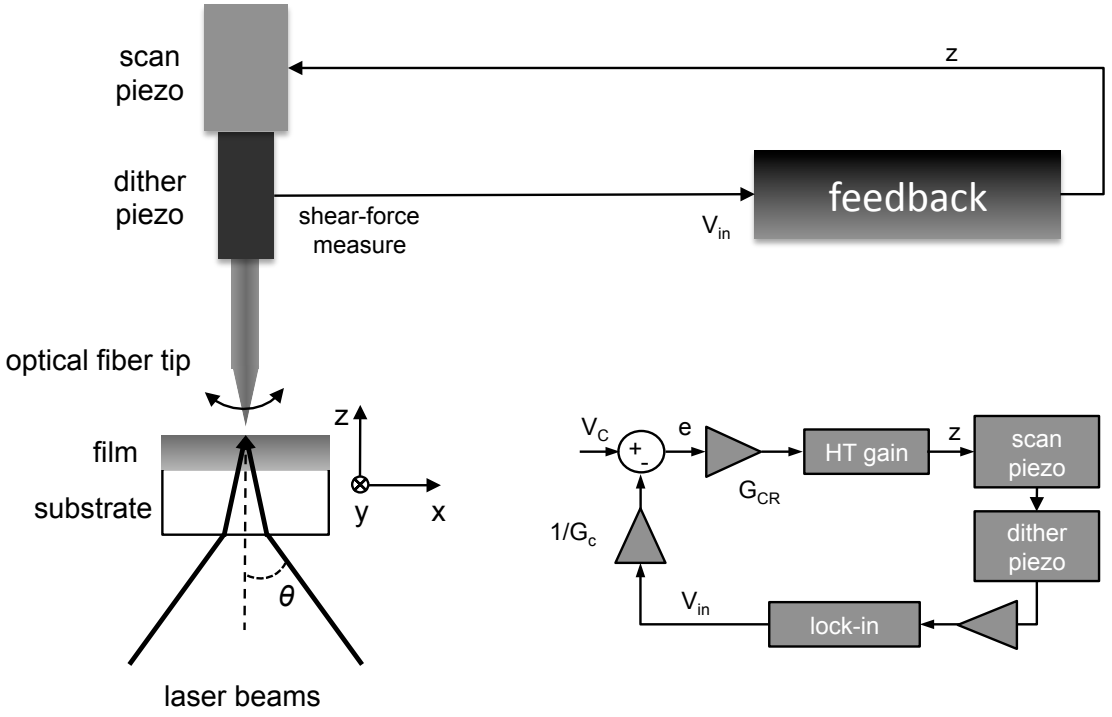

FIGURE 4.5: Tip-sample interactions: experimental setup. Dither piezo: shear-force measurement; (x, y, x) scan piezo: displacement.

4.2 Near-field photomechanical response of hybrid metal/azo-polymer layered structures

In section 3.4.5 we have seen that, in photochromic thin films, near-field irradiation, either in the case of illumination through a small aperture tip [2, 3] or with an aperture-less SNOM tip [4], induces matter accumulation under the light nano-source, where the intensity of the $\vec{E}_\perp$ field component is preponderant. This is coherent with several other observations, under far-field irradiation, of matter accumulation towards the $\vec{E}_\perp$ field components and away from $\vec{E}_\parallel$. However, the interpretation of the near-field photomechanical response of photochromic thin films does not take into account the possible mechanical interaction between the tip and the surface.

In this section we present photodeformation phenomena observed in hybrid metal/azo-polymer layered structures in the presence of a near-field probe. We will show that the photoinduced pattern is completely different from the deformation obtained on an uncoated photochromic film and that the interactions between the local probe and the metallic surface play a predominant role in the deformation process.

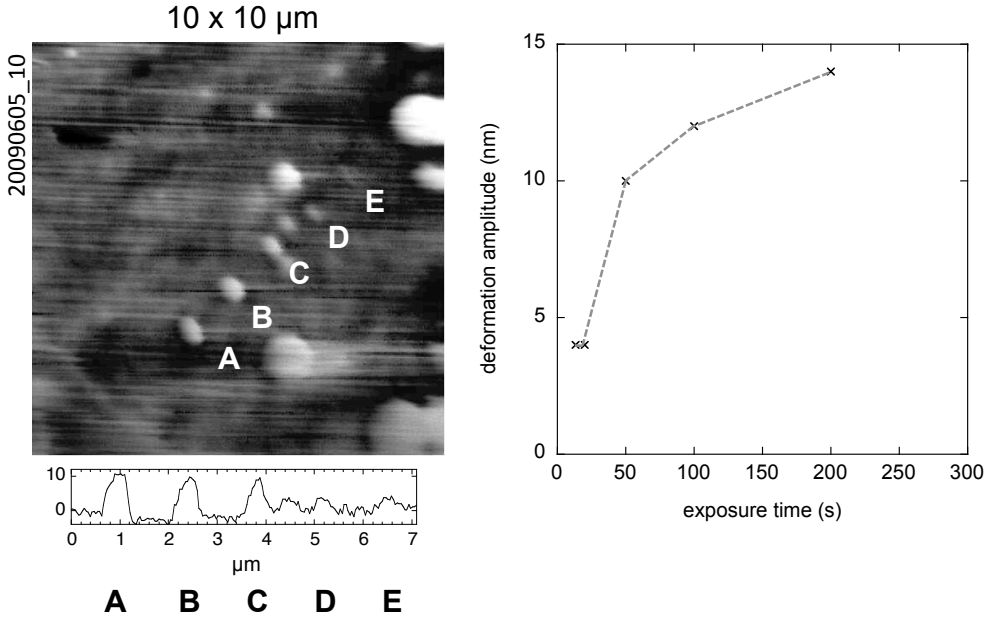

FIGURE 4.6: Apertureless near-field photomechanical effects in a 200 nm thick sol-gel Si-DR1 film: the tip-to-sample distance corresponds to a shear-force set-point of $4V$. Five different exposure times have been used: τ_{exp} = A: 200 s, B:100 s, C:50 s, D:20 s, E: 13 s. The sample is illuminated with a p-polarized single beam of wavelength $\lambda = 473$ nm and of power density 1 mW/mm^2 the incidence angle is $\theta = 16.5°$.

4.2.1 Apertureless near-field photomechanical response of an uncoated azobenzene-containing thin film

Before studying the near-field photomechanical response of the hybrid metal/azo-polymer layered structures we have measured the near-field photodeformation of the uncoated photochromic films when using our optical fiber tip as apertureless light nano-source. We expect to observe a less efficient effect with a glass tip with respect to what previously reported with metallized tips [5], which are known to exhibit enhanced near-field effects.

4.2.1.1 Deformation induced in the tip near-field under uniform illumination

In **Figure 4.6** we show 5 dots (A-E), separated one another by 1.2 μm. Each dot has been obtained by keeping the tip in the same position during illumination with a single p-polarized beam (1 mW/mm^2). The tip-to-sample shear-force interaction amplitude is measured at the lock-in output signal and is kept constant by choosing the set-point through the gain G_C (**Figure 4.5**)[2]. In the present experiment, the set-point was

[2]For more details see **Chapter 2**.

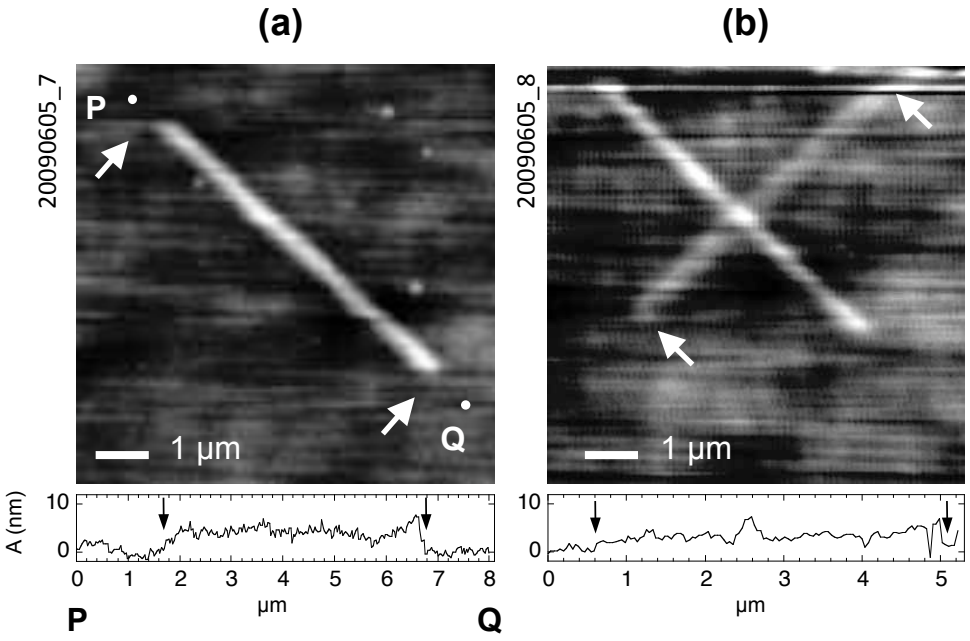

FIGURE 4.7: Photomechanical effects of the tip-sample interactions in a sol-gel Si-DR1 film: strong 4 V interaction, scan on, single beam. (a) exposure time = 200 s under single p-polarized light beam ($1\,mW/mm^2, \lambda = 473\ nm$). Sample = sol-gel Si-DR1, 200 nm thick. (b) Same as in (a), but the single line scan direction is rotated 90°.

4 V, which corresponds to a tip-to-sample distance of $\simeq 1\ nm$. The different dots are obtained with different exposure times τ_{exp}. The deformation amplitude (dot height) increases stiffly for short exposure time and then tends to saturate. This is coherent with what was observed in previous near-field apertureless experiments. Note that in the absence of illumination, no surface deformation is observed, indicating that the tip-sample interaction is not strong enough to induce a mechanical patterning.

When scanning the tip along a line during illumination, in the same experimental conditions (**Figure 4.7**(a)), we observe the growth of a linear relief whose width is equal to the dot size previously obtained (400 nm) and whose length is equal to the scan width of 5 μm. The height of the structure is $\simeq 5\,nm$ for $\tau_{exp} = 250\ s$, which is comparable to the height of a dot obtained after a $\tau_{exp} = 25\ s$. Considering that the lateral size of the dot is 400 nm, which is about 10 times smaller than the line length, it is coherent that a dot and a line of same height are obtained with exposure times that differs by a factor ten.

In figure (b) we show the deformation obtained in the same conditions, but scanning the tip in the perpendicular direction. We see that the photoinduced deformation has almost the same amplitude observed in the first case ($\simeq 3\ nm$) and it has the same width. A 2 nm peak is present at the crossing point of this structure with the one previously

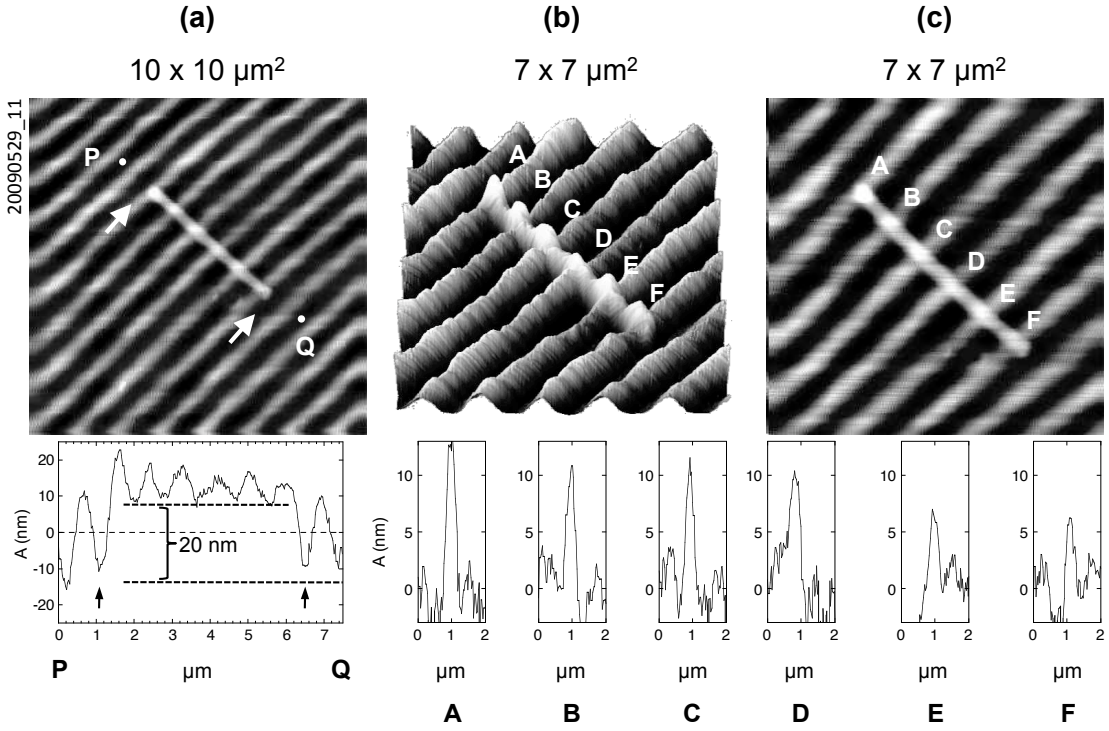

FIGURE 4.8: Photomechanical effects of the tip-sample interactions (4 V) in a sol-gel Si-DR1 film: superstructure on top of the surface gratings. Tip-surface interaction = $4V$. Scanning frequency = 1 Hz, laser: p-polarized interfering beams, 1 mW/mm^2 per beam, $\lambda = 473$ nm. (a-c) scan duration and $\tau_{exp} = 360$ s. Sample = sol-gel Si-DR1, 200 nm thick.

inscribed. This indicates that the deformation is independent from the relative direction of the tip scan and of the illumination polarization.

4.2.1.2 Direct comparison between near-field and far-field deformation effects

In order to compare directly the near-field and the far-field photodeformation effects we expose the sample to a p-polarized interference pattern and at the same time we scan the tip in shear-force interaction with the surface, along a direction perpendicular to the interference intensity gradient.

We perform this experiment using the same experimental conditions as in 4.2.1.1 (scan width of 5 μm, shear-force interaction amplitude of 4 V), except that the p-polarized illumination is no longer uniform, but exhibits both an intensity and a polarization spatial modulation. In **Figure 4.8**(a-c) we show the photodeformation effects obtained with $\tau_{exp} = 360s$. We observe the formation of a linear super-structure perpendicularly to the 20 nm high SRG induced by the interference pattern. Its profile shows that the

linear structure length is 5 μm (indicated by the two arrows), which corresponds to the tip scan width. A 20 nm high matter accumulation is present within the SRG grooves, while on top of the reliefs 6 peaks (A-F) are formed. Their exceeding height is between 5 and 10 nm, while their width is $\simeq 400\,nm$.
We can distinguish the far-field induced deformation from the near-field tip induced photodeformation effect. As shown in **Figure 4.9**(a), the surface profile a_{far} in the absence of the tip during illumination takes the form:

$$a_{far}(x) = A^0_{far}\phi(x) \tag{4.1}$$

where A^0_{far} is the amplitude of the SRG formed with the far-field interference illumination and $\phi(x)$ is the periodic function corresponding to the spatial modulation (i.e. $cos^2(k_x x)$ or $sin^2(k_x x)$ in our case).
In **Figure 4.9**(b), we plot the surface profile a_{line} obtained with the tip scanning near the surface during illumination, which takes the form:

$$a_{line}(x) = A^0_{line}\phi(x) + \bar{a}_{line} \tag{4.2}$$

where, A^0_{line} is the amplitude of the SRG formed under the tip and $\bar{a}_{line}$ is the average contribution of the tip near field to the deformation. The deformation measured under the scanning tip corresponds to the superimposition of a far-field effect and the tip effect:

$$a_{line}(x) = a_{far}(x) + a_{tip}(x) \tag{4.3}$$

From eq. 4.1, 4.2 and 4.3 we can extract the deformation effects due to the presence of the tip as:

$$a_{tip}(x) = a_{line}(x) - a_{far}(x) = \bar{a}_{line} + \left(A^0_{line} - A^0_{far}\right)\phi(x) \tag{4.4}$$

The tip induced deformation is plotted in **Figure 4.9**(c).

Note, first, that, in these experimental conditions, the photodeformation induced in the near field has the same order of magnitude as the far-field photoinduced deformation. Second, it is remarkable that the deformation induced under the tip is opposite to the far-field effect: a_{tip} maxima coincide with $a_{far}(x)$ minima. The tip-induced matter accumulation occurs in both the darker and the brighter fringes of the interference pattern. It is larger in the brighter fringes, which correspond to $\vec{E}_{\parallel}$ maxima, while we

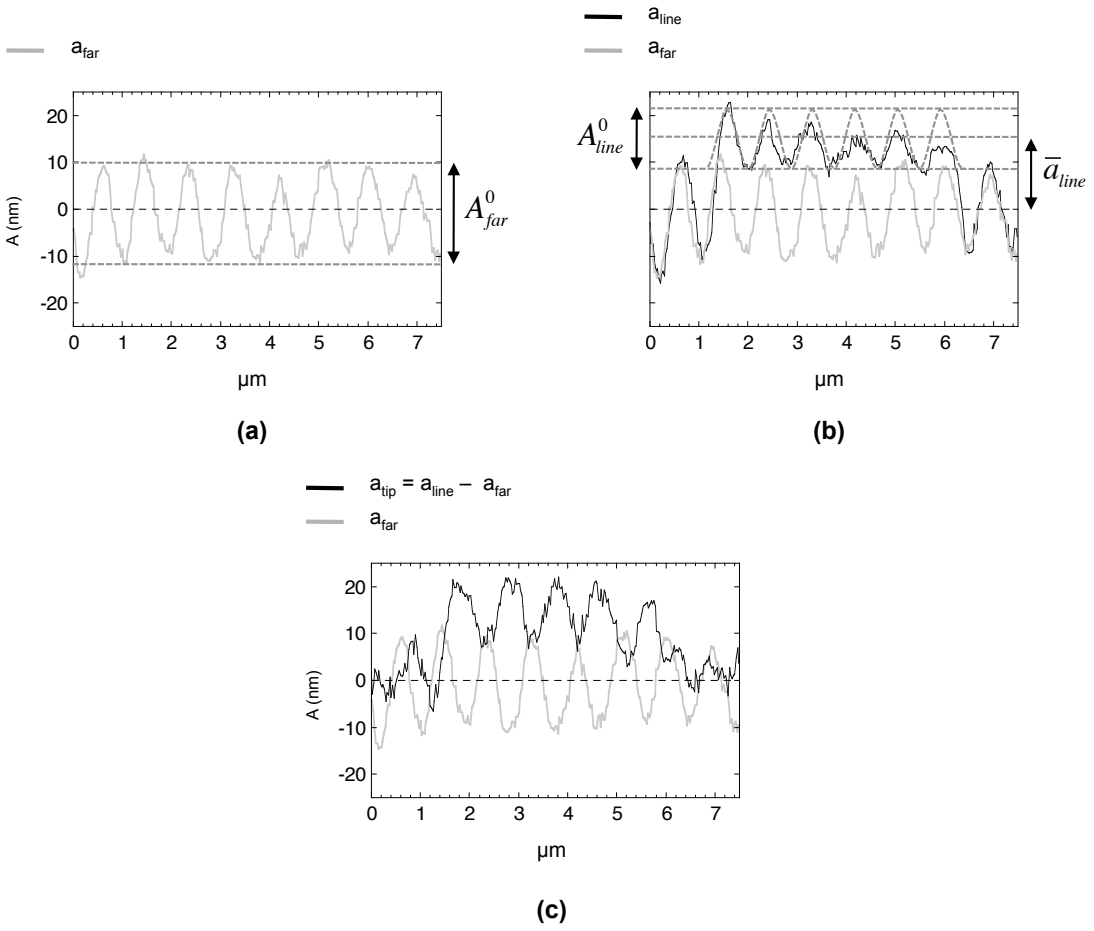

FIGURE 4.9: Photomechanical effects of the tip-sample interactions ($4\ V$) in a sol-gel Si-DR1 film: far-field and near-field photodeformation. $\bar{a}_{line} = 15.6\ nm$, $A^0_{line} = 14.2\ nm$, $A^0_{far} = 20\ nm$.

would have expected an enhancement of the matter accumulation only in the darker fringes, in correspondence of the $\vec{E}_\perp = \vec{E}_z$ field component maxima.

We also calculate the spatial average near-field deformation over a spatial period Λ_s as:

$$\bar{a}_{tip} = \frac{1}{\Lambda_s} \int_0^{\Lambda_s} a_{tip}(x)\, dx \tag{4.5}$$

and we obtain $\bar{a}_{tip} = 12.7\ nm$. This value is coherent with the 5 nm deformation obtained with the same shear-force set point of $4\ V$ but under illumination with a single beam and for a dose about three times smaller (see section 4.2.1.1).

A striking behavior is observed when diminishing the tip-sample shear-force set-point to $2\ V$. In this case (**Figure 4.10**), we still observe the formation of a linear super-structure perpendicular to the photoinduced SRG. The topography cross section between the points P and Q confirms that the profile length coincides with the tip scan width of

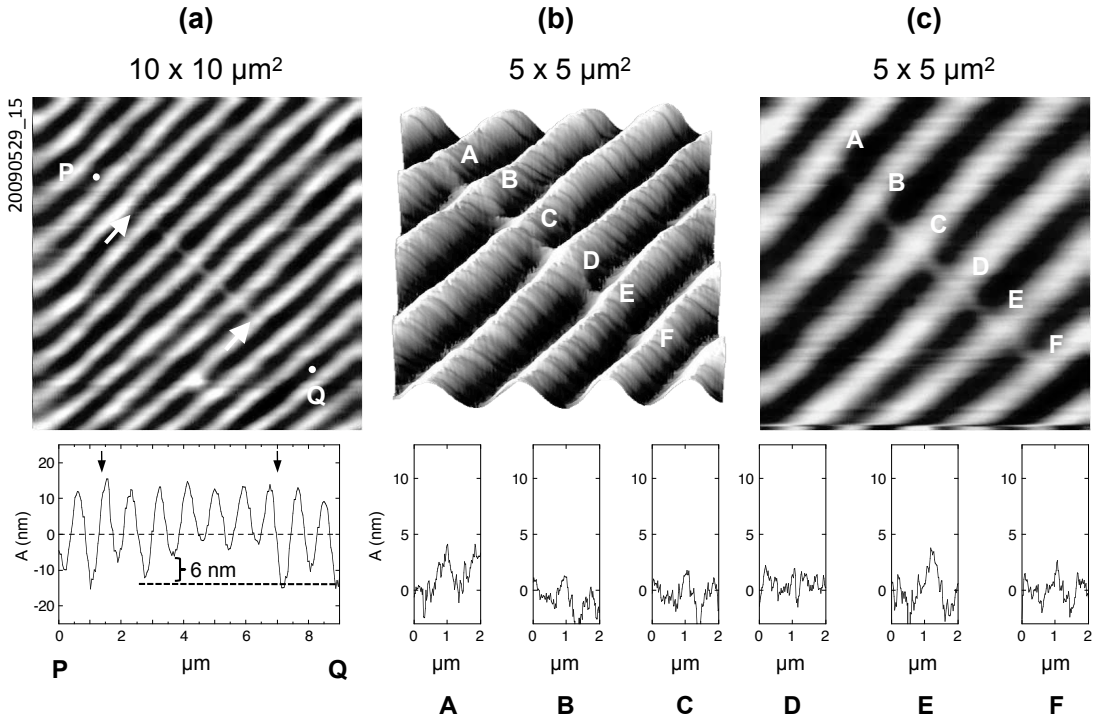

FIGURE 4.10: Photomechanical effects of the tip-sample interactions in a sol-gel Si-DR1 film: superstructure on top of the surface gratings. Interaction amplitude = $2V$, scanning frequency = 1 Hz, τ_{exp} = 600 s, laser = p-polarized interfering beams, 1 mW/mm^2 per beam, $\lambda = 473$ nm. Sample = sol-gel Si-DR1, 200 nm thick.

5 μm (indicated by the two arrows). The structure width of 400 nm is similar to those previously obtained. This structure corresponds to a matter accumulation superimposed onto the 20 nm high SRG. Matter accumulation is clearly more important in the SRG grooves than on top of the SRG reliefs. In **Figure 4.11** we have plotted the tip-induced deformation $a_{tip}(x)$ extracted from the measured profiles $a_{line}(x)$ and $a_{far}(x)$ (see eq. 4.4). The deformation amplitude $\left(A^0_{line} - A^0_{far}\right)$ reaches 6 nm while the average deformation $\bar{a}_{tip}$ due to the near-field interaction is 3.7 nm for 600 s of exposure. These are much smaller values than those obtained with a tip-to-sample shear-force set-point of 4 V for even shorter exposure time. This is very surprising, since when changing the set-point from 4 V to 2 V one only changes the tip-to-sample distance by about 1 nm. This is not likely to induce a significant change in the optical near field, which hardly explains the different photo-deformation amplitude observed. On the other hand, the strong effect of the distance on the near-field photodeformation efficiency could rather be related to the mechanical interaction between the tip and the sample surface.

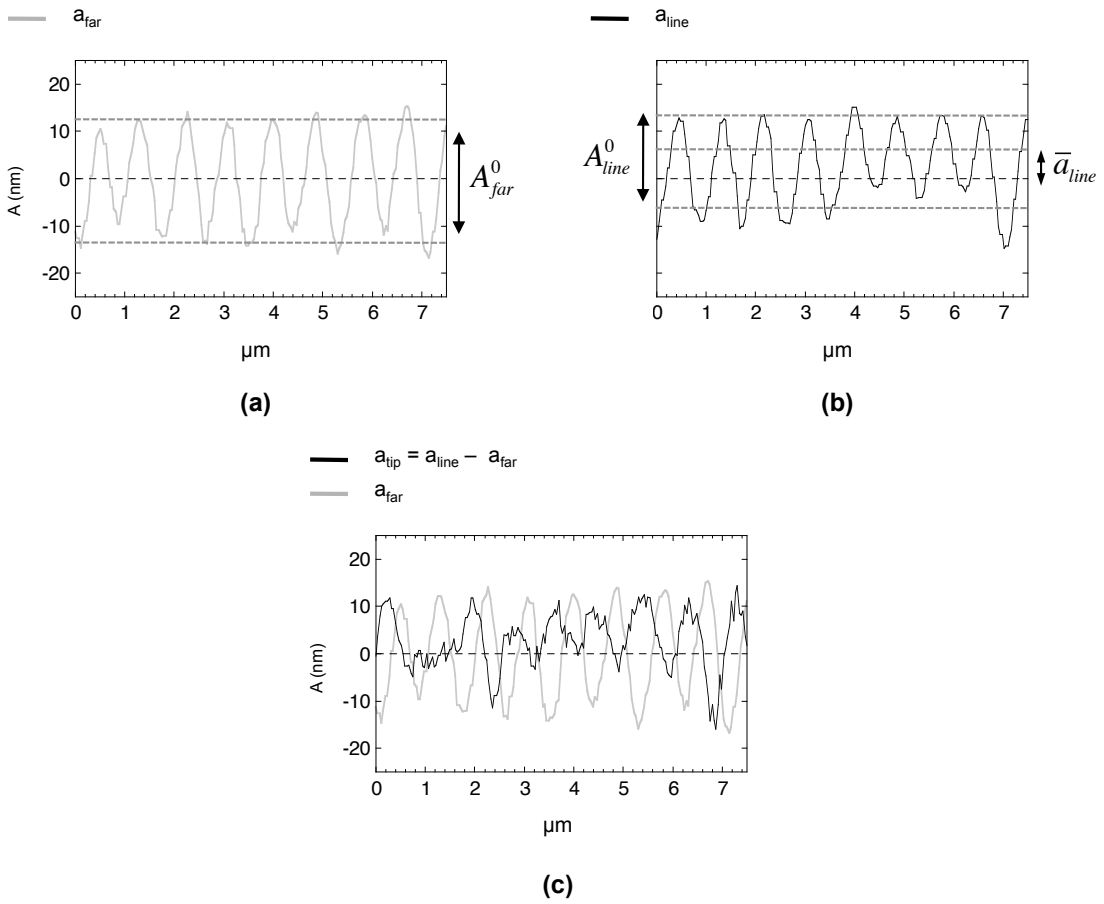

FIGURE 4.11: Photomechanical effects of the tip-sample interactions (2 V) in a sol-gel Si-DR1 film: far-field and near-field photodeformation. $\bar{a}_{line} = 4.5\ nm$, $A^0_{line} = 18.4\ nm$, $A^0_{far} = 20\ nm$.

4.2.1.3 Discussion

We have observed a tip-related near-field photodeformation effect, which can be comparable to the photodeformation induced under far-field illumination. In **Figure 4.12** we summarize the near-field deformation amplitudes observed under p-polarized uniform illumination (a) and the average near-field deformation $\bar{a}_{tip}$ observed under projection of a p-polarized interference pattern (b), for different doses and tip-sample interaction amplitudes. As expected, increasing the dose increases the deformation height, which tends to saturate for high doses (a, ×). However, the near-field effect seems to critically depend on the tip-surface interaction. In particular, the photodeformation strongly varies when changing the tip-to-sample distance by only a few nanometers, which is a too steep behavior to be attributed to a near-field optical effect only.

The irradiation using an interference pattern has shown that the near-field photodeformation is present in both the bright and the dark fringes, while we would have expected

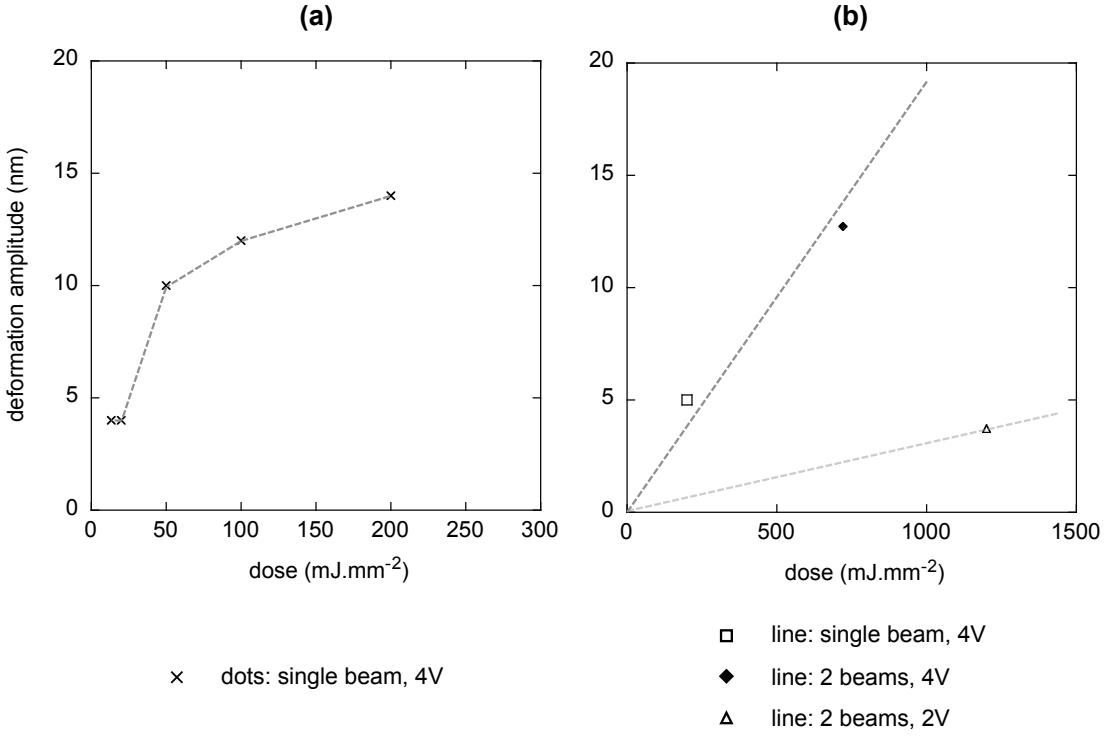

FIGURE 4.12: Photomechanical effects of the tip-sample interactions in a sol-gel Si-DR1 film. Laser ($\lambda = 473\ nm$) power density: 1 mW/mm^2 per beam (interference pattern); 1 mW/mm^2 (single beam). Sample = sol-gel Si-DR1, 200 nm thick. (a) Near-field deformation amplitude under p-polarized uniform illumination (single beam); (b) near-field average deformation under p-polarized interference pattern (2 beams).

only an enhancement of the $\pi - phase$ deformation, in correspondence of the perpendicular field maxima. We could relate this effect to the tip size and geometry, which could change significantly the local distribution of the different light field components. However, we have observed a significant decrease of the photo-deformation when increasing by 1 nm the tip-surface distance, which, on the other hand, doesn't change much the spatial field distribution due to the tip. This indicates that the photo-deformation effect is probably mainly dependent on the mechanical properties of the material under illumination and on the tip-sample mechanical interaction, rather than simply on an optical near-field effect. However, this remains an open question, which requires further investigations.

4.2.2 Apertureless near-field photomechanical response of hybrid metal/azo-polymer layered structures

We study the near-field photoinduced deformation of a hybrid metallic/photochromic layerd structure consisting in a gold layer 20 nm thick evaporated on an azobenzene-containing sol-gel film 200 nm thick, which had been spin-coated over a glass plate (**Figure 4.13**(a)). The study of the far-field photomechanical response of this system has been presented in 4.1.
Performing the single-line scan experiment as described in 4.2.1.2 (scan width = 5 μm, tip-sample shear-force interaction = $4V$), produces the deformation reported in **Figure 4.13**(b). The structure A is obtained after scanning along the same line during 200 s at a frequency of 1.15 Hz in the dark. The structure B is obtained in the same scanning conditions but under exposure to a single p-polarized light beam of power density $1\,mW/mm^2$. We see the remarkable mass depletion of the zone scanned by the tip, which is almost three times deeper when exposing the sample to illumination (B, $15\,nm$) than with no irradiation (A, $5\,nm$), the width of the groove also being larger in B (280 nm) then in A (130 nm). Moreover, we observe a weak matter accumulation around the grooves, which is more evident in B ($4\,nm$) while it is difficult to evaluate in A.

In (c) we report the same experiment, but using different scanning durations. With 80 s we obtain the deformations C (light on) and D (light off) while with 200 s we observe the deformations shown in E (light on) and F (light off). The deformation effect is indeed more efficient under illumination in C ($[depth, width] = [6, 78]$ nm) and E ($[15, 130]$ nm) than with no irradiation in D ($[3, 60]$ nm) and F ($[5, 118]$ nm). Moreover, we observe also in this case the weak matter accumulation on the edges of the deformation in E (4 nm) and F (2 nm), while it is difficult to estimate for C and D.
These results are visualized in **Figure 4.14**, where the values of the deformation depth and width obtained under illumination (□) and without illumination (■) are plotted.

Our observations indicate that also in the case of a hybrid system constituted by a metallic layer on a photochromic thin film, the tip-sample interaction induces a mechanical deformation. Unlike the uncoated sol-gel Si-DR1 film, we observe a depletion of the zone underneath the tip. The deformation amplitude depends on the scan duration and is enhanced under illumination. It seems that matter is mechanically dragged by the tip, while under irradiation the photomechanical effect in the photochromic thin film leads the tip to dig deeper into the gold film.

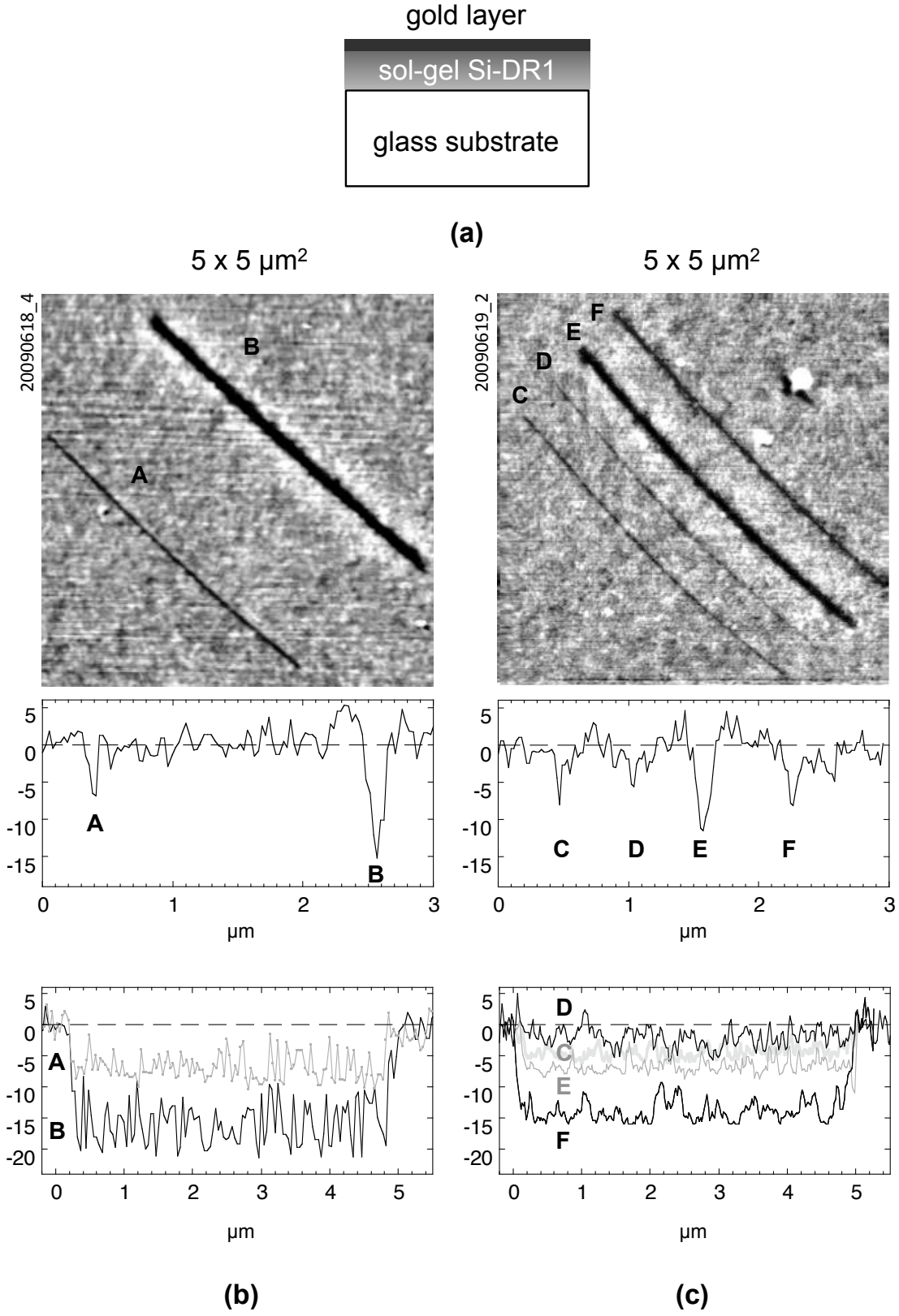

FIGURE 4.13: Hybrid metallic/photochromic layerd structure: 4V tip-sample interaction, influence of the scan duration and of the exposure time. (a) Sample type (b) deformation obtained after 200 s scanning (A) in the darkness and (B) under irradiation; (c) deformation obtained after 80 s (C) under irradiation and (D) in the darkness, and after 200 s (E) under irradiation and (F) in the darkness. Laser: single p-polarized light beam ($1\,mW/mm^2, \lambda = 473nm$). Scan frequency = 1 Hz.

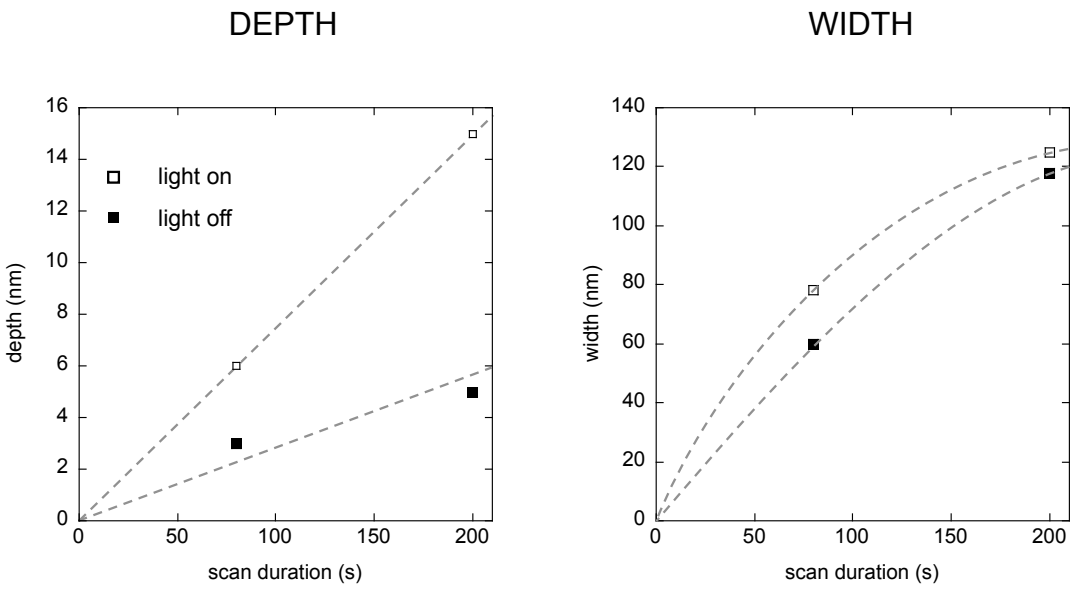

FIGURE 4.14: Hybrid metallic/photochromic layerd structure: 4V tip-sample interaction, influence of the scan duration and of the exposure time. Data measured in the experiment shown in **Figure 4.13**(b): interaction amplitude = 4V, deformation obtained after 200 s: A (light off) and C (light on); after 80 s B (light off) and D (light on). Laser: single p-polarized light beam ($1\,mW/mm^2, \lambda = 473nm$). Scan frequency = 1 Hz.

4.2.2.1 Discussion

The deformation obtained when scanning the tip over the metallic surface increases with the light exposure time. Moreover, a deformation is also observed when scanning the tip in the dark. This deformation is smaller than under illumination, but it also increases when increasing the scanning time.

The dynamic groove deformation obtained in the dark is related to the interaction between the tip and the sample surface and is enhanced when the underlying photochromic layer is optically activated. This suggests that the illumination changes the photomechanical properties of the underlying photochromic film [6], which strongly influences the mechanical effect of the tip on the overlying metallic layer.

4.3 Conclusions

In this chapter we have evidenced local mechanical and photomechanical effects induced by the tip-surface interaction in azo-containing polymer-like thin films and in hybrid metal/azo-polymer layered structures.

In an azo-containing sol-gel sample, we observe the growth of reliefs in the vicinity of the tip, whose height increases with the tip-sample interaction amplitude and with the exposure time. The amplitude of the "near-field" induced deformation can be comparable to the deformation induced under far-field illumination. These phenomena are found to strongly depend on the tip-to-sample distance over the nm range. Such a sharp dependence can not be fully explained by a near-field optical effect and the tip-sample mechanical interaction is found to play a predominant role.
Unexpectedly, when irradiating with a p-polarized interference pattern, the growth of near-field induced reliefs is observed in both the brighter and the darker fringes, which may be related to local polarization effects due to the tip size and geometry, or, more likely, to the tip-sample mechanical interaction.

On a hybrid gold/photochromic layered structure we observe the formation of grooves in the vicinity of the tip, whose dimensions depend mostly on the tip-sample interaction. In this case, the deformation is present also without illumination, which suggests a preponderant mechanical phenomenon. Under illumination the amplitude of the deformation increases, which could be related to the photoinduced softening of the photopolymer underlying the gold layer that allows a deeper indentation of the tip into the sample surface.

The existence of such peculiar local photomechanical effects related to the tip-sample interaction reveals an important issue concerning every local probe experimental technique employed in the study of optical properties of materials, since these techniques can strongly perturb the system.

Bibliography

[1] Nirmal K. Viswanathan, Srinivasan Balasubramanian, Lian Li, Jayant Kumar, and Sukant K. Tripathy. Surface-initiated mechanism for the formation of relief gratings on azo-polymer films. *The Journal of Physical Chemistry B*, 102(31):6064–6070, 07 1998. URL http://dx.doi.org/10.1021/jp981425z.

[2] N. Landraud, J. Peretti, F. Chaput, G. Lampel, J. P. Boilot, K. Lahlil, and V. I. Safarov. Near-field optical patterning on azo-hybrid sol-gel films. *Applied Physics Letters*, 79(27):4562–4564, December 2001.

[3] Nathalie Landraud. *Ph.D. Thesis: Nanostructuration optique de films sol-gel photochromiques par microscopie en champ proche*. Ecole Polytechnique, 2002.

[4] R. Bachelot, A. Bouhelier, G. Wiederrecht, Y. Gilbert, L. Novotny, and P. Royer. Longitudinal sensitivity of the photoinduced molecular migration in azobenzene-containing films. *Proceedings of the SPIE - The International Society for Optical Engineering*, 6335:63350E–1–9, 2006.

[5] Renaud Bachelot, Fekhra H'Dhili, Dominique Barchiesi, Gilles Lerondel, Radouane Fikri, Pascal Royer, Nathalie Landraud, Jacques Peretti, Frederic Chaput, Georges Lampel, Jean-Pierre Boilot, and Khalid Lahlil. Apertureless near-field optical microscopy: A study of the local tip field enhancement using photosensitive azobenzene-containing films. *Journal of Applied Physics*, 94(3):2060–2072, 2003. doi: 10.1063/1.1585117. URL http://link.aip.org/link/?JAP/94/2060/1.

[6] P. Karageorgiev, D. Neher, B. Schulz, B. Stiller, U. Pietsch, M. Giersig, and L. Brehmer. From anisotropic photo-fluidity towards nanomanipulation in the optical near-field. *Nature Materials*, 4(9):699–703, 2005.

Chapter 5

Nanostructured hybrid systems

The photodeformation phenomena observed in azo-containing materials have stimulated a wide variety of possible applications. One of the most studied field is the high density holographic data storage [1–4], by using the photoinduced deformation to record information. Also, light driven actuation has recently drawn great attention, and the demonstration of bending free standing films [5–7] and oscillating micro-cantilevers [8] governed by the polarization of the light has shown the feasibility of this kind of applications. Finally, the nanostructuration obtained using the the photodeformable materials as tools and moulds has been demonstrated to have a great potential in the field of nanofabrication [9, 10].

In this chapter we explore some possible applications of the deformation processes studied in the previous chapters. These applications concern nanostructured hybrid metal/azo-polymer systems. First, we show preliminary results on the displacement of gold nanoparticles deposited on the surface of a photochromic film. Then, we present a large scale parallel nano-patterning experiment based on the combination of optical patterning and of subsequent deposition steps. Finally, we show an attempt to use a nano-structured material obtained with this technique for an experiment of optical pattern transfer.

5.1 Gold nanoparticles

In the previous chapter we have studied the photoresponse of a hybrid metallic/photochromic layered system, consisting in a 40 nm thick gold layer overlying an azobenzene containing photochromic thin film. We have observed that, while inhibiting the photoexpansion deformation, the presence of the gold layer does not prejudice the mass migration mechanisms. An important question is whether the gold layer is also involved

in the transport process. In this case, it would be possible to use the photoinduced mass migration for the displacement of objects present on the surface of the photochromic film. In order to investigate on this point, we have studied the photo-response of a sol-gel Si-DR1 photochromic thin film whose surface was coated with gold nanoparticles.

5.1.1 Gold nanoparticles on a non functionalized photochromic surface

In **Figure 5.1**(a) we show the structures obtained by spin coating, on a sol-gel Si-DR1 free surface, 10 μL of a colloidal solution of gold nanoparticles having a diameter $\phi = 20\ nm$ synthesized using the Turkevitch method [11]. On the surface, most of the nanoparticles coalesce into 2D aggregates, having sizes ranging from 100 nm to 1 μm, and a thickness equal to a single nanoparticle diameter.
The exposure of the sample to p-polarized interfering beams (1 mW/mm^2 per beam, $\lambda = 473\ nm$) leads to the photo-induced deformation of the hybrid system, which is shown in figures **Figure 5.1**(b-e). On the left we report the topographic images showing the time-evolution of the sample topography. In the middle we show the topography profile corresponding to the white dotted line, the small white arrow representing the direction of the cut. In **Figure 5.1**(c) we also report the optical image (right) and the light intensity profile (middle-top). The comparison with the corresponding topography image (left) and profile (middle-bottom) clearly shows that the deformation of the photochromic film in $\pi - phase$ with the bright fringes of the interference pattern, which is in line with our previous findings.
The gold structures follow the surface deformation. As an example, we clearly see the collapsing of some structures into the evolving grooves, indicated by two white arrows on each image (and the corresponding black arrows on the profiles). On the other hand, all the structures that are located in a dark fringe raise up with the relief growth.
However, we do not clearly observe structures located in a bright fringe moving towards a darker one, so we cannot affirm that lateral displacement is observed. This may be due to insufficient resolution, supposing that only small particle displacement could be appreciable, while the relative small movement of big structures is not visible or inhibited. On the other hand, it could indicate that the mass migration is more a bulk than a surface process.
Similar results are obtained using a higher concentration of nanoparticles. In this case **Figure 5.2**(a) we see a more dense aggregation, resulting in a series of gold domains. Exposed to p-polarized interference (b-c), they behave as in the previous case, following the deformation of the surface, in $\pi - phase$ with the bright fringes of the interference pattern. Plotting the profile of the deformation amplitude's time evolution (d,

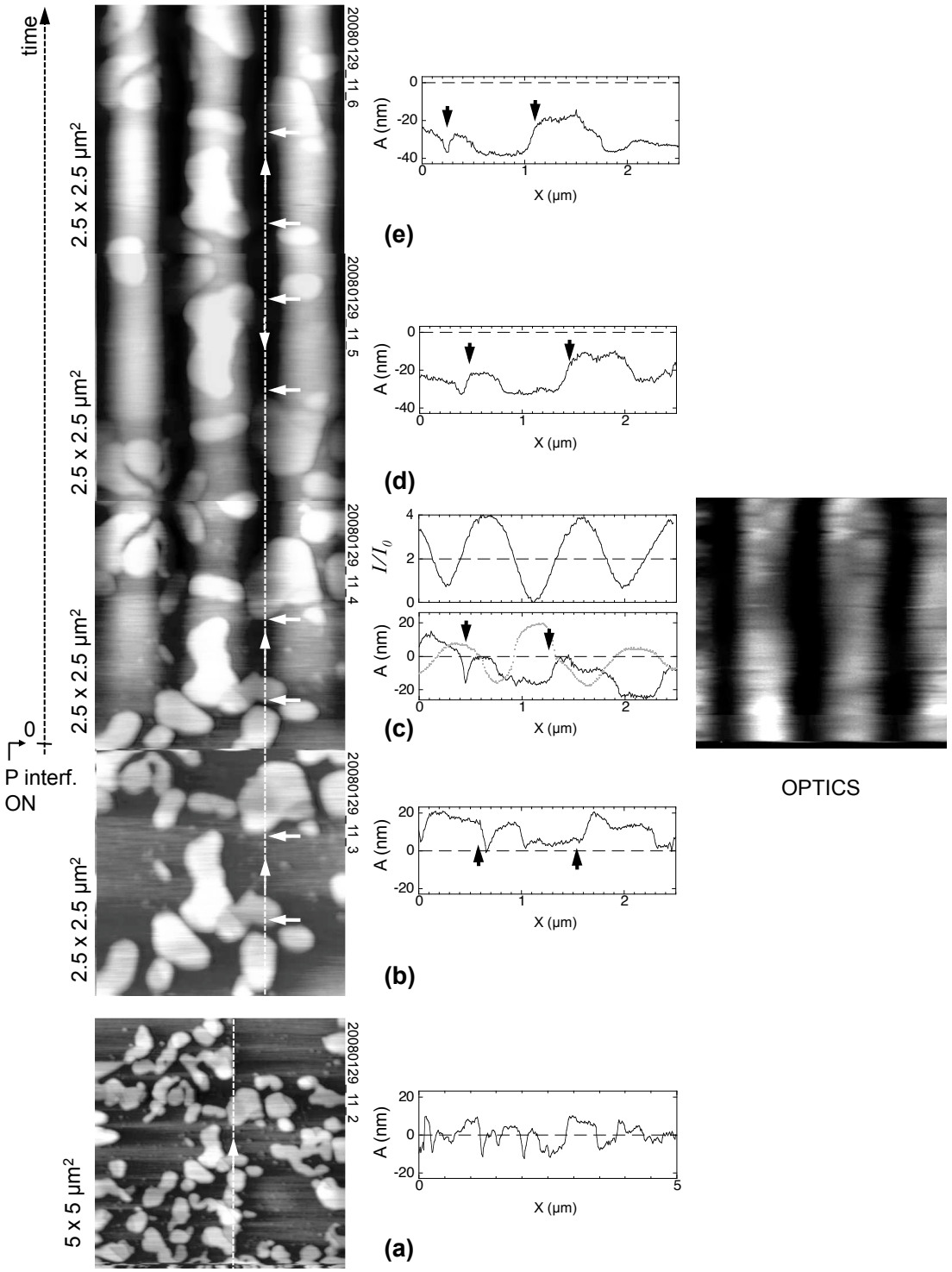

FIGURE 5.1: Gold nanoparticles on sol-gel Si-DR1 ($\simeq 200\ nm$ thick). Particle diameter $= 20 - 30\ nm$. (a) $5 \times 5\ \mu m$ shear-force topography image; (b-e) left side: $2.5 \times 2.5\ \mu m$ topography images during exposure to p-polarized interfering beams; middle: topography profile corresponding to the vertical cut reported in each figure. The optical image is shown for the first 200 s of illumination, in (c), right side. In the middle, we report the optical (top) and topographical (bottom, gray dotted curve) profiles. Note the spatial half-a-period shift between the SRG and the interference pattern. Laser wavelength $= 473\ nm$, power density $= 1\ mW/mm^2$ per beam, incidence angle $= 16.5°$, spatial period $\simeq 830\ nm$.

dark curve) we confirm that the gold domains do not change the mass migration SRG growth, compared to the uncoated case (gray curve).

5.1.2 Particle dispersion and surface functionalization

In order to avoid particle coalescence into bigger structures, it is possible to force them to bind to specific sites on the surface. This can be achieved functionalizing the surface using an amminic layer, which creates $NH - NH$ sites, where gold nanoparticles are trapped.

In **Figure 5.3** we show the results obtained using a 23-(2- aminoethylamino)- propyltrimethoxysilane (AEAPTMS) layer on a sol-gel Si-DR1 thin film (200 nm) deposited on a glass plate (a). The deposition of the AEAPTMS layer is done by evaporation in controlled atmosphere, after strong heating (150°, 8 hrs) of the sol-gel Si-DR1 fillm, since we observed the dissolution of the photochromic film without strong thermal treatment. As shown in (b), after a 3 min dip-coating into a gold nanoparticle solution, we obtain a good dispersion of the nanoparticles on the surface.

In the aim to detect whether, under illumination, a lateral movement of the nanoparticles is associated to the SRG growth, we use a Kretshmann configuration to fabricate the interference pattern, with an inter-fringe of $\simeq 230$ nm, which allows to induce a deformation approximately one order of magnitude wider than the nanoparticle size.

Unfortunately, as shown in (c-d), we observe a very weak deformation ($\simeq 2$ nm) under exposure to p-polarized light interference, with an intensity of $1 mW/mm^2$ per beam. Probably, this is due to the strong thermal treatment of the sample prior to the functionalization, which has radically diminished the matrix mobility[1].

Using a good compromise between the AEAPTMS concentration and the thermal treatment, it should be possible to obtain well dispersed nanoparticles and to preserve matter mobility, hence to determine with more precision whether a lateral movement of small gold structures can be induced by the matter migration processes.

In conclusion, in a sol-gel Si-DR1 sample coated with gold nanoparticles, we do not observe any lateral movement of the gold structures present on the surface associated to the photoinduced mass migration. Indeed, they follow the same deformation of the underlying photochromic film, so that only their vertical displacement is induced. This result seems to confirm that the mass migration phenomena are rather bulk than surface processes.

[1] The small difference of the nanoparticle distribution observed between (c) and (d) could be due to a combined effect of tip-dragging and imaging artefacts.

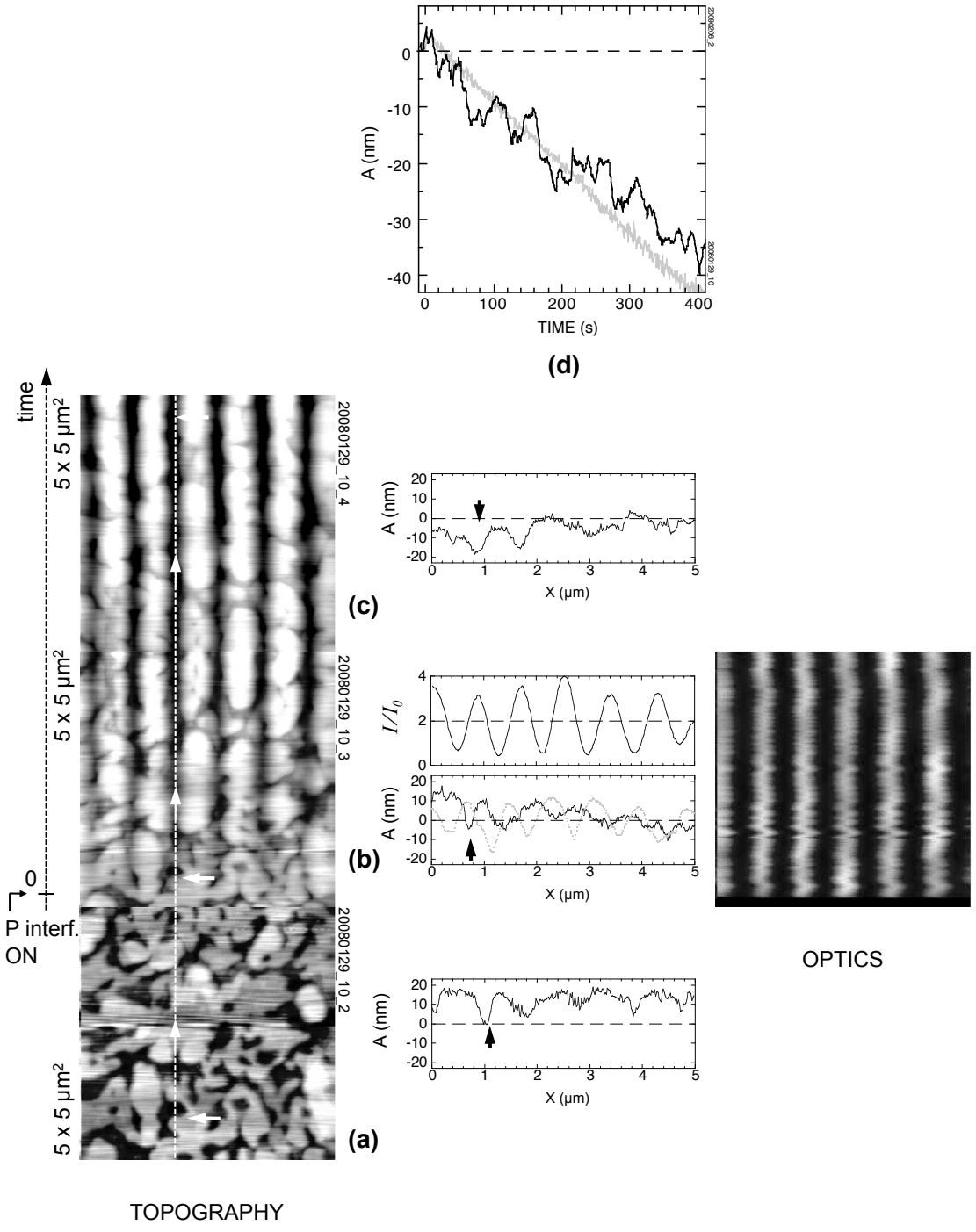

FIGURE 5.2: Gold nanoparticles on sol-gel Si-DR1 ($\simeq 200\ nm$ thick). Particle diameter $= 20-30\ nm$. (a-c) left side: $5\times5\ \mu m$ shear-force topography images during exposure to p-polarized interfering beams; middle: topography profile corresponding to the vertical cut reported in each figure. The optical image is shown for the first 200 s of illumination, in (b), right side. In the middle, we report the optical (top) and topographical (bottom, gray dotted curve) profiles. Note the spatial half-a-period shift between the SRG and the interference pattern. (d) SRG growth time evolution under p-polarized light in the free-surface sample (grey curve) and in the sample coated with gold nanoparticles (dark curve). Laser wavelength $= 473\ nm$, power density $= 1\ mW/mm^2$ per beam, incidence angle $= 16.5°$, spatial period $\simeq 830\ nm$.

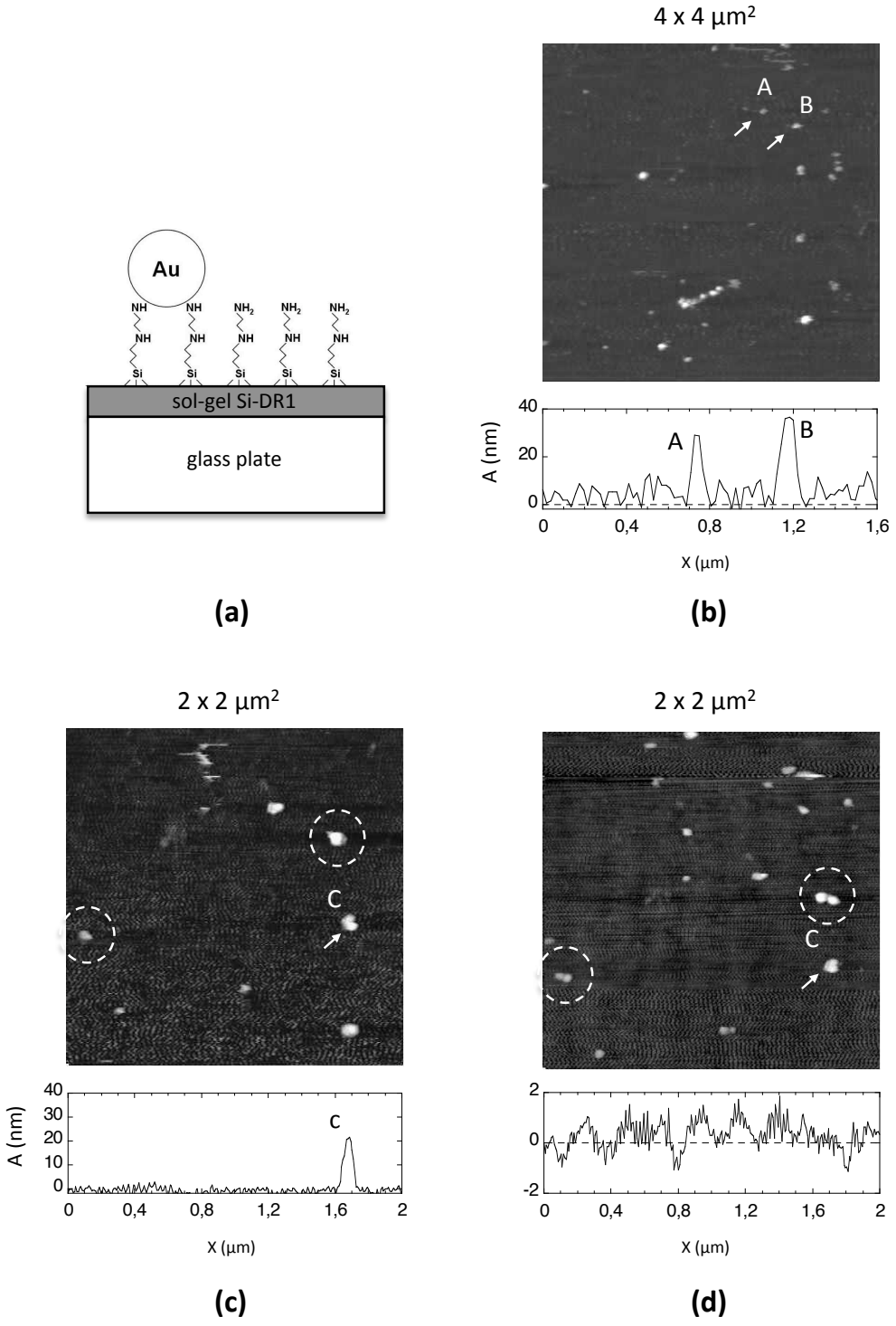

FIGURE 5.3: Gold nanoparticles on a sol-gel Si-DR1 film (surface functionalization). Particle diameter $= 20 - 30\ nm$, film thickness $\simeq 200nm$. (a) AEAPTMS surface functionalization; (b) $4 \times 4\ \mu m$ topographical image with the detail of two nanoparticles (A and B); (c) $2 \times 2\ \mu m$ topographical image of the surface before illumination and (d)under illumination. Laser (blue, $\lambda = 473\ nm$) power density: $1\ mW/mm^2$ per beam, spatial period $\simeq 460\ nm$.

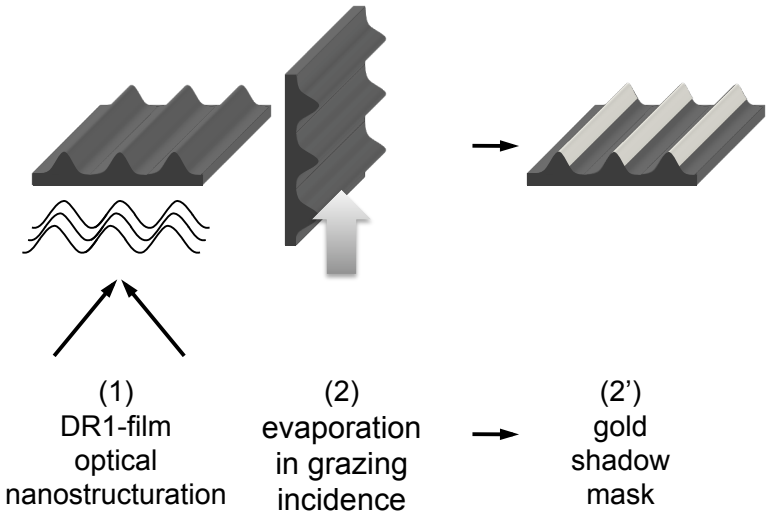

FIGURE 5.4: Large scale patterning process of gold coated PMMA-DR1. From left to right: (1) optical nanostructuration of a PMMA-DR1 sample under p-polarized interfering beams, laser (blue, $\lambda = 473\ nm$) power density: 1 mW/mm^2 per beam, incidence angle = 16.5°, spatial period $\simeq 830\ nm$; (2) evaporation of a 40 nm thick gold layer in grazing incidence in order to obtain a deposition only on the sides of the nanostructured periodic pattern, which constitutes (2') a gold shadow-mask.

5.2 Hybrid optically nano-structured organized surfaces

In section 4.1 we have shown that the optical patterning of hybrid metal/azo-polymer layered structures can be achieved, exploiting the photodeformation capabilities of the underlying photochromic material. Here we will present some preliminary results demonstrating the possibility to elaborate more complex large scale nano-structured systems.

5.2.1 Complex structures

5.2.1.1 Grid fabrication

In **Figure 5.4** we show a simple two-step process that allows to obtain a metallic stripe array on an azo-polymer film, which is shown in **Figure 5.5**. In step (1) we induce a periodic photodeformation on a PMMA-DR1 thin film by means of two polarized interfering beams (1 mW/mm^2 per beam), using the same experimental setup as in the previous section. For a film thickness of 200 nm the typical relief height is 80 nm. Then (step 2) we grow a gold shadow mask, having a thickness of approximately 40 nm, by evaporation in grazing incidence. In this way (2') we obtain a gold deposition only on one side of the periodic reliefs previously inscribed. SEM images of the obtained gold stripe array are reported in **Figure 5.5**(a), while in **Figure 5.5**(b) we show the topography measurement performed by shear-force microscopy. We observe that the

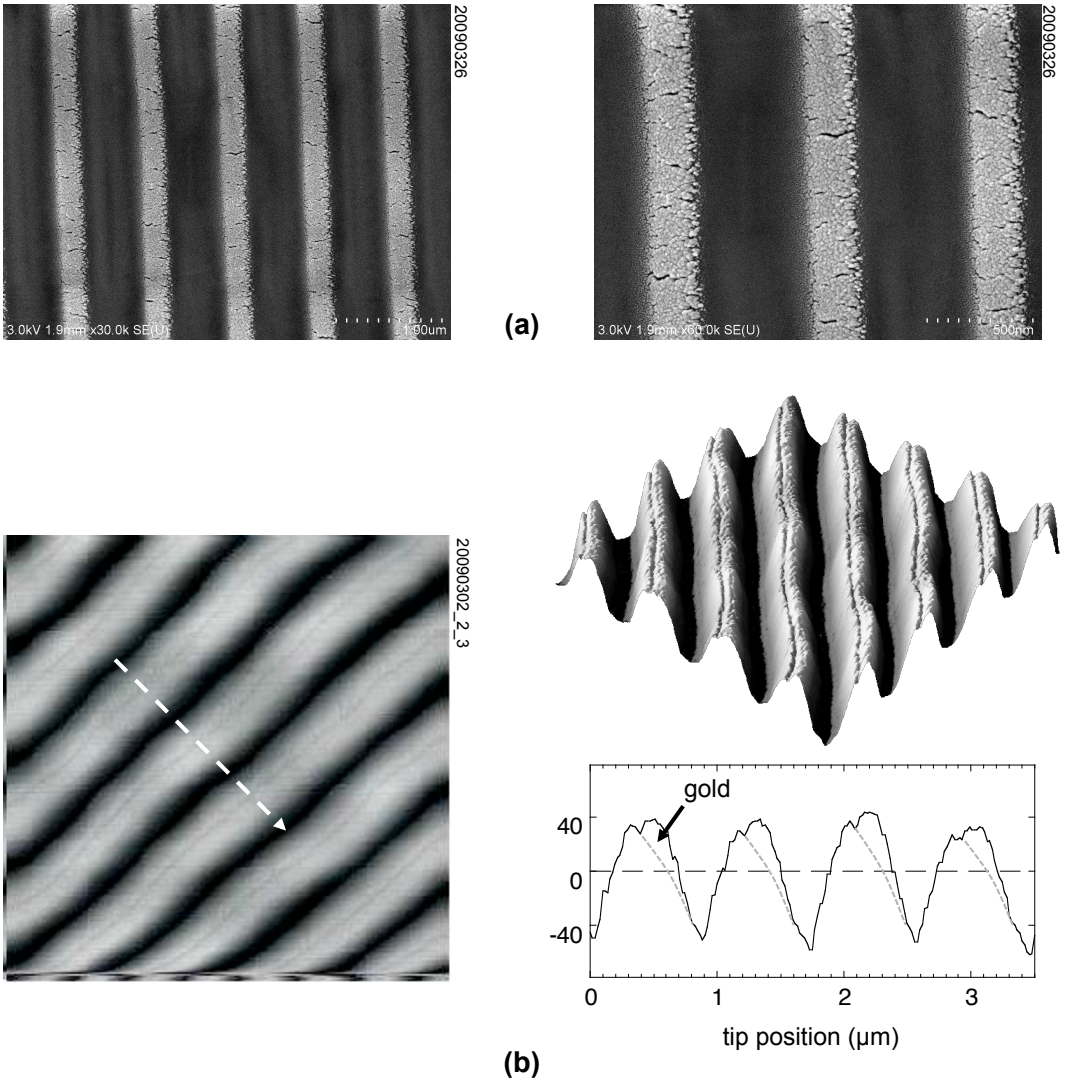

FIGURE 5.5: Gold coated PMMA-DR1: nanopatterning. (a) SEM images corresponding to step (2') in **Figure 5.4**. (b) Shear force topography image of the structures in (a), (256×256 pixel, 5×5 μm), recorded scanning long a direction making a 45°angle with the x-axis. The plot shows the profile corresponding to the white dashed line shown in the topography image. The grey dashed lines in the plot indicates the edge of the lateral gold layer deposited on one side of the underlying relief. A 3D representation is also reported.

lateral gold stripes are indeed deposited on one side of each previously inscribed relief, clearly visible on the shear-force topography profile (b-bottom). We indicate the edge of the gold deposition with a grey dashed line.

Note that, after the gold deposition under vacuum, the photochromic film is still photoactive and a new optical pattern can be superimposed onto the gold stripe array. For instance, by projecting a two-beam interference pattern onto the sample, rotated

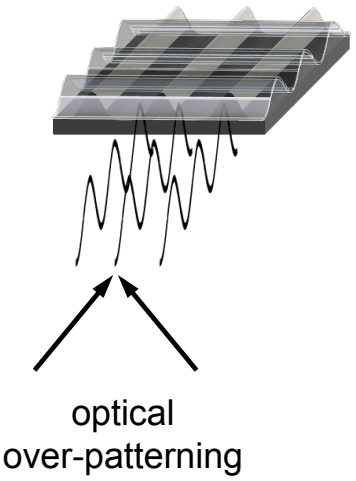

FIGURE 5.6: Large scale patterning process of gold coated PMMA-DR1. Optical over-patterning exposing the sample to an interference pattern orthogonal with respect to **Figure 5.5**(1).

by 90° with respect to the previous patterning experiment (**Figure 5.6**) we obtain an over-modulation along the gold stripes, shown in **Figure 5.7**.

This more complex structure is constituted by a very regular grid having a step size corresponding to the interference pattern's spatial period, where each convex element has an asymmetric form due to the presence of the golden layer on one side. Such a peculiar pattern is likely to exhibit special optical properties [10].

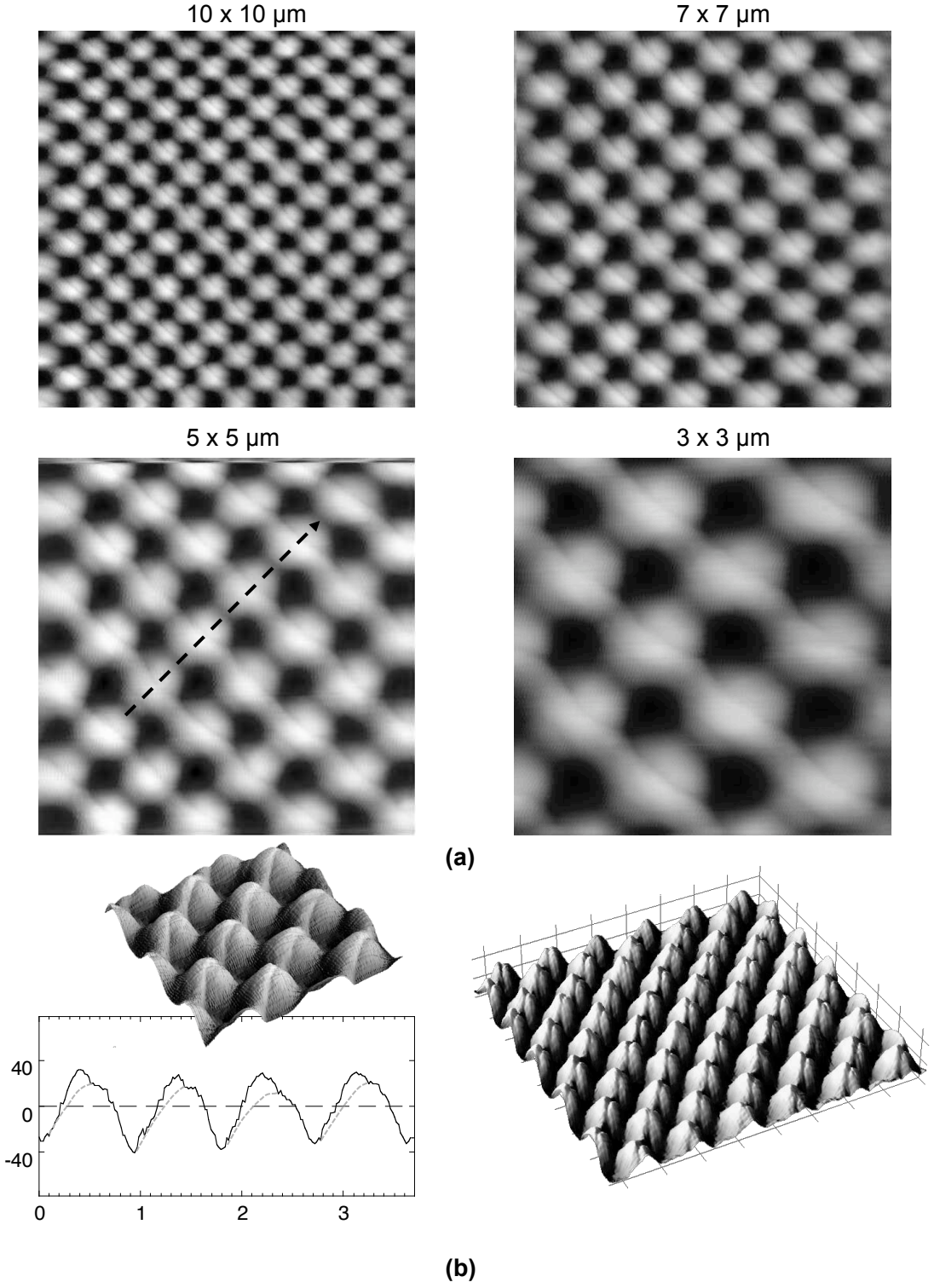

FIGURE 5.7: Hybrid metal/azo-polymer complex pattern obtained after sequential processing. (a) Shear force images (256×256 pixels) corresponding to various scan ranges (10×10, 7×7, 5×5 and 3×3 μm). (b) Topography profile corresponding to the dark dashed line in (a) bottom-left: the grey dashed line on the plot indicates the edge of the lateral gold layer deposited on one side of the underlying relief; 3D representations of the topography (3×3 and 7×7 μm).

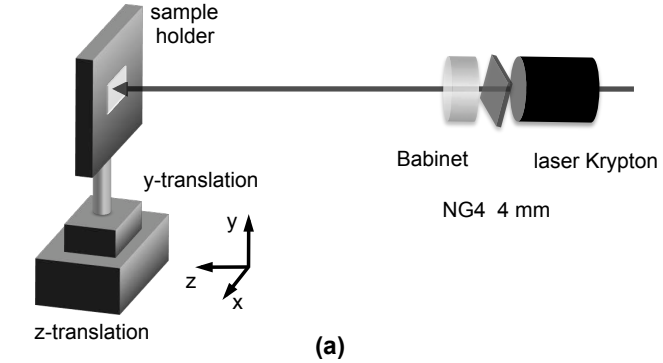

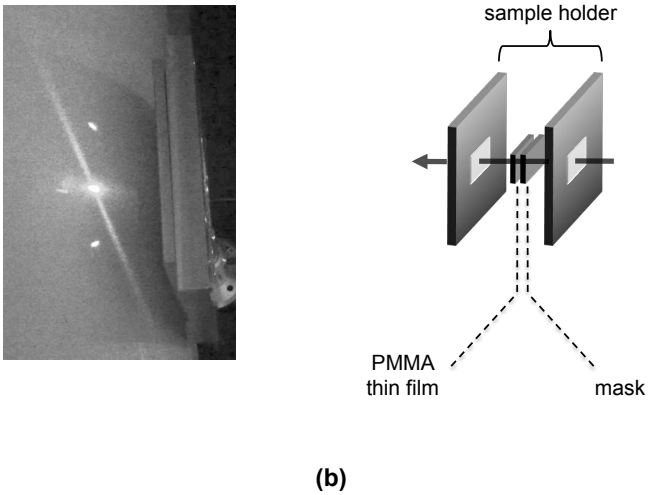

FIGURE 5.8: Gold coated PMMA-DR1: lithography mask. (a) Experimental setup (b) Detail of the sample holder and of the first order diffraction spots used to align the mask and the laser beam. Laser beam power intensity = 5 $mW/mm^2, \lambda = 477\ nm$, exposure time = 30 min.

5.2.2 Optical pattern tansfer

The optical nanostructuration processes presented in the previous sections are potentially well adapted for the patterning of masks and moulds for nanolithography and nanoimprinting. The fabrication processes adopted to realize these elements are generally extremely slow, since the desired pattern must be written, using a focused beam, feature by feature, in order to guarantee accuracy, which leads to low yields and to big costs [12, 13]. Moreover, surface treatment is needed for the masks to be used in a contact pattern transfer application (such as soft lithography, nanoimprinting, etc.), in order to eliminate contact defects and to preserve the mask lifetime.

The possibility to use photostructured azo-containing thin films as masks for nanolithography processes has been shown in [14] using non contact lithography. In this case, the patterned mask is projected 1:1 on a photochromic film.

In our case, we used the hybrid systems described in section 5.2.1.1 (see **Figure 5.5** and **Figure 5.7**) as lithographic masks in a contact lithography process as depicted in **Figure 5.8**. In (a) we show the experimental setup, constisting in a Krypton laser beam ($\lambda = 477\ nm$, power density $= 5\ mW/mm^2$) polarized through a Babinet device. As specified in (b) the beam is normally incident on the mask which is put in contact via the sample holder with the photochromic thin film sample. In order to align the laser beam with the mask, we optimize the first diffraction order of the mask, as depicted in (b)[2].

In **Figure 5.8** we report the mask (a) and the photoinduced patterning (b) obtained after 1h of irradiation at $5\ mW/mm^2$. We recognize the same spatial period ($\simeq 830\ nm$) and almost the same deformation amplitude ($60\ nm$), which confirms that the pattern has been successfully transferred from the mask to the sample. However, as we notice in (c), where we report a wider scan ($15 \times 15\ \mu m^2$) of the patterned sample, we observe some inhomogeneities in the relief profile along the fringes, which can reach a height of $20\ nm$. This is probably due to light scattering during the lithographic process.

If we look at the SEM images of the mask before and after the lithographic process (**Figure 5.10**(a-b)), we note that it has not undergone important modifications, since the same defects appear in the two cases. Probably, in order to evaluate more precisely the impact of the contact with the sample on the mask, we should repeat the experiment with a more homogeneous mask, which could be obtained using more precise gold deposition methods. It would be very interesting to deeply investigate this nano-fabrication process, since it provides an optical pattern transfer method that is not affected by problems relative to the stability of the optical path, which, instead, are fundamental issues in every direct interferential patterning process.

5.3 Conclusions

The use of the photodeformation properties of azo-containing photochromic films for the optical nano-structuration of other materials seems to be a promising technique. We have demonstrated the feasibility of this process in hybrid metallic/photochromic layered systems. It is possible to obtain the patterning of complex gold structures by using a combination of deposition and photodeformation steps. This allows the direct nano-patterning of gold structures by means of the photochromic underlying layer, which can be used as a tool for the nano-fabrication.

[2] During the alignment we use a non absorbing wavelength, typically red.

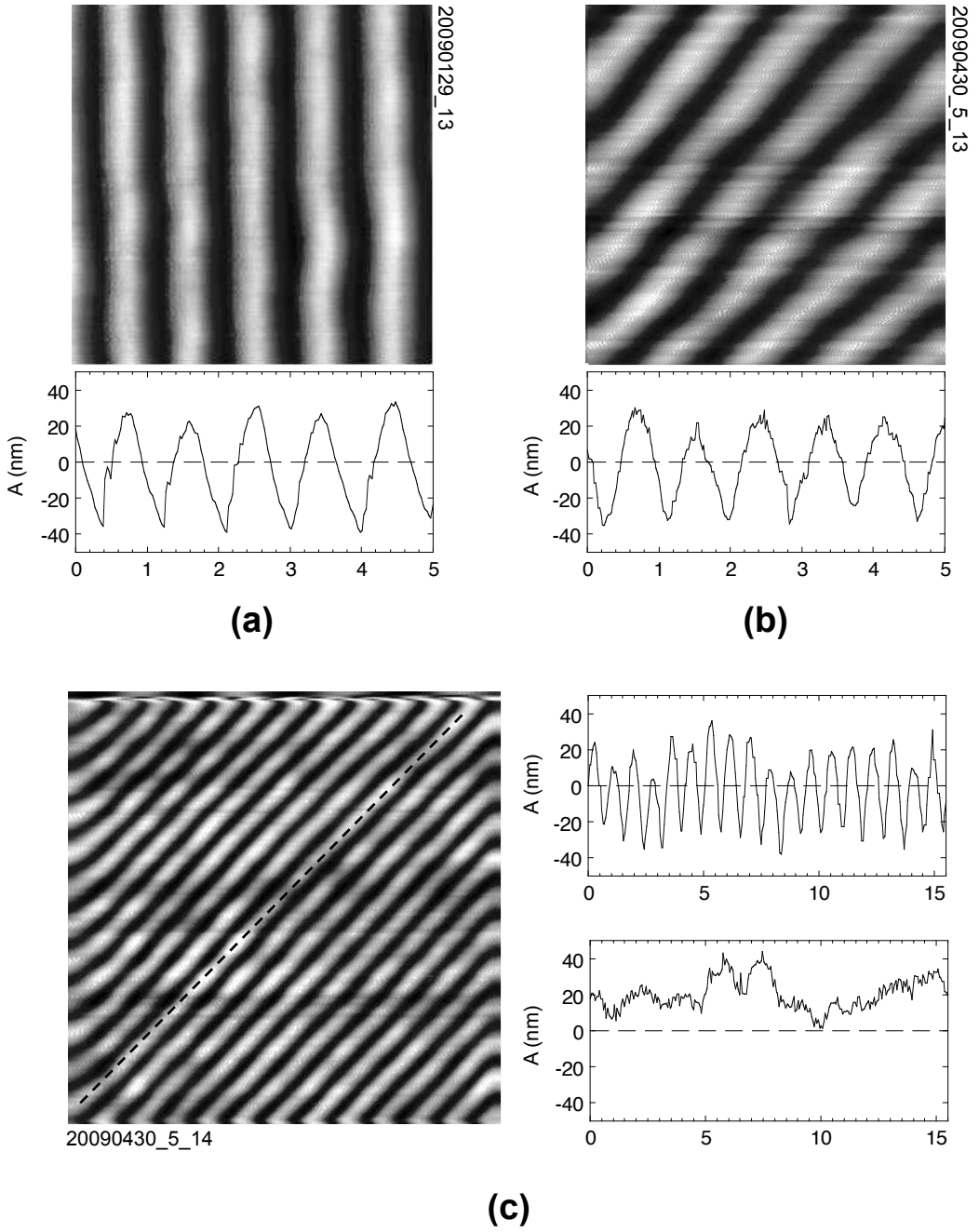

FIGURE 5.9: Gold coated PMMA-DR1: lithography mask. (a) Photomask (b) Patterned sample (5×5 μm scan); (c) patterned sample (15×15 μm scan), the dashed line corresponds to the right-bottom profile.

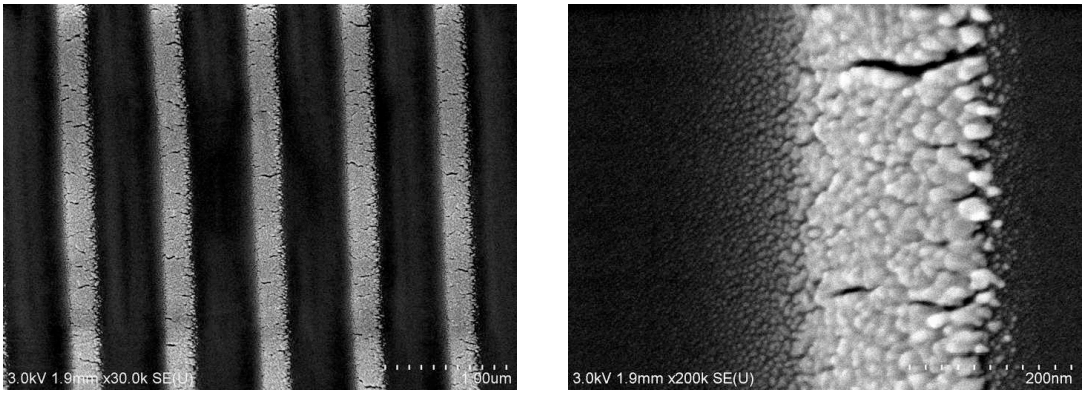

(a)

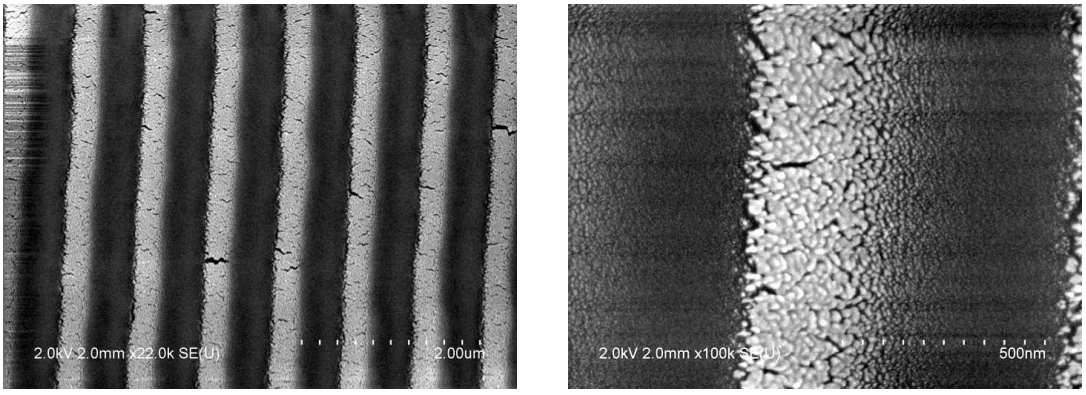

(b)

FIGURE 5.10: Gold coated PMMA-DR1: lithography mask. (a) SEM images before lithography; (b) SEM images after lithography.

Bibliography

[1] A. Natansohn, P. Rochon, M. S. Ho, and C. Barret. Azo polymers for reversible optical storage .6. poly[4-[2-(methacryloyloxy)ethyl]azobenzene]. *Macromolecules*, 28(12):4179–4183, June 1995.

[2] N. Landraud, J. Peretti, F. Chaput, G. Lampel, J. P. Boilot, K. Lahlil, and V. I. Safarov. Near-field optical patterning on azo-hybrid sol-gel films. *Applied Physics Letters*, 79(27):4562–4564, December 2001.

[3] S. Orlic, S. Ulm, and H. J. Eichler. 3d bit-oriented optical storage in photopolymers. *Journal Of Optics A-Pure And Applied Optics*, 3(1):72–81, January 2001.

[4] O.N. Oliveira et Al. Optical storage and surface-relief gratings in azobenzene-containing nanostructured films. *Advances in colloidal interface science*, 116:179–192, 2005.

[5] Y. L. Yu, M. Nakano, and T. Ikeda. Directed bending of a polymer film by light - miniaturizing a simple photomechanical system could expand its range of applications. *Nature*, 425(6954):145–145, September 2003.

[6] T. Ikeda, M. Nakano, Y. L. Yu, O. Tsutsumi, and A. Kanazawa. Anisotropic bending and unbending behavior of azobenzene liquid-crystalline gels by light exposure. *Advanced Materials*, 15(3):201, February 2003.

[7] N. Tabiryan, S. Serak, X. M. Dai, and T. Bunning. Polymer film with optically controlled form and actuation. *Optics Express*, 13(19):7442–7448, September 2005.

[8] T. J. White, N. V. Tabiryan, S. V. Serak, U. A. Hrozhyk, V. P. Tondiglia, H. Koerner, R. A. Vaia, and T. J. Bunning. A high frequency photodriven polymer oscillator. *Soft Matter*, 4(9):1796–1798, 2008.

[9] C. Cocoyer, L. Rocha, L. Sicot, B. Geffroy, R. de Bettignies, C. Sentein, C. Fiorini-Debuisschert, and P. Raimond. Implementation of submicrometric periodic surface structures toward improvement of organic-solar-cell performances. *Applied Physics Letters*, 88(13):133108, 2006. doi: 10.1063/1.2188600. URL http://link.aip.org/link/?APL/88/133108/1.

[10] Leonid M. Goldenberg, Yuri Gritsai, Olga Kulikovska, and Joachim Stumpe. Three-dimensional planarized diffraction structures based on surface relief gratings in azobenzene materials. *Opt. Lett.*, 33(12):1309–1311, 2008. URL http://ol.osa.org/abstract.cfm?URI=ol-33-12-1309.

[11] J. Hillier J. Turkevich, P. C. Stevenson. A study of the nucleation and growth processes in the synthesis of colloidal gold. *Discussions of the Faraday Society*, 11: 55, 1951.

[12] Bharat Bhushan. *Springer Handbook of Nano-technology*. Springer, 2004.

[13] Syed Rizvi. *Handbook of photomask manufacturing technology*. Taylor & Francis, 2003.

[14] X. L. Jiang, L. Li, J. Kumar, D. Y. Kim, and S. K. Tripathy. Unusual polarization dependent optical erasure of surface relief gratings on azobenzene polymer films. *Applied Physics Letters*, 72(20):2502–2504, May 1998.

Conclusions

In this work we have studied the photodeformation effects induced at nanoscale in photochromic thin films constituted of the Disperse Red 1 (DR1) molecule grafted to a sol-gel or to a PMMA matrix. We have mainly investigated the mechanisms at the origin of the SRG growth observed under exposure to an interference pattern. Using a coupled technique of shear-force topography measurement and SNOM light detection, we have been able to achieve a very direct, in-situ and real-time nanoscale correlation of the light field pattern with the photoinduced deformation.

Our results demonstrate that the photomechanical response of polymer-like materials containing azobenzene derivatives is a very complex problem involving several different microscopic mechanisms. The microscopic origin of these mechanisms and their exact relationship with the azobenzene photoisomerization are not fully determined, but we have been able to identify each of these processes by their specific response to light polarization and intensity patterns.

It turns out that the different theoretical models that have been proposed to describe the photoinduced deformation phenomena in azo-containing materials constitute relevant partial descriptions of the experimental observations. The apparent contradictions between these models only reflect the existence of mechanisms of different nature, whose relative efficiencies depend on the illumination conditions and on the material structure. The coexisting microscopic processes can be independently addressed and controlled by using appropriate experimental conditions and give rise to a great diversity of phenomenological behaviors.

Moreover, these phenomena can be extended to more complex systems and we have for instance demonstrated the possibility to exploit the photodeformation phenomena for the patterning of hybrid metallic/azo-polymer structures. In the near field we have put in evidence the contribution of the mechanical interaction between the local probe and the sample's surface, which plays a crucial role towards the efficiency and the directionality of the photoinduced deformation. Also, we have shown that, in layered metal/azo-polymer structures, the deformation induced on the photochromic film is mechanically transferred on the overlying metallic layer, either under far-field irradiation or

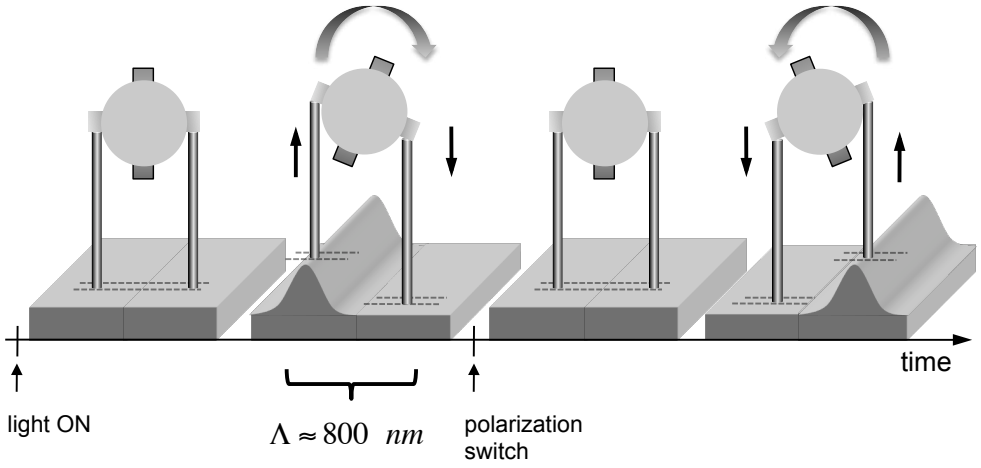

FIGURE 5.11: Reversible, oscillating actuation: a potential application.

using near-field probe-sample photomechanical interactions, which sets the basis for new nanofabrication techniques. It also demonstrates that the photo-induced deformation of the photoactive layer is capable of performing a mechanical work on an overlying layer.

The improved knowledge on the origin of the matter migration phenomena, the demonstration of the reversible, directional matter transport obtained by switching the polarization of the light and the demonstrated capability of the photo-induced deformation to perform mechanical work on other bodies open the way to an innovative potential application of the photodeformation phenomena. For instance, it is possible to produce a reversible oscillating surface deformation addressing simultaneously nanometric features over the entire illuminated surface. Each oscillating structure produces a vertical displacement and a vertical force, which can be transmitted to overlying objects, as it is demonstrated with the vertical motion of gold nanoparticles in section 5.1.
In **Figure 5.11** we illustrate the principle on a single working unit. On the surface, a couple of nano-rods is linked to a nano-wheel, which is actuated by the surface deformation through a transmission provided by the nano-rods. Latest results in the field of the micro-nano machining demonstrate the possibility to fabricate components in the sub-micron range, as reported, for example, in ref. [1] where supra-mulecular architectures of platinum(II) complexes having the shape of rods and wheels of the order of $200 \div 800\ nm$ have been obtained.
At $t = 0$ the surface is flat. Illuminating with an interference pattern induces the growth of SRG, which can be reversed switching the polarization of the light, providing light-driven, reversible actuation of the wheel. We can think of a parallel architecture, where reversible movement is optically induced on a large surface of working units. Indeed, this application constitutes an interesting new technique of light driven parallel actuation at micro-nanoscale.

Bibliography

[1] Chi-Ming Che et Al. A submicrometer wire-to-wheel metamorphism of hybrid tridentate cyclometalated platinum (ii) complexes. *Nanoletters*, 47:4568–4572, 2008.

Appendix A

Electromagnetic field calculations

A.1 Calculation of the electric field polarization spatial distribution

We provide the expression of the electric field for the geometry used in this work (**Figure A.1**). We write the equations that hold inside the glass substrate, which has a refractive index $n_g \simeq 1.51$.

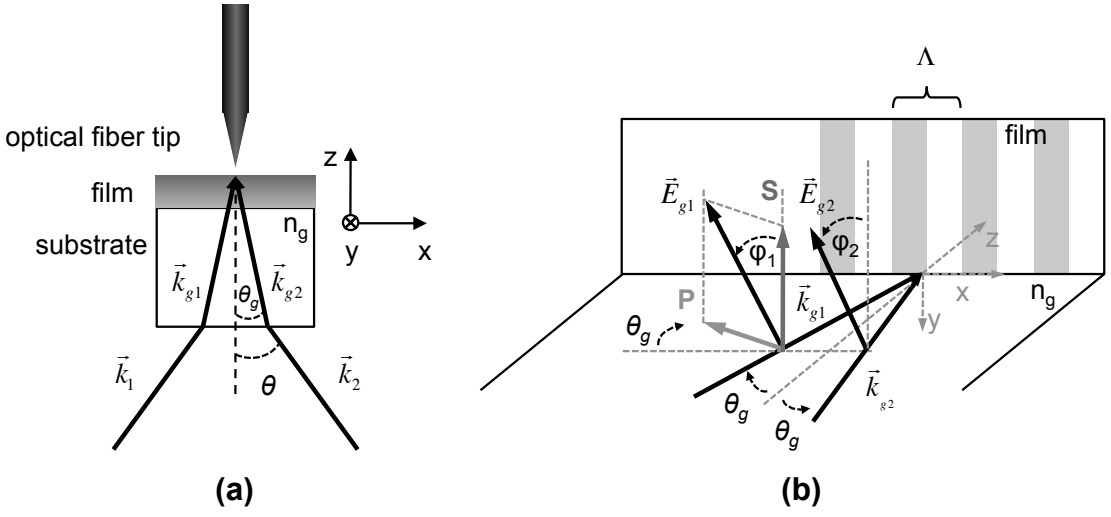

FIGURE A.1: Geometry at the sample surface. In the experiment presented in the main text $\theta = 16.5°$, $\lambda = 473\ nm$ and $\Lambda \simeq 830\ nm$.

Being θ_g the angle of incidence at the sample surface, we give the expressions of k_{g1}, k_{g2}, the wave vectors for the left and right blue beams inside the substrate, respectively:

$$\vec{k}_{g1} = k \begin{pmatrix} n_g sin\theta_g \\ 0 \\ n_g cos\theta_g \end{pmatrix} = \begin{pmatrix} k_x \\ 0 \\ k_z \end{pmatrix} \tag{A.1}$$

$$\vec{k}_{g2} = k \begin{pmatrix} -n_g sin\theta_g \\ 0 \\ n_g cos\theta_g \end{pmatrix} = \begin{pmatrix} -k_x \\ 0 \\ k_z \end{pmatrix} \tag{A.2}$$

where $k = 2\pi/\lambda$ ($\lambda = 473\ nm$).

Changing the polarization angle φ_1, φ_2 for the two beams leads to vary the respective components' amplitude along the different axes[1].

$$\vec{E}_{g1}(t,\vec{r}) = \vec{E}^0_{g1} cos\left(\omega t + \vec{k}_{g1}\cdot\vec{r}\right) = E^0_{g1} \begin{pmatrix} -sin\varphi_1\ cos\theta_g \\ -cos\varphi_1 \\ sin\varphi_1 sin\theta_g \end{pmatrix} cos\left(\omega t + \vec{k}_{g1}\cdot\vec{r}\right) \tag{A.3}$$

$$\vec{E}_{g2}(t,\vec{r}) = \vec{E}^0_{g2} cos\left(\omega t + \vec{k}_{2}\cdot\vec{r}\right) = E^0_{g2} \begin{pmatrix} -sin\varphi_2\ cos\theta_g \\ -cos\varphi_2 \\ -sin\varphi_2\ sin\theta_g \end{pmatrix} cos\left(\omega t + \vec{k}_{g2}\cdot\vec{r}\right) \tag{A.4}$$

where E^0_{g1}, E^0_{g2} are the respective field amplitudes inside the substrate. We can now write the expression for the total interfering light field.

$$\vec{E}_{g,tot}(t,\vec{r}) = \vec{E}_{g1}(t,\vec{r}) + \vec{E}_{g2}(t,\vec{r}) \tag{A.5}$$

On the plane of incidence we have:

$$\begin{aligned} \vec{E}_{g,tot}(t,\vec{r}) &= \vec{E}^0_{g1} cos(\omega t + kn_g(xsin\theta_g + zcos\theta_g)) \\ &+ \vec{E}^0_{g2} cos(\omega t + kn_g(-xsin\theta_g + zcos\theta_g)) \end{aligned} \tag{A.6}$$

Defining: $\alpha = \omega t + kn_g zcos\theta_g$ and $\beta = -kn_g xsin\theta_g$ we can write the three x, y, z field components.

[1] In the case of SS and PP interferences $\varphi_1 = \varphi_2 = 0°$ and $\varphi_1 = \varphi_2 = 90°$, respectively.

For $i = x, y, z$, being $\hat{i}$ the i-axis versor we obtain:

$$\vec{E}_{g,tot}(t,\vec{r}) = \sum_{i=x,y,z} \hat{i}\left[cos\alpha cos\beta(E_{g1}^{0,i} + E_{g2}^{0,i}) + sin\alpha sin\beta(E_{g1}^{0,i} - E_{g2}^{0,i})\right] \tag{A.7}$$

For two beams of same intensities we have $E_{g1}^0 = E_{g2}^0 = E_g^0$ which gives:

$$\vec{E}_{g,tot} = \vec{E}_{g,tot}^x + \vec{E}_{g,tot}^y + \vec{E}_{g,tot}^z \tag{A.8}$$

$$\begin{aligned}\vec{E}_{g,tot}^x = & -(sin\varphi_1 + sin\varphi_2)\left[E_g^0 cos\left(\omega t + k_z z\right) cos\theta_g\right] cos(k_x x)\hat{x} \\ & +(sin\varphi_1 - sin\varphi_2)\left[E_g^0 sin\left(\omega t + k_z z\right) cos\theta_g\right] sin(k_x x)\hat{x}\end{aligned} \tag{A.9}$$

$$\begin{aligned}\vec{E}_{g,tot}^y = & -(cos\varphi_1 + cos\varphi_2)\left[E_g^0 cos\left(\omega t + k_z z\right)\right] cos(k_x x)\hat{y} \\ & +(cos\varphi_1 - cos\varphi_2)\left[E_g^0 sin\left(\omega t + k_z z\right)\right] sin(k_x x)\hat{y}\end{aligned} \tag{A.10}$$

$$\begin{aligned}\vec{E}_{g,tot}^z = & (sin\varphi_1 - sin\varphi_2)\left[E_g^0 cos\left(\omega t + k_z z\right) sin\theta_g\right] cos(k_x x)\hat{z} \\ & -(sin\varphi_1 + sin\varphi_2)\left[E_g^0 sin\left(\omega t + k_z z\right) sin\theta_g\right] sin(k_x x)\hat{z}\end{aligned} \tag{A.11}$$

In particular, in the case where $\varphi_1 = -\varphi_2 = \varphi$, which corresponds to the experiments of section 3.3, these expressions become[2]:

$$\vec{E}_{g,tot}^x = 2E_g^0 cos\theta_g sin\varphi sin(k_x x)\left[sin\left(\omega t + k_z z\right)\right]\hat{x} \tag{A.12}$$

$$\vec{E}_{g,tot}^y = -2E_g^0 cos\varphi cos(k_x x)\left[cos\left(\omega t + k_z z\right)\right]\hat{y} \tag{A.13}$$

$$\vec{E}_{g,tot}^z = 2E_g^0 sin\theta_g sin\varphi cos(k_x x)\left[cos\left(\omega t + k_z z\right)\right]\hat{z} \tag{A.14}$$

The total field intensity is defined as:

$$I_{tot} = 2 < \vec{E}_{g,tot}\vec{E}_{g,tot}^* >= \frac{2}{T}\int_{t_0}^{t_0+T} \vec{E}_{g,tot}\vec{E}_{g,tot}^*\, dt = I_x^{tot} + I_y^{tot} + I_z^{tot} \tag{A.15}$$

[2] $\varphi \neq 90°$, see A.1.2

hence for each component we have[3]:

$$I_x^{tot} = 4(E_g^0)^2 cos^2\theta_g sin^2\varphi sin^2 k_x x \cdot \frac{2}{T}\int_{t_0}^{t_0+T} sin^2(\omega t + k_z z)\, dt \tag{A.16}$$
$$= 4I_{0,x} sin^2 k_x x$$

$$I_y^{tot} = 4(E_g^0)^2 cos^2\varphi cos^2 k_x x \cdot \frac{2}{T}\int_{t_0}^{t_0+T} cos^2(\omega t + k_z z)\, dt \tag{A.17}$$
$$= 4I_{0,y} cos^2 k_x x$$

$$I_z^{tot} = 4(E_g^0)^2 sin^2\theta_g sin^2\varphi cos^2 k_x x \cdot \frac{2}{T}\int_{t_0}^{t_0+T} cos^2(\omega t + k_z z)\, dt \tag{A.18}$$
$$= 4I_{0,z} cos^2 k_x x$$

where:

$$I_{0,x} = (E_g^0)^2 cos^2\theta_g sin^2\varphi \tag{A.19}$$
$$I_{0,y} = (E_g^0)^2 cos^2\varphi \tag{A.20}$$
$$I_{0,z} = (E_g^0)^2 sin^2\theta_g sin^2\varphi \tag{A.21}$$

The interference pattern spatial period Λ along the x-axis is defined by:

$$\Lambda = \frac{\lambda}{2sin\theta} \simeq 830\ nm \tag{A.22}$$

So, we obtain that for $\varphi_1 = -\varphi_2 = \varphi$ and for every fixed z, the x-component intensity is $\Lambda/2$ spatially shifted with respect to the other two components.

We write the total field intensity I_{tot} in three particular polarization configurations:

A.1.1 *s*-polarized interfering beams ($\varphi_1 = \varphi_2 = 0°$)

In this case only $\vec{E}_{g,tot}^{\,y} \neq 0$ so:

$$I_{tot} = 4I_{0,y} cos^2 k_x x = 4(E_g^0)^2 cos^2 k_x x = 4(E_g^0)^2 \left[\frac{1 + cos(2k_x x)}{2}\right] \tag{A.23}$$

[3] With an appropriate choice of t_0.

A.1.2 *p*-polarized interfering beams ($\varphi_1 = \varphi_2 = 90°$)

In this case:

$$\begin{aligned}
\vec{E}^{x}_{g,tot} &= -\left(sin\varphi_1 + sin\varphi_2\right)\left[E^0_g cos\left(\omega t + k_z z\right) cos\theta_g\right] cos(k_x x)\hat{x} && \text{(A.24)}\\
&= -2\left[E^0_g cos\left(\omega t + k_z z\right) cos\theta_g\right] cos(k_x x)\hat{x} \\
\vec{E}^{y}_{g,tot} &= 0 && \text{(A.25)}\\
\vec{E}^{z}_{g,tot} &= -\left(sin\varphi_1 + sin\varphi_2\right)\left[A_0 sin\left(\omega t + k_z z\right) sin\theta_g\right] sin(k_x x)\hat{z} && \text{(A.26)}\\
&= -2\left[E^0_g sin\left(\omega t + k_z z\right) sin\theta_g\right] sin(k_x x)\hat{z}
\end{aligned}$$

So:

$$\begin{aligned}
I_{tot} &= I^{tot}_x + I^{tot}_z = 4((E^0_g)^2 cos^2\theta_g) cos^2 k_x x + 4((E^0_g)^2 sin^2\theta_g) sin^2 k_x x \\
&= 4(E^0_g)^2\left[cos^2\theta_g cos^2 k_x x + sin^2\theta_g sin^2 k_x x\right] \\
&= 4(E^0_g)^2\left[\frac{1 + cos(2\theta_g) cos(2k_x x)}{2}\right] && \text{(A.27)}
\end{aligned}$$

A.1.3 $\pm 45°$ polarized interfering beams ($\varphi_1 = -\varphi_2 = 45°$)

$$\begin{aligned}
I_{tot} &= 4I_{0,x} sin^2 k_x x + \left[4I_{0,y} + 4I_{0,z}\right] cos^2 k_x x \\
&= 4(E^0_g)^2\left[\frac{1}{2} cos^2\theta sin^2 k_x x + \frac{1}{2}\left(1 + sin^2\theta_g\right) cos^2 k_x x\right] \\
&= 4(E^0_g)^2\left[\frac{1 + sin^2\theta_g cos 2k_x x}{2}\right] && \text{(A.28)}
\end{aligned}$$

where for $\theta_g = 10.8°$, $sin^2\theta_g \simeq 0.03$ and $cos^2\theta_g \simeq 0.97$.

Changing the value of φ allows to shift from a configuration of complete intensity spatial modulation ($\varphi = 0°$, *s*-polarized light) to a configuration of complete[4] polarization spatial modulation ($\varphi = 45°$), which allows to distinguish the effects due to the intensity from the effects caused by the polarization.

[4] Approximately complete, the exact value of φ would be such that $I_{0,x} = I_{0,y} + I_{0,z}$, that is $cos2\theta_g = (tg\varphi)^{-2}$, in our case, for $\theta_g \simeq 10.8°$ we obtain $\varphi \simeq 47.5°$.

Appendix B

Photoisomerization dynamics

B.1 Photostationary equilibrium

Let us consider the populations of the TRANS and CIS azobenzene isomers (N_{TRANS} and N_{CIS}). The variation of each population depends on the TRANS $\rightarrow$ CIS and CIS $\rightarrow$ TRANS isomerization rate, that is:

$$\frac{dN_{TRANS}}{dt} = -\frac{N_{TRANS}}{\tau_{T \rightarrow C}} + \frac{N_{CIS}}{\tau_{C \rightarrow T}} \tag{B.1}$$

$$\frac{dN_{CIS}}{dt} = -\frac{N_{CIS}}{\tau_{C \rightarrow T}} + \frac{N_{TRANS}}{\tau_{T \rightarrow C}} \tag{B.2}$$

where $\tau_{i \rightarrow j}$ is the characteristic time of the $i \rightarrow j$ photoisomerization event.

The TRANS $\rightarrow$ CIS isomerization is induced essentially by light irradiation, while the inverse transition can be obtained either by illumination or thermal relaxation of the metastable CIS isomer to the most stable TRANS isomer. This is expressed by:

$$\frac{1}{\tau_{T \rightarrow C}} = \frac{P}{h\nu}\frac{\rho_T(cos\theta)^2}{C}\alpha_T = \frac{P}{h\nu}\gamma_T \tag{B.3}$$

$$\frac{1}{\tau_{C \rightarrow T}} = \frac{P}{h\nu}\frac{\rho_C(cos\theta)^2}{C}\alpha_C + \frac{1}{\tau^{\text{th}}_{C \rightarrow T}} = \frac{P}{h\nu}\gamma_C + \frac{1}{\tau^{\text{th}}_{C \rightarrow T}} \tag{B.4}$$

where:

- P is the light power density
- C is the molecule concentration in the considered volume
- $h\nu$ is the photon energy
- ρ_T, ρ_C are the quantum yields for the isomerization of TRANS and CIS forms
- α_T, α_C are the absorption coefficients of the material when all the molecules are respectively in the TRANS and CIS forms
- $\tau^{\text{th}}_{C \to T}$ is the CIS $\to$ TRANS time constant due to the CIS form thermal relaxation.

Considering:

- $x_1(t) = N_{TRANS}(t), \qquad x_2(t) = N_{CIS}(t), \qquad x(t) = \begin{pmatrix} x_1(t) \\ x_2(t) \end{pmatrix}$
- $\psi = 1/\tau_{T \to C}, \qquad \xi = 1/\tau_{C \to T}$

we can rewrite the model in the following form:

$$\frac{dx(t)}{dt} = \begin{pmatrix} \dot{x_1} \\ \dot{x_2} \end{pmatrix} = \begin{pmatrix} -\psi & \xi \\ \psi & -\xi \end{pmatrix} \begin{pmatrix} x_1(t) \\ x_2(t) \end{pmatrix} \tag{B.5}$$

whose solution can be written as:

$$\begin{aligned} x(t) &= \frac{e^{\lambda_1 t}}{1+\xi/\psi} \begin{pmatrix} \xi/\psi \\ 1 \end{pmatrix} \left(x_1^0 + x_2^0\right) + \\ &+ \frac{e^{\lambda_2 t}}{1+\xi/\psi} \begin{pmatrix} 1 \\ -1 \end{pmatrix} \left(x_1^0 - \frac{\xi}{\psi} x_2^0\right) \end{aligned} \tag{B.6}$$

where $\begin{pmatrix} x_1^0 \\ x_2^0 \end{pmatrix}$ is the initial condition, $\lambda_1 = 0$ and $\lambda_2 = -(\psi + \xi)$, which gives:

$$x(t) = \frac{1}{1+\xi/\psi} \left[\begin{pmatrix} \xi/\psi \\ 1 \end{pmatrix} \left(x_1^0 + x_2^0\right) + e^{-(\psi+\xi)t} \begin{pmatrix} 1 \\ -1 \end{pmatrix} \left(x_1^0 - \frac{\xi}{\psi} x_2^0\right) \right] \tag{B.7}$$

Since $\lambda_2 = -(\psi + \xi) = -\left(\frac{1}{\tau_{T\to C}} + \frac{1}{\tau_{C\to T}}\right) < 0$ the second addend of **Equation B.7** vanishes for $t \gg 1$. Moreover, we can reasonably suppose that no molecules are in the CIS state at $t = 0$, so $x_2^0 = 0$. This leads to:

$$x(t) = \frac{1}{1+\xi/\psi}\left[\begin{pmatrix} \xi/\psi \\ 1 \end{pmatrix} x_1^0\right] \tag{B.8}$$

It is now straightforward to obtain the ratio x_1/x_2 for $t \gg 1$, which provides an expression of the photostationary equilibrium that can be observed:

$$\frac{x_1}{x_2}\Big|_{t\to\infty} = \frac{\xi}{\psi} \qquad \Rightarrow \qquad \frac{N_{TRANS}}{N_{CIS}}\Big|_{t\to\infty} = \frac{\tau_{T\to C}}{\tau_{C\to T}} \tag{B.9}$$

Considering eq. B.3 and B.4 we can express the photostationary equilibrium as:

$$\begin{aligned} \frac{N_{TRANS}}{N_{CIS}}\Big|_{t\to\infty} &= \frac{\gamma_C}{\gamma_T}\left[1 + \frac{h\nu}{P}\cdot\frac{1}{\gamma_C \tau^{\text{th}}_{C\to T}}\right] = \\ &= \frac{\gamma_C}{\gamma_T}\left[1 + \frac{P^{\text{th}}}{P}\right] \end{aligned} \tag{B.10}$$

where $P^{\text{th}} = \dfrac{h\nu}{\gamma_C \tau^{\text{th}}_{C\to T}}$ indicates the power such that the TRANS $\to$ CIS isomerization has the same probability to be induced either optically or thermally.

In particular, for sufficiently low power densities, that is $P \ll P^{\text{th}}$, the photostationary equilibrium is essentially dependent on P:

$$\frac{N_{TRANS}}{N_{CIS}}\Big|_{t\to\infty} \simeq \frac{\gamma_C}{\gamma_T}\left[\frac{P^{\text{th}}}{P}\right] \tag{B.11}$$

On the other hand, for $P \gg P^{\text{th}}$ the photostationary equilibrium can be considered as independent from P:

$$\frac{N_{TRANS}}{N_{CIS}}\Big|_{t\to\infty} \simeq \frac{\gamma_C}{\gamma_T} \tag{B.12}$$

Appendix C

Photo-induced mechanical work

C.1 Deformation energy estimation

In section 4.1 we have demonstrated that in hybrid metallic/photochromic layered structures the photodeformation induced on the photochromic film is transferred to the overlying 20 nm thick golden layer. The deformation amplitude of both layers is of the same order of magnitude, about 60 nm. This means that a mechanical work is exerted by the film surface on the overlying metal layer. We can try to estimate this energy. Supposing that we can treat the gold layer as a continuos material we can slice it in stripes having the length of the film, as described in **Figure C.1**(a). Each slice has a width δ equal to the semi-period $\frac{\Lambda}{2} \simeq 400\ nm$ of the inscribed pattern. For each slice we consider a unit beam, described in (b), having a unitary length $u = 1\ nm$ and thickness $e = 20\ nm$. We can calculate the load q (expressed in nN) that must be applied to the unit beam to obtain a sinusoidal deformation ν (expressed in nm) having a total amplitude $2A = 60\ nm$, observed experimentally in the case of $\pm 45°$ polarized light (**Figure 4.4**). This will lead to the deformation energy W_u per unit beam.

The classical Euler-Bernulli beam equation is:

$$\frac{\partial^2}{\partial x^2}\left(EI\frac{\partial^2 \nu}{\partial x^2}\right) = q \tag{C.1}$$

where $I = u \cdot e^3/12$ is the second moment of area of the unit beam and the deformation ν can be described by:

$$\nu = Asin\left(\frac{2\pi}{\delta}x\right) \tag{C.2}$$

A being the half of the total deformation amplitude.

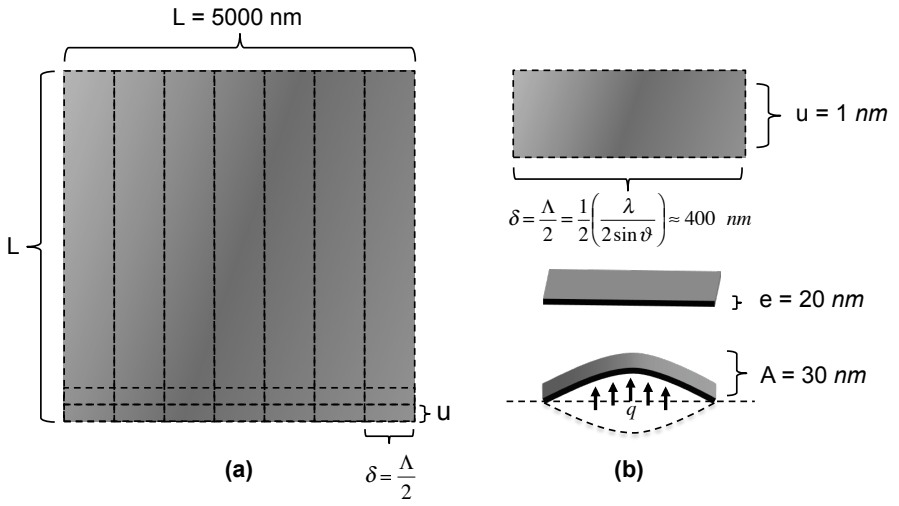

FIGURE C.1: Deformation force calculation.

So the work done to bend a single unit is:

$$W_u = \int_0^{\delta} q\, dx \tag{C.3}$$

In our case, $W_u = 1.5\ nJ$, which is the equivalent of a $0.15\ nN \cdot m$ torque for an hypothetical $5°$ rotation of a nano wheel of a few μg, for a radius of rotation $r = 400\ nm$. Note that this energy is larger than the optical energy necessary to actually produce the deformation in the gold layer that we have studied. This is probably due to the fact that the calculation is made for a single gold crystal, while the thin gold layer that we have deposited is poly-crystalline and its mechanical properties are defined by the grain boundaries, rather than the crystalline lattice. The W_u value can be a rough evaluation of the energy that can be transferred during a photodeformation process. However, as we have seen in section 4.1.2 in the case of a PMMA matrix, the time evolution of the photo-induced deformation, for the uncoated and the gold-coated films are almost identical, which means that the photochromic film makes almost *no effort* to deform the overlying golden layer. It would be interesting to have a more precise estimation of the energy that can be transfered and of the force that could be exerted by the surface photodeformation on a mechanical nanodevice.

Appendix D

Photo-induced deformation in PMMA-DR1

D.1 Polarization effects in PMMA-DR1 at different power densities

In **Chapter 3** we have shown that in PMMA-DR1 matter migration is observed under both *s*- and *p*-polarized interferences. Here we report the results of our observations at different illumination power densities, in both polarization configurations.

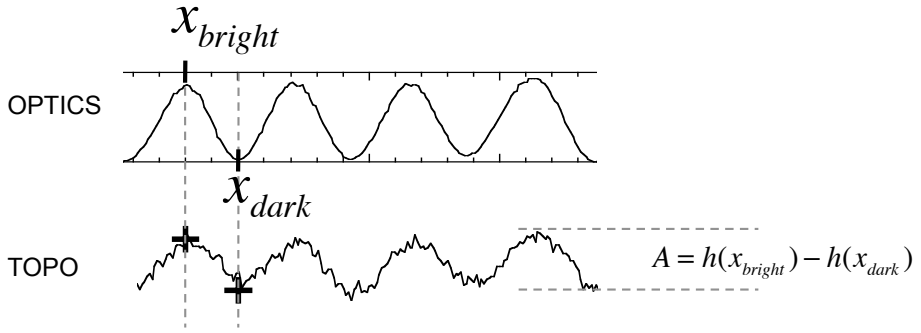

FIGURE D.1: Deformation amplitude convention.

We use the convention adopted in section 3.4, where we consider the intensity pattern spatial distribution as the absolute spatial reference. The deformation amplitude A is given by:

$$A = h(x_{bright}) - h(x_{dark}) \tag{D.1}$$

where x_{bright} and x_{dark} are defined in **Figure D.1**. So, $A > 0$ indicates matter accumulation in the brighter fringes, while $A < 0$ indicates matter accumulation in the

n.	light power density (mW/mm^2) and pol.	av. migr. rate $t < 10$ (nm/s)	av. migr. rate (nm/s)	max matrix photoexp. (nm)	max matter migr. (nm)
A	0.07 - (S)	0.07	0.012	0.9	10
B	0.4 - (S)	0.3	0.025	1.4	15
C	2.3 - (S)	0.71	0.16	1.9	17
A'	0.07 - (P)	0.05	0.02	1.3	24
B'	0.4 - (P)	0.4	0.05	1.2	38
C'	2.3 - (P)	0.9	0.2	1.8	53

TABLE D.1: PMMA-DR1: photodeformation dependence on the light intensity and on the polarization. The average migration rate has been estimated on each curve 1) during the first 10 s and 2) considering the maximum deformation obtained and the first instant corresponding to this value.

darker fringes. For every scan-line, we consider the average value of A obtained over five interference periods.

In **Figure D.2** we show the photodeformation obtained under s- and p-polarized interfering beams at different light power densities (0.07, 0.4[1] and 2.3 mW/mm^2). The corresponding experimental values are reported in table D.1.
In both polarization configurations, two deformation regimes are observed. First, matrix photoexpansion produces the fast growth of weak amplitude SRG (< 2 nm) in the brighter fringes, i.e. *in phase* with the interference pattern. Subsequently, matter migration induces a slow matter displacement towards the darker fringes, producing SRG growth of higher amplitude and half-a-period spatially shifted with respect to the interference pattern (so-called π-*phase*). Under s-polarized interference (**Figure D.2**(a)) the maximum absolute value of the deformation does not exceed 17 nm, while under p-polarized interference (**Figure D.2** (b)) we observe higher deformation amplitudes, with a maximum of 53 nm for the highest power density. On the other hand, the SRG growth rate[2] for both polarization configurations is quite similar, for each power density.

[1] 0.07 and 0.4 mW/mm^2 have been obtained through NG4 filters 3 mm and 2 mm thick respectively.
[2] Considering the average growth rate during the first 10 s.

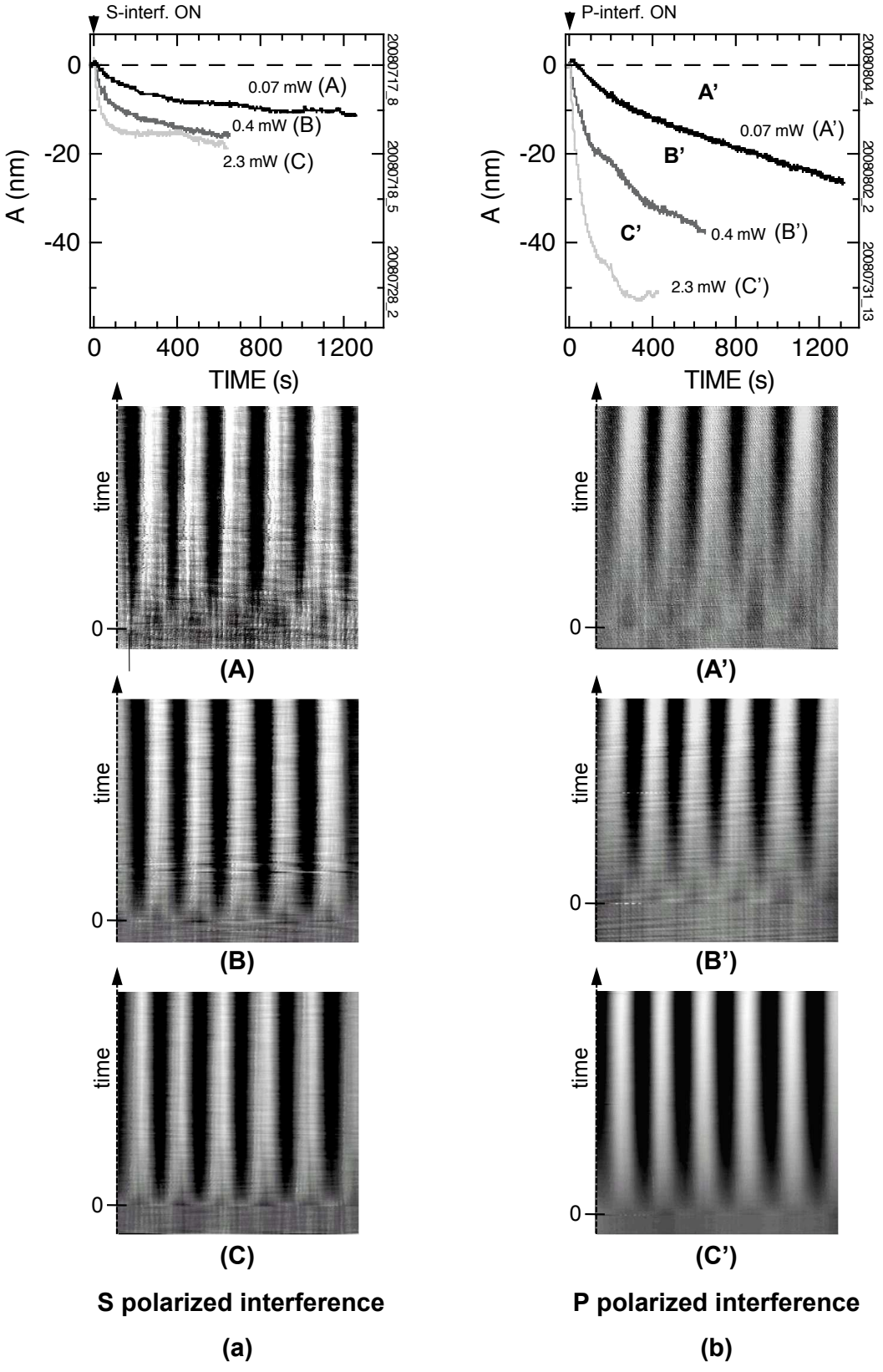

FIGURE D.2: PMMA-DR1 photoinduced deformation. (a) From top to bottom: time evolution of the photoinduced deformation under *s*-polarized light for different power densities (A: 0.07 mW/mm^2), (B: 0.4 mW/mm^2), (C: 2.3 mW/mm^2) and the corresponding topography images; (b) same, under *p*-polarized light. Topography images (256 $\times$ 256 points) are obtained scanning over the same line, on the x axis, at 1.15 Hz, scan-range = 5 μm. Laser wavelength: 473 nm; the sample is a PMMA-DR1 film having a thickness of $\simeq$ 180 nm.

Bibliography

[1] A. Natansohn, P. Rochon, M. S. Ho, and C. Barret. Azo polymers for reversible optical storage .6. poly[4-[2-(methacryloyloxy)ethyl]azobenzene]. *Macromolecules*, 28(12):4179–4183, June 1995.

[2] D. Y. Kim, S. K. Tripathy, Lian Li, and J. Kumar. Laser-induced holographic surface relief gratings on nonlinear optical polymer films. *Applied Physics Letters*, 66 (10):1166–1168, 1995. doi: 10.1063/1.113845. URL http://link.aip.org/link/?APL/66/1166/1.

[3] Almeria Natansohn and Paul Rochon. Photoinduced motions in azo-containing polymers. *Chemical Reviews*, 102(11):4139–4176, 10 2002. URL http://dx.doi.org/10.1021/cr970155y.

[4] Kevin G. Yager and Christopher J. Barrett. Novel photo-switching using azobenzene functional materials. *Journal of Photochemistry and Photobiology A: Chemistry*, 182(3):250 – 261, 2006. ISSN 1010-6030. doi: DOI:10.1016/j.jphotochem.2006.04.021. URL http://www.sciencedirect.com/science/article/B6TGY-4K18VSP-1/2/c00807901259cd303aba19c5442fe822. Proceedings of 7th AIST International Symposium on Photoreaction Control and Photofunctional Materials, 7th AIST International Symposium on Photoreaction Control and Photofunctional Materials.

[5] Ke Yang, Suizhou Yang, Xiaogong Wang, and Jayant Kumar. Enhancing the inscription rate of surface relief gratings with an incoherent assisting light beam. *Applied Physics Letters*, 84(22):4517–4519, 2004. doi: 10.1063/1.1757643. URL http://link.aip.org/link/?APL/84/4517/1.

[6] N. Landraud, J. Peretti, F. Chaput, G. Lampel, J. P. Boilot, K. Lahlil, and V. I. Safarov. Near-field optical patterning on azo-hybrid sol-gel films. *Applied Physics Letters*, 79(27):4562–4564, December 2001.

[7] S. P. Bian, J. M. Williams, D. Y. Kim, L. A. Li, S. Balasubramanian, J. Kumar, and S. Tripathy. Photoinduced surface deformations on azobenzene polymer films. *Journal Of Applied Physics*, 86(8):4498–4508, October 1999.

[8] Nirmal K. Viswanathan, Srinivasan Balasubramanian, Lian Li, Sukant K. Tripathy, and Jayant Kumar. A detailed investigation of the polarization-dependent surface-relief-grating formation process on azo polymer films. *Japanese Journal of Applied Physics*, 38(Part 1, No. 10):5928–5937, 1999. doi: 10.1143/JJAP.38.5928. URL http://jjap.ipap.jp/link?JJAP/38/5928/.

[9] N. K. Viswanathan, D. Y. Kim, S. P. Bian, J. Williams, W. Liu, L. Li, L. Samuelson, J. Kumar, and S. K. Tripathy. Surface relief structures on azo polymer films. *Journal Of Materials Chemistry*, 9(9):1941–1955, September 1999.

[10] S. Bian, L. Li, J. Kumar, D. Y. Kim, J. Williams, and S. K. Tripathy. Single laser beam-induced surface deformation on azobenzene polymer films. *Applied Physics Letters*, 73(13):1817–1819, 1998. doi: 10.1063/1.122292. URL http://link.aip.org/link/?APL/73/1817/1.

[11] T. Fukuda and D. Barada. Photoinduced mass transport by one-dimensional gaussian beam irradiation: Width and polarization dependence. *Japanese Journal of Applied Physics*, 45(1B):470–474, JAN 2006. ISSN 0021-4922. doi: 10.1143/JJAP.45.470. 3rd International Conference on Molecular Electronics and Bioelectronics, Tokyo, JAPAN, MAR 03-04, 2005.

[12] T. Grosjean and D. Courjon. Photopolymers as vectorial sensors of the electric field. *Optics Express*, 14(6):2203–2210, 2006.

[13] Masahide Itoh, Kenji Harada, Shun ichi Kamemaru, and Toyohiko Yatagai. Holographic recording on azo-benzene functionalized polymer film. *Japanese Journal of Applied Physics*, 43(7B):4968–4971, 2004. doi: 10.1143/JJAP.43.4968. URL http://jjap.ipap.jp/link?JJAP/43/4968/.

[14] D. Garrot, Y. Lassailly, K. Lahlil, J. P. Boilot, and J. Peretti. Real-time near-field imaging of photoinduced matter motion in thin solid films containing azobenzene derivatives. *Applied Physics Letters*, 94(3):033303, 2009. doi: 10.1063/1.3073742. URL http://link.aip.org/link/?APL/94/033303/1.

[15] Renaud Bachelot, Fekhra H'Dhili, Dominique Barchiesi, Gilles Lerondel, Radouane Fikri, Pascal Royer, Nathalie Landraud, Jacques Peretti, Frederic Chaput, Georges Lampel, Jean-Pierre Boilot, and Khalid Lahlil. Apertureless near-field optical microscopy: A study of the local tip field enhancement using photosensitive

azobenzene-containing films. *Journal of Applied Physics*, 94(3):2060–2072, 2003. doi: 10.1063/1.1585117. URL http://link.aip.org/link/?JAP/94/2060/1.

[16] K. Yang, S. Z. Yang, and J. Kumar. Formation mechanism of surface relief structures on amorphous azopolymer films. *Physical Review B*, 73(16):165204, April 2006.

[17] B. Bellini, J. Ackermann, H. Klein, Ch Grave, Ph Dumas, and V. Safarov. Light-induced molecular motion of azobenzene-containing molecules: a random-walk model. *Journal of Physics-Condensed Matter*, 18(33, Sp. Iss. SI):S1817–S1835, AUG 23 2006. ISSN 0953-8984. doi: {10.1088/0953-8984/18/33/S04}. Meeting on Molecular Nanomachines, Les Houches, FRANCE, JAN 17-21, 2005.

[18] M. L. Juan, J. Plain, R. Bachelot, P. Royer, S. K. Gray, and G. P. Wiederrecht. Stochastic model for photoinduced surface relief grating formation through molecular transport in polymer films. *Applied Physics Letters*, 93(15):153304, 2008. doi: 10.1063/1.2999625. URL http://link.aip.org/link/?APL/93/153304/1.

[19] X. L. Jiang, L. Li, J. Kumar, D. Y. Kim, and S. K. Tripathy. Unusual polarization dependent optical erasure of surface relief gratings on azobenzene polymer films. *Applied Physics Letters*, 72(20):2502–2504, May 1998.

[20] CR Mendonca, A Dhanabalan, DT Balogh, L Misoguti, DS dos Santos, MA Pereira-da Silva, JA Giacometti, SC Zilio, and ON Oliveira. Optically induced birefringence and surface relief gratings in composite langmuir-blodgett (lb) films of poly[4 '-[[2-(methacryloyloxy)ethyl]ethylamino]-2-chloro-4-nitroazobenzene] (hpdr13) and cadmium stearate. *Macromolecules*, 32(5):1493–1499, 1999. ISSN 0024-9297.

[21] P. Lefin, Fiorini C., and Nunzi J-M. Anisotropy of the photo-induced translation diffusion of azobenzene dyes in polymer matrices. *Pure and Applied Optics: Journal of the European Optical Society Part A*, 7:71–82(12), 1998. URL http://www.ingentaconnect.com/content/iop/pao/1998/00000007/00000001/art00011.

[22] G. S. Hartley. The cis-form of azobenzene. *Nature*, 140:281, 1937.

[23] K. Ichimura, S. K. Oh, and M. Nakagawa. Light-driven motion of liquids on a photoresponsive surface. *Science*, 288(5471):1624–1626, June 2000.

[24] C Hubert, C Fiorini-Debuisschert, I Maurin, JM Nunzi, and P Raimond. Spontaneous patterning of hexagonal structures in an azo-polymer using light-controlled mass transport. *Advanced Materials*, 14(10):729, 2002. ISSN 0935-9648.

[25] T. Ikeda, M. Nakano, Y. L. Yu, O. Tsutsumi, and A. Kanazawa. Anisotropic bending and unbending behavior of azobenzene liquid-crystalline gels by light exposure. *Advanced Materials*, 15(3):201, February 2003.

[26] P. Karageorgiev, D. Neher, B. Schulz, B. Stiller, U. Pietsch, M. Giersig, and L. Brehmer. From anisotropic photo-fluidity towards nanomanipulation in the optical near-field. *Nature Materials*, 4(9):699–703, 2005.

[27] Yann Gilbert, Renaud Bachelot, Alexandre Vial, Gilles Lerondel, Pascal Royer, Alexandre Bouhelier, and Gary Wiederrecht. Photoresponsive polymers for topographic simulation of the optical near-field of a nanometer sized gold tip in a highly focused laser beam. *Opt. Express*, 13(10):3619–3624, 2005. URL http://www.opticsexpress.org/abstract.cfm?URI=oe-13-10-3619.

[28] T Muraoka, K Kinbara, and T Aida. Mechanical twisting of a guest by a photoresponsive host. *Nature*, 440(7083):512–515, 2006. ISSN 0028-0836. doi: 10.1038/nature04635.

[29] Sarah Angelos, Eunshil Choi, Fritz Vogtle, Luisa De Cola, and Jeffrey I. Zink. Photo-driven expulsion of molecules from mesostructured silica nanoparticles. *The Journal of Physical Chemistry C*, 111(18):6589–6592, May 2007. ISSN 1932-7447. URL http://dx.doi.org/10.1021/jp070721l.

[30] Leonid M. Goldenberg, Yuri Gritsai, Olga Kulikovska, and Joachim Stumpe. Three-dimensional planarized diffraction structures based on surface relief gratings in azobenzene materials. *Opt. Lett.*, 33(12):1309–1311, 2008. URL http://ol.osa.org/abstract.cfm?URI=ol-33-12-1309.

[31] H. Rau. *Photochemistry and Photophysics, Volume II.* CRC - Boca Raton, FL, 1989.

[32] T. Buffeteau, F. Lagugne Labarthet, M. Pezolet, and C. Sourisseau. Dynamics of photoinduced orientation of nonpolar azobenzene groups in polymer films. characterization of the cis isomers by visible and ftir spectroscopies. *Macromolecules*, 34 (21):7514–7521, 09 2001. URL http://dx.doi.org/10.1021/ma010279j.

[33] Thomas Garm Pedersen, P. S. Ramanujam, Per Michael Johansen, and Søren Hvilsted. Quantum theory and experimental studies of absorption spectra and photoisomerization of azobenzene polymers. *J. Opt. Soc. Am. B*, 15(11):2721–2730, 1998. URL http://josab.osa.org/abstract.cfm?URI=josab-15-11-2721.

[34] R. Loucif-Saibi, K. Nakatani, J. A. Delaire, M. Dumont, and Z. Sekkat. Photoisomerization and second harmonic generation in disperse red one-doped and -functionalized poly(methyl methacrylate) films. *Chemistry of Materials*, 5(2):229–236, 05 1993. URL http://dx.doi.org/10.1021/cm00026a014.

[35] Akihiro Abe, Hideyuki Kobayashi, Tokiji Kawamura, Masazumi Date, Toshiyuki Uryu, and Kei Matsuzaki. Statistical properties of the poly(n-vinylcabazole) chain

as estimated from an nmr analysis of 2,4-bis-n-cabazolylpentane. *Macromolecules*, 21(12):3414–3419, 05 2002. URL http://dx.doi.org/10.1021/ma00190a011.

[36] Takuya Naito, Kazuyuki Horie, and Itaru Mita. Photochemistry in polymer solids: 12. effects of main-chain structures and formation of hydrogen bonds on photoisomerization of azobenzene in various polymer films. *Polymer*, 34(19): 4140 – 4145, 1993. ISSN 0032-3861. doi: DOI:10.1016/0032-3861(93)90680-9. URL http://www.sciencedirect.com/science/article/B6TXW-48DYJYS-JP/2/37738f5b094ac9744a1da7051ed1b5c5.

[37] Bharat Kumar and K. A. Suresh. Kinetics of trans-cis isomerization in azobenzene dimers at an air-water interface. *Physical Review E (Statistical, Nonlinear, and Soft Matter Physics)*, 80(2):021601, 2009. doi: 10.1103/PhysRevE.80.021601. URL http://link.aps.org/abstract/PRE/v80/e021601.

[38] J. Lemarie J. Royanette, R. Arnaud. *Can. J. Chem.*, 52:1858, 1974.

[39] Hermann Rau and Erik Lueddecke. On the rotation-inversion controversy on photoisomerization of azobenzenes. experimental proof of inversion. *Journal of the American Chemical Society*, 104(6):1616–1620, 05 2002. URL http://dx.doi.org/10.1021/ja00370a028.

[40] Nathalie Landraud. *Ph.D. Thesis: Nanostructuration optique de films sol-gel photochromiques par microscopie en champ proche*. Ecole Polytechnique, 2002.

[41] T. Todorov, L. Nikolova, and N. Tomova. Polarization holography. 1: A new high-efficiency organic material with reversible photoinduced birefringence. *Appl. Opt.*, 23(23):4309–4312, 12 1984. URL http://ao.osa.org/abstract.cfm?URI=ao-23-23-4309.

[42] Bruno Darracq, Frédéric Chaput, Khalid Lahlil, Jean-Pierre Boilot, Yves Levy, Valerie Alain, Lionel Ventelon, and Mireille Blanchard-Desce. Novel photorefractive sol-gel materials. *Optical Materials*, 9(1-4):265 – 270, 1998. ISSN 0925-3467. doi: DOI:10.1016/S0925-3467(97)00151-1. URL http://www.sciencedirect.com/science/article/B6TXP-3VN034S-1R/2/d8ca3a3d5859c851560f624c5988f362. Materials, Physics and Devices For Molecular Electronics and Photonics.

[43] Christopher J. Barrett, Almeria L. Natansohn, and Paul L. Rochon. Mechanism of optically inscribed high-efficiency diffraction gratings in azo polymer films. *The Journal of Physical Chemistry*, 100(21):8836–8842, 05 1996. URL http://dx.doi.org/10.1021/jp953300p.

[44] Nirmal K. Viswanathan, Srinivasan Balasubramanian, Lian Li, Jayant Kumar, and Sukant K. Tripathy. Surface-initiated mechanism for the formation of relief gratings

on azo-polymer films. *The Journal of Physical Chemistry B*, 102(31):6064–6070, 07 1998. URL http://dx.doi.org/10.1021/jp981425z.

[45] Daisuke Barada, Takashi Fukuda, Masahide Itoh, and Toyohiko Yatagai. Numerical analysis of photoinduced surface relief grating formation by particle method. *Optical Review*, 12(4):271–273, 07 2005. URL http://dx.doi.org/10.1007/s10043-005-0271-z.

[46] Md. Zahangir Alam, Tomoko Ohmachi, Tomonari Ogata, Takamasa Nonaka, and Seiji Kurihara. Photoisomerization behavior and photoinduced surface relief gratings on azopolymer film by a monochromatic light irradiation. *Optical Materials*, 29(4):365 – 370, 2006. ISSN 0925-3467. doi: DOI:10.1016/j.optmat.2005.10.005. URL http://www.sciencedirect.com/science/article/B6TXP-4HWXP03-1/2/a147cc79fda983a71b38c57eca1896f8.

[47] Jayant Kumar, Lian Li, Xin Li Jiang, Dong-Yu Kim, Taek Seung Lee, and Sukant Tripathy. Gradient force: The mechanism for surface relief grating formation in azobenzene functionalized polymers. *Applied Physics Letters*, 72(17):2096–2098, 1998. doi: 10.1063/1.121287. URL http://link.aip.org/link/?APL/72/2096/1.

[48] Oleh M. Tanchak and Christopher J. Barrett. Light-induced reversible volume changes in thin films of azo polymers: The photomechanical effect. *Macromolecules*, 38(25):10566–10570, 11 2005. URL http://dx.doi.org/10.1021/ma051564w.

[49] O. Henneberg, Th. Geue, M. Saphiannikova, U. Pietsch, A. Natansohn, P. Rochon, and K. Finkelstein. Investigation of material flow on inscribing a polymer surface grating probing x-ray and vis light scattering. *Colloids and Surfaces A: Physicochemical and Engineering Aspects*, 198-200:107–111, 2 2002. URL http://www.sciencedirect.com/science/article/B6TFR-454JBTJ-H/2/38ea38366b3f32725df1c36aec2d7c14.

[50] R. Bachelot, A. Bouhelier, G. Wiederrecht, Y. Gilbert, L. Novotny, and P. Royer. Longitudinal sensitivity of the photoinduced molecular migration in azobenzene-containing films. *Proceedings of the SPIE - The International Society for Optical Engineering*, 6335:63350E–1–9, 2006.

[51] Singiresu S. Rao. *Mechanical Vibrations (4th Edition)*. Prentice Hall, 2003.

[52] Damien Garrot. *PhD Thesis: Etude par microscopie en champ proche des phénomènes de migration de matière photo-induite dans les matériaux photochromiques*. Ecole Polytechnique, 2006.

[53] C. Barrett, A. Natansohn, and P. Rochon. Cis-trans thermal isomerization rates of bound and doped azobenzenes in a series of polymers. *Chemistry of Materials*, 7 (5):899–903, 05 2002. URL http://dx.doi.org/10.1021/cm00053a014.

[54] B. Darracq. *PhD thesis: Etude de mecanisme de migration et d'orientation moleculaire dans des films minces sol-gel : deformation de surface et proprietes optiques non-lineaires quadratiques.* Université Paris-Sud, 1999.

[55] J. Biteau, F. Chaput, K. Lahlil, J. P. Boilot, G. M. Tsivgoulis, J. M. Lehn, B. Darracq, C. Marois, and Y. Levy. Large and stable refractive index change in photochromic hybrid materials. *Chemistry Of Materials*, 10(7):1945–1950, July 1998.

[56] Ke Yang, Suizhou Yang, Xiaogong Wang, and Jayant Kumar. Response to "comment on 'enhancing the inscription rate of surface relief gratings with an incoherent assisting light beam' " [appl. phys. lett. [bold 86], 146101 (2005)]. *Applied Physics Letters*, 86(14):146102, 2005. doi: 10.1063/1.1899756. URL http://link.aip.org/link/?APL/86/146102/1.

[57] Bert Hecht and Lukas Novotny. *Principles of Nano-Optics.* Cambridge University Press, NY, 2006.

[58] Yann Gilbert, Renaud Bachelot, Pascal Royer, Alexandre Bouhelier, Gary P. Wiederrecht, and Lukas Novotny. Longitudinal anisotropy of the photoinduced molecular migration in azobenzene polymer films. *Opt. Lett.*, 31(5):613–615, 2006. URL http://ol.osa.org/abstract.cfm?URI=ol-31-5-613.

[59] S. Patane, A. Arena, M. Allegrini, L. Andreozzi, M. Faetti, and M. Giordano. Near-field optical writing on azo-polymethacrylate spin-coated films. *Optics Communications*, 210(1-2):37 – 41, 2002. ISSN 0030-4018. doi: DOI:10.1016/S0030-4018(02)01764-9. URL http://www.sciencedirect.com/science/article/B6TVF-46DM01B-1/2/8b0232f74db3ef8025b362e10902392d.

[60] S. Orlic, S. Ulm, and H. J. Eichler. 3d bit-oriented optical storage in photopolymers. *Journal Of Optics A-Pure And Applied Optics*, 3(1):72–81, January 2001.

[61] O.N. Oliveira et Al. Optical storage and surface-relief gratings in azobenzene-containing nanostructured films. *Advances in colloidal interface science*, 116:179–192, 2005.

[62] Y. L. Yu, M. Nakano, and T. Ikeda. Directed bending of a polymer film by light - miniaturizing a simple photomechanical system could expand its range of applications. *Nature*, 425(6954):145–145, September 2003.

[63] N. Tabiryan, S. Serak, X. M. Dai, and T. Bunning. Polymer film with optically controlled form and actuation. *Optics Express*, 13(19):7442–7448, September 2005.

[64] T. J. White, N. V. Tabiryan, S. V. Serak, U. A. Hrozhyk, V. P. Tondiglia, H. Koerner, R. A. Vaia, and T. J. Bunning. A high frequency photodriven polymer oscillator. *Soft Matter*, 4(9):1796–1798, 2008.

[65] C. Cocoyer, L. Rocha, L. Sicot, B. Geffroy, R. de Bettignies, C. Sentein, C. Fiorini-Debuisschert, and P. Raimond. Implementation of submicrometric periodic surface structures toward improvement of organic-solar-cell performances. *Applied Physics Letters*, 88(13):133108, 2006. doi: 10.1063/1.2188600. URL http://link.aip.org/link/?APL/88/133108/1.

[66] J. Hillier J. Turkevich, P. C. Stevenson. A study of the nucleation and growth processes in the synthesis of colloidal gold. *Discussions of the Faraday Society*, 11: 55, 1951.

[67] Bharat Bhushan. *Springer Handbook of Nano-technology*. Springer, 2004.

[68] Syed Rizvi. *Handbook of photomask manufacturing technology*. Taylor & Francis, 2003.

[69] Chi-Ming Che et Al. A submicrometer wire-to-wheel metamorphism of hybrid tridentate cyclometalated platinum (ii) complexes. *Nanoletters*, 47:4568–4572, 2008.